



# Deformation mechanisms of metastable stainless steels accessed locally by monotonic and cyclic nanoindentation

Ina Sapezanskaia

## ► To cite this version:

Ina Sapezanskaia. Deformation mechanisms of metastable stainless steels accessed locally by monotonic and cyclic nanoindentation. Mechanics of materials [physics.class-ph]. Université de Lorraine, 2016. English. NNT : 2016LORR0128 . tel-01752370

**HAL Id: tel-01752370**

**<https://hal.univ-lorraine.fr/tel-01752370>**

Submitted on 22 Jul 2018

**HAL** is a multi-disciplinary open access archive for the deposit and dissemination of scientific research documents, whether they are published or not. The documents may come from teaching and research institutions in France or abroad, or from public or private research centers.

L'archive ouverte pluridisciplinaire **HAL**, est destinée au dépôt et à la diffusion de documents scientifiques de niveau recherche, publiés ou non, émanant des établissements d'enseignement et de recherche français ou étrangers, des laboratoires publics ou privés.



## AVERTISSEMENT

Ce document est le fruit d'un long travail approuvé par le jury de soutenance et mis à disposition de l'ensemble de la communauté universitaire élargie.

Il est soumis à la propriété intellectuelle de l'auteur. Ceci implique une obligation de citation et de référencement lors de l'utilisation de ce document.

D'autre part, toute contrefaçon, plagiat, reproduction illicite encourt une poursuite pénale.

Contact : [ddoc-theses-contact@univ-lorraine.fr](mailto:ddoc-theses-contact@univ-lorraine.fr)

## LIENS

Code de la Propriété Intellectuelle. articles L 122. 4

Code de la Propriété Intellectuelle. articles L 335.2- L 335.10

[http://www.cfcopies.com/V2/leg/leg\\_droi.php](http://www.cfcopies.com/V2/leg/leg_droi.php)

<http://www.culture.gouv.fr/culture/infos-pratiques/droits/protection.htm>

# **Deformation mechanisms of metastable stainless steels accessed locally by monotonic and cyclic nanoindentation**

**Doctoral Dissertation** submitted to Universitat Politècnica de Catalunya and Université de Lorraine for the double degree of Doctor of Philosophy in frame of the European Joint Doctoral Program in Materials Science and Engineering (DocMASE) by

**Ina Sapezanskaia**

Universitat Politècnica de Catalunya, Departament de Ciència dels Materials i Enginyeria Metal·lúrgica

Institut Jean Lamour –UMR 7198- Département CP2S – Equipe 303

Thesis advisors:

**Professor Dr. Antonio Manuel Mateo García (UPC)**

**Professor Dr. Abdelkrim Redjaïmia (UdL)**

**July 21, 2016**



**UNIVERSITAT POLITÈCNICA DE CATALUNYA  
BARCELONATECH**

Departament de Ciència dels Materials  
i Enginyeria Metal·lúrgica



**UNIVERSITÉ  
DE LORRAINE**



**UNIVERSITAT POLITÈCNICA DE CATALUNYA**  
**BARCELONATECH**

**Departament de Ciència dels Materials  
i Enginyeria Metal·lúrgica**



**UNIVERSITÉ  
DE LORRAINE**



# **Deformation mechanisms of metastable stainless steels accessed locally by monotonic and cyclic nanoindentation**

Présentée pour l'obtention du titre de :  
**DOCTEUR de L'UNIVERSITÉ DE LORRAINE**  
Spécialité: Sciences de matériaux  
Par :

**Ina Sapezanskaia**

## **Membres du jury :**

### *Rapporteur*

**Christian MOTZ**, Professeur, Lehrstuhl für Experimentelle Methodik der Werkstoffwissenschaften, Universität Des Saarlandes (Saarbrücken-Allemagne)

### *Rapporteur*

**Jean-Bernard VOGT**, Professeur, Université de Lille, Unité Matériaux Et Transformations, Université de Lille (Lille, France)

### *Directeur de thèse*

**Antonio M. MATEO**, Professeur, Departament de Ciència dels Materials i Enginyeria Metal·lúrgica, Universitat Politècnica de Catalunya (Barcelona, Espagne)

### *Co-Directeur de thèse*

**Abdelrim REDJAÏMIA**, Professeur, IJL, Université de Lorraine (Nancy)

-

*Institut Jean Lamour –UMR 7198- Département SI2M – Equipe 303  
Parc de Saurupt - CS 50840- 54011 NANCY Cedex  
Université de Lorraine – Pôle M4 : matière, matériaux, métallurgie, mécanique*



## Résumé étendu

Les aciers inoxydables austénitiques métastables, matériaux étudiés dans la présente thèse, se distinguent par leur sensibilité à l'effet TRIP (Transformation Induced Plasticity). Cette transformation induite par la déformation plastique déclenche mécaniquement la transformation austénite → martensite et confère ainsi au matériau des propriétés mécaniques remarquables : une limite d'élasticité et un allongement pouvant atteindre, respectivement, 1000 MPa et 30 % <sup>1</sup>. Ces propriétés impliquent, après écrouissage à froid, une mise en forme aisée de l'acier à l'état recuit et une résistance mécanique élevée. Cependant, une grande vitesse d'écrouissage leur confère une grande capacité d'absorption d'énergie dans des conditions d'impact sévère, en faveur d'une bonne résistance aux chocs <sup>2</sup>.

Les propriétés de fatigue des aciers inoxydables métastables sont remarquables et peuvent être adaptées en ajustant les fractions de phases, austénite-martensite <sup>3</sup>. Cela ouvre une voie d'amélioration des propriétés par un procédé adéquat de mise en forme <sup>4,5</sup>.

A cause de leurs performances mécaniques et en dépit de leur coût élevé, les aciers inoxydables austénitiques métastables sont appelés à se substituer, dans de nombreuses applications, aux aciers au carbone. Cependant, l'inconvénient majeur de ces aciers est la difficulté de prévoir exactement leur comportement mécanique qui dépend principalement des caractéristiques particulières de la microstructure : en effet, la quantité de martensite est aussi pertinente que son type, sa morphologie et sa distribution <sup>6</sup>. Différents mécanismes de déformation peuvent également être activés dans les aciers métastables, notamment le glissement des dislocations, le maclage mécanique et la formation de bandes de cisaillement. Ces mécanismes conduisent en fait à des configurations complexes où coexistent des paquets de macles de déformation, des plaquettes de martensite-ε ainsi que des défauts d'empilement <sup>7,8</sup>.

La compréhension du comportement global de déformation des aciers inoxydables métastables est centrale pour améliorer leur performance et pour adapter correctement les procédés industriels de leur fabrication <sup>3,9</sup>. Les études classiques, à l'échelle macroscopique, ne sont pas suffisantes pour comprendre complètement les mécanismes ci-dessus mentionnés. Suite à ce constat, des techniques de caractérisation, à une échelle locale, sont de plus en plus mises en œuvre <sup>10-15</sup>. La nano-indentation s'est avérée une technique appropriée pour étudier les aciers TRIP, puisque la taille de la zone testée et la précision de la localisation de l'indenteur permettent de caractériser séparément chaque grain de la structure. En outre, l'enregistrement des courbes de charge-déplacement permet un accès complet aux propriétés micromécaniques. Il est ainsi aisé de caractériser des matériaux anisotropes et multiphasés <sup>16-22</sup>.

La présente thèse est consacrée à l'étude des mécanismes de déformation d'un alliage métallique complexe, un acier inoxydable austénitique métastable. Ces aciers sont *stigmatisés* comme complexes car

leurs mécanismes de déformation sont pluriels et se déclenchent souvent de façon concomitante. En effet, les transformations de phases peuvent être activées au cours d'une déformation plastique. Pour parvenir à une meilleure compréhension de ces mécanismes, des expériences de nano-indentation ont été initiées pour déformer à une échelle microscopique et locale le matériau. Cette technique expérimentale permet l'accès à la réponse mécanique des grains individuels via l'analyse des courbes de chargement-déchargement. La nano-indentation cyclique permet aussi l'accumulation progressive de la déformation et d'accéder ainsi aux caractéristiques de la sous-structure par une combinaison de microscopies et diffractions électroniques, notamment les microscopies électroniques à balayage (MEB) et en transmission (MET-HRTEM) ainsi que la diffraction des électrons en mode rétrodiffusés (EBSD).

Les courbes de nano-indentation, en mode chargement-déchargement, ont permis d'accéder à des informations très détaillées sur les propriétés mécaniques sous-jacentes qui pourraient être liées à une reconstruction exhaustive de la sous-structure de déformation, aussi bien en surface du matériau que dans sa masse. Différentes techniques d'investigation, à une échelle très fine, ont permis, entre autres, d'accéder à des caractéristiques telles que la déformation en fonction du temps, la transformation des phases réversible sous charge, l'anisotropie cristalline et l'influences de la taille de grains, en plus de la transmission de la plasticité et de la tenue en fatigue.

La thèse est structurée autour de huit chapitres :

Dans le premier chapitre, nous présentons les aciers métastables ainsi que la technique de nano-indentation. L'état de l'art sur les essais de nano-indentation concernant les aciers inoxydables métastables est passé en revue.

Le deuxième chapitre donne une description de l'acier, objet de cette étude, et les techniques expérimentales mises en œuvre.

Dans le troisième chapitre, nous présentons la caractérisation microstructurale et mécanique de l'acier dans différentes conditions avant nano-indentation. La taille des grains, leur morphologie, la distribution des phases, la texture, ainsi que différents défauts de structure sont passés en revue et analysés.

Dans le quatrième chapitre, différents essais de nano-indentation monotones et cycliques sont conduits sur des grains sélectionnés. Les courbes de chargement-déchargement respectifs sont analysées afin d'accéder localement à la réponse du matériau en termes de transformation de phase, de propagation de la plasticité, de déformation en fonction du temps et de l'évolution cyclique des propriétés mécaniques.

Au cinquième chapitre, les mécanismes de déformation en surface, à partir d'essais de nano-indentation, sont étudiés par microscope et diffraction électronique en mode FESEM, EBSD, TEM et HRTEM. Les caractéristiques de la structure de déformation telles que la formation des bandes de cisaillement microscopiques et finement structurées, la germination de la martensite- $\alpha'$  aux intersections des bandes de

cisaillement ainsi que les bandes de glissement en début de formation ont été étudiées et imagées en haute résolution (HREM). L'étude s'est aussi focalisée sur l'influence des joints de grains lors de la déformation en surface.

Le sixième chapitre est consacré à l'étude des mécanismes de déformation résultant des expériences de nano-indentation juste en-dessous de la surface. Les analyses en MET sont réalisées en fonction de la taille et de l'orientation cristalline des grains indentés. A cet effet, l'influence du mode de test (le contrôle de la charge et/ou de la profondeur d'indentation) et le nombre de cycles d'indentation sont étudiés.

Dans le septième chapitre, une étude par imagerie FIB (Faisceau Ionique Focalisé) et par tomographie est conduite pour compléter les connaissances obtenues par la caractérisation au MET. La caractérisation par FIB a permis une reconstruction 3D de la phase martensitique- $\alpha'$  naissantes sous la pointe du nano-indentateur et a permis de suivre les mécanismes sous-jacents de la propagation de la plasticité.

Enfin, au huitième chapitre, les différents aspects des mécanismes de déformation, mis en exergue dans les chapitres précédents, sont résumés et corrélés.

Certains des principaux résultats, mis en évidence au cours de cette thèse, sont repris ci-après :

Il a été mis en évidence, qu'en fonction de la taille du grain austénitique et de son orientation cristallographique, différents arrangements des dislocations s'opèrent dans les aciers inoxydables métastables, lorsque ces derniers sont soumis à des essais de nano-indentation. Ces deux facteurs ont aussi un impact sur la transformation martensitique. Ainsi, il a été mis en évidence que la martensite- $\alpha'$  est étroitement liée à la relation entre l'orientation des plans de glissement actifs et de l'axe de chargement. En outre, tous les mécanismes de déformation et la transmission de la plasticité sont fortement influencés par la localisation de la contrainte aux joints de grains.

Nous avons constaté que la transformation réversible de la martensite- $\epsilon$  se produit au cours des essais de nano-indentation cycliques. Ce phénomène, connu pour les alliages à mémoire de forme, n'a, à notre connaissance, jamais été rapporté pour les aciers inoxydables. Apparemment, la composition chimique du présent alliage, en particulier son teneur élevée en azote, plaide en faveur de ce comportement. Au cours de cette thèse, nous avons trouvé que ce comportement se produit après un certain nombre de cycles de nano-indentation. Ceci indique qu'une certaine organisation de dislocations doit se produire pour faciliter la transformation de la phase réversible, tel que rapporté dans la littérature <sup>189</sup>.

Sur les courbes charge-déplacement, une non-linéarité, aux faibles charges d'indentation, a été relevée. Ce qui conduit ainsi à des changements de pente dans les courbes. Ce résultat est en bon accord avec ceux de la littérature, rapportés pour la transformation de phase réversible. La formation de la martensite- $\epsilon$  a été mise en évidence. Cette dernière montre un comportement anisotrope et adopte la relation d'orientation de Shoji-Nishiyama, avec une préférence de formation dans les grains orientés de façon appropriée par

rapport à l'axe de chargement. Ce fait a aussi été démontré par la taille de la boucle d'hystérésis enregistrée, lors des essais de nano-indentation cycliques. Cette boucle est plus large pour les grains orientés favorablement pour la transformation martensitique- $\epsilon$ . Le comportement de la transformation réversible est probablement lié au fait que les plaques de la martensite- $\epsilon$ , formées sous les charges appliquées, ont une épaisseur moyenne inférieure à 1 nm, résultat obtenu dans le cadre de cette thèse, et donc, ne sont pas suffisamment stables pour persister après le déchargement. Il est également intéressant de mentionner que la transformation de phase liée aux pop-ins provient de la martensite- $\epsilon$ . Contrairement à cette dernière, la formation de la martensite- $\alpha'$  n'a pu être détectée à partir des courbes P-h.

Dans les tests classiques de fatigue macroscopique, le comportement d'adoucissement est connu pour se produire dans les aciers inoxydables recuits en raison d'une part, de la génération de dislocations mobiles supplémentaires et d'autre part, des configurations de dislocations de basse énergie <sup>245,246</sup>. Les deux mécanismes ont été observés dans cette étude. La génération de dislocations supplémentaires sous charge a été détectée et corrélée au pop-ins, tandis que les arrangements cellulaires des dislocations ont été clairement observés par MET. De ce point de vue, la nano indentation cyclique peut être considérée comme une technique d'analyse du comportement local de fatigue. Les courbes P-h ont montré que généralement l'adoucissement l'emporte sur le durcissement induit par la transformation de phases, alors que le durcissement secondaire ne se produirait que pour certaines orientations cristallines (par exemple  $\langle 111 \rangle$ ) quand la martensite a été formée et s'est développée verticalement sous l'empreinte résiduelle.

En rapport avec l'adoucissement cyclique, un comportement dépendant du temps a été mis à jour : certains chercheurs <sup>229, 233, 362-364</sup> ont trouvé une dépendance avec les vitesses de déformation à la température ambiante, dans les aciers inoxydables AISI 304 et 316. Aux basses déformations imposées, ce comportement conduit à un adoucissement cyclique qui prévaut sur le durcissement cyclique <sup>234</sup>. Ces résultats pourraient être surprenants pour un acier inoxydable métastable qui se distingue normalement par un comportement net de durcissement <sup>231</sup>. La clé pour expliquer le comportement observé est la faible amplitude de contrainte appliquée dans la présente étude, tandis que le durcissement est généralement connu pour se produire lorsqu'il dépasse un certain niveau minimum de déformation.

Nous avons également constaté que les caractéristiques de déformation sont différentes lorsque le mode de chargement est cyclique ou de déplacement, en raison du comportement d'adoucissement. En effet, en mode de chargement, le déplacement ou la profondeur de pénétration augmente avec chaque cycle, conduisant à une accumulation de déformation significative, tandis qu'en mode de déplacement, la déformation imposée est principalement localisée dans le domaine élastique (ou pseudo-élastique).

Ainsi, la nano-indentation offre la possibilité d'étudier le comportement de la déformation dans une plage de déformation plus faible que celle qu'offrent les techniques de tests macroscopiques. Par ailleurs, il faut

signaler que la nano-indentation permet également de déformer à des charges nettement plus élevées que celles qui sont appliquées ici dans cette étude.

Nous avons aussi montré que la pré-déformation stabilise l'acier contre la poursuite de la transformation de phases avec le comportement d'adoucissement cyclique ou de durcissement.

Pour comprendre les phénomènes observés, les deux points suivants doivent être considérés :

1. Contrairement à la transformation  $\gamma \rightarrow \alpha'$ , la transformation  $\gamma \rightarrow$  martensite- $\epsilon$  implique une contraction volumique <sup>365, 366</sup>. Par conséquent, la déformation en traction favorise la formation de la martensite- $\alpha'$  et supprime celle de la martensite- $\epsilon$ . Pour la déformation en compression, c'est le cas contraire qui se produit <sup>365</sup>.

Il est, par ailleurs, bien établi que la réponse pseudo-élastique des alliages à mémoire de forme est beaucoup plus marquée pour la nano-indentation que pour les essais de traction <sup>187</sup>. Par conséquent, l'apparition transformation de martensite- $\alpha'$  se produit pour la nano-indentation (principalement en compression) avec un décalage vers des valeurs de contrainte plus élevées, par rapport aux procédés de mise en formes macroscopiques, tels que le laminage à froid <sup>365</sup>. Ceci explique pourquoi, dans la présente d'étude, la formation des bandes de cisaillement a été facilement observée, alors que la martensite- $\alpha'$  était encore dans son état initial de formation.

2. Il est également connu que la formation de la martensite- $\epsilon$  conduit à un adoucissement <sup>367, 368</sup>. Cette circonstance est en très bon accord avec l'adoucissement observé au-dessous du changement de pente (coude) relevé sur la courbe. La région avec une faible pente en-dessous du coude correspond à la majorité des pop-ins, en relation avec la formation réversible de la martensite- $\epsilon$ . D'autre part, étant donné que la caractérisation par MET a révélé qu'au moins une partie de la martensite- $\epsilon$  formée est stabilisée sous forme de bandes de cisaillement après le déchargement. La formation de la martensite- $\epsilon$  domine celle des bandes de cisaillement et pourrait contribuer, en collaboration avec le mouvement des dislocations, au comportement d'adoucissement observé.

## Conclusions finales

Dans la présente thèse, le comportement de déformation des grains individuels austénitiques, dans un acier inoxydable métastable polycristallin, a été étudiée par nano-indentation. Cette technique d'essais mécaniques a non seulement l'avantage de fournir des informations avec une grande précision à partir de « petits domaines » mais aussi d'accéder de manière sélective aux mécanismes de déformation avec une résolution spatiale meilleure que celle des techniques d'analyse conventionnelles.

L'analyse des courbes (P-h) de chargement-déchargement et leur corrélation avec les caractéristiques structurales que dispense le MET, a permis d'accéder aux caractéristiques des mécanismes de déformation dans les aciers inoxydables austénitiques métastables, en effet :

- les mécanismes de déformation obtenu par nano-indentation sont, de façon qualitative, similaires à ceux issus des essais macroscopiques classiques
- le comportement de la déformation résultant des essais de nano-indentation fournit des informations à deux niveaux: local, avec accès directement aux grandes contraintes de cisaillement dans les IPZ (zone de pénétration de l'indenteur) et global, par extension à tout le grain indenté.
- la structure de déformation, par nano-indentation, se distingue par des rotations des structures locales, des bandes de cisaillement nano-structurées et par la formation subséquente d'îlots de martensite.
- la structure globale de déformation comprend des arrangements de dislocations, suite au cisaillement homogène à l'intérieur du grain, des défauts plans sur des sites préférentiels (par exemple des joints de grains) ; les joints de grains, jouant le rôle d'obstacles à la transmission de la plasticité.
- les déformations aussi bien globales que spécifiques à la nano-indentation sont fortement anisotropes; elles sont directement liées à l'orientation cristalline de chaque grain du matériau.
- la réponse mécanique à l'indentation et par conséquent les structures de déformation qui en résultent sont fortement dépendantes du volume de confinement, déterminé par la taille et la forme des grains.
- Il a été établi que l'acier AISI 301LN se déforme, au début de sa plasticité, principalement par la formation d'abord des bandes de cisaillement ensuite par d'autres structures de déformation, tels que les arrangements à faible énergie des dislocations ou encore la formation de la martensite- $\alpha'$ .
- la transformation de la martensite- $\varepsilon$  réversible prend place sous chargement de nano-indentation.
- les embryons de martensite- $\alpha'$  germent et coalescent aux intersections des bandes de cisaillement.
- trois types de pop-ins peuvent être obtenus à partir des courbes de P-h, en raison d'abord de la transmission élasto-plastique ensuite de la transformation  $\gamma \leftrightarrow \varepsilon$  et enfin de la transmission de la plasticité à travers les joints de grains.

Concernant les techniques avancées de caractérisation, un bilan peut également être établi:

- la nano-indentation cyclique est un outil puissant pour le suivi de l'évolution des mécanismes de déformation, tandis que le MET est un outil puissant pour la caractérisation de la structure de déformation résultante. La combinaison de la déformation par nano-indentation et la caractérisation ultérieure par MET réalisée pour différentes conditions expérimentales, ont permis une reconstruction *ex-situ* des principes fondamentaux sous-jacents.



- il a été démontré qu'il existe une bonne corrélation entre les données enregistrées au cours d'essais de nano-indentation, et la microstructure liée. Ainsi, à partir de la seule analyse des courbes P-h, des informations importantes sur la dynamique de la déformation, l'influence des joints de grains, le transfert de la plasticité et l'anisotropie cristalline peuvent être recueillies pour la caractérisation du matériau sans avoir besoin de plus de temps ni de coûts d'analyse supplémentaires.
- il a également été confirmé, par corrélation entre les courbes P-h de nano-indentation cyclique et des études de MET, que les pop-ins à des charges élevées (ou nombre élevé de cycles) correspondent effectivement à la transmission de la plasticité.
- il est important de caractériser les structures de déformation du matériau, aussi bien en surface que dans la masse sous-jacente, afin d'accéder à une compréhension globale de son comportement.
- L'intérêt de la technique d'imagerie SIM a été mis en évidence pour la caractérisation de l'évolution des structures fines du matériau ainsi déformé. Par rapport aux autres techniques de caractérisation avancées, telles que l'EBSD pour la caractérisation de la surface et le MET pour la caractérisation dans la masse, le SIM est plus rapide, plus facile et plus rentable. Par rapport à la tomographie transversale, l'imagerie SIM peut fournir des informations plus complètes sur la transformation de la microstructure en 3D.

Pour conclure, cette thèse comprend une approche novatrice concernant la caractérisation à petite échelle des mécanismes de déformation dans les aciers inoxydables austénitiques métastables, en particulier, et dans les matériaux métalliques de façon générale.

# Acknowledgements

I would like to thank my thesis advisor Antonio Mateo and my co-advisor Abdelkrim Redjaïmia for their time, guidance and assistance throughout the course of my thesis. I also appreciate the commitment of Christian Motz and Jean-Bernard Vogt to being my thesis reviewers and members of the jury.

I am grateful to Joan for guiding and encouraging me during these years as a colleague, office mate and friend.

I thank Alan and William, as well as all the other fellow PhDs from CIEFMA and IJL for sharing with me many happy moments during and after work.

And of course I also thank all the members from IJL who welcomed me during my stays in Nancy and with whom I enjoyed many Pause Café and Goûter du Jeudi.

I appreciate the support of Trifon and Isaac at the UPC, as well as of Richard, Gaël, Arnaud, Sylvie, Christine, Jaafar and Erwan at IJL.

I feel committed to Erasmus Mundus for supporting my thesis financially, and to Flavio and Manja, as well as other organizers of the DOCMASE program, for contributing to the success of this international cooperation.

But first of all, I am grateful to my family and friends who supported and encouraged me during all these years.

## Preface

*I have no special talent. I am only passionately curious.*

*Albert Einstein*

Metastable austenitic stainless steels - the material group studied in the present thesis, are distinguished by their susceptibility to the TRIP (Transformation Induced Plasticity) effect, where austenite to martensite transformation is triggered mechanically. This results in a material with outstanding mechanical properties: a yield strength of about 1000 MPa with simultaneous elongation up to 30% have been reported <sup>1</sup>. These properties imply an easy conformation of the steel in the annealed state, combined with a high strength after cold forming. Furthermore, the resulting high work hardening rate confers the steels a high energy absorption capacity under impact condition, interesting for crashworthiness <sup>2</sup>.

Moreover, fatigue properties of metastable stainless steels are outstanding and can be tailored by adjusting the fraction of austenite and martensite <sup>3</sup>. This gives potential for a further improvement of properties by an adequate forming process <sup>4,5</sup>.

As a consequence of those characteristics, it is expected that, in spite of their higher cost, metastable austenitic stainless steels will substitute in many applications the carbon steels used so far. However, the major drawback of using those steels is the difficulty to predict exactly their mechanical behavior, since it depends predominantly on the particular microstructural characteristics: not only the amount of martensite is relevant, but also its type, morphology and distribution <sup>6</sup>. Furthermore, other deformation mechanisms may also be activated in metastable steels, such as dislocations glide, mechanical twinning and formation of shear bands, whereby the latter comprises bundles of coexisting deformation twins,  $\epsilon$ -martensite plates and stacking faults <sup>7,8</sup>.

Consequently, understanding the overall deformation behavior of metastable stainless steels is essential for improving their performance and also to properly tailor the manufacturing of industrial components <sup>3,9</sup>. In this sense, conventional studies at macroscopic scale are not sufficient to completely understand the above mentioned mechanisms, and hence small-scale techniques are increasingly applied <sup>10-15</sup>. Particularly, nanoindentation has proven to be a suitable tool to study TRIP steels, since the size of the indenter tip and the lateral precision of indenter placement allow separate testing of every single grain. Furthermore, the recording of load-displacement curves can give a comprehensive access to the

micromechanical properties. Thus, it is readily applied to characterize anisotropic and multi-phase materials <sup>16-22</sup>.

On the other hand, it is plausible to assume that the evolution of deformation features can be followed up with repeated nanoindentation loading on the same location, *i.e.* cyclic nanoindentation. This investigation approach is relatively scarce yet. For example, cyclic nanoindentation tests at constant load/penetration amplitude have been reported for materials such as GaN thin films to analyze deformation mechanisms <sup>23</sup>, in CaCO<sub>3</sub> to study fatigue-induced crack formation <sup>24</sup> and in NiTi shape memory alloys to investigate phase transformations <sup>25</sup>. However, to the best knowledge of the authors, cyclic nanoindentation testing has never been performed for any steel grade.

One of the most convenient techniques for subsurface characterization of metallic alloys is TEM (Transmission Electron Microscopy). Saka and Nagaya performed the first TEM examination of a cross section of a residual nanoindentation imprint in 1995 <sup>26</sup>. Since then, this methodology has become increasingly common to evaluate the deformation mechanisms activated by nanoindentation testing <sup>27-30</sup>. Nevertheless, no detailed studies have been performed to evaluate the influence of local microstructure and testing conditions on the obtained deformation substructure. Thus, within this thesis a combination of nanoindentation performed under various conditions, and subsequent characterization of the induced deformation will be performed.

# Table of Contents

<i>Résumé étendu .....</i>	<i>i</i>
<i>Acknowledgements .....</i>	<i>viii</i>
<i>Preface .....</i>	<i>ix</i>
<i>Table of Contents.....</i>	<i>xi</i>
<i>List of Figures .....</i>	<i>xiv</i>
<i>List of Tables .....</i>	<i>xvii</i>
<i>List of abbreviations and symbols .....</i>	<i>xviii</i>
<i>Thesis Outline.....</i>	<i>1</i>
<b>1 Literature review.....</b>	<b>3</b>
<b>1.1 Metastable Austenitic stainless steels.....</b>	<b>3</b>
1.1.1 Stainless steels .....	3
1.1.2 Austenitic stainless steels.....	5
1.1.3 Metastable austenitic stainless steels .....	6
1.1.4 Deformation mechanisms and phase transformation behavior in metastable austenitic stainless steels	9
1.1.5 Fatigue properties .....	24
<b>1.2 Instrumented Indentation Technique (Nanoindentation) .....</b>	<b>27</b>
1.2.1 Resolution and stability .....	28
1.2.2 Indenters .....	28
1.2.3 Characteristics of the load-displacement curves .....	29
1.2.4 Indentation Size Effect.....	31
<b>1.3 State of the Art: Combined small scale testing and characterization of metastable stainless steels</b>	<b>32</b>
1.3.1 TEM characterization.....	32
1.3.2 Nanoindentation studies of TRIP steels.....	32
1.3.3 Cyclic nanoindentation .....	36
<b>1.4 Summary.....</b>	<b>41</b>

<b>2</b>	<b><i>Material and Experimental Procedures</i></b>	<b>42</b>
<b>2.1</b>	<b>Studied Material</b>	<b>42</b>
2.1.1	Designation	42
2.1.2	Microstructural characteristics	42
2.1.3	Mechanical properties	43
2.1.4	Material conditions	45
<b>2.2</b>	<b>Experimental procedure</b>	<b>47</b>
2.2.1	Samples preparation	47
2.2.2	TEM lamellae preparation	48
2.2.3	Nanoindentation Testing	49
2.2.4	Characterization techniques	51
<b>3</b>	<b><i>Original microstructure</i></b>	<b>53</b>
<b>3.1</b>	<b>Characterization by EBSD</b>	<b>53</b>
<b>3.2</b>	<b>Characterization by TEM</b>	<b>55</b>
<b>4</b>	<b><i>Mechanical response to nanoindentation</i></b>	<b>59</b>
<b>4.1</b>	<b>Motivation</b>	<b>59</b>
<b>4.2</b>	<b>Results and discussion</b>	<b>59</b>
4.2.1	Monotonic nanoindentation tests	59
4.2.2	Two-cycles nanoindentation tests	62
4.2.3	Constant loading vs. constant displacement testing	63
4.2.4	Tests in constant displacement mode	65
4.2.5	Evaluation of elbow formation in cyclic P-h curves under loading mode	69
4.2.6	Reversible phase transformation	71
4.2.7	Time-dependent plasticity	77
4.2.8	Propagation of plasticity	80
<b>4.3</b>	<b>Appendix /Supplementary: Verification of equipment stability</b>	<b>84</b>
4.3.1	Creep & thermal drift study	84
4.3.2	Cyclic evolution of mechanical properties	86
<b>4.4</b>	<b>Conclusions</b>	<b>87</b>
<b>5</b>	<b><i>Characterization of surface deformation</i></b>	<b>89</b>
<b>5.1</b>	<b>Motivation</b>	<b>89</b>

<b>5.2</b>	<b>Results and discussion .....</b>	<b>90</b>
5.2.1	General aspect of residual nanoimprints .....	90
5.2.2	Surface deformation patterns induced by nanoindentation .....	91
5.2.3	Characterization of underlying defects .....	93
5.2.4	Fine structure characterization .....	96
5.2.5	$\alpha'$ -martensite formation.....	99
5.2.6	Correlation between applied characterization techniques .....	103
<b>5.3</b>	<b>Conclusions .....</b>	<b>104</b>
<b>6</b>	<b><i>Characterization of subsurface deformation.....</i></b>	<b>106</b>
<b>6.1</b>	<b>Motivation .....</b>	<b>106</b>
<b>6.2</b>	<b>Results and discussion .....</b>	<b>107</b>
6.2.1	Monotonic nanoindentation .....	107
6.2.2	Deformation in weakly confined grains.....	108
6.2.3	Deformation in uniaxially confined grains.....	114
6.2.4	Transmission of plasticity through grain boundaries.....	117
6.2.5	Deformation in strongly confined grains and crystalline anisotropy.....	118
6.2.6	Plasticity evolution .....	128
6.2.7	Evolution of deformation for prestrained condition .....	131
<b>6.3</b>	<b>Conclusions .....</b>	<b>133</b>
<b>7</b>	<b><i>Supplementary subsurface characterization and 3D reconstruction .....</i></b>	<b>135</b>
<b>7.1</b>	<b>Motivation .....</b>	<b>135</b>
<b>7.2</b>	<b>Results and discussion .....</b>	<b>136</b>
<b>7.3</b>	<b>Conclusion.....</b>	<b>142</b>
<b>8</b>	<b><i>Closing Discussion .....</i></b>	<b>143</b>
<b>9</b>	<b><i>Final Conclusions.....</i></b>	<b>145</b>
<b>10</b>	<b><i>Future Outlook.....</i></b>	<b>147</b>
<b>11</b>	<b><i>Bibliography.....</i></b>	<b>148</b>
	<b><i>Abstract.....</i></b>	<b>172</b>
	<b><i>Resumen .....</i></b>	<b>173</b>
	<b><i>Résumé.....</i></b>	<b>174</b>

## List of Figures

Figure 1. Schaeffler-Delong diagram. Microstructure of stainless steels as a function of the chemical composition...	4
Figure 2. Microstructure of AISI 301LN after 31% of cold rolling .....	7
Figure 3. Positioning of different steel groups as a function of their ultimate tensile strength and total elongation...	7
Figure 4. Positioning of different steel groups as a function of their yield strength and total elongation .....	8
Figure 5. Formation of stacking faults.....	9
Figure 6. Stacking faults as observed by TEM under different tilt angles. ....	10
Figure 7. Deformation twins in an austenitic stainless steel. ....	11
Figure 8. Stacking fault sequences .....	11
Figure 9. Faulted intersecting $\epsilon$ -plates in an austenitic matrix .....	12
Figure 10. Evolution of the $\epsilon$ martensite fraction with increasing strain. ....	13
Figure 11. Coexistence of nanoscopic twins and $\epsilon$ -martensite.....	14
Figure 12. The preferential mechanism of martensitic transformation .....	15
Figure 13. Schematics of the austenite-martensite orientation. ....	16
Figure 14. Stereographic projection of the Kurdjumov-Sachs and Nishiyama-Wasserman relationships.....	17
Figure 15 .Illustration of the habit plane between austenite and martensite .....	18
Figure 16. Accommodation of the martensitic shape .....	18
Figure 17. $\alpha'$ -martensite nucleation at the intersection $\epsilon$ plates in 316LN. ....	19
Figure 18. Different deformation mechanisms in function of the SFE. ....	20
Figure 19. Effect of temperature .....	21
Figure 20. Martensitic transformation in AISI301LN steels at different temperatures .....	22
Figure 21. Dislocation structures in the fatigue plastic zones .....	23
Figure 22. The maximum strain rate of martensitic transformation in dependence on the grain size .....	24
Figure 23. SEM image of the surface of AISI 316L submitted to low cycle fatigue testing. ....	26
Figure 24. Cyclic fatigue behavior of metastable austenitic stainless steels. ....	27
Figure 25. Typical load-displacement curve of a nanoindentation.....	28
Figure 26. Illustration of relevant parameters in nanoindentation .....	30
Figure 27. Load-displacement curves of nanograin and coarse grain AISI 301 LN exhibiting pop-ins. ....	33
Figure 28. Comparison of nanoindentation curves of dual phase steels for martensite and austenite grains .....	34
Figure 29. Dislocation structure in deformed $\alpha'$ martensite with interference of dislocations in several slip systems	34
Figure 30. Austenitic grain in TRIP steels after a nanoindentation test of 70 nm displacement into the surface. ....	35
Figure 31. Deformation structure surrounding a residual imprint in a medium-Mn TRIP steel. ....	36
Figure 32. Formation of $\epsilon$ -martensite induced by nanoindentation.....	36
Figure 33. Spherical nanoindentation load-displacement response for repeated spherical nanoindentation .....	37



Figure 34. Spherical indents along the $\langle 0001 \rangle$ direction in graphite single crystals.....	38
Figure 35. Cyclic nanoindentation of $\text{CaCO}_3$ .....	38
Figure 36. Cyclic evolution of P-h curves in shape-memory alloys. ....	39
Figure 37. Evolution of NiTi response to cyclic nanoindentation with a Berkovich tip. ....	40
Figure 38. Cyclic nanoindentation behavior of different metals. ....	40
Figure 39. Properties of AISI 301LN.....	43
Figure 40. Mechanical properties of AISI 301LN. ....	44
Figure 41. Stress-strain curves of 301LN obtained from tensile tests, as function of the test temperature <sup>86</sup> .....	45
Figure 42. Schematics of the fabrication of the test material. ....	46
Figure 43. Illustration of the plane-view lamella extraction .....	49
Figure 44. Optical micrograph of the sample surface .....	53
Figure 45. EBSD mapping of the initial material. ....	54
Figure 46. IPF distributions corresponding to Figure 45a and Figure 45b, respectively. ....	54
Figure 47. TEM Bright Field images of the investigated AISI 301LN steel in the as-received condition. ....	56
Figure 48. Deformation mechanisms in AISI 301LN steel in the skin-pass condition. ....	57
Figure 49. Characteristic dislocation arrangement of skin-passed AISI301LN. ....	58
Figure 50. Monotonic nanoindentation in annealed AISI 301LN.....	60
Figure 51. Nanoindentation testing in the load range of elastoplastic transition.....	61
Figure 52. Two-cycle nanoindentation test. ....	62
Figure 53. 50-cyclic nanoindentation tests.....	64
Figure 54. Cyclic evolution of hardness and Young's modulus .....	64
Figure 55. Cyclic evolution of P-h curves for $\langle 001 \rangle$ grain in annealed sample, $h_{\max} = 250$ nm. ....	66
Figure 56. Cyclic evolution of P-h curves for $\langle 111 \rangle$ grain in annealed sample, $h_{\max} = 250$ nm. ....	66
Figure 57. Cyclic evolution of P-h curves for $\langle 111 \rangle$ grain in annealed sample, $h_{\max} = 500$ nm. ....	66
Figure 58. Cyclic evolution of P-h curves for $\langle 111 \rangle$ grain in skin-passed sample, $h_{\max} = 250$ nm.....	67
Figure 59. Evolution of the hysteresis area beginning with the 2 <sup>nd</sup> indentation cycle.....	67
Figure 60. Cyclic evolution of P-h curves for $\langle 001 \rangle$ grain in annealed sample in loading mode.....	69
Figure 61. Cyclic evolution of P-h curves for different indentation conditions in $\langle 001 \rangle$ grains in annealed sample ..	70
Figure 62. Illustration of reversible pop-in formation. ....	73
Figure 63. Multistep nanoindentation testing with 1800 s holding periods.....	77
Figure 64. Monotonic loading with different holding times.....	78
Figure 65. Time-dependent plasticity at small loads.....	79
Figure 66. Time-dependent displacement during cyclic loading and constant holding in comparison. ....	81
Figure 67. Occurrence of pop-ins after prolonged cyclic nanoindentation.....	82
Figure 68. Nanoindentation test featuring a large pop-in during the first and 38 <sup>th</sup> cycle.....	83
Figure 69. Nanoindentation creep measurements.....	86

Figure 70. Cyclic evolution of contact stiffness and $\delta$ .....	87
Figure 71. Indentation matrices in annealed samples. ....	90
Figure 72. Close view of an indent in Figure 1c. ....	90
Figure 73. SEM images of the deformed nano-indented grains along $\langle 001 \rangle$ and $\langle 111 \rangle$ directions.....	92
Figure 74. a) EBSD IPF map and b) SEM image of the area around the residual imprint along $\langle 111 \rangle$ direction. ....	93
Figure 75. a) TEM BF and b) DF images of the lamella extracted from the area marked in Figure 74.....	94
Figure 76. a) BF and b) DF images of the deformation bands from Area A In Figure 75 . ....	94
Figure 77. Magnified view of Area B in Figure 5. ....	95
Figure 78. HRTEM analysis of the bands composition.....	99
Figure 79. Deformation band at the edge of the residual imprint. ....	100
Figure 80. a) Magnified view of the region of interest. ....	101
Figure 81. a) magnified TEM BF image of an $\alpha'$ -martensite nucleus at a shear band intersection. ....	102
Figure 82. Residual imprint after monotonic nanoindentation testing in large $\langle 111 \rangle$ oriented grain.....	108
Figure 83. Substructure surrounding the nanoimprint after cyclic nanoindentation in displacement mode. ....	109
Figure 84. Cross section of residual imprint after 50 cycles of nanoindentation in constant load mode. ....	110
Figure 85. Comparison of a), b) austenitic, and c), d) martensitic, shear band sections.....	112
Figure 86. Magnified view of martensitic particle formed under the nanoindenter tip. ....	113
Figure 87. Cross section of a nanoimprint in a “flat” $\langle 111 \rangle$ oriented grain.....	115
Figure 88. Magnified view of the martensitic phase formed in the IPZ.....	116
Figure 89. View of the grain boundary region in Figure 87. ....	118
Figure 90. TEM images from a cross section lamella corresponding to a small $\langle 111 \rangle$ oriented grain after cyclic nanoindentation testing.....	120
Figure 91. Area of high dislocation density surrounding the martensite under the residual imprint. ....	121
Figure 92. TEM characterization of the lateral grain boundary. ....	122
Figure 93. TEM characterization of the cross section of an imprint after 50 nanoindentation cycles in a $\langle 001 \rangle$ ....	124
Figure 94. Close view of the deformed region surrounding the nanoimprint.....	125
Figure 95. Calculated shape of plastic zones under nanoimprints in Cu .....	127
Figure 96. Small $\langle 111 \rangle$ oriented grain after 200 nanoindentation cycles.....	129
Figure 97. Deformation band system at the grain boundary. ....	130
Figure 98. BF TEM images of the grain boundary region corresponding to different tilt angles. ....	131
Figure 99. 50-cyclic nanoindentation test in a small grain of a skin-passed sample.....	132
Figure 100. Characterization of the deformation structure in a SP sample by SIM.....	137
Figure 101. Cross section of a residual imprint after monotonic nanoindentation. ....	138
Figure 102. Cross section of a residual imprint after cyclic nanoindentation.....	140
Figure 103. 3D tomographic reconstruction of the cross-sections under the nanoimprint produced by the cyclic indentation.....	141

## List of Tables

<i>Table 1. Typical nominal chemical composition of selected austenitic stainless steels. Data from Outokumpu.</i>	6
<i>Table 2. Stacking fault energy of various fcc materials at room temperature<sup>109</sup>.</i>	20
<i>Table 3. Chemical composition in wt.% obtained by EPMA for N and by EDX-Spectroscopy for the other elements.</i>	42
<i>Table 4. Space groups and lattice parameters of austenitic and martensitic phases in AISI301LN.</i>	43
<i>Table 5. Properties of the steel in the different conditions.</i>	46
<i>Table 6. Mechanical of AISI 301 LN in annealed and skin-passed condition.</i>	47
<i>Table 7. Summary of employed nanoindentation test conditions.</i>	49
<i>Table 8. Distinction between different stacking sequence defects by TEM</i>	52
<i>Table 9. Lattice parameters <math>a</math> and <math>c</math>, and distances between closest-packed planes in AISI 301LN</i>	74
<i>Table 10. Crystallographic relationship between the indented and the adjacent grains.</i>	84
<i>Table 11. Comparison of nano-hardness values for different crystallographic orientations and maximum displacements.</i>	128

## List of abbreviations and symbols

$a$	contact radius
$a$	lattice parameter
$A_c$	Contact area
$b$	Burgers vector
$b_p$	Burgers vectors of the partial dislocations
bcc	body centered cubic
BF	Bright Field
$c$	lattice parameter
$Cr_{eq}$	Chrome equivalent
$E$	Young's modulus
$E_{eff}$	Effective Young's Modulus
EBSD	Electron Back-Scatter Diffraction
ESF	Extrinsic Stacking Fault
DF	Dark Field
EPMA	Electron Probe Micro-Analysis
fcc	face centered cubic
FESEM	Field Emission Secondary Electron Microscopy
FIB	Focused Ion Beam
$G$	shear modulus
GND	Geometrically Necessary Dislocation
hcp	hexagonal close-packed
$h$	displacement into the surface
$h_c$	contact depth
$h_f$	final depth
$h_{max}$	maximum displacement

$h_{\min}$	minimum displacement
HRTEM	High Resolution Transmission Electron Microscopy
ISF	Intrinsic Stacking Fault
IPF	Inverse Pole Figure
IPZ	Indenter Penetration Zone
KS	Kurdjumov-Sachs
$m'$	misorientation factor
$M_{d(x/y)}$	Temperature at which x % of austenite will transform to martensite after y % of deformation
$M_s$	Martensite start temperature
$M_s^\sigma$	Transition point between stress-assisted and strain-induced martensitic transformation
$n -$	work hardening coefficient
$n$	creep exponent
$N$	cycle number in fatigue testing
$Ni_{eq}$	Nickel equivalent
NW	Nishiyama-Wassermann
OR	Orientation Relationship
$p_o$	mean contact pressure
$P$	Load
P-h curve	Load-displacement curve
$P_{\max}$	Maximum load
$P_{\min}$	Minimum load
$R$	Indenter radius
$S$	contact stiffness
SAED	selected area electron diffraction
SEM	Secondary Electron Microscopy
SF	Stacking Fault
SFE	Stacking Fault Energy

SIM	Secondary Ion Microscopy
SN	Shoji-Nishiyama relationship
STEM	Scanning Transmission Electron Microscopy
TEM	Transmission Electron Microscopy
TOR	Triangular Orientation Relationship
TWIP	Twin-induced Plasticity
TRIP	Transformation-induced plasticity
TS	Tensile Strength
wt. %	weight per cent
XRD	X-Ray diffraction
YS	Yield Strength
$\alpha'$	tetragonal or cubic martensite
$\beta$	geometry shape factor
$\epsilon$	hexagonal martensite
$\gamma$	austenite
$\gamma$	Stacking fault energy

# Thesis Outline

The present thesis is devoted to the study of the deformation mechanisms in a complex metallic alloy: a metastable austenitic stainless steel. These steels are branded as complex because different and simultaneous deformation mechanisms, including phase transformations, can be activated when plastically deformed. Therefore, with the motivation of achieving a deeper understanding of these mechanisms, nanoindentation experiments have been performed to locally deform the material at microscopic scale. This experimental technique allows the characterization of the response of individual selected grains by analyzing loading-unloading curves. Moreover, cyclic nanoindentation enables the gradual accumulation of deformation, in order to study the resulting substructural features by a combination of SEM, EBSD and TEM.

The thesis is arranged as following:

In **Chapter 1**, metastable steels are introduced and the nanoindentation technique is explained. Furthermore, the current state of the art of nanoindentation experiments performed in metastable stainless steels is reviewed.

**Chapter 2** gives a description of the investigated steel and the applied experimental procedures.

In **Chapter 3**, microstructural and mechanical characterization of the studied steel in different conditions prior to nanoindentation is carried out. Grain size and morphology, phase distribution, crystallographic texture, as well as presence and characteristics of different defects are studied.

In **Chapter 4**, different monotonic and cyclic nanoindentation tests are conducted in selected grains and the respective loading-unloading curves are evaluated to access the local material response in terms of phase transformation, propagation of plasticity, time-dependent deformation and cyclic evolution of mechanical properties.

Surface deformation mechanisms developing from nanoindentation tests are studied by FESEM, EBSD, TEM and HRTEM in **Chapter 5**. Therefore, deformation features such as formation of fine-structured microscopic shear bands, nucleation of  $\alpha'$ -martensite at intersections of those shear bands and incipient slip band formation are imaged with high resolution. Furthermore, the influence of grain boundaries on surface deformation is studied.

**Chapter 6** is dedicated to the study of the deformation mechanisms resulting from the nanoindentation experiments at subsurface level. TEM investigations are conducted as a function of size and

crystallographic orientation of the indented grains. Furthermore, the influence of testing mode (load or penetration depth control) and the number of indentation cycles are investigated.

In **Chapter 7**, a FIB imaging and tomography study is performed to complete the insights obtained by TEM characterization, Thereby, FIB enabled a 3D reconstruction of the  $\alpha'$ -martensitic phase emerging under the nanoindenter tip and permitted to track the underlying plasticity propagation mechanisms.

Finally, in **Chapter 8**, the different aspects of deformation mechanisms discerned within the previous chapters are summarized and correlated.



# 1 Literature review

## 1.1 Metastable Austenitic stainless steels

### 1.1.1 Stainless steels

Stainless steels are high alloyed steels, characterized by their resistance to corrosion and temperature. They are defined as alloys with a minimum percentage of 11% Cr and usually a low carbon content ( $<0.08\%$ )<sup>31</sup>. Chromium forms a passive oxide layer on the surface, which gives to these steels their high resistance against corrosion. This layer can be further stabilized by addition of other alloying elements, such as Ni or Mo.

Originally, stainless steels were developed in the search of an inert material, which would be resistant to harsh environmental conditions. Thus, already in 1821 Pierre Berthier found that Fe-Cr alloys were resistant to acids. The development of a carbon-free chromium extraction process by Hans Goldschmidt, at the end of the XIX century, eliminated the problem of brittleness due to high carbon levels. This permitted Léon Guillet to perform excessive studies on ferritic and martensitic low-carbon Fe-Cr alloys. In 1912, the first austenitic stainless steel was patented by ThyssenKrupp Nirosta, while in the same year Harry Bearley discovered the martensitic stainless steel and started its massive production. Monnartz was the first one to study and understand the passivation effect of stainless steels and also to point out the importance of a minimum Cr content, besides the benefit of additional alloying elements like Mo. As a consequence, he can be considered as one of the main developers of modern austenitic stainless steels, similar to those still used today<sup>32,33</sup>.

### Types of stainless steels

Stainless steels can be sub-divided according to their microstructure into:

- **Ferritic**
- **Austenitic**
- **Martensitic**
- **Duplex**
- **Precipitation hardened**

Ferritic stainless steels consist mainly of iron and chromium, are magnetic and exhibit a good welding behavior. Austenitic stainless steels are obtained by alloying with important amounts of Ni or Mn<sup>34</sup> and are distinguished by especially high corrosion resistance, as well as high ductility; while martensitic stainless steels feature a higher carbon content than ferritic ones and possess the highest hardness.

Duplex type forms a two-phase ferritic-austenitic or ferritic-martensitic compound, combining the positive properties of the two phases, like the strength of the harder phase and the ductility of the softer matrix. Precipitation Hardened (PH) steels can be martensitic, austenitic or mixed, and their strength can be increased by intended formation of precipitates during an ageing treatment <sup>35</sup>.

The microstructure of stainless steels depends on the chemical composition and can be approximately predicted using the Schaeffler-diagram (Figure 1). Chromium and Nickel are the most important alloying elements, whereas other elements which exhibit the same effect as Cr or Ni can be considered, with an appropriate weighting factor, respectively as chromium or nickel equivalent <sup>36</sup> with

$$Ni - equivalent = wt\%Ni + 30(wt\%C + wt\%N) + 0.5(wt\%Mn + wt\%Cu + wt\%Co) \quad (1)$$

$$Cr - equivalent = wt\%Cr + 1.5wt\%Si + wt\%Mo \quad (2)$$

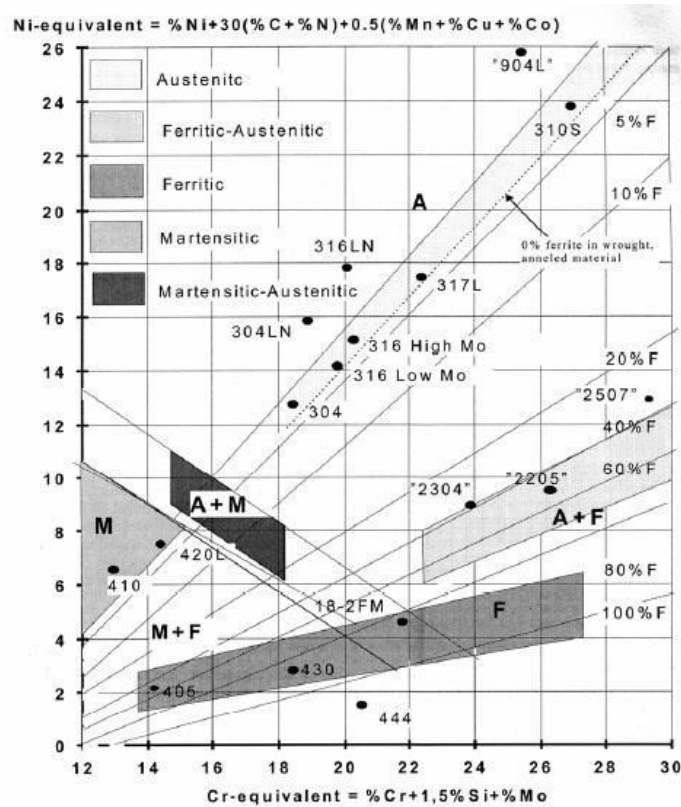


Figure 1. Schaeffler-Delong diagram. Microstructure of stainless steels as a function of the chemical composition <sup>36</sup>.

The martensitic transformation is characterized by two material specific temperature values:  $M_s$  – the temperature below which the phase transformation starts, and  $M_f$  – the temperature at which the martensitic transformation is completed. These temperatures are likewise determined by the chemical

composition of the alloy and can be approximately estimated by Equation (3) developed by Eichelman and Hull <sup>37</sup>:

$$Ms(^{\circ}C) = 1302 - 42(wt\%Cr) - 61(wt\%Ni) - 33(wt\%Mn) - 28(wt\%Si) - 1667 (wt\%[C + N]) \quad (3)$$

The principal effects of the main alloying elements in stainless steels are summarized in the following <sup>33</sup>:

### **Chromium**

Chromium is the main component of all stainless steels and an important alpha-stabilizer. The higher the chromium content, the more stable the passive film.

### **Nickel**

Nickel is the most important gamma-gene element. It improves the corrosion resistance, also when the passive layer is damaged. Furthermore, it increases ductility, fracture toughness and workability.

### **Manganese**

Manganese is an important gamma-stabilizer representing along with Ni a common alloying element in austenitic stainless steels. Furthermore, it prevents hot cracking.

### **Molybdenum**

Molybdenum assists the formation of the passive layer and protects it against damage. Thus, it improves the corrosion resistance properties, especially regarding local corrosion like pitting. Molybdenum is an alpha-gene.

### **Carbon**

Carbon has a pronounced gamma-gene effect. It is also a good solid strengthener, increasing the yield strength, but it tends to form chromium carbides which lead to sensitization and decrease the corrosion resistance. For the martensitic phase, elevated C content increases the distortion of the crystalline lattice.

### **Nitrogen**

Nitrogen is an austenite stabilizer and a good solid solution strengthener, similar to carbon, without the disadvantage of forming carbides. It has a higher solubility in the alloy than carbon, so the formation of nitrides is less likely. As a consequence, nitrogen significantly increases the strength of the steel, at the same time preserving good fracture toughness. Furthermore, nitrogen improves the corrosion behavior.

## **1.1.2 Austenitic stainless steels**

Austenitic stainless steels are the most commonly used steels within the stainless family, due to their high corrosion resistance, good formability and high work hardening <sup>4,35,38-40</sup>.

According to their chemical composition, they can be basically divided into 200- and 300-series. Thereby, the latter is Ni-based, while in the 200-series a part of the nickel is replaced by Mn, in order to avoid the elevated costs of Ni.

Important for the properties of austenitic stainless steels is the carbon and nitrogen content, being both interstitial elements strongly gammagene. C contributes to the stabilization and strengthening of austenite. However, it can form chromium carbides which cause an increase of the grain boundary corrosion. Thus, carbon content in stainless steels is usually kept low and, in many modern grades, it is partially substituted by N.

Table 1 represents the chemical composition of austenitic stainless steels of the 300-series. From all degrees, AISI 301 and 301LN steels exhibit the lowest content of alloy elements.

**Table 1. Typical nominal chemical composition of selected austenitic stainless steels. Data from Outokumpu.**

Steel	C	N	Cr	Ni	Mo	Others
301LN	0.02	0.14	17.7	6.5	–	–
304	0.04	–	18.1	8.3	–	–
304L	0.02	–	18.1	8.3	–	–
304LN	0.02	0.14	18.5	10.5	–	–
321	0.04	–	17.3	9.1	–	Ti
316	0.04	–	17.2	10.2	2.1	–

In low-alloy austenitic stainless steels, the fcc phase is not sufficiently stabilized and can transform under load to martensite, producing the TRIP effect. This effect is also known from multiphase steels with different compositions<sup>41–43</sup>, while in case of austenitic stainless steels this phenomenon is referred to as metastability.

### 1.1.3 Metastable austenitic stainless steels

$M_s$  temperature of austenitic stainless steels is significantly below room temperature<sup>44</sup>, which means that at room temperature martensitic transformation will not take place spontaneously<sup>8</sup>. However, the necessary driving force can be also provided mechanically, inducing martensitic transformation after application of strain or stress.

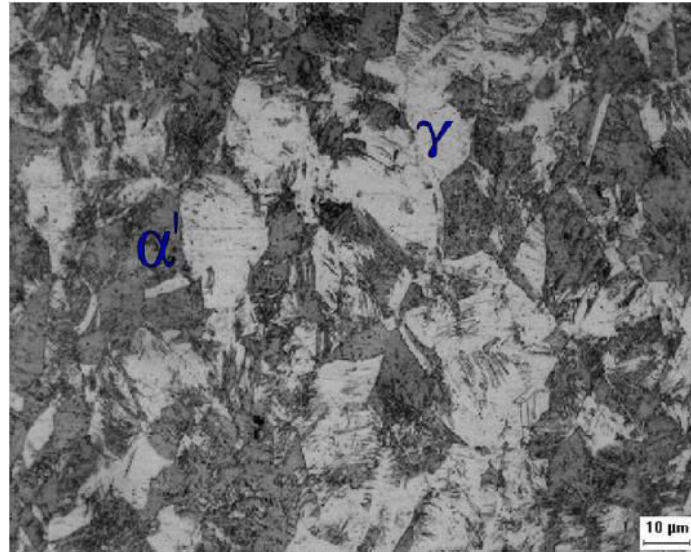


Figure 2. Microstructure of AISI 301LN after 31% of cold rolling<sup>45</sup>. Coexisting austenite and martensite phases characteristic for metastable austenitic stainless steels.

As a consequence, an adjustable phase transformation at room temperature can be achieved, leading to an increase in hardness and yield strength. This phase transformation goes along with an increase of plasticity and is therefore called Transformation Induced Plasticity or TRIP effect. Figure 2 shows an optical micrograph of the characteristic microstructure of a deformed metastable stainless steel.

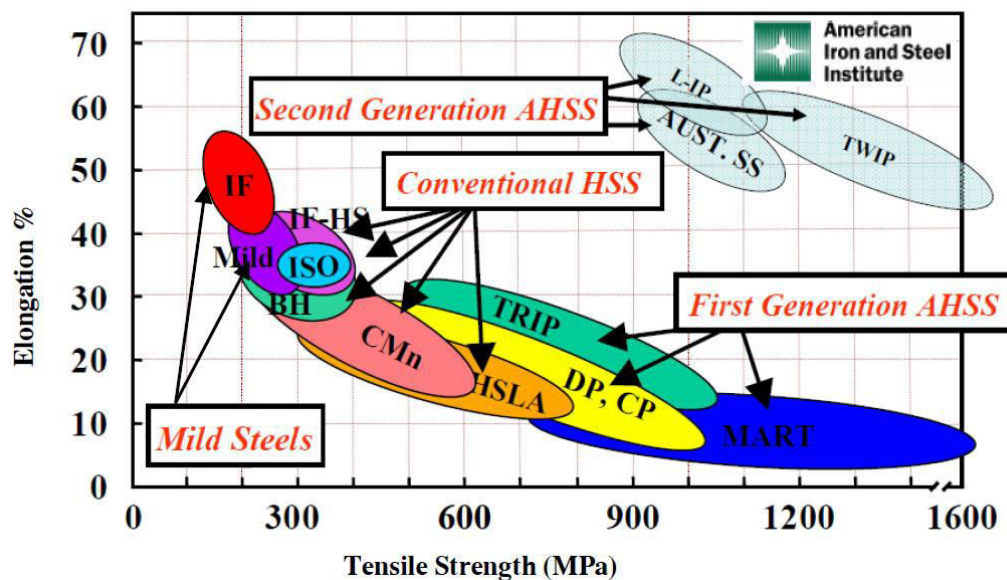


Figure 3. Positioning of different steel groups as a function of their ultimate tensile strength and total elongation<sup>46</sup>.

Due to the smaller packing density of bcc phase in comparison to fcc, the martensitic transformation implies a volume expansion of around 3%<sup>47,48</sup>, which involves creation of an internal stress field and

affects the mechanical properties, as well as the further transformation behavior. The combination of phase transformation and the strain hardening of the retained austenite leads to the outstanding work hardening of metastable austenitic stainless steels, going along with high plasticity<sup>49</sup> and range them into the category of advanced or second generation HSS (High Strength Steels). This is illustrated in Figure 3 and Figure 4, which show that, in comparison to other steels, advanced TRIP steels are distinguished by an excellent compromise between high strength and high ductility. Taking into account the simultaneous high corrosion resistance, distinguishable fatigue properties and the possibility to tailor mechanical properties like yield strength, hardness and damage tolerance, metastable austenitic stainless steels are materials of high interest for multiple engineering applications<sup>5,50,51</sup>.

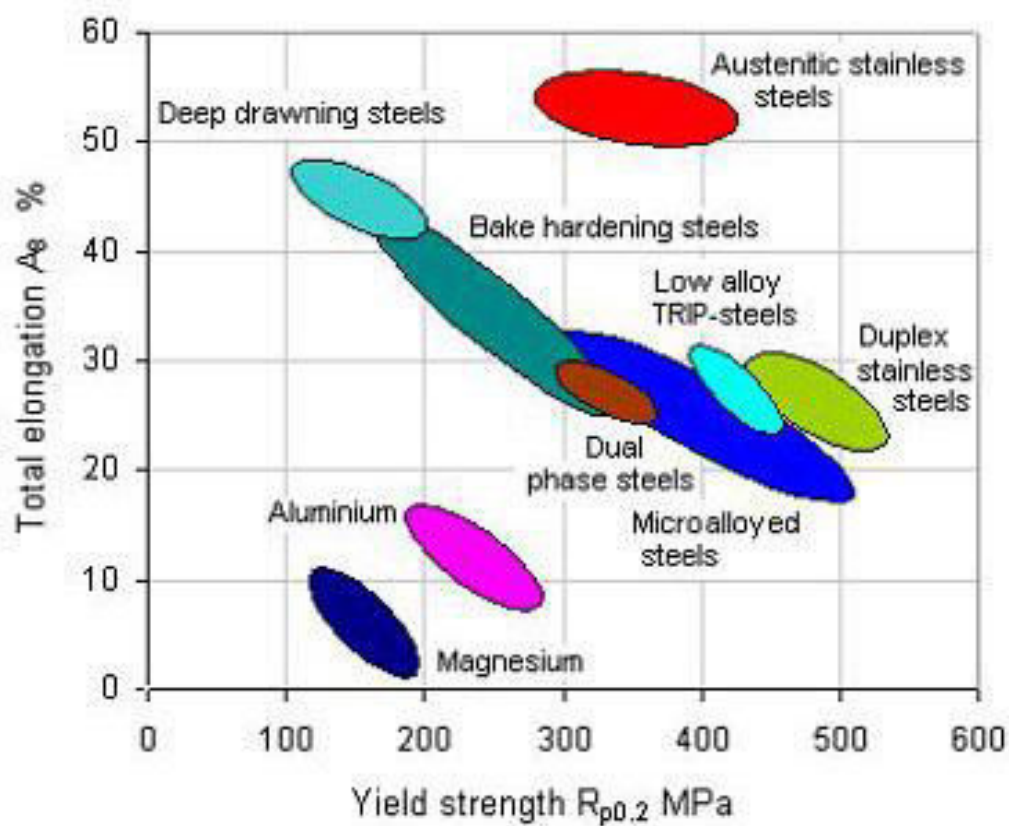


Figure 4. Positioning of different steel groups as a function of their yield strength and total elongation<sup>52</sup>.

The mechanical properties of metastable austenitic stainless steels are highly influenced by a combination of multiple deformation mechanisms<sup>53</sup>. Some of them are briefly explained in the following section.

### 1.1.4 Deformation mechanisms and phase transformation behavior in metastable austenitic stainless steels

#### Stacking faults

In certain cases, it is energetically favorable for dislocations to split into two partial dislocations, thereby creating stacking faults. For fcc materials, it is  $a/2\langle 110 \rangle$  dislocations dissociating into two  $a/6\langle 211 \rangle$  partial dislocations, also called Shockley dislocations.

The normal atomic order of fcc crystals normal to the (111) plane has the sequence ABCABCABC. Stacking faults are planar defects, whereby a SF resulting from a single partial dislocation motion is called intrinsic and leads to a missing plane in the stacking sequence: ABCBCABCA. On the other hand, two overlapping stacking faults result in a stacking sequence ABCBABCAB, which means the insertion of an additional plane B, as illustrated in Figure 5<sup>54</sup>.

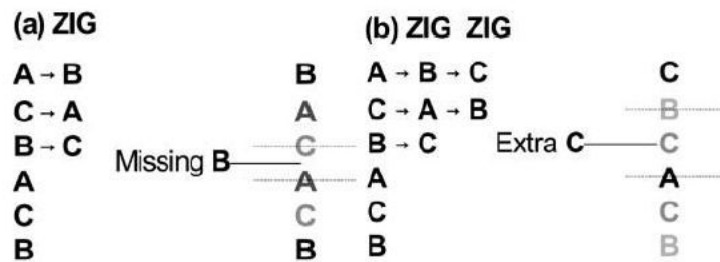


Figure 5. Formation of stacking faults. a) Intrinsic stacking fault produced by a partial dislocation motion; b) Extrinsic stacking fault produced by two successive partial dislocation motions.<sup>55</sup>

The energy necessary to induce a stacking fault is called stacking fault energy<sup>56</sup>. As can be withdrawn from Equation (4) developed by Cottrell<sup>57</sup>, the stacking fault width  $w$  is inversely proportional to the SFE.

$$w = \frac{Gb_p^2}{4\pi\gamma} \quad (4)$$

Stacking faults are widely present in fcc metals, including both annealed and deformed austenitic stainless steels. An example is given in Figure 6. They interact with dislocations and serve as a precursor for formation of various other defects, as illustrated in the following images.

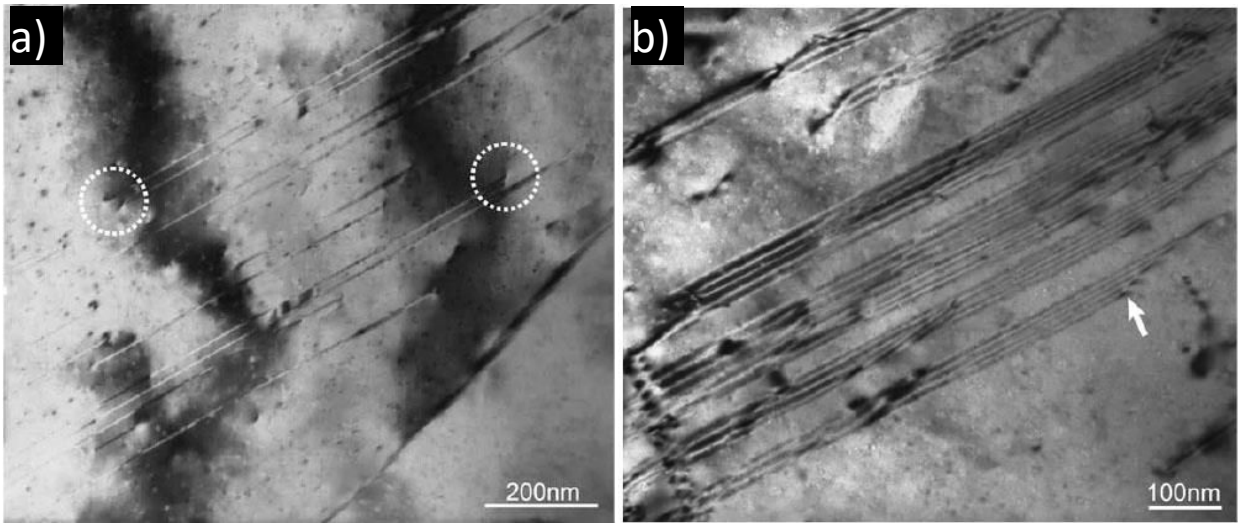


Figure 6. Stacking faults as observed by TEM under different tilt angles. a) Appearing as straight, thin lines; b) Exhibiting the characteristic fringes<sup>58</sup>.

### Twinning

Twinning is a deformation mechanism obtained by shearing of part of a crystal against the matrix, which is particularly common in fcc structures. It can be defined as the overlapping of intrinsic stacking faults on every successive plane<sup>55</sup>, resulting in a sequence ABCBACBACBABC. If many ISFs come together and overlap, the atomic order will be completely reversed – *i.e.* mirrored, forming a  $60^\circ$  angle to the mirror plane. The band with the mirrored structure is called twin. Its thickness depends on the number of SFs overlapping. The twin has the same crystalline structure as the rest of the crystal; however, its presence has important consequences the mechanical properties of the material, since the twin boundary creates an obstacle for movement of dislocations, analogue to a grain boundary<sup>53</sup>.

There are two possible types of twin formation in austenitic stainless steels:

Annealing twins, as first observed by Carpenter and Tamura in 1926<sup>59</sup> are mostly explained by the “Growth accident theory”. They form at high temperatures during growth or recrystallization processes. Annealing twins can occupy a significant part of the grain. When they grow, eventually the whole grain can transform into the twinned crystalline sequence.

Mechanical or deformation twins are created by mechanical strain, in order to accommodate the associated deformation<sup>60</sup>. Typically, they form many thin bands, with a width of around or below 100 nm and corresponding spacing (Figure 7). Deformation twinning is an important mechanism of plastic deformation in many austenitic steels<sup>61–64</sup>.





$$(111)_\gamma \parallel (0002)_\epsilon$$

$$[\bar{1}10]_\gamma \parallel [11\bar{2}0]_\epsilon$$

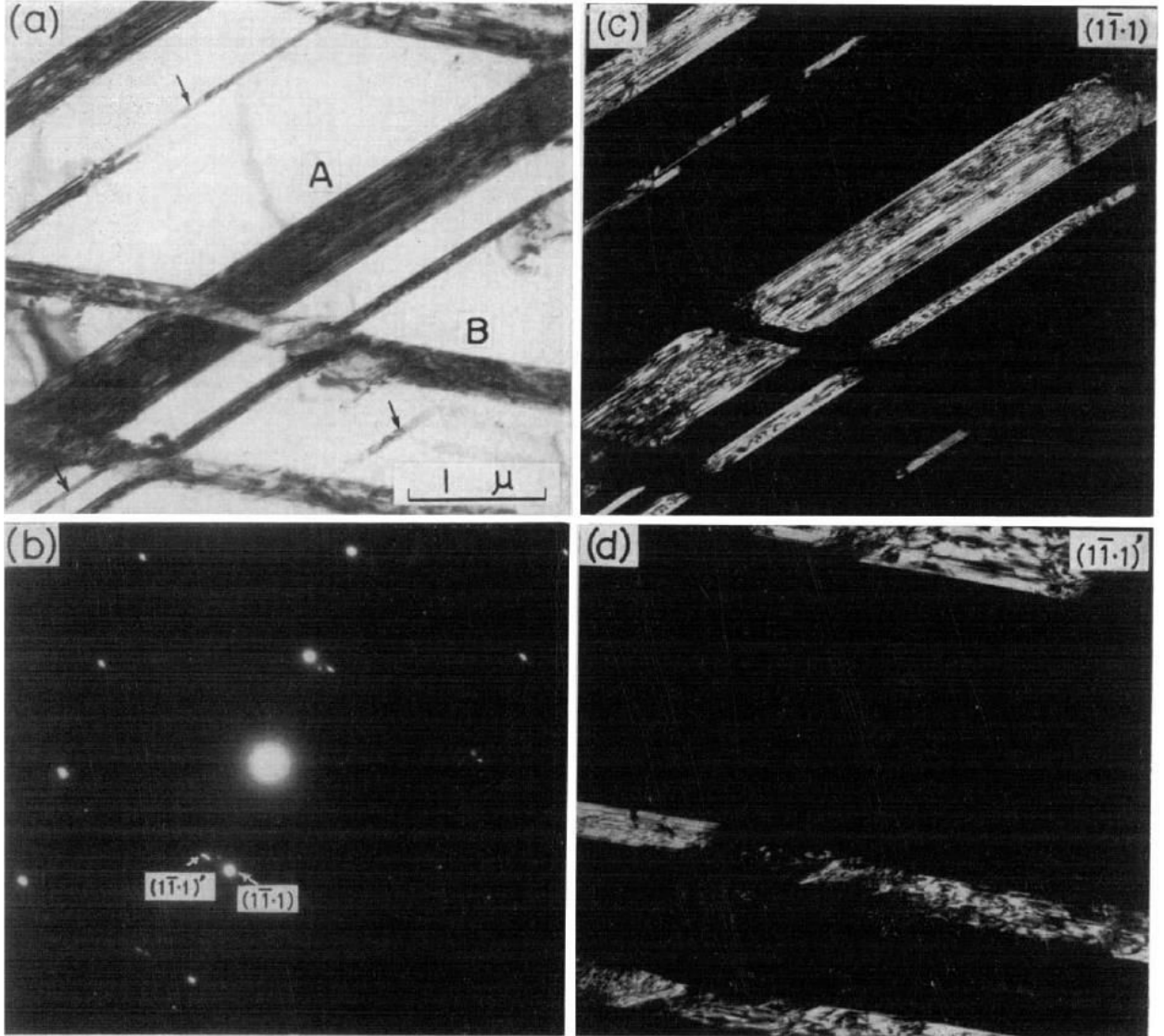


Figure 9. Faulted intersecting  $\epsilon$ -plates in an austenitic matrix<sup>68</sup>. a) TEM BF image; b) Corresponding diffraction pattern with two different  $\{111\}$  reflections; c) and d) DF images obtained with the two different reflections.

The nucleation of  $\epsilon$ -martensite usually starts from randomly spaced overlapping SFs, thus during the initial stages of deformation it is always faulted<sup>69</sup>. This leads to a characteristic streaky appearance, as can be appreciated in Figure 9.

These thin, faulty  $\epsilon$ -platelets can grow under further deformation to thicker and more regular  $\epsilon$ -plates. A high fraction of  $\epsilon$ -martensite embrittles the material due to its hcp nature<sup>73</sup>. However, the content of  $\epsilon$  in Fe-Cr-Ni steels rarely surpasses the order of few %. Actually, its fraction in the steel can be too small to be detected by methods like conventional XRD<sup>74,75</sup> or EBSD<sup>76</sup>. However, it can be readily observed by TEM or detected by high energy XRD. The common quoted reason for the small fraction of  $\epsilon$  in a metastable austenitic stainless steel is either that the microstructure saturates on it, as proposed by Hedström *et al.*<sup>77</sup> (see Figure 10a)), or that it is “consumed” by the  $\alpha'$  martensite to which it is further transformed, as proposed by Blanc *et al.*<sup>78</sup> (see Figure 10b)).

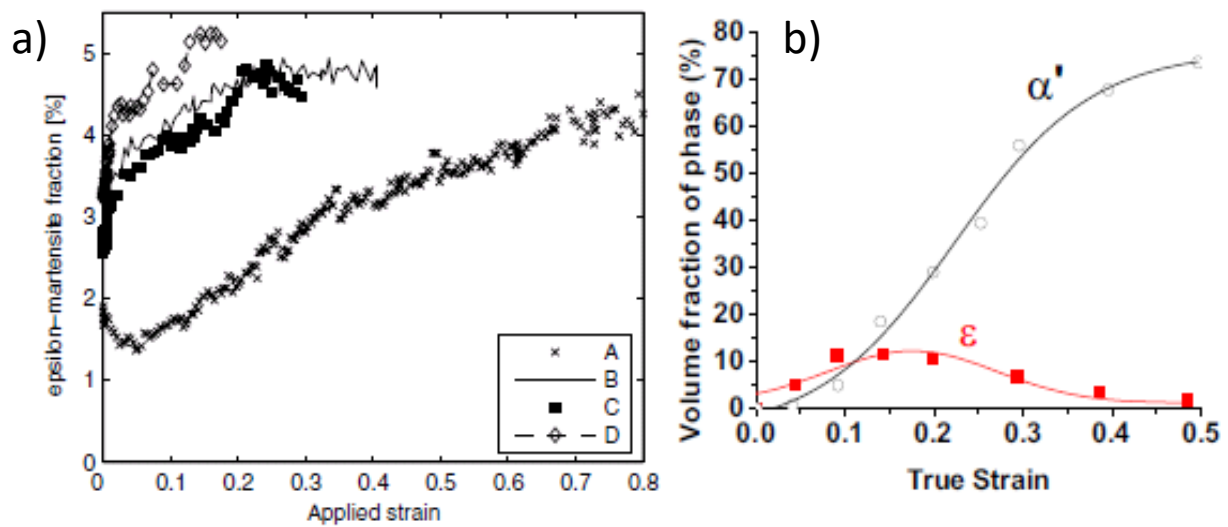


Figure 10. Evolution of the  $\epsilon$  martensite fraction with increasing strain. a) AISI 301 with different deformation degrees previous to the experiment (sample A 2%, B 23%, C 36% and D 42% cold rolling), content of  $\epsilon$  saturates around 4-5%<sup>77</sup>. b) In CrNi 18/7 steels,  $\epsilon$  content is observed not only to saturate, but also to decrease at higher strains, while the fraction of  $\alpha'$  keeps increasing, adapted from<sup>78</sup>.

### Shear band formation

The similarities and differences between deformation twins and  $\epsilon$  martensite are a little bit controversial. Some authors claim that twins originate from extrinsic and martensite from ISF, while other authors have found that it is other way around<sup>79,80</sup>. Either twins or  $\epsilon$ -martensite is more likely to form under application of strain depending on the SFE of the material<sup>81</sup>.

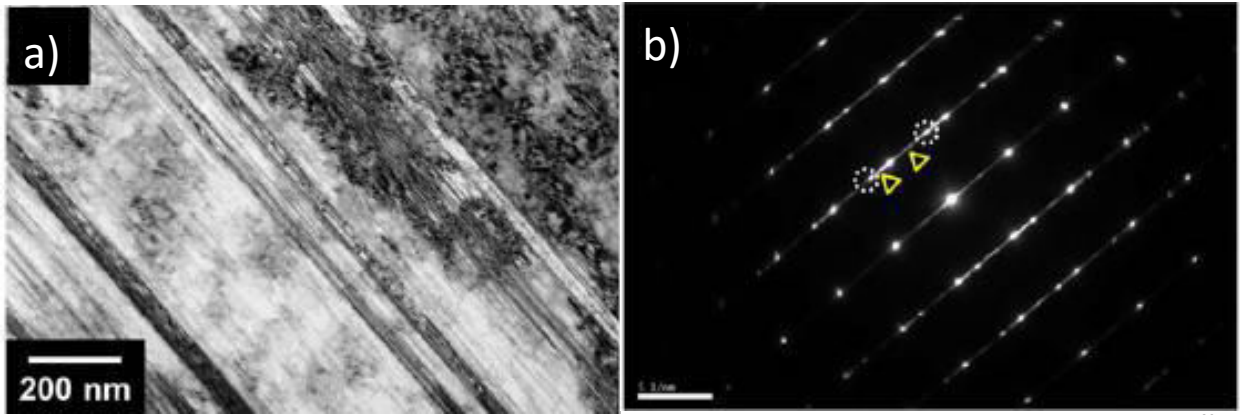


Figure 11. Coexistence of nanoscopic twins and  $\epsilon$ -martensite. a) STEM BF image; b) SAD pattern ( $z = [\bar{1}10]_{\gamma} \parallel [11\bar{2}0]_{\epsilon}$ )<sup>82</sup>.

However, as can be withdrawn from Figure 11, twins and  $\epsilon$ -martensite often coexist. Thus, due to the similarities and overlapping of those deformation mechanisms and the associated difficulties to distinguish between the corresponding structures, the conjunction of  $\epsilon$  martensite, SFs and mechanical twins is summarized under the common name of shear bands<sup>7</sup>.

Shear band formation is, along with twinning and dislocation slip, one of the most common deformation mechanisms in many austenitic alloys.

## Mechanically induced $\alpha'$ -martensitic transformation

### Fundamental mechanisms

The metastability of an alloy is defined by its  $M_d$  temperature – the highest temperature at which martensitic transformation by mechanical induction is possible. It can be defined as the temperature at which a certain fraction of the material, after a certain amount of deformation, will transform to martensite. So,  $M_{d(30/50)}$  is the temperature at which 30 % of austenite will transform to martensite after application of a true strain of 50%<sup>83</sup>. Several equations have been proposed to estimate the  $M_d$  temperature, the most common are the ones Nohara's<sup>84</sup>, which considers also the grain size GS according to ASTM:

$$M_d(30/50)(^{\circ}\text{C}) = 551 - 462(\text{C} + \text{N}) - 9.2\text{Si} - 8.1\text{Mn} - 13.7\text{Cr} - 29.0(\text{Ni} + \text{Cu}) - 18.5\text{M} - 68\text{Nb} - 1.42(v - 8.0) \quad (5)$$

with  $v$  being the ASTM grain size number, and Sjöberg's<sup>85</sup>, who considers the effects of carbon and nitrogen independently:

$$M_{d(30/50)}(^{\circ}\text{C}) = 608 - 515(\text{C}) - 821(\text{N}) - 7.8(\text{Si}) - 12(\text{Mn}) - 13(\text{Cr}) - 34(\text{Ni}) - 6.5(\text{Mo}) \quad (6)$$

In principle, all austenitic steels can be considered as metastable; however the degree of metastability depends on the mechanical driving force required for the phase transformation.

As mentioned above, the mechanical driving force for martensitic transformation can be supplied in form of stress or strain<sup>86,87</sup>, whereby the stress-assisted transformation can occur already at stresses below the yield strength of the material, while for strain-induced transformation first a minimal amount of plastic deformation has to occur – that is, the material has to be stressed above the yield strength. The effects of mechanical induction of martensitic transformation are two: on one hand side the stress application decreases the activation energy for the martensite nucleation and, in addition, plastic deformation increases the number of available low energy nucleation sides. The temperature up to which the effect of only stress is enough to provide the necessary transformation energy is called  $M_s^{\sigma}$ , while at higher temperatures (limited by  $M_d$ ), additional strain is necessary to induce the transformation, see Figure 12.

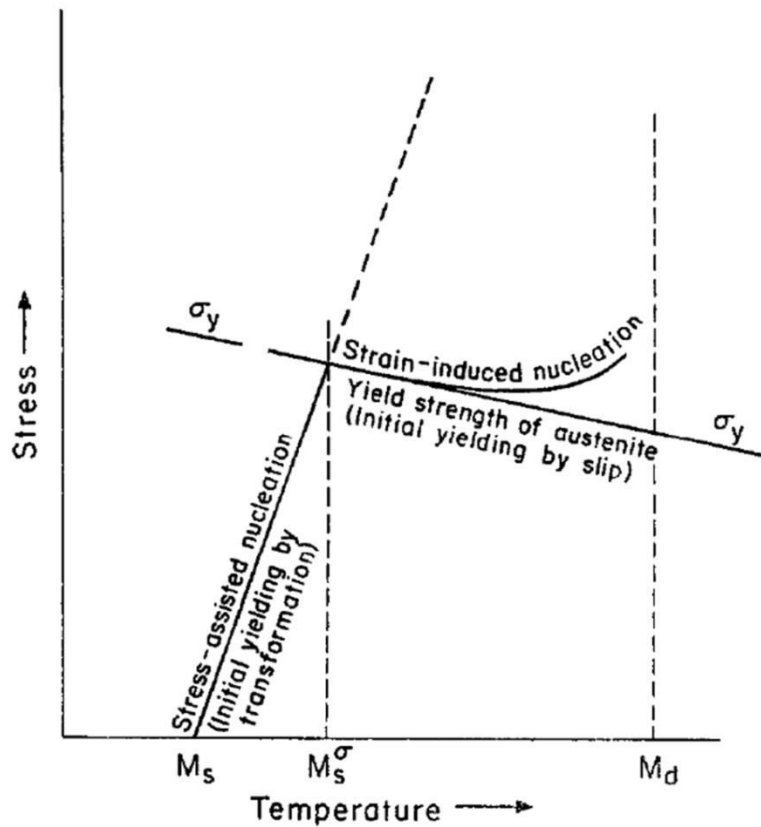


Figure 12. The preferential mechanism of martensitic transformation (thermal, strain-induced or strain assisted) depends on the respective temperature<sup>86</sup>.

It was found that the martensitic transformation in austenitic stainless steels at room temperature is mainly strain-induced, since in comparison to Fe-Ni alloys, the Fe-Cr-Ni steels exhibit a significantly wider gap between the  $M_s$  and the  $M_d$  temperatures<sup>88</sup>. This is due to the fact that plastic transformation

leads to creation of defects, as mentioned in the previous chapters, which represent favorable nucleation sites for heterogeneous martensite nucleation and thus reduce the necessary chemical driving force. However, the transformation mechanism will convert into stress assisted at sufficiently low temperatures.

Suzuki *et al.*<sup>89</sup> concluded that in the case of the strain induced nucleation, it is not directly the external stress that produces the mechanical driving force, but the internal stress, due to dislocations piled-up to the shear band intersections. Fang and Dahl<sup>71</sup> suggested that the mechanical driving force originates from the energy stored by the dislocations in the austenite.

The martensitic transformation takes place at the speed of sound<sup>90</sup>, which makes difficult to study it in detail. However, the transformation behavior is often schematically modeled by the Bain strain<sup>91</sup>, which accounts for a phase transformation with a minimum atomic motion. It can be considered as a stacking of two fcc cells, compressed 20% in z direction and simultaneously expanded 12% in the lateral directions.

However, martensitic transformation must be an invariant-plane strain, since this represents the configuration with the smallest strain energy<sup>91</sup>. In order to achieve this, the Bain strain must be complemented by additional rotation as shown in Figure 13.

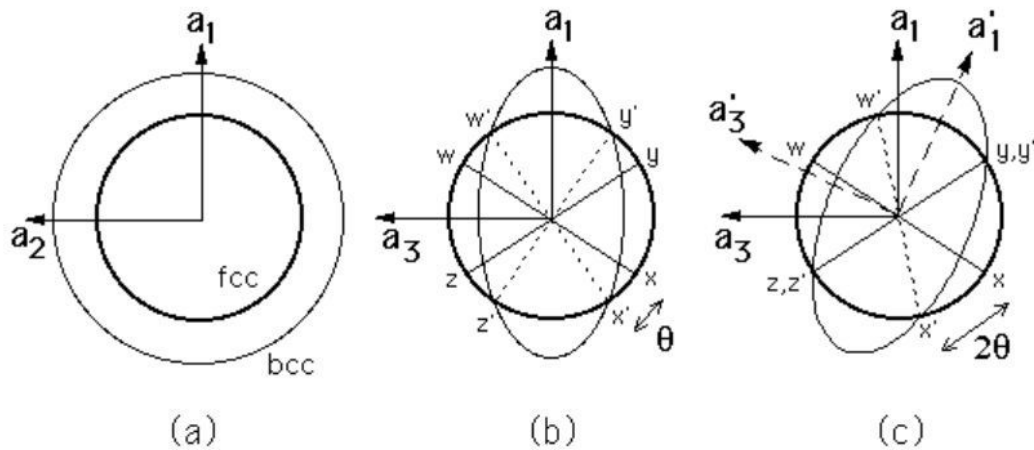


**Figure 13. Schematics of the austenite-martensite orientation. a) Undeformed austenite represented as a sphere b) Bain-strained austenite distorted to an ellipsoid c) Bain-strained and rotated austenite exhibiting invariant-lines<sup>91</sup>.**

The resulting martensite lattice exhibits a fixed relationship to the parent austenite lattice. So, the close-packed planes of both phases - (110) in martensite and (111) in austenite are usually parallel, just as the corresponding directions. The two most common relationships in stainless steels are the Kurdjumov-Sachs<sup>92</sup> and the Nishiyama-Wasserman<sup>72</sup> relationship:

$$(1\ 1\ 1) \parallel (0\ 1\ 1), [-1\ 0\ 1] \parallel [-1\ 1\ 1] \quad (\text{Kurdjumov and Sachs})$$

$$(1\ 1\ 1) \parallel (0\ 1\ 1), [1\ -1\ 0] \parallel [0\ 0\ 1] \quad (\text{Nishiyama-Wasserman})$$

where the respectively first plane and direction is referring to austenite and the second one to martensite. They are related to each other by a rotation of  $5.25^\circ$  about  $[011]_\alpha$  as illustrated in Figure 14.

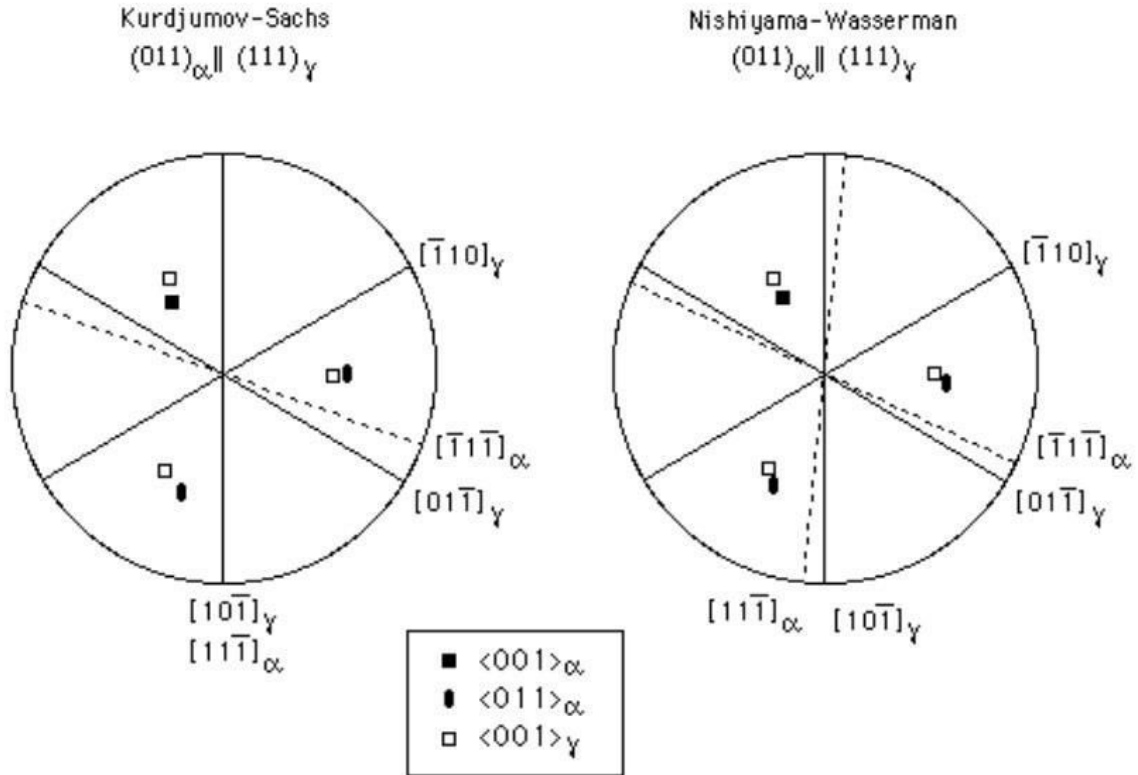


Figure 14. Stereographic projection of the Kurdjumov-Sachs and Nishiyama-Wasserman relationships<sup>91</sup>.

The interface between austenite and martensite on macroscopic scale is the habit plane, which is common to both phases. So, the martensitic transformation can be regarded as a cooperative shearing against this habit plane. Since in most of the cases the martensitic transformation can be assumed to be constrained, strain energy will be minimized by a curvature of the habit plane<sup>64</sup>. Figure 15 illustrates this relationship.

Although the martensitic phase is sheared in relationship to the austenitic matrix, due to confinement it must accommodate macroscopically to the shape of the previous austenite structure. It can do so by two mechanisms as shown in Figure 16: either by twinning or by slipping.

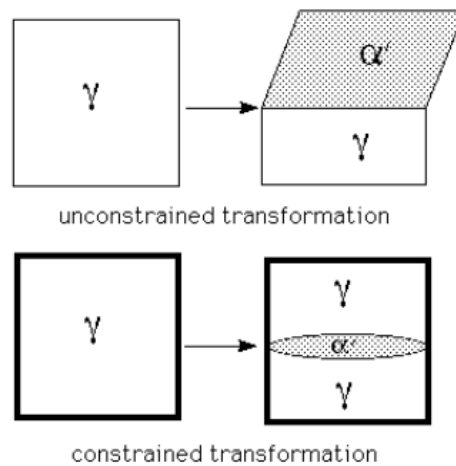


Figure 15 .Illustration of the habit plane between austenite and martensite in the constrained and unconstrained case <sup>91</sup>.

Carbide formation is of big importance for the martensitic transformation: when chromium carbides  $\text{Cr}_{23}\text{C}_6$  precipitate, the rest of the matrix becomes depleted of those elements and thus, the  $M_s$  temperature increases locally <sup>93</sup>.

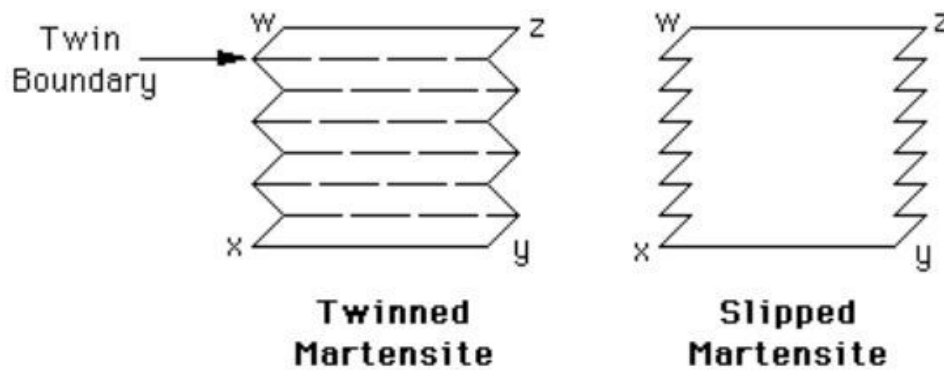


Figure 16. Accommodation of the martensitic shape a) by twinning b) by slipping <sup>91</sup>.Formation

In metastable austenitic stainless steels, the transformation from austenite to  $\alpha'$  martensite can occur either directly austenite  $\gamma$  (fcc)  $\rightarrow$  martensite  $\alpha'$  (bcc) or via an intermediate state: hexagonal martensite  $\epsilon$  <sup>61,62,94,95</sup>

austenite  $\gamma$  (fcc)  $\rightarrow$  martensite  $\epsilon$  (hcp)  $\rightarrow$  martensite  $\alpha'$  (bcc)

It has been observed in numerous studies that in metastable stainless steels  $\alpha'$  nucleates at the intersection of shear bands <sup>62,69,96,97</sup>, such as demonstrated in Figure 17. The nucleation at a single shear band <sup>76,98–100</sup>, at grain boundaries <sup>3</sup> or dislocation pile-ups <sup>69</sup> has also been reported, although it is less common.



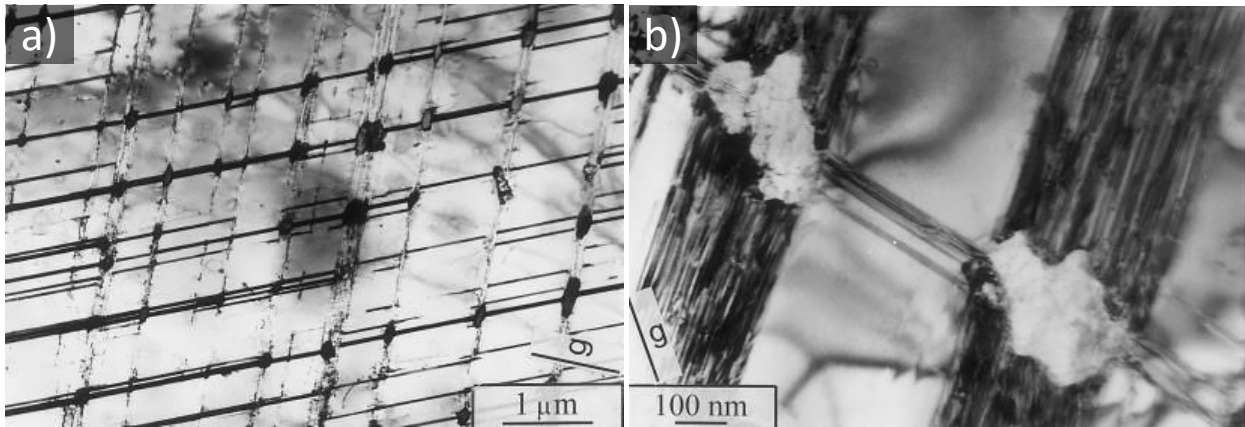


Figure 17.  $\alpha'$ -martensite nucleation at the intersection  $\epsilon$  plates in 316LN. a) General view and b) Magnification<sup>101</sup>.

The expansion of the  $\alpha'$ -martensitic phase occurs by growth and coalescence of the nuclei<sup>96,99,102</sup>.

In the steel grades where it occurs,  $\alpha'$ -martensitic transformation and presence has a key role for the properties of the respective material.

### Plasticity transmission

High deformation is expected to contribute to an accumulation or pile-up of dislocations at grain boundaries<sup>103</sup>. This leads to an accumulation of plasticity at the grain boundary<sup>104,105</sup>, whereby the resulting localized stress concentration can be different for individual grains in a polycrystalline compound – depending on several factors, *e.g.* the grain size or crystallographic orientation in respect to the loading axis. As a consequence, with increasing strain, dislocations can be transmitted from the grain with the higher stress concentration to the one with the lower. Thus, plasticity propagation through grain boundaries is possible. Thereby, the easiness of transmission is determined by the misorientation between the slip systems in the two adjacent grains<sup>106</sup>.

### Factors affecting the deformation mechanisms

#### SFE

Twinning,  $\epsilon$ -martensite formation and dislocation slip, as well as  $\alpha'$ -martensitic transformation are known to be competing deformation mechanisms on austenitic steels<sup>8,53,107</sup>. Thereby, the preferential transformation mechanisms in a metastable austenitic stainless steel are related to the Stacking Fault Energy, as can be appreciated in Figure 18<sup>81</sup>. In order to activate deformation mechanisms like cross slip or intersection, the dissociated dislocations need to recombine – otherwise only planar slip of the two partial dislocations together is possible. Thus, if the SFE is high and recombination of dissociated dislocations is

easy, plasticity takes places preferentially by dislocation movement. In case of a small SFE the distance between the separated dislocations is wider, which leads to planar dislocation structures. This in turn favors formation of bands with defaulted stacking sequences, such as mechanical twins, while dislocation mobility is reduced<sup>108</sup>. At even lower SFE, shear band formation and martensitic phase transformation may result in being the most energetically favorable deformation mechanism<sup>108,109</sup>.

So, in austenitic stainless steels the mechanically induced formation of  $\epsilon$  martensite is reported to occur when the SFE is below 18 mJ/m<sup>2</sup><sup>108</sup> and coexists with  $\alpha'$  martensite forms if the SFE is below 12 mJ/m<sup>2</sup>. Between 12 and 18 mJ/m<sup>2</sup>, twinning represents the preferential deformation mechanism. Furthermore, not only the formation of  $\alpha'$ -martensite at all, but also the type of transformation (directly or via the intermediate state  $\epsilon$ ), depends on the SFE of the material<sup>34110</sup>.

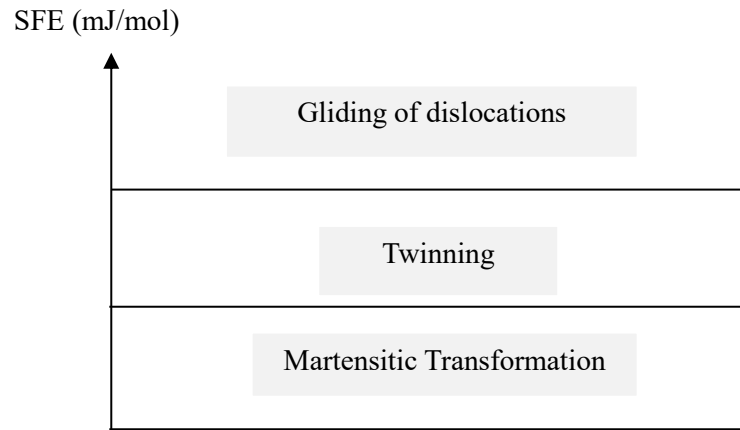


Figure 18. Different deformation mechanisms in function of the SFE. Adapted from<sup>108</sup>.

The SFE is a function of the chemical composition and temperature. Schramm and Reed<sup>111</sup> developed an equation for an approximate determination of the SFE depending on the alloy composition:

$$SFE (mJ/m^2) = -53 + 6.2 (wt\%Ni) + 0.7 (wt\%Cr) + 3.2 (wt\%Mn) + 9.3 (wt\%Mo) \quad (7)$$

Brofman and Ansell<sup>109</sup> elaborated an equation which might be more suitable for Cr-Ni-Fe steels, since it leaves out Mn, not present in significant quantities, but considers the C which is higher in this steel group compared to others and strongly affects the SFE:

$$SFE (mJ/m^2) = 16.7 + 2.1(wt\%Ni) - 0.9(wt\%Cr) + 26(wt\%C) \quad (8)$$

Table 2. Stacking fault energy of various fcc materials at room temperature<sup>109</sup>.

Material	301LN	316L	304	Ag	Cu	Ni	Al
SFE [mJ/m <sup>2</sup> ]	12-14	14	17	22	78	90	166

Table 2 gives an overview of the SFE of different fcc metals. Noticeably, all austenitic stainless steels together with Ag have a significantly lower SFE than most other fcc metals. Thus, opposed to the latter dislocation slip is less important in austenitic stainless steels and twinning, shear bands and phase transformation prevail. Thereby, the SFE of AISI 301 LN is estimated to be between 12 and 14 mJ/m<sup>2</sup> <sup>861</sup>, being thus the lowest of all metastable steels <sup>40</sup>.

## Temperature

Since the SFE increases with temperature, consequently, both twinning and  $\epsilon$ - or  $\alpha'$ -transformation respectively decrease <sup>73</sup>. Especially, the driving force for  $\alpha'$ -martensitic transformation is highly dependent on the temperature <sup>89,112,113</sup>, as can be appreciated in Figure 19, since the latter determines the necessary driving force for the transformation. Figure 20 shows  $\alpha'$ -martensite formation rate with strain at different temperatures. It clearly illustrates that at low temperatures, below  $M_s^\sigma$ , where the driving force for phase transformation is high, stress-assisted  $\alpha'$ -martensitic transformation occurs already during elastic deformation, while at higher temperature a certain strain must precede the beginning of phase transformation (strain-induced phase transformation).

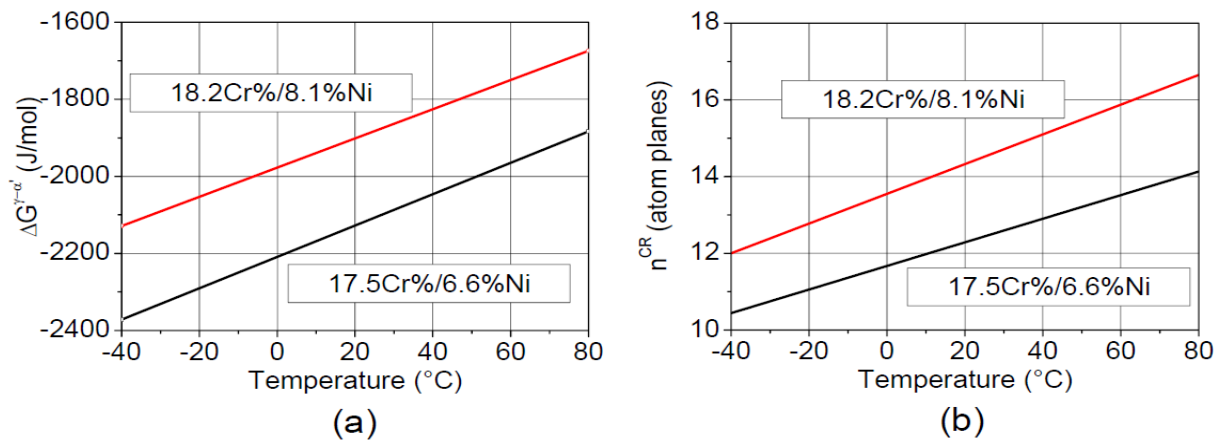


Figure 19. Effect of temperature on  $\alpha'$ -martensite formation. a) chemical driving force  $\Delta G_{\gamma \rightarrow \alpha'}$  and b) critical embryo size  $n^{CR}$  of  $\alpha'$ -martensite phase in two Fe-Cr-Ni alloys <sup>114</sup>.

The transformation also exhibits a saturation level as shown in the same figure. One explanation for this behavior is the inhibition of growth of the martensite phase by the continuing increase of the dislocation density in the surrounding austenite phase. These dislocations have to be moved for the martensitic phase to grow. When the force required to move those dislocations becomes higher than the driving force for martensitic transformation, which is especially given at low temperatures, the driving force provided by the deformation might not be sufficient and the growth of martensite stops. In this case, the retained austenite is mechanically stabilized <sup>115</sup>.

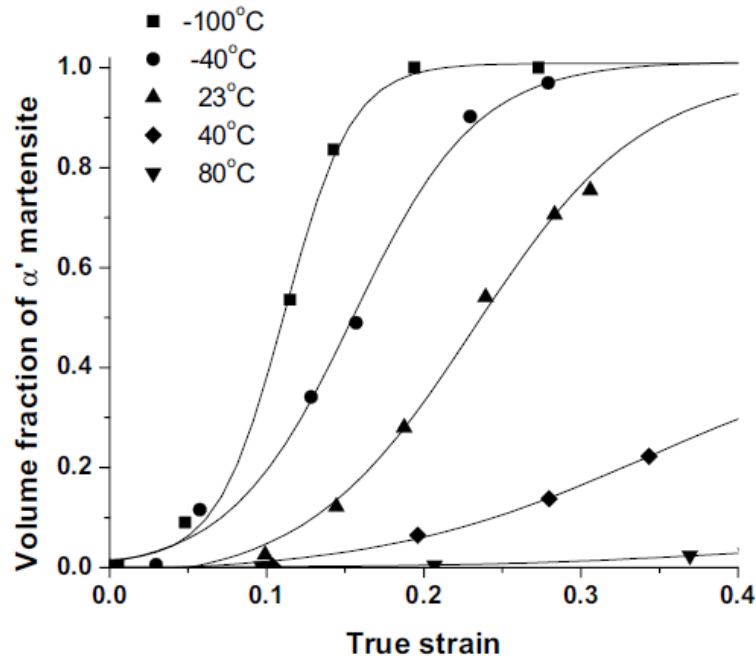


Figure 20. Martensitic transformation in AISI301LN steels at different temperatures <sup>116</sup>.

On the other hand, twinning and dislocation glide become the dominant deformation mechanisms at temperatures where the driving force for martensitic transformation is not sufficient <sup>117</sup>.

### Chemical composition

From equations (3), (7) and (8), it becomes clear why the chemical composition is an important factor. Also, one essential alloy element, which is not accounted for in (7) and (8), is nitrogen. Its influence on the SFE is controversial. It is reported to both increase <sup>81,118</sup> and decrease <sup>56,111</sup> the SFE, or evolve non-monotonically <sup>119,120</sup>. In moderate contents, the increase of SFE prevails <sup>53,121</sup>, having thus a strong impact on the deformation microstructure <sup>122</sup>. As already mentioned, N is a powerful  $\gamma$  stabilizer and strengthener and thus, already a slight local variation in can change the transformation mechanism. So, it modifies the dislocation slip and arrangement <sup>123</sup>, as discernible in Figure 21, where dislocation structures of 316L (0.04% N nitrogen) and 316LN (0.14% N) are compared: in the former alloy a disordered dislocation tangle can be observed, while in the later N promotes planar slip, as often observed in literature <sup>124–126</sup>. Thus, nitrogen is also known to improve the fatigue properties of metastable austenitic stainless steels <sup>53,127</sup>. Furthermore, it suppresses twinning <sup>53</sup> and  $\alpha'$ -martensitic transformation <sup>127</sup>.

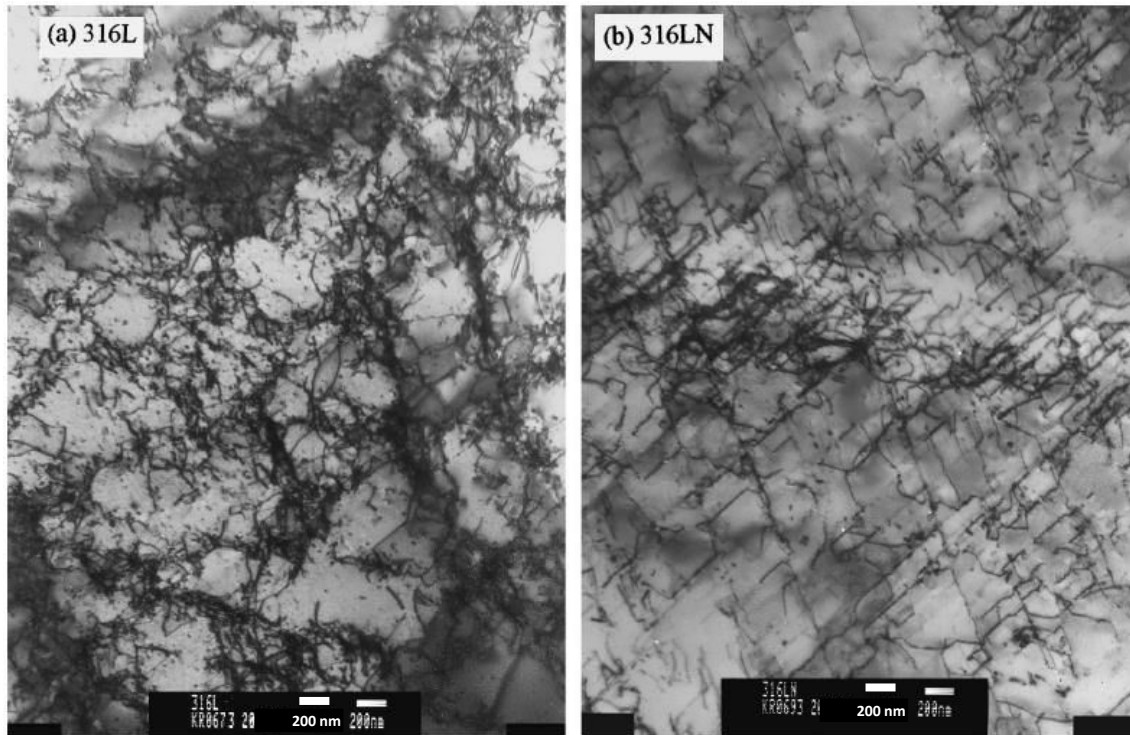


Figure 21. Dislocation structures in the fatigue plastic zones of a) 316L and b) 316LN<sup>124</sup>.

### Grain size

The grain size dependence is given by the interplay between the influence of the  $M_d$  temperature of the martensitic transformation and the SFE. As a consequence, the effective grain size dependence of the  $\alpha'$ -transformation rate is not monotonic, as can be withdrawn from Figure 22. The martensitic transformation rate both for  $\alpha'$ <sup>128–130</sup> and  $\epsilon$ -martensite<sup>116,131</sup> is in general higher for large grains, while for smaller grains twins and stacking faults prevail as deformation mechanisms<sup>132</sup>. However, in the nanorange and in alloys exhibiting planar slip, the behavior reverses<sup>116</sup>. On one hand, this can be due to the high density of intersecting planar faults in small grain  $\alpha'$ -martensitic nucleation as favored again<sup>133</sup>. On the other hand,  $\alpha'$ -nucleation at grain boundaries is favored in a steel with small grains and thus, a high fraction of grain boundaries<sup>116</sup>.

Grain size also influences the dislocation motion and arrangement. Thus, grain refinement can significantly improve the yield and tensile strength, as well as the fatigue properties<sup>134,135</sup>. Furthermore, the grain size determines the creep strain rate in metals.<sup>136</sup>

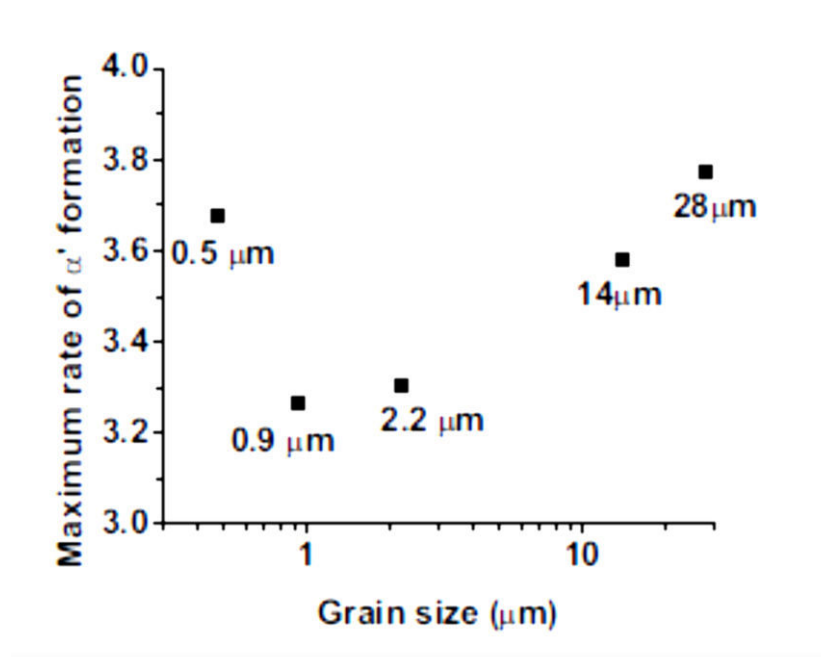


Figure 22. The maximum strain rate of martensitic transformation in dependence on the grain size is not monotonic <sup>111</sup>.

To summarize, grain size significantly influences the work hardening behavior of metastable austenitic stainless steels <sup>4,137</sup>: on one hand, as mentioned above, large grains exhibit a higher tendency towards phase transformation; but on the other hand, in agreement with the Hall-Petch law <sup>138,139</sup>, hardening mechanisms for austenite are more pronounced for a high fraction of grain boundaries, *i.e.* for small grain sized steels <sup>140–142</sup>.

### Loading conditions

Strain rate affects  $\varepsilon$ - and  $\alpha'$ -martensite in a different way: while shear band formation is favored by high strain rates <sup>143</sup>, the adiabatic heating related to high strain rates decreases the driving force for  $\alpha'$  formation <sup>38,144</sup>. On the other side, the increase in  $\varepsilon$ -martensite content favors the indirect transformation  $\gamma \rightarrow \varepsilon \rightarrow \alpha'$  <sup>75,77,78,98</sup>, which results in a different morphology of  $\alpha'$ -martensite under high strain rates <sup>96</sup>.

Furthermore, the martensite formation depends on the type and degree of deformation, as well as the stress state, <sup>3,4,114</sup>. However, there are some controversies, as for the impact of the parameters mentioned above on the martensite formation <sup>108,81</sup>.

### 1.1.5 Fatigue properties

Fatigue can be defined as material behavior due to accumulation of stress/strain induced modifications, which lead, after a certain number of cycles, to a response of the material which can be achieved in

monotonic loading only at higher load/strain threshold values. Thereby, a differentiation between high and low cycle fatigue is made. The former refers to fatigue behavior resulting from repetitive loading clearly below the yield strength, *i.e.* in the elastic regime, and corresponding tests are usually carried out in constant stress mode. Low cycle fatigue occurs when significant plastic strain occurs in each cycle and thus cyclic accumulation of plastic strain can take place. Resulting strain localization leads to premature failure already at relatively low number of cycles (usually  $N < 10^4$ ).

Austenitic stainless steels exhibit a low cycle fatigue behavior which is partly common with other fcc metals, *e.g.* based on dislocation slip<sup>145</sup>. The corresponding strain localization can be observed in form of surface slip traces, as visualized in Figure 23. Thereby, the direction of slip traces corresponds to the orientation of the active slip planes with regard to the loading axis. Usually different fatigue stages can be distinguished, and each one goes along with a characteristic dislocation substructure<sup>146–148</sup>. In the first stage, planar arrangements are typically observed. Thereby, strain localization can result in formation of well-defined dislocation slip bands. At later stages, the increasing dislocation density can lead, in crystals oriented for multiple slip, first to the formation of tangles and later to substructural arrangements such as veins and channels, and also cell structures.

On the other hand, with increasing degree of metastability, the influence of martensitic transformation on the fatigue behavior of austenitic stainless steels increases. Martensitic transformation was found to occur in metastable austenitic steels under cyclic loading at stress/strain amplitudes significantly lower than the threshold value required in case of monotonic loading. This is explained by the fact that nucleation occurs at a cumulative plastic strain<sup>149,150</sup>.

Moreover, it is important to take into account the contribution of both, preexisting and newly formed martensite on the fatigue properties. Thus, the presence of martensite previously to cyclic loading can have a negative impact on the fatigue resistance due to the brittleness of martensite and the fact that crack propagation in martensitic zones is faster than in austenite<sup>151</sup>. On the other side, martensite formation during fatigue loading was found to be rather beneficial, since the associated volume expansion and the resulting compressive residual stress, as well as the strain hardening, contribute to the reduction of crack propagation rate<sup>39,150</sup>. Thus, the effect of martensite depends on the particular experimental or service conditions.

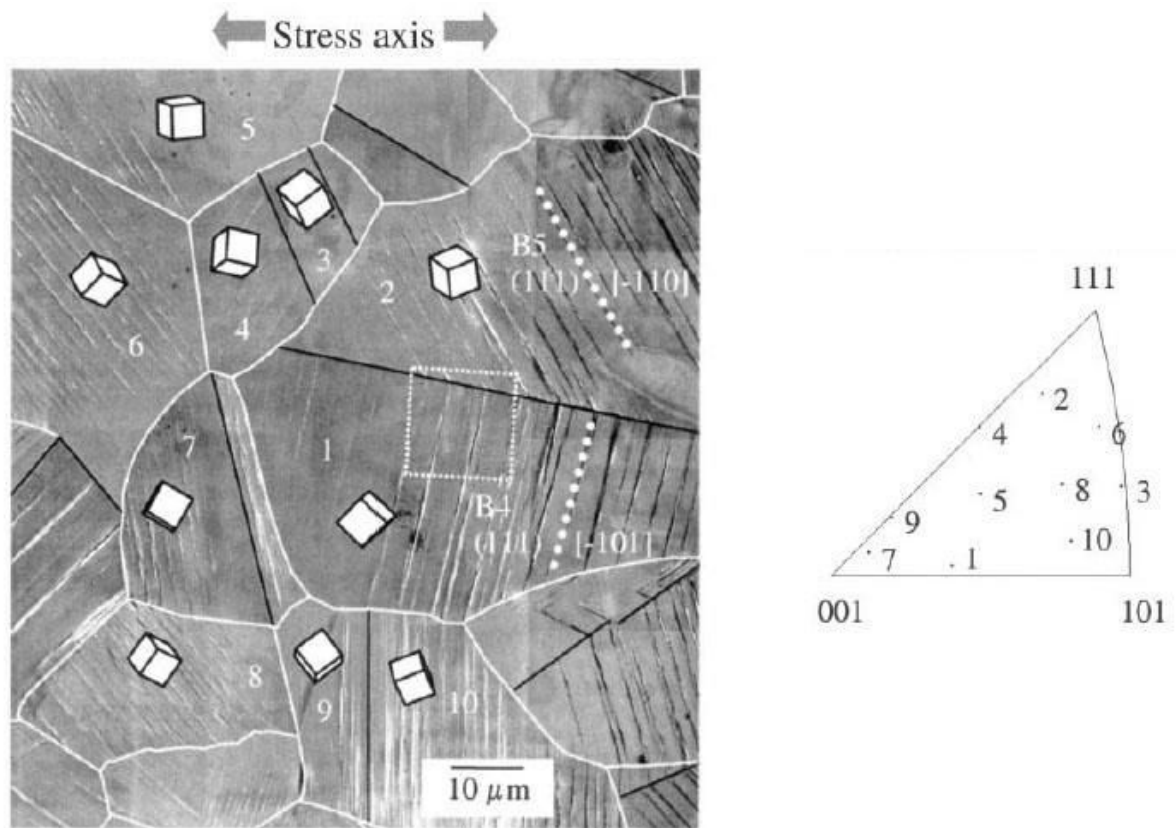


Figure 23. SEM image of the surface of AISI 316L submitted to low cycle fatigue testing. The surface normal of each grain is reported in the standard triangle<sup>145</sup>.

It becomes clear that the overall fatigue properties of metastable austenitic stainless steels are dependent on the collective properties of initial microstructure and the interplay of different deformation mechanisms. Consequently, the resulting fatigue behavior typically exhibits several characteristic softening and hardening stages.

Accordingly, the work-hardening of austenite usually leads to a hardening behavior in the first fatigue stage, while at later stages a softening can occur due to dislocation rearrangement, as illustrated in Figure 24a. This figure also shows the strong dependence of the cyclic response on the nitrogen content.

On the other hand, in prestrained samples a softening behavior is often predominant due to dynamic recovery<sup>152</sup>, as in Figure 24b. Likewise, appreciable in the figure is a second hardening, which can occur at elevated number of cycles, usually attributed to martensitic transformation. Thereby, according to the characteristics of strain-induced martensitic transformation, the latter must be preceded by a sufficient accumulation of strain, as discernible in the strain amplitude dependent shift of the number of cycles at which secondary hardening occurs.



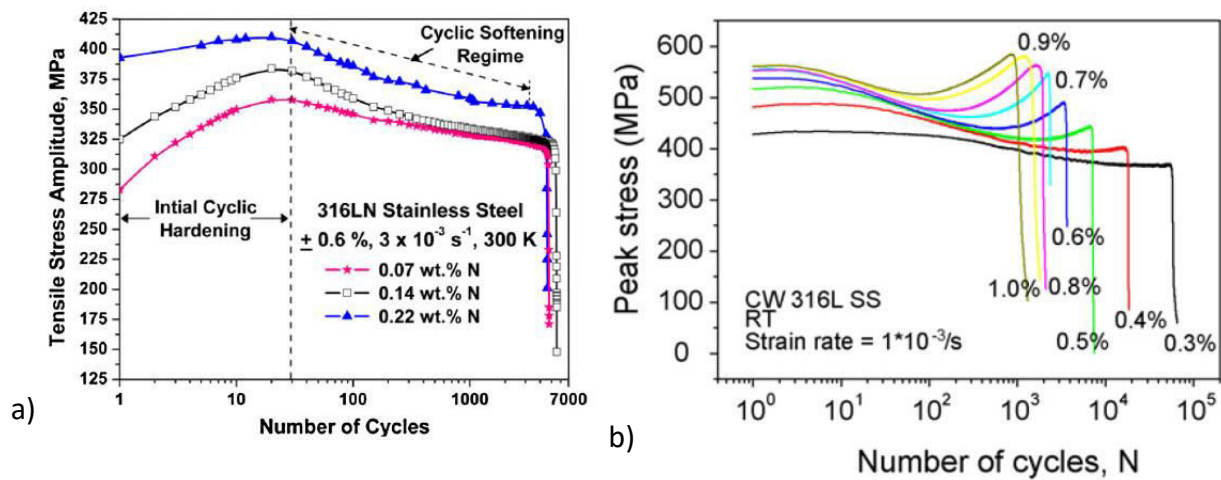


Figure 24. Cyclic fatigue behavior of metastable austenitic stainless steels. a) Cyclic stress response of annealed 316LN with different contents of nitrogen tested at a strain amplitude of 0.6 %<sup>126</sup>; b) Cyclic stress response of a 17%-prestrained 316L at different strain amplitudes<sup>152</sup>.

The exact relationship of optimal preexisting and transforming martensite content, the chemical composition of the material, the influence of the cyclic loading mode, load amplitude and speed, as well as the difference between loading in stress and strain control, have been studied by several authors<sup>153–155</sup>. However, the understanding of the influence of the martensitic transformation on austenitic stainless steels is still not sufficiently understood and it is crucial to obtain a better knowledge in this respect. Thus, one of the aims of this thesis is estimating the fatigue properties of a metastable austenitic stainless steel by cyclic loading of single grains by nanoindentation.

## 1.2 Instrumented Indentation Technique (Nanoindentation)

Nanoindentation is a technique for instrumented mechanical testing on micro- and sub micrometer scale. It is used for characterization of mechanical properties, like hardness and Young's modulus, on small scale. This is especially interesting for thin films, but also for polycrystalline materials, since it allows characterizing structures at small depths and lateral dimensions.

One of the key features of nanoindentation is the instrumented testing: it implies that during the indentation not only the necessary load, but also the corresponding penetration depth are simultaneously measured and constantly recorded. The result is a load-displacement or P-h curve, as depicted in Figure 25.

In general, the loading and unloading curves do not match as a result of plastic deformation: while the loading segment typically includes contributions from both plastic and elastic deformation, the unloading

is largely elastic. Residual imprints with a depth  $h_f$  remain on the surface as a consequence of plastic deformation.

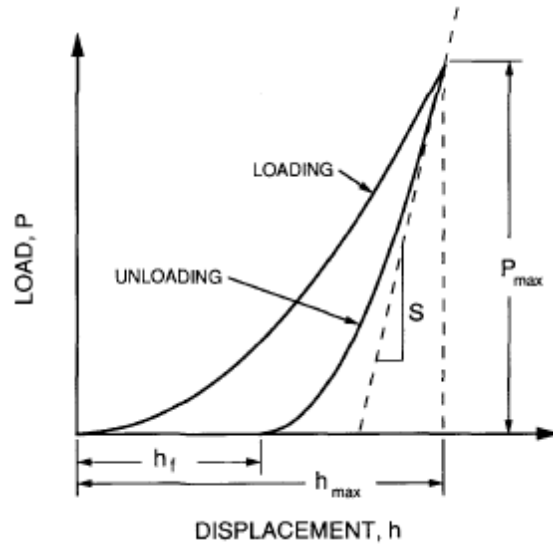


**Figure 25. Typical load-displacement curve of a nanoindentation <sup>156</sup>. With the characteristic parameters maximal load  $P_{max}$ , maximal displacement  $h_{max}$ , final depth of the impression after unloading  $h_f$  and the initial unloading contact stiffness  $S$ .**

The information which can be extracted from such a curve is the displacement  $h_{max}$  at the maximal load  $P_{max}$ , the final impression depth after unloading  $h_f$  and the initial unloading contact stiffness  $S$ , which is the derivative of load at the start of the unloading.

### 1.2.1 Resolution and stability

Given the small scale of testing, stability against vibration and thermal drift is important. Thus, a nanoindentation equipment is typically mounted on a vibration isolating frame and encased in a thermally isolating housing. Additional features, such as active surface referencing used by CSM Instruments can significantly improve the thermal stability <sup>157</sup>.

### 1.2.2 Indenters

In principle, different geometries of nanoindenter tips are possible. The most common of them are presented in the following:

**Vickers:** The Vickers indenter manifests a four-sided pyramidal geometry. The obvious reason to use Vickers indenters is the fact that it is the indenter most commonly used for micro- and macrometric length scale, facilitating thus a congruity of the test results at different scales.

**Berkovich:** It is a three-sided pyramidal indenter having the same area function as Vickers and thus providing comparable test behavior and results. Since a sharp tip is easier to fabricate for a three-sided rather than a four-sided pyramid <sup>158</sup>, Berkovich is the most popular indenter for the measurement of hardness and Young's modulus.

**Cube-Corner:** It is also a three-sided pyramidal indenter, however with a sharper tip apex. Consequently, in comparison with other indenters it creates a significantly higher stress and strain at the same load level and is widely employed for characterization of failure mechanisms and estimation of fracture toughness <sup>159</sup>.

**Spherical indenter:** The spherical indenter has a large contact radius in comparison to the pyramidal indenters <sup>160</sup> and is therefore interesting for characterization of the elastic behavior and the contact pressure and the transition from elastic to elasto-plastic contact. It can also be used to study the stress-strain behavior, which can be calculated from the indentation curve, providing information about the yield strength and work hardening of the material. On the other hand, H and E measurements carried out with a spherical indenter are usually less precise than with a sharp tip, furthermore the stress fields created by a spherical indenter are lower, so it is less suitable to induce localized plastic deformation into the indented material.

**Flat punch:** The flat punch is used for homogeneous compression of small structures, such as micropillars <sup>13</sup>. Its main advantage is the fact that the contact area remains constant during the whole loading range and thus, errors related with estimation of the contact area can be excluded.

### 1.2.3 Characteristics of the load-displacement curves

As can be withdrawn from Figure 26, the depth of the impression is not equal to  $h_{max}$ , since the elastic deformation of the whole surface, as well as the compliance of the indenter during load, contributes to the total indenter displacement.

The real depth of the indent under load can be approximated by  $h_c$ , which, assuming that the initial unloading is elastic, can be approached by

$$h_c = h_{max} - \varepsilon \frac{P}{S} \quad (9)$$

where  $\varepsilon$  is a parameter dependent on the indenter geometry (*e.g.* 0.75 for Berkovich). The contact area in nanoindentation is determined in a different way than during conventional testing: in the latter it is measured manually, by visualizing the indent. However, for small indentations this leads to significant errors. In nanoindentation the displacement of the indenter is known, so that with an appropriate area function the corresponding projected contact area  $A_c$  can be calculated.

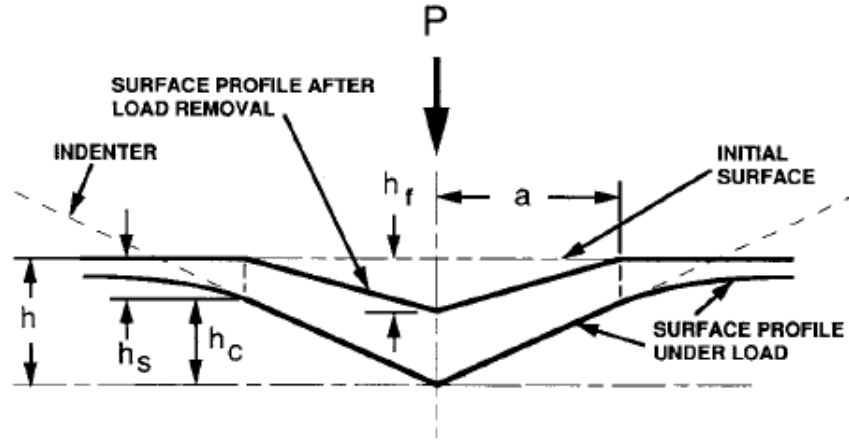


Figure 26. Illustration of relevant parameters in nanoindentation <sup>156</sup>.

It is important to point out that the  $A_c$  estimated at maximal load is not equal to the remaining contact area estimated after unloading in case of conventional indentation testing. The difference, as illustrated in Figure 26, originates from the circumstance that during unloading the elastic part of the deformation recovers.  $A_c$  is related to  $h_c$ , adopting *e.g.* in case of an ideal Berkovich indenter the value of approx.  $24,5 h_c^2$ . However, due to the imperfections or wear of the tip, usually the exact area function is calculated by indenting a material with well-known mechanical properties and correlating the measured contact depth with the corresponding area:

$$A_c(h_c) = 24.5h_c^2 + C_1h_c^1 + C_2h_c^{1/2} + C_3h_c^{1/4} + \dots \quad (10)$$

The hardness of the material, which is defined as

$$H = P / A_c \quad (11)$$

can be calculated if  $A_c$  is known. From the  $S$  and  $A_c$  also the Young's modulus can be estimated according to the equation:

$$E_{eff} = \beta \frac{\sqrt{\pi}}{2} \frac{S}{\sqrt{A_c}} \quad (12)$$

where  $\beta$  is the geometry shape factor which accounts for the asymmetry of the indenter tip and  $E_{eff}$  is the effective Young's modulus, determined by the respective moduli and Poisson's ratios  $\nu$  of sample and indenter materials:

$$\frac{1}{E_{eff}} = \frac{(1-\nu_{sample}^2)}{E_{sample}} + \frac{(1-\nu_{indenter}^2)}{E_{indenter}} \quad (13)$$

For a Berkovich tip  $\beta$  is 1.034. Thus, knowing the indenter characteristics, the sample modulus can be calculated.

In the incipient stage of deformation, the material response is regarded to be fully elastic – until the critical load for activation of dislocations and thus initiation of plasticity is achieved. In the elastic regime, the indenter-sample contact can be approached by the Hertzian contact <sup>161</sup>

$$P = \frac{4}{3} \sqrt{R} E_{eff} (h - h_f)^{3/2} \quad (14)$$

whereby the indenter radius  $R$  can be estimated for spherical indenters from the slope, when plotting  $a^2$  against  $h_c$ -given the relationship

$$a^2 = 2Rh_c - h_c^2, \quad (15)$$

which according to Field and Swain <sup>10</sup> is the relationship between contact depth, contact radius and indenter radius for spherical tips. Thereby, also pyramidal tips can be approximated at small loads as spherical, due to the always present tip rounding.

The mean contact pressure  $p_0$  can be calculated within the elastic regime <sup>10,23,162,163</sup> as

$$p_0 = \frac{P}{\pi a^2} = \frac{4}{3\pi} E_{eff} \left( \frac{a}{R} \right) = \left( \frac{6PE_{eff}^2}{\pi^3 R^2} \right)^{1/3} \quad (16)$$

The elastoplastic transition is usually marked by a change in slope and often accompanied by strain burst in the P-h curve – called pop-ins. The corresponding maximum shear stress before the elastoplastic can be calculated with (14), (15) and (16) in agreement with <sup>164</sup> as

$$\tau_{max} = 0.31 \left( \frac{6PE_{eff}^2}{\pi^3 R^2} \right)^{1/3} \quad (17)$$

#### 1.2.4 Indentation Size Effect

The plastic fraction of the deformation caused by nanoindentation exhibits a size effect <sup>165–167</sup>, since GNDs must be generated in order to accommodate the deformation. The flow stress is determined by both, statistically stored and geometrically necessary dislocations. However, for small contact areas the density of GNDs is higher, and thus, their contribution to the total penetration resistance more pronounced for shallow indents.

## **1.3 State of the Art: Combined small scale testing and characterization of metastable stainless steels**

### **1.3.1 TEM characterization**

Transmission Electron Microscopy (TEM) is an extremely useful technique to characterize the crystalline structure of materials with high resolution. Thereby, the sample is exposed to an electron beam with an energy of several hundred keV, so that a significant part of the electrons will be transmitted through the sample. This implies the fabrication of a lamella, thin enough to allow the penetration of electrons.

The transmitted electrons will be diffracted, if they encounter a plane in Bragg position. Other contrast mechanisms are caused by variation of thickness, chemical and crystalline structure. Due to the small wavelength of electrons, resolution up to sub-Å can be achieved, which is used in High-Resolution Transmission Microscopy (HRTEM) for atomic imaging.

For crystallographic characterization, diffraction is the most important contrast mechanism, since it enables the visualization of grains, grain boundaries and defects such as twins, dislocations, stacking faults, precipitates etc. Moreover, the diffraction pattern gives quantitative information about the crystalline structure and can be used for identification of phases and determination of the crystallographic orientation. Also, the features corresponding to a concrete diffraction spot can be selectively chosen to be imaged in dark field (DF) providing a high contrast between the corresponding crystallographic structure and its surroundings. All this makes TEM an important tool for characterization of metals on small scale.

### **1.3.2 Nanoindentation studies of TRIP steels**

Recently, nanoindentation evolved from a pure characterization technique to a manipulation method. It can be deliberately used to induce permanent modification of the material on small scale and thus investigating deformation mechanisms, such as pile-up or sink-in around the impression, formation and/or emergence of defect structures like dislocations, twins or slip traces on the surface, providing clues about the strengthening mechanisms.

Lately, also characterization by TEM, after extracting lamellae of the area below a nanoindentation has been performed. Especially interesting is this mechanical manipulation on small scale for materials exhibiting the TRIP effect, since phase transformation can be induced by nanoindentation and subsequently observed by TEM. For example, Misra *et al.*<sup>101</sup> observed in dual-phase steels the formation of twins and twin-type strained-induced martensite due to deformation by nanoindentation.

An interesting feature in nanoindentation experiments are pop-ins (see Figure 27), which can be described as displacement bursts in the load-displacement curve. There are multiple possible origins of pop-ins, which in many cases are not certainly clear. However, it was found that the first pop-in is likely to be due to the transition from elastic to elasto-plastic contact, and the related surpassing of the yield point involving nucleation or activation of dislocations<sup>30,64,168–170</sup>. Successive pop-in events have been assigned to moving or formation of pile-ups of dislocations, formation of twins<sup>171</sup>, slip bands<sup>22,30,64,169,172</sup>, as well as in association with phase transformation in steels with TRIP effect<sup>22,64,172</sup>. It is speculated that a phase transformation can be detected as pop-ins because of the accompanied sudden geometrical softening<sup>30</sup>.

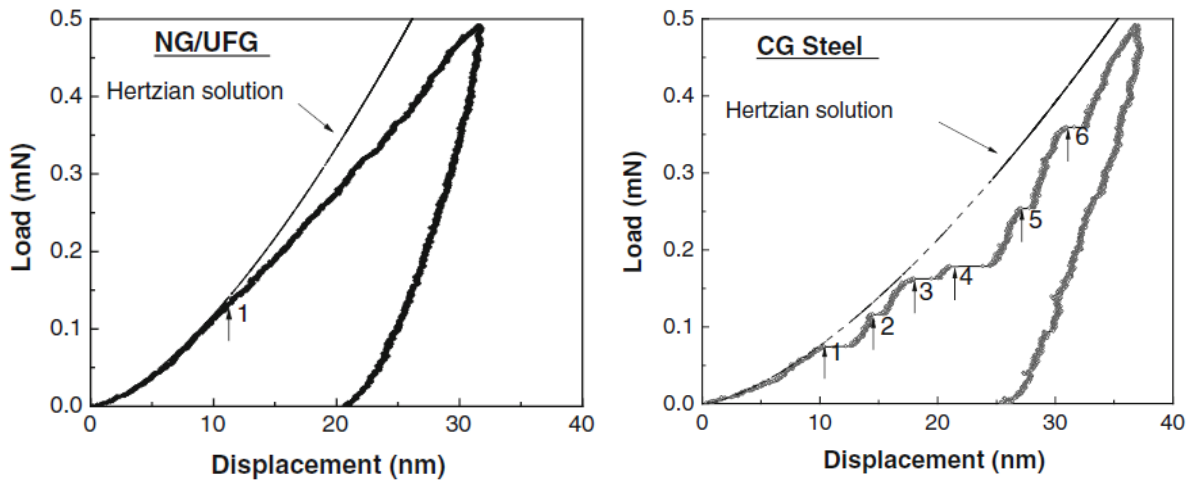


Figure 27. Load-displacement curves of nanograin and coarse grain AISI 301 LN exhibiting pop-ins. Adapted from<sup>173</sup>.

Misra *et al.* carried out several studies involving nanoindentation of selective grains of austenitic-martensitic steels including AISI301LN<sup>64,101,173–176</sup>. Part of their results is summarized in Figure 27-Figure 29. They found that normal or ultrafine austenitic grains in AISI 301LN exhibit only a slope discontinuity at the elasto-plastic transition, while the coarse-grain material exhibited several pop-ins, which were attributed to martensitic transformation. Martensite nucleates at the intersection of shear bands and various pop-ins (Figure 27) are present in the nanoindentation curve, while in the case of fine grains no pop-ins are visible and the microstructure exhibits a high content on mechanical twins<sup>173</sup>. Those results are in agreement with the dependence of the SFE and the preferential deformation mechanism on the grain size, as mentioned in previous sections.

The assumption of a correlation between pop-ins and phase transformation is supported by Figure 28, which depicts a comparison of an indentation curve in austenite and martensite: It shows that only austenitic grains exhibited pop-ins, but not the martensitic ones. Figure 29 shows the corresponding dislocation structure observed in the cross section of the residual imprint of the martensitic grain. Analogous observations of the austenitic grain were not provided by Misra *et al.*<sup>64,101,173–176</sup>.

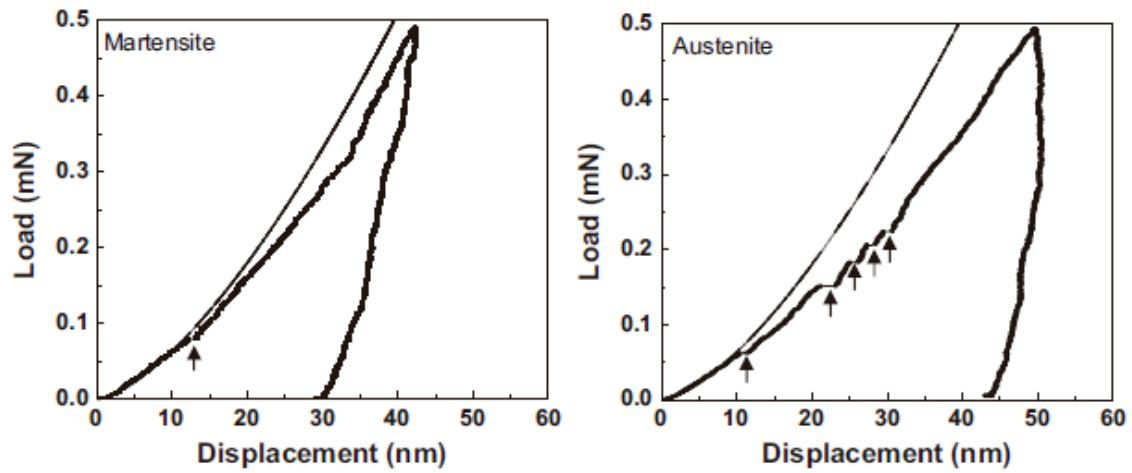


Figure 28. Comparison of nanoindentation curves of dual phase steels for martensite and austenite grains <sup>101</sup>.

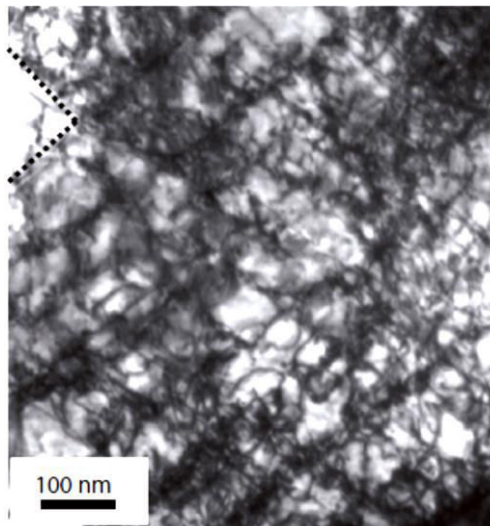


Figure 29. Dislocation structure in deformed  $\alpha'$  martensite with interference of dislocations in several slip systems <sup>101</sup>.

A TEM lamella from an austenitic grain of a Fe-Mn TRIP steel, indented up to the occurrence of three pop-ins, was extracted by Ahn *et al.* <sup>30</sup> who observed the presence of a martensitic grain directly under the indenter. Previously, they confirmed by EBSD that the corresponding grain was completely austenitic before the indentation. Furthermore, they tried to explain why the martensitic transformation causes pop-ins proposing the concept of favorable variant selection, implying that a martensite variant with a Bain distortion parallel to the compressive axis will be chosen and the pop-in will occur as a response to the respective compression.



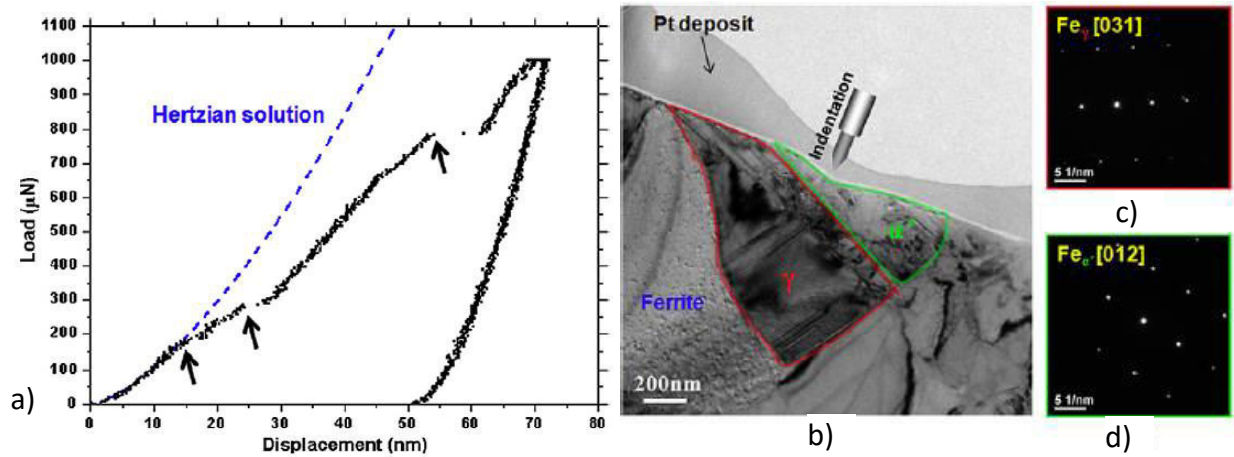
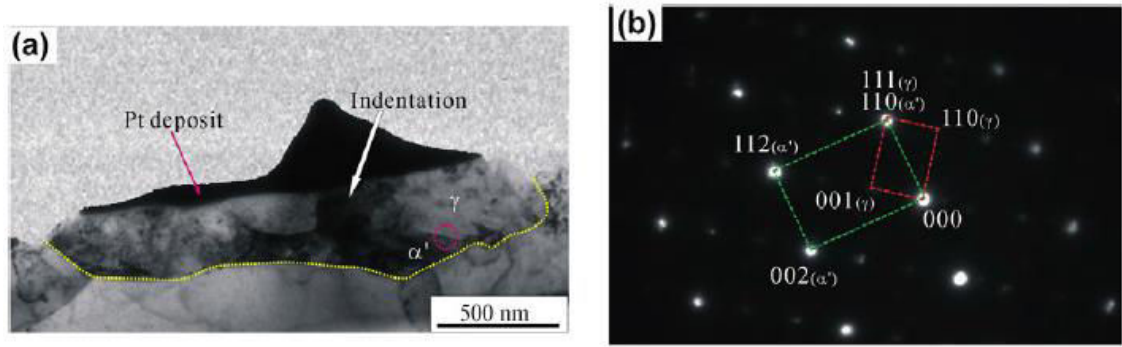


Figure 30. Austenitic grain in TRIP steels after a nanoindentation test of 70 nm displacement into the surface. Corresponding P-h curve; b) Formation Martensitic grain observed directly below the indent b) and c) diffraction patterns of the martensitic and austenitic phases obtained during subsequent TEM characterization. Adapted from <sup>30</sup>.

Also, He *et al.* <sup>172</sup> found that in case of pop-ins in the P-h curve, the martensite formed exhibited Kurdjumov-Sachs relationship with the surrounding austenite (see Figure 31), indicating that it evolved from the austenitic phase. Besides, they also concluded that only the pop-ins which conduct to an increase in the load-displacement slope, *i.e.* a hardness increase, are caused by martensitic transformation; while the other pop-ins might be due to the transmission of dislocations across low angle grain boundaries. This hypothesis is supported by the work of Sekido *et al.* <sup>177</sup> who observed in Fe-Mn alloys that the active deformation mechanism (either slip or formation of  $\epsilon$  martensite) is correlated with the P-h curve slope. Since the martensite lath was formed not directly under the indenter, and thus was not in contact with the tip, they explained the hardness increase after martensitic transformation by dispersion hardening: the presence of martensite increases the dislocation density in the surrounding austenite, which following the Taylor relation, rises its hardness <sup>178</sup>.

However, Kim *et al.* <sup>169</sup>, who performed an in-situ study using nanoindentation in TEM, found that although the pop-ins are related to the phase transformation they are not directly caused by this event. Moreover, Sekido *et al.* assumed that the pop-in might be due to the preceding formation of the  $\epsilon$ -martensite <sup>177</sup>.



**Figure 31.** Deformation structure surrounding a residual imprint in a medium-Mn TRIP steel. a) TEM bright field image and b) corresponding diffraction pattern revealing Kurdjumov-Sachs relationship between the martensite and austenite phases <sup>172</sup>.

Indeed, when in 2015, Ahn *et al.* performed another study in a high-nitrogen Fe-Cr-Mn steel <sup>179</sup>, and found the presence of both  $\epsilon$  and  $\alpha'$ -martensite under the nanoindenter (Figure 32), they concluded that pop-ins are due to  $\epsilon$ - and not  $\alpha'$ -formation. Also, they could correlate the width of the pop-ins with the displacement parallel to the indentation axis expected for  $\epsilon$ -martensitic transformation on the active slip system. On the other hand, they calculated the contraction for  $\epsilon \rightarrow \alpha'$ -transformation parallel to the indentation direction to be too small to be detected as a pop-in. Thus,  $\alpha'$ -martensitic transformation occurs without any corresponding reflection in the P-h curve.

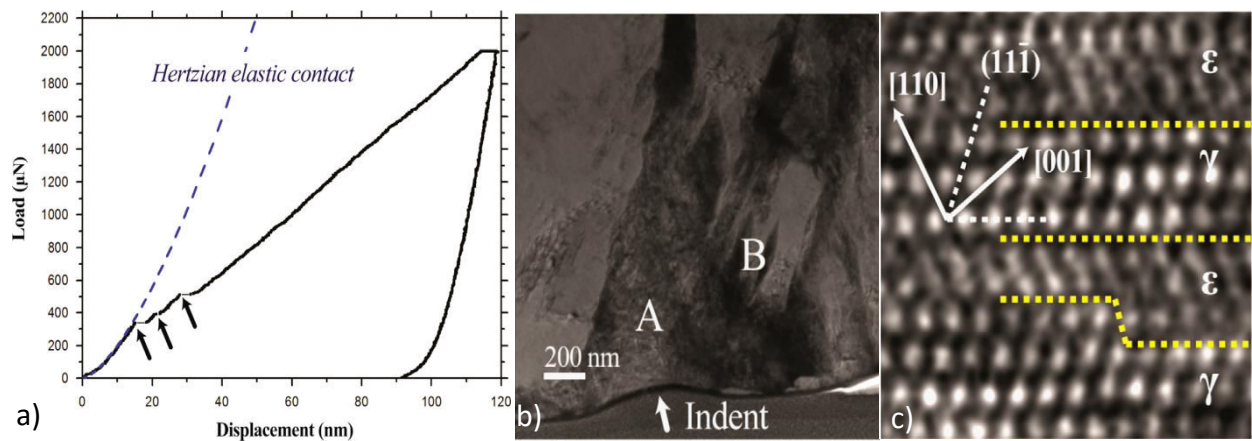


**Figure 32.** Formation of  $\epsilon$ -martensite induced by nanoindentation. . a) Corresponding P-h curve; b) Cross section of the residual imprint, exhibiting  $\gamma$  and  $\alpha'$  in region A, as well as  $\epsilon$  in region B; c) Atomic resolution of thin  $\epsilon$ -platelets found in region B. Adapted from <sup>179</sup>.

### 1.3.3 Cyclic nanoindentation

Cyclic nanoindentation refers to the repetitive loading at the same location of a sample. This kind of testing can give evidence on plasticity evolution, as well as on reversible deformation under load. Thus,

cyclic nanoindentation has been increasingly applied in the last years and several interesting studies have been published, some of which are commented in the following paragraphs.

For example, cyclic nanoindentation loading on glasses at loads below the yield point has been performed. Such loading could induce hardening of the glass via shear band formation, provided the applied load surpasses a minimum threshold amplitude<sup>180–182</sup>.

Exhaustive cyclic nanoindentation studies have been dedicated to study Kinking Non-linear Elasticity (KNE), phenomenon exhibited by a number of solids such as graphite, sapphire, mica, GaN or carbides. Hereby, cyclic P-h curves exhibited reversible hystereses. This was explained by the occurrence of fully reversible formation of kink bands under the indenter, due to KNE, caused by reversible motion of dislocations. An anisotropic behavior was found by Basu *et al.* for GaN<sup>23,183</sup>: due to the different characteristics in dislocation motion, the response to repeated nanoindentation was different for A (basal) and C (prismatic) planes: while for the former the unloading and reloading curves overlapped, as can be expected for elastic behavior, only the latter featured hysteresis loops involving energy dissipation (Figure 33).

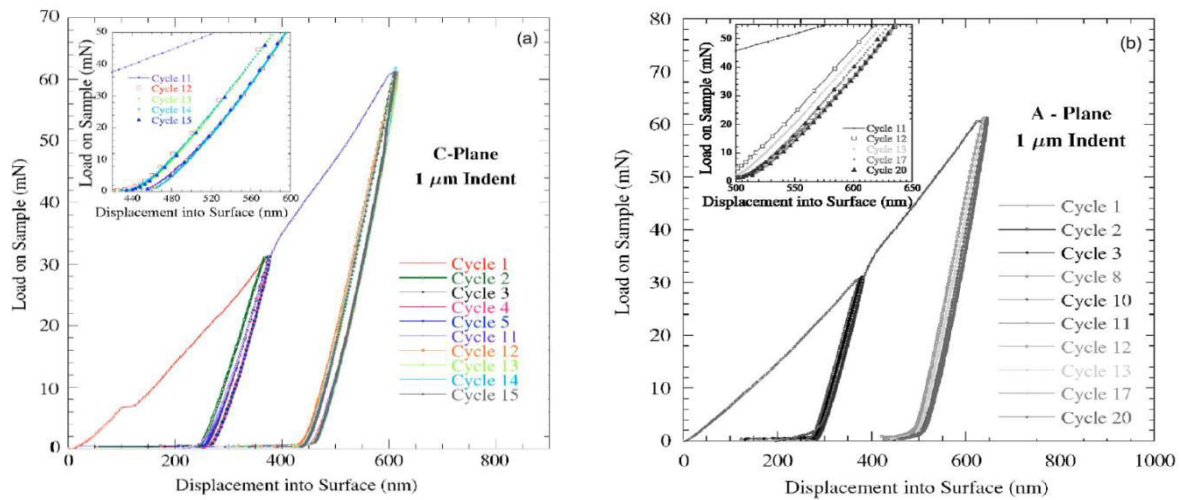


**Figure 33. Spherical nanoindentation load-displacement response for repeated spherical nanoindentation on the same location with a 1  $\mu\text{m}$  spherical indenter. The applied load was 30 mN for the first 10 cycles and 60 mN thereafter. a) C plane and b) A plane. The insets magnify cycles 11–15 for the C plane and 11–20 for the A plane.<sup>23</sup>**

KNE was found to be temperature-dependent<sup>184</sup> and load-dependent<sup>130,184,185</sup>. Thus, it was found that kink bands dominate the cyclic indentation behavior for small loads, for higher loads the formation of mobile dislocation walls (MDWs) leads to cyclic softening (See Figure 34, while at even higher loads the coalescence of MDWs leads to cyclic hardening. Moreover, the authors observed the first hysteresis loop to be open, both for spherical and Berkovich indenters.

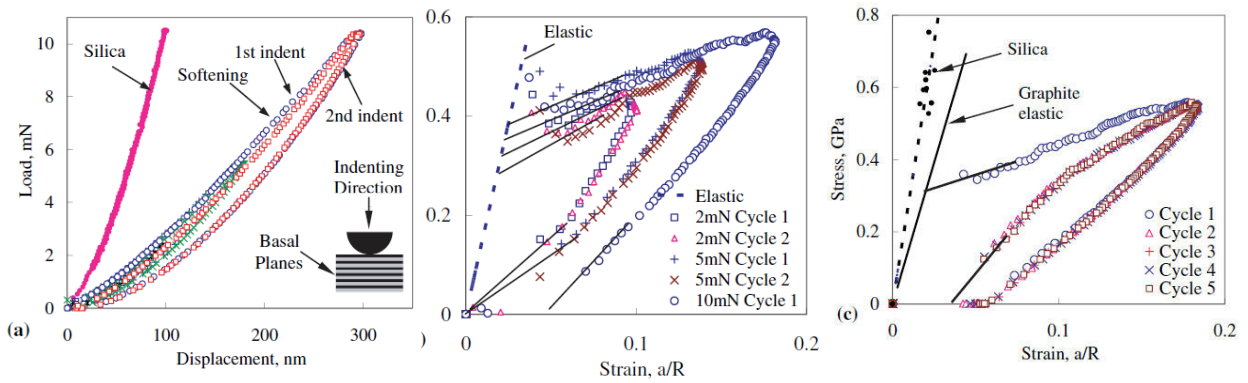


**Figure 34. Spherical indents along the  $\langle 0001 \rangle$  direction in graphite single crystals . (a) Multiple indents at 2, 5 and 10 mN. Only the first two successive indents at each loading are shown for clarity. Note softening in the first loading at 10mN load cycle between 5 and 10 mN. Second and subsequent indents to 10 mN are harder than the first. (b) Stress versus strain curves obtained from results shown in a. Low load indentations show full reversibility, but at 10 mN, the first loop is open. (c) Stress versus strain curves for cyclic loading at 10 mN. First cycle in open; subsequent indents are fully reversible and repeatable with a reproducibility that is noteworthy<sup>130</sup>.**

Cyclic nanoindentation has also been applied to study the fatigue behavior of minerals. So, cracks could be triggered by cyclic nanoindentation in  $\text{CaCO}_3$ <sup>24</sup>, going along with a pronounced pop-in. However, already before the occurrence of this pop-in fatigue characteristics could be observed, namely cycle opening (Figure 35a), which leads to a slow, but continuous sliding of the indenter tip into the surface, *i.e.* cyclic softening. On the other hand, decrease in contact stiffness induced by cyclic nanoindentation can be employed to characterize the fatigue behavior of thin films<sup>15</sup>.

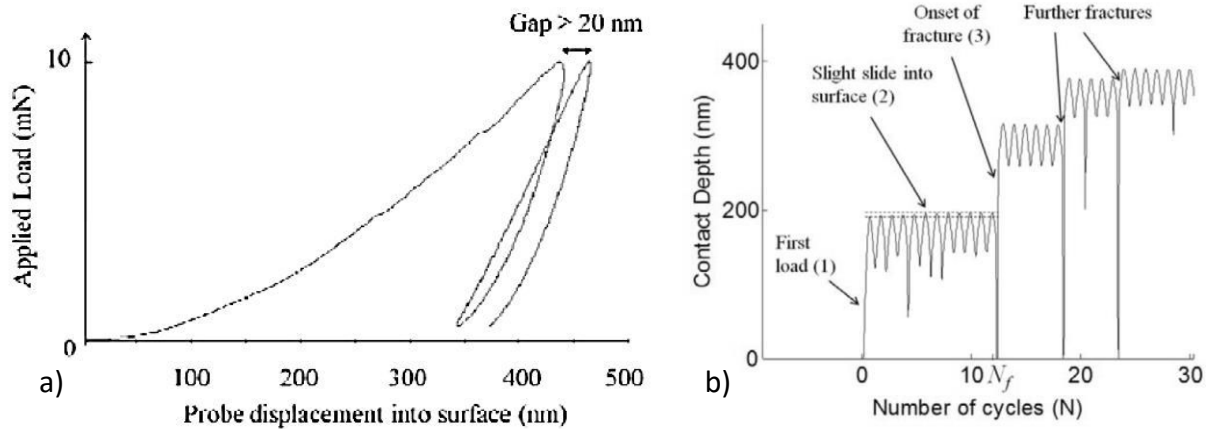


**Figure 35. Cyclic nanoindentation of  $\text{CaCO}_3$ . a) Indentation curve on  $\text{CaCO}_3$ , (maximum load = 10 mN); b) Contact depth as a function of the number of cycles (N) for a maximum load = 2.5 mN.**

Another widely employed field for cyclic nanoindentation study is phase transformation in shape-memory alloys<sup>25,186–188</sup>. So, Zhang and Komvopoulos<sup>187</sup> found that nanoindentation can induce reversible phase transformation under load. The initial P-h curve exhibits irreversible plasticity, such as can be expected for most of the solids, however, after a certain amount of training cycles, the anelastic deformation under

load becomes fully reversible and stable for small loads, as can be appreciated in Figure 36a. For CuAlNi this pseudoelastic behavior was predominant at small loads, while at higher loads plastic deformation prevails.

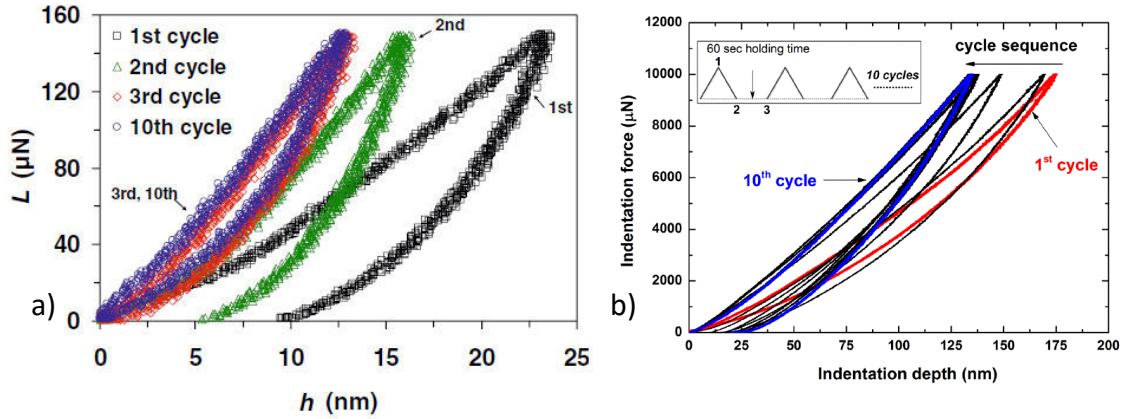


**Figure 36. Cyclic evolution of P-h curves in shape-memory alloys. a)** Nanoindentation curves of single-crystal Cu–Al–Ni alloy at room temperature illustrating a stable pseudoelastic behavior after three nanoindentation cycles (training period) for a maximum load of 150  $\mu\text{N}$ <sup>187</sup>; **b)** Indentation curves of NiTi: 10 consecutive cycles with 10000  $\mu\text{N}$  maximum indentation force on the same indentation spot<sup>25</sup>.

Different results were obtained by Pan *et al.* for NiTi<sup>189</sup>, where a certain minimum load was necessary in order to produce sufficient plastic deformation of the austenitic phase resulting in hardening. This in turn, was necessary to increase the yield stress above the phase transformation stress and thus, enable evolution of superelastic behavior during the subsequent nanoindentation cycles. The work hardening induced during the first cycle, was reflected in the nanoindentation hardness during the second cycle (Figure 37b), while during the subsequent cycles softening was observed due to reorganization of dislocations. Interesting was the shape evolution of the corresponding P-h curves (Figure 37a): while the second cycle exhibited a steeper slope corresponding to the highest hardness value, the P-h curves of the subsequent cycles, correlated with superelastic behavior, exhibited a kink in their slope, similar to the elbows reported elsewhere<sup>190–198</sup>. Pan *et al.* did not mention this issue, however within the scope of the present thesis the origin of these elbows is discussed.



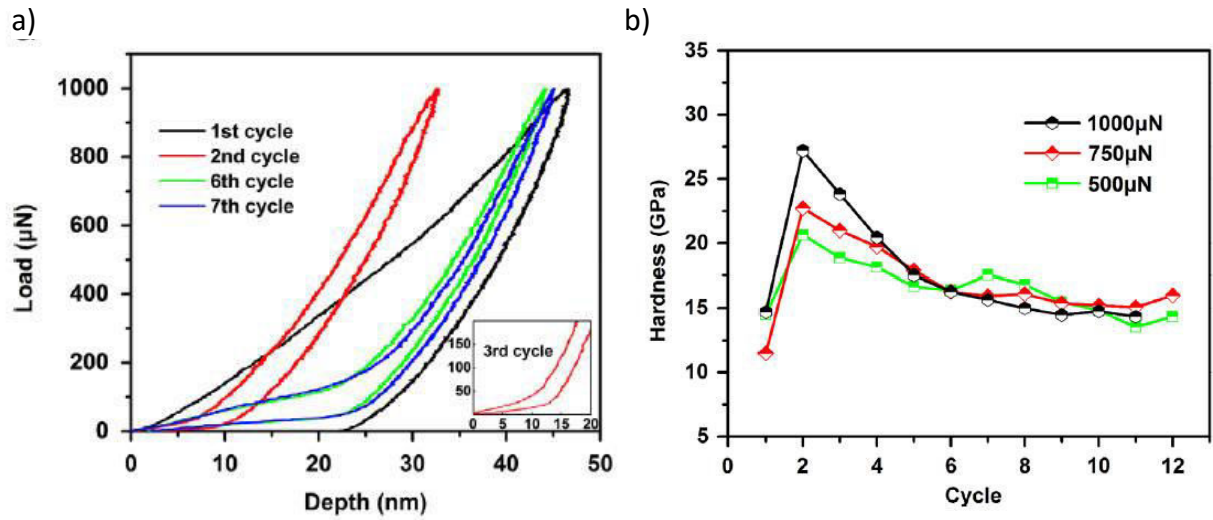


Figure 37. Evolution of NiTi response to cyclic nanoindentation with a Berkovich tip. a) P-h curves; b) corresponding hardness evolution<sup>189</sup>.

Amini *et al.*<sup>25</sup> studied NiTi and found that the hysteresis originating from the phase transformation increases with augmenting nanoindentation cycles (Figure 36b): This was explained by the reorientation phenomenon, which favors the phase transformation with cyclic deformation.

Cyclic nanoindentation studies on metals were performed by Fang *et al.*<sup>199</sup>, who found that small displacements took place after each reloading cycle, due to continuing plastic deformation (Figure 38). This led to a hardness decrease with cycling, although less pronounced for metals than for semiconductors.

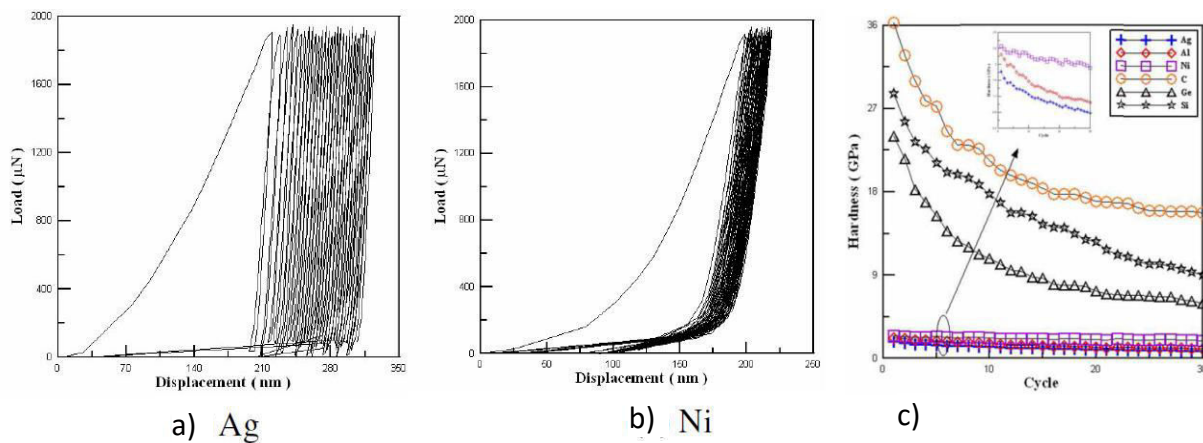


Figure 38. Cyclic nanoindentation behavior of different metals. a) and b): Cyclic displacements are more or less pronounced for different materials; c) Corresponding cyclic Hardness evolution<sup>199</sup>.

However, cyclic nanoindentation testing has not been reported for any steel grade. Therefore, in the present thesis - constant-amplitude cyclic nanoindentation tests with a sharp diamond tip have been

performed in order to increase the cumulative deformation in a controlled way with the number of cycles. The emerging deformation mechanisms manifest themselves in the shape of the corresponding P-h curves.

## **1.4 Summary**

This chapter illustrated the complexity of deformation mechanisms in metastable stainless steels and the potential of nanoindentation in combination with TEM as a powerful tool for the study of the latter. However, so far the response of metastable austenitic stainless steels to deformation by nanoindentation is not completely understood and has not been methodically studied.

Thus, the aim of this thesis is to perform a systematic study of the response to nanoindentation testing of a metastable stainless steel. In doing so, different grain sizes and crystallographic orientations have been considered. Also, other factors such as prestrain and the magnitude of the applied load have been studied. A significant part of the study is dedicated to cyclic experiments, with the intention to observe step-wise nucleation and growth of phase transformations, as well as the deformation substructure development - analogously to conventional cyclic deformation studies on macroscale.

## 2 Material and Experimental Procedures

### 2.1 Studied Material

The material investigated in this thesis is an AISI 301LN (EN 1.4318 grade) provided by Outokumpu Stainless (Finland) in form of 1.5 mm thick sheets with the nominal chemical composition indicated in Table 3.

**Table 3. Chemical composition in wt.% obtained by EPMA for N and by EDX-Spectroscopy for the other elements.**

C	Si	Mn	Cr	Ni	Cu	Mo	P	N	Fe
0.02	0.48	1.29	18.63	6.38	0.14	0.04	0.03	0.07	balance

#### 2.1.1 Designation

The designation AISI 301 LN consists of four parts:

1. “AISI” stands for “American Iron and Steel Institute”, which is one of the most accepted instances nowadays as for classification and designation for steels.
2. “301” is a grade of the 300 series, which is the group of the Cr-Ni austenitic stainless steels distinguished from other stainless steels by its nickel content. The difference between the particular grades of the 300-steels is the exact content of Cr and Ni, as well as of other alloying elements.
3. “L” stands for low carbon, which gives the material a better weldability, however also a lower strength.
4. “N” stands for high nitrogen, which contributes to several positive properties, like increasing strength and corrosion resistance.

#### 2.1.2 Microstructural characteristics

AISI 301 grades have the smallest content of alloying elements from all Cr-Ni austenitic stainless steels (see Table 1). As a consequence, they also possess together with AISI 316L, the lowest SFE of the whole 300-series (see Table 2), which makes them the most metastable, as can be appreciated in Figure 39a.

As discussed in section 1.1.1, the nitrogen content has a significant impact on the properties of AISI 301LN steel<sup>53,61,200</sup>. Furthermore, due to its low C content of 0.02 %, AISI 301LN undergoes easily phase transformation under deformation and as becomes clear from Figure 39b, the resulting  $\alpha'$ -martensite can be considered as nearly cubic – in agreement with literature reports<sup>78,201</sup>.



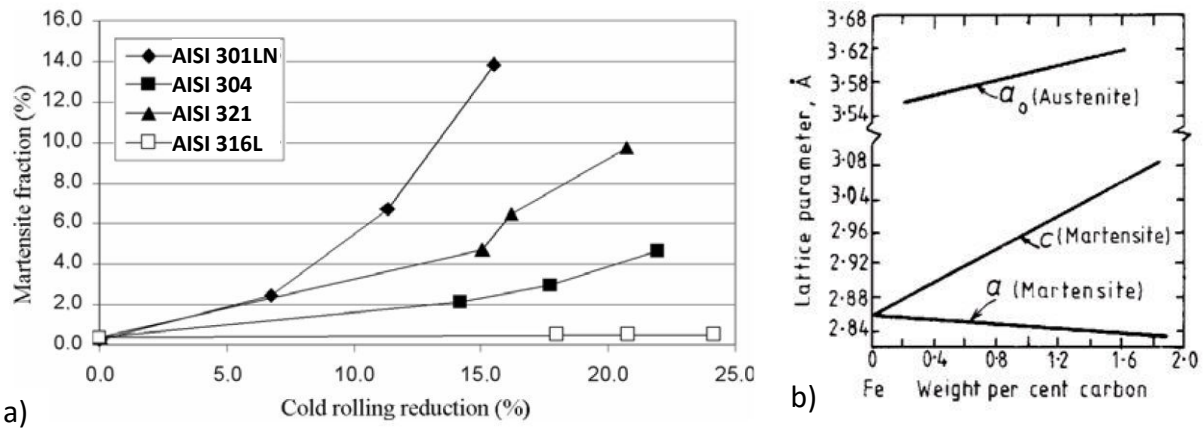


Figure 39. Properties of AISI 301LN. a) Evolution of  $\alpha'$ -martensitic fraction with thickness reduction<sup>4</sup>; b) The dependence of lattice parameters of austenite and martensite on the carbon content<sup>52</sup>.

Table 4 summarizes the space groups and lattice parameters of the different crystallographic phases occurring in AISI 301LN with the given chemical composition<sup>202,203</sup>.

Table 4. Space groups and lattice parameters of austenitic and martensitic phases in AISI301LN.

Phase	$\gamma$	$\epsilon$	$\alpha'$
Space group	Fm-3m	P63/mm6	Im3m
a [Å]	3.61	2.54	2.86
c [Å]	-	4.16	-

### 2.1.3 Mechanical properties

AISI 301LN steels are characterized by a high work hardening coefficient, which gives them outstanding mechanical properties<sup>51,204</sup>. This fact is illustrated in Figure 40a: initial yield strength of around 370 MPa increases with cold rolling. After around 60% of thickness reduction, it reaches values of 450% compared to the initial value, very close to its tensile strength which for its part more than doubles. Ductility however, decreases from more than 30% to almost zero.

Figure 40b shows the characteristic stress-strain curves for different cold rolling degrees of AISI 301 LN. It illustrates how the initially low yield strength and high ductility reverses with increasing deformation. Thus, depending on the desired application, the corresponding degree of predeformation can be applied.

The martensite content of sample A in Figure 40b is 5%, while sample B exhibits 10% of martensite—only 5% more<sup>77</sup>. Therefore, the strong increase of yield strength after cold rolling to 23 % cannot be explained by the martensite formation only, but is rather due to work hardening of the austenitic phase<sup>205</sup>.

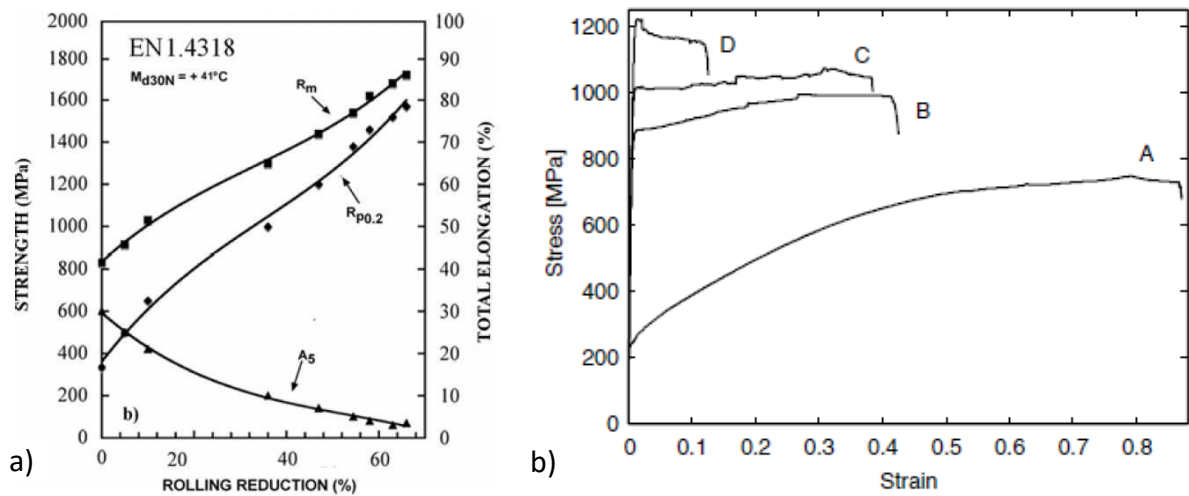


**Figure 40. Mechanical properties of AISI 301LN.** a) Tensile and yield strength, as well as total elongation as a function of rolling reduction (adapted from <sup>4</sup>); b) The stress-strain curves of AISI 301 LN of different cold rolling degrees. A = 2%, B = 23%, C = 36% and D = 42% <sup>77</sup>.

Work hardening occurs in two steps, as can be deduced from the two different slopes in curve A. It is commonly assumed that the first stage is mainly related to the hardening mechanisms of the austenite itself, while in the second stage also the martensitic transformation gains on importance <sup>206</sup>. This circumstance is visualized in Figure 41, where tensile tests have been performed at different temperatures. At 80 °C, where no martensitic transformation is expected, the curve has a constant and moderate work hardening rate. At lower temperatures, the two stages of work hardening become more and more obvious, indicating that the second stage is due to phase transformation. The total work hardening is significantly higher than in case of pure austenite hardening. The high work hardening rate in turn, means that a lower degree of strain is necessary to achieve the same degree of strength, and thus, hardening of the material occurs more homogeneously, with a lower strain localization <sup>207</sup>.

This circumstance is visualized in Figure 41, where tensile tests have been performed at different temperatures. At 80 °C, where no martensitic transformation is expected, the curve has a constant and moderate work hardening rate. At lower temperatures, the two stages work hardening becomes more and more obvious, indicating that the second stage is due to phase transformation. The total work hardening is significantly higher than in case of only austenite hardening. High work hardening rate in turn, means that a lower degree of strain is necessary to achieve the same degree of strength, and thus the hardening of the material occurs more homogeneously, with a lower strain localization <sup>207</sup>.

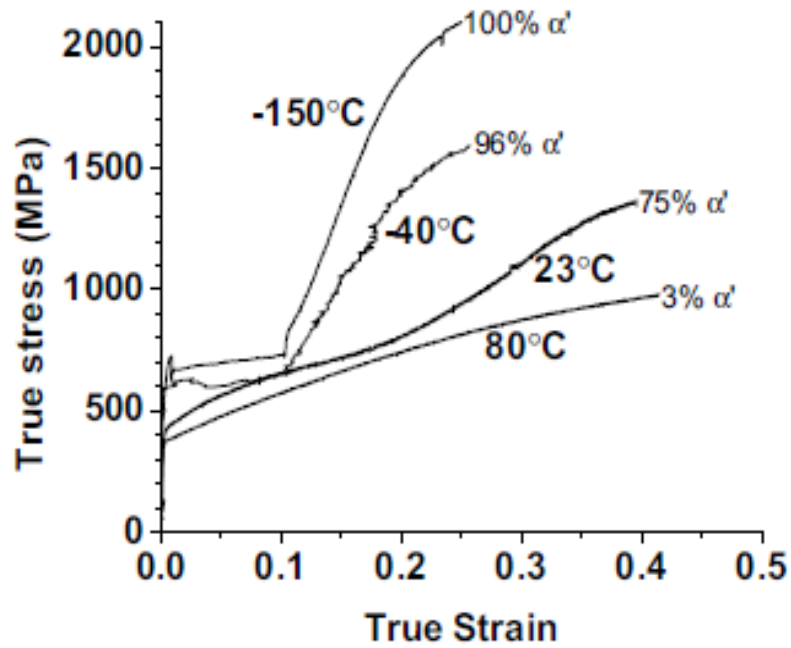


Figure 41. Stress-strain curves of 301LN obtained from tensile tests, as function of the test temperature <sup>86</sup>.

#### 2.1.4 Material conditions

Within the scope of this thesis, AISI 301LN in three different conditions was studied:

- Annealed, small grain size (SG)
- Skin-passed, 17% thickness reduction, small grain size (SP)
- Annealed, coarse grain size (CG)

Steel sheets were delivered by Outokumpu in annealed and skin-passed condition. The later refers to a cold rolling process, with a very low reduction of thickness. In both delivery conditions, average austenite grain size was small.

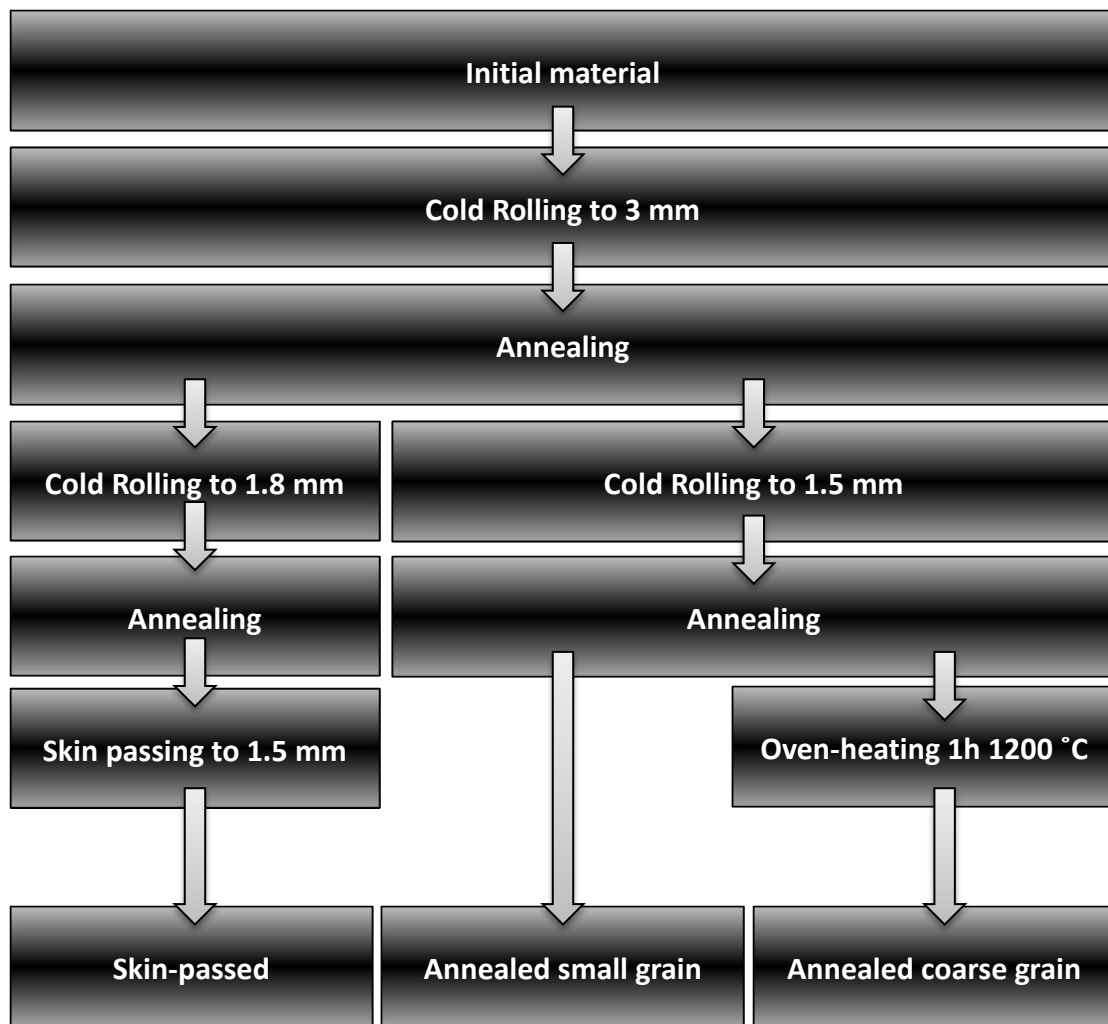


Figure 42. Schematics of the fabrication of the test material.

Table 6 summarizes the mechanical characteristics, as provided by Outokumpu, for SG and SP conditions. For the SP material no significant dependence on the orientation to the rolling direction was observed, indicating quite homogeneous mechanical properties within the steel sheet.

Table 5. Properties of the steel in the different conditions.

Material condition	SG	SP	CG
Grain size [ $\mu\text{m}$ ]	$12.0 \pm 2.4$	$17.9 \pm 10.3$	$132 \pm 16$
$\alpha'$ -martensite content (%)	0	$\approx 5$	0

**Table 6. Mechanical of AISI 301 LN in annealed and skin-passed condition. Data provided by Outokumpu.**

Condition	Rp0,2 [MPa]	Rm [MPa]	Ag [%]
	Annealed SG		
Transversal (TR-T)	350	770	47
Longitudinal (TR-L)	342	768	47
	Skin-passed		
Transversal (TR-T)	711	1077	26
Longitudinal (TR-L)	725	1059	23

## 2.2 Experimental procedure

### 2.2.1 Samples preparation

Prior to the microstructural and micromechanical characterization, it is necessary to prepare the surface of interest by mechanical polishing. Due to the metastable character of the steel, phase transformation uses to take place during mechanical polishing. Thus, polishing was carried out gently (with a holding force of 5 N and a disc rotation speed of 150 rpm). Subsequently, the deformed surface layer was removed by electropolishing.

Prior to any testing or characterization, the samples were prepared in the following way:

1. Mechanical polishing with diamond suspensions, gradually reducing the particle size from 30  $\mu\text{m}$  to 1  $\mu\text{m}$ ;
2. Electrochemical polishing using the Struers Electropol 5 equipment with the commercial polishing solution Struers A2 ((% perchloric acid), working at 23 V and a temperature of around 15 °C for 6 min (to remove at least the upper 100  $\mu\text{m}$  of the surface, ensuring to eliminate plastic deformation and phase transformation induced by the mechanical polishing) ;
3. Cleaning successively with acetone, ethanol, analytical methanol, Triton X-100 and deionized water.

## 2.2.2 TEM lamellae preparation

TEM samples were extracted either by FIB or by twin-jet electrolytic thinning.

For comparison with the deformation induced by nanoindentation, first, thin foils of the annealed SG and SP conditions were prepared and characterized. They were obtained by twin-jet polishing:

1. Material sheet is cut in approx. 2 x 2 cm sized squares, mounted on a flat metallic holder and grinded down with a 30  $\mu\text{m}$  diamond suspension until a final thickness of 200  $\mu\text{m}$ ;
2. Discs of 3 mm diameter are punched from the thinned sheet;
3. Discs are mounted with wax on the holder again and polished from both sides with a 6  $\mu\text{m}$  and 3  $\mu\text{m}$  diamond suspension to a final thickness of below 100  $\mu\text{m}$ ;
4. Discs are etched by twin-jet electrolytic thinning at 20V and -15  $^{\circ}\text{C}$  until formation of a fine hole in the center of the disc.

### Cross-sectional TEM sample preparation by FIB

5  $\mu\text{m}$  x 5  $\mu\text{m}$  x 500 nm lamellas of selected areas, *e.g.* below a nanoindent, were cut out from the samples by a FIB beam, lifted out and welded to a TEM grid by a micromanipulator and thinned to electron transparency ( $< 100$  nm). In order to avoid eventual damage or phase transformation in the sample <sup>208–210</sup>, an initial beam current of 900 pA was chosen for the lift-out process and it was gradually reduced during subsequent polishing steps until 10 pA. The amorphous layer on the surface eventually caused by the FIB beam was removed by plasma cleaning previously to introduction into the TEM.

### Surface in-plane TEM lamella preparation

A plan view thin foil parallel to the sample surface, including the upper surface layer, was extracted from the surrounding area of a residual imprint by the FIB lift-out method with a  $\text{Ga}^+$  beam. Thereby, first a thin Pt layer was deposited over the area of interest. Subsequently, a prismatic-shaped volume around the imprint was cut out with the FIB beam and lifted out by a micromanipulator (Figure 43a). It was welded to a Cu-grid and subsequently thinned with the FIB from the backside, until a thin horizontal section immediately from the surface layer remained. The Pt layer was gently removed from the surface by fine polishing with the  $\text{Ga}^+$  beam (Figure 43b).

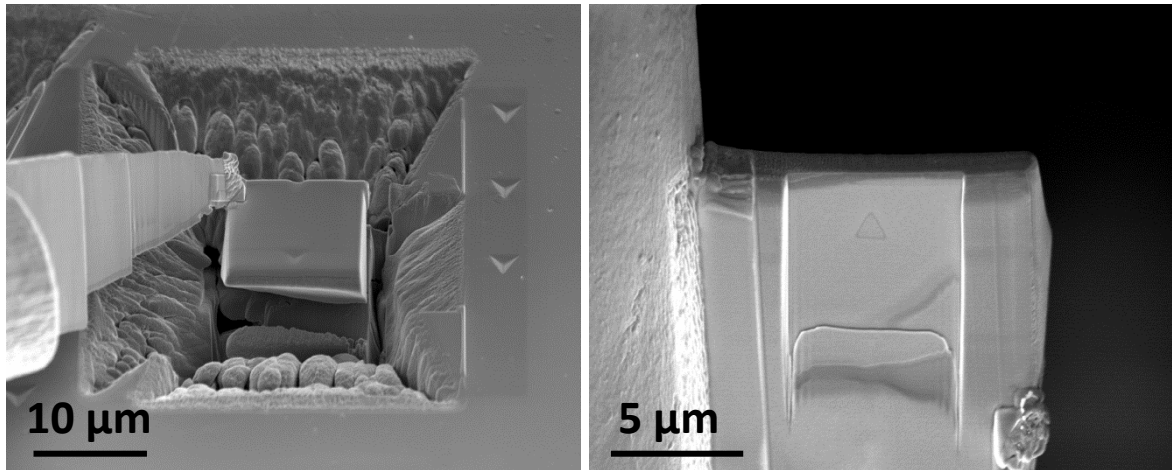


Figure 43. Illustration of the plane-view lamella extraction a) Lift-out process from the sample b) Final thinning operation.

### 2.2.3 Nanoindentation Testing

Nanoindentation experiments have been performed with a diamond Berkovich indenter with a tip radius of approx. 170 nm, as estimated from (15). The employed equipment was a UNHT from CSM Instruments (now Anton Paar) with a vertical displacement resolution of 0.001 nm, a force resolution of 0.01  $\mu\text{N}$ , an internal noise uncertainty of 0.1 nm and thermal drift below 0.5 nm/min<sup>157</sup>.

Nine different types of tests were designed and performed. As a function of the specific objective of each one, different experimental conditions were selected, as summarized in Table 7.

Table 7. Summary of employed nanoindentation test conditions.

Test	Upper limit	Lower limit between cycles	Cycle number	Holding time (s) at P <sub>max</sub>	Loading rate (mN/min)
<b>Monotonic</b>	$P_{\text{max}} = 6 \text{ mN}$ / $h_{\text{max}} = 250 \text{ nm}$	-	1	10	15
<b>Monotonic at small load</b>	$P_{\text{max}} = 200 \text{ }\mu\text{N}$	-	1	10	0.5
<b>2-Cycles</b>	$P_{\text{max}} = 6 \text{ mN}$	$P_{\text{min}} = 0.1 \text{ mN}$	2	0 / 10	15
<b>Cyclic</b>	$h_{\text{max}} = 250 \text{ nm}$ / 500 nm	$h_{\text{min}}$ adjusted for each test to $P_{\text{min}}$	100	10	15
<b>Cyclic</b>	$P_{\text{max}} = 6 \text{ mN}$	$P_{\text{min}} = 0.1 \text{ mN}$ / 0.25 mN/ 0.5 mN	50	10	15
<b>Multi-step</b>	$P_{\text{max}} = 6 \text{ mN}$	Loading /Unloading in 20 steps from 0 mN to 6 mN and back		3600 after each loading/ unloading segment	15
<b>Monotonic, creep measurement</b>	$h_{\text{max}} = 250 \text{ nm}$	-	1	10 / 60 / 120 / 300 / 600	15
<b>Time-dependent plasticity at small scale</b>	$P_{\text{max}} = 100 \text{ }\mu\text{N}$ / 200 $\mu\text{N}$	-/ 50 $\mu\text{N}$	1/10	60	0.5
<b>Drift-corrected creep measurements</b>	$P_{\text{max}} = 0.6 \text{ mN}$ / 6 mN	-	1	3600	15

As can be concluded from section 1.1, the deformation behavior of metastable austenitic stainless steels strongly depends on the temperature. Thus, in order to prevent excessive heating of the samples during testing, loading and unloading rate were kept at 15 mN/min, for both monotonic and cyclic indentation.

### **Monotonic nanoindentation**

The response to nanoindentation experiments as a function of the indented phase, grain orientation and size, as well as applied load, has been investigated. Deformation features on the surface have been characterized by optical and electron microscopy, as well as AFM, while the influence of the indentation on the material under the indent has been investigated by TEM. Phase transformation on the sample surface has been detected by comparison of EBSD phase maps before and after the indentation.

### **Cyclic nanoindentation**

The biggest challenge for cyclic nanoindentation is to assure the stability of the nanoindentation system along all the duration of the test. Thus, during this study an ultra nanohardness tester UNHT equipment from CSM instruments was used, which exhibits ultra-high resolution and very low noise, as well as excellent thermal stability. Load-displacement curves have been analyzed, with respect to presence of pop-ins and evolution of the slopes. After the occurrence of relevant pop-ins or other features, the sample was immediately unloaded and the origin of those events investigated by extracting TEM lamella from the impression area to perform the characterization of the corresponding substructural changes.

### **Time-dependent plasticity**

In this case, samples were hold after loading for a relatively long time at constant load  $P_{\max}$ .



## **2.2.4 Characterization techniques**

### **FESEM**

The FESEM used in this study was a JEOL 7001F. It was used to characterize the surface deformation surrounding residual imprints after nanoindentation.

### **EBSD**

EBS mapping was performed in order to access to phase identification, grain morphology, crystallographic orientation and to identify grain boundaries. It was applied to:

1. Characterize the initial microstructure of annealed SG, annealed CG and SP
2. Select specific sites for nanoindentation
3. Study eventual surface deformation after nanoindentation

EBS mapping was conducted with a constant scanning step of 100 nm at an acceleration voltage of 20 kV. The used equipment was a field emission scanning electron microscopy (FESEM) JEOL 7001F equipped with an orientation imaging microscopy system from Nordlys. Inverse Pole Figures (IPF) were measured with the z-direction perpendicular to the surface.

### **FIB**

FIB is a powerful tool not only for lifting of cross sections and fabrication of TEM lamella, but it also allows surface / cross section imaging (Scanning Ion Microscopy imaging / SIM) with a high contrast, provided by the channeling effect. This effect is significantly more pronounced for ions than for electrons, due to the higher mass of the latter. Within these studies SIM images for characterization of the sample surface and cross sections were acquired with a beam current of 50 pA and a pixel dwell time of 18  $\mu$ s in line integration mode.

Furthermore, for in-depth characterization, a tomography of a nanoindent was performed by sectioning the sample in 25 nm steps by the FIB beam, at a current of 100 pA. The dimensions of the total examined volume were 4.3 x 3.7 x 1.8  $\mu$ m. The 3D reconstruction was performed with the software FEI Avizo 8.0.

## TEM

TEM characterization was carried out to access the aspects of microstructure like morphology and crystallographic orientation of austenitic grains, as well as the induced martensites. Besides, defects like shear bands, mechanical twins, stacking faults, dislocation structures, etc. were studied by analysis of images and diffraction patterns. Differences between the annealed and the cold rolled material, before and after deformation by different experiments were examined.

Thin foils were observed with a Philips CM200 TEM, whereas atomic resolution imaging was performed in a High Resolution TEM (HRTEM) Jeol JEM-ARM200F-FEG – both equipped with a double-tilt holder. Bright Field (BF) and Dark Field (DF) imaging, as well as Selected Area Electron Diffraction analysis (SAED), were performed at an acceleration voltage of 200 kV. Diffraction patterns from different regions of the HREM image were recorded with the Digital Micrograph software®.

The different defects in stacking sequence can be distinguished by a combination of TEM images and diffraction patterns, as illustrated in Table 8. Indexation of TEM diffraction patterns has been performed based on crystallographic data as indicated in Table 4.

**Table 8. Distinction between different stacking sequence defects by TEM<sup>55</sup>.**

Partial motion	Faults	Twins (two mirror planes)	TEM	
			Image	Diffraction
ZIG/ ZAG\	no	no	dislocation line	normal
Successive ZIG/ ZAG\	no	no	dislocation line; channel band	normal
ZIG/	intrinsic	one-layer nanotwins	dislocation line; SF fringes; twin band	streaks
ZIG/ ZIG/	extrinsic	two-layer nanotwins	dislocation line; SF fringes; twin band	streaks
ZIGs on <i>n</i> -successive planes	twin boundary	<i>n</i> -layer coherent nanotwins	dislocation line; SF fringes; twin band; channel band	twin spots
ZIGs on every other plane	h.c.p. stacking	nanotwins	dislocation line; SF fringes; twin band; h.c.p./martensite; channel band	streaks; h.c.p./bct spots
Combination of all the above	intrinsic; extrinsic; twin boundary; h.c.p.	single to multilayer nanotwins	dislocation line; SF fringes; twin band; h.c.p./martensite; channel band	streaks and twin spots

### 3 Original microstructure

Previously to any mechanical testing, the original microstructure after sample preparation was characterized for the three studied material conditions.

Figure 44 shows the mechanically polished sample surface before and after electrochemical polishing. Noticeably, after mechanical polishing a large part of the microstructure has undergone the martensitic transformation ( $\alpha'$ -martensite corresponds to both the grey and black-contrasted features, as could be confirmed by a comparison with EBSD phase mapping). However, this damage is restricted to the upper surface layer, and can be completely removed, as evident from Figure 44.

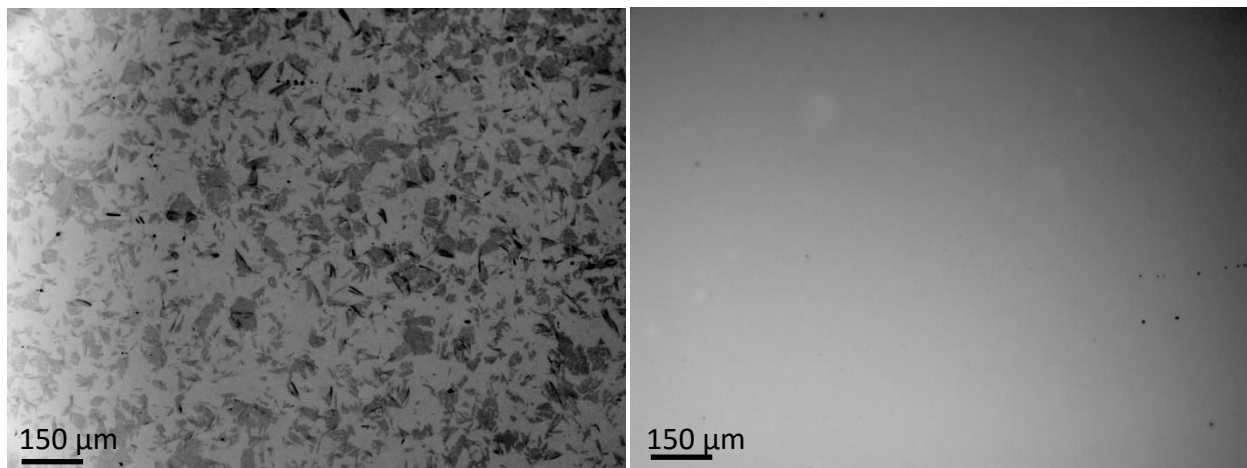


Figure 44. Optical micrograph of the sample surface (annealed SG) before (left) and after (right) electrochemical polishing.

#### 3.1 Characterization by EBSD

Figure 45 represents IPF and phase EBSD maps corresponding to the different material conditions. Apart from the grain size, the microstructures of the SG condition in Figure 45a and of the CG condition in Figure 45b are similar, *i.e.* purely austenitic, randomly distributed equiaxial grains with abundant annealing twins.

Figure 45c illustrates characteristic EBSD maps of the skin-passed condition. Due to the imposed deformation, the crystallographic orientation evolves within single grains, as can be deduced from color transitions in the IPF map given in Figure 45c. Most grains are crossed by numerous parallel, not indexable bands, pointing either in a single or in two intersecting directions. Thin bands are perfectly straight, while thicker ones become more irregular and wavy and feature small  $\alpha'$ -martensitic particles, as visible in the phase map (Figure 45d).

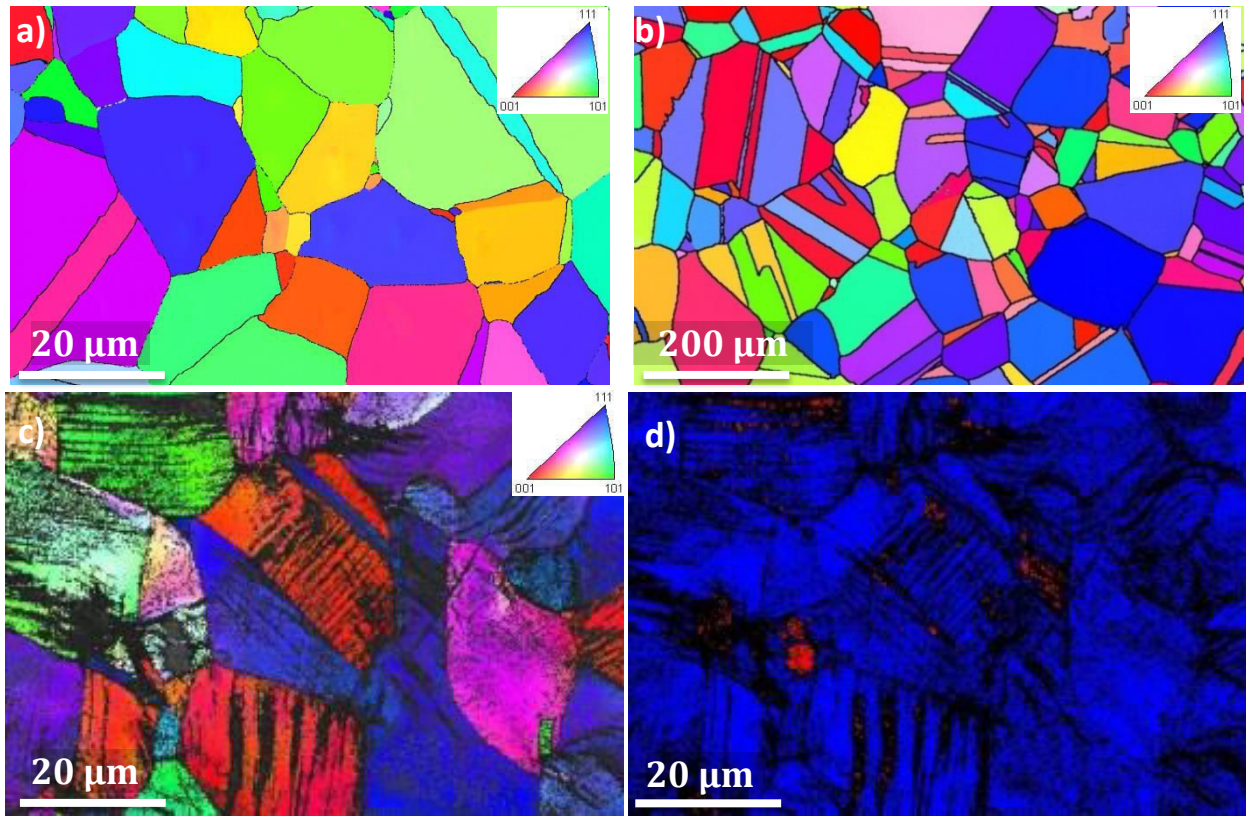


Figure 45. EBSD mapping of the initial material. a) IPF map of annealed SG, b) annealed CG and c) SP samples; d) Phase map of SP corresponding to the area in c).

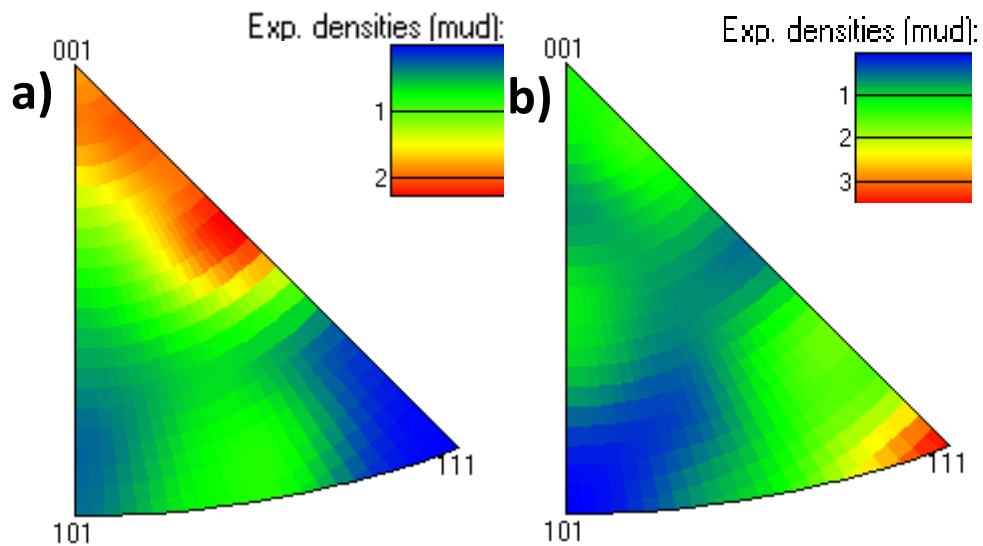


Figure 46. IPF distributions corresponding to Figure 45a and Figure 45b, respectively.

Figure 46 shows that, while for the initial material (annealed SG) there is a pronounced texture between  $\langle 001 \rangle$  and  $\langle 112 \rangle$  orientations, for the grain-enlarged condition texture has shifted distinctly to  $\langle 111 \rangle$  pole. Similar results were observed by other authors who carried out grain coarsening treatments on fcc materials<sup>211</sup>. Indeed, grain enlargement treatments lead to a change of preferred crystallographic orientation, resulting in difficulties to separate the influences of grain size and texture<sup>212–215</sup>. This points out the potential of nanoindentation, allowing to probe individual grains of selected orientations, independently of the average texture of the material. Thus, the respective influences of crystallographic orientation and grain size can be decoupled.

## 3.2 Characterization by TEM

In this section, the characteristic microstructures of annealed SG and SP conditions are presented, such as obtained from TEM characterization of thin films obtained by twin-jet polishing.

Figure 47 shows the typical substructural features of the annealed SG material. It shows that austenitic grains exhibited a low density of defects, mostly stacking faults (SFs) and planar arranged dislocations. As usual, a higher dislocation density is observed near the grain boundaries (Figure 47c). Occasionally, transmission of piled-up dislocations through an annealing twin boundary was seen (Figure 47d).

Steel in the skin-passed condition exhibited a wide range of features characteristic of predeformed stainless steels<sup>61,100,216,217</sup>, such as planar bands of defected stacking sequences, *i.e.*  $\epsilon$ -martensite or SFs, and microscopic shear bands featuring bundles of irregular stacking sequence defects. Some of the observed defect structures are presented in Figure 48 and Figure 49. Hence, in Figure 48a, a profusion of microbands in parallel arrays are present, typically following two intersecting systems.

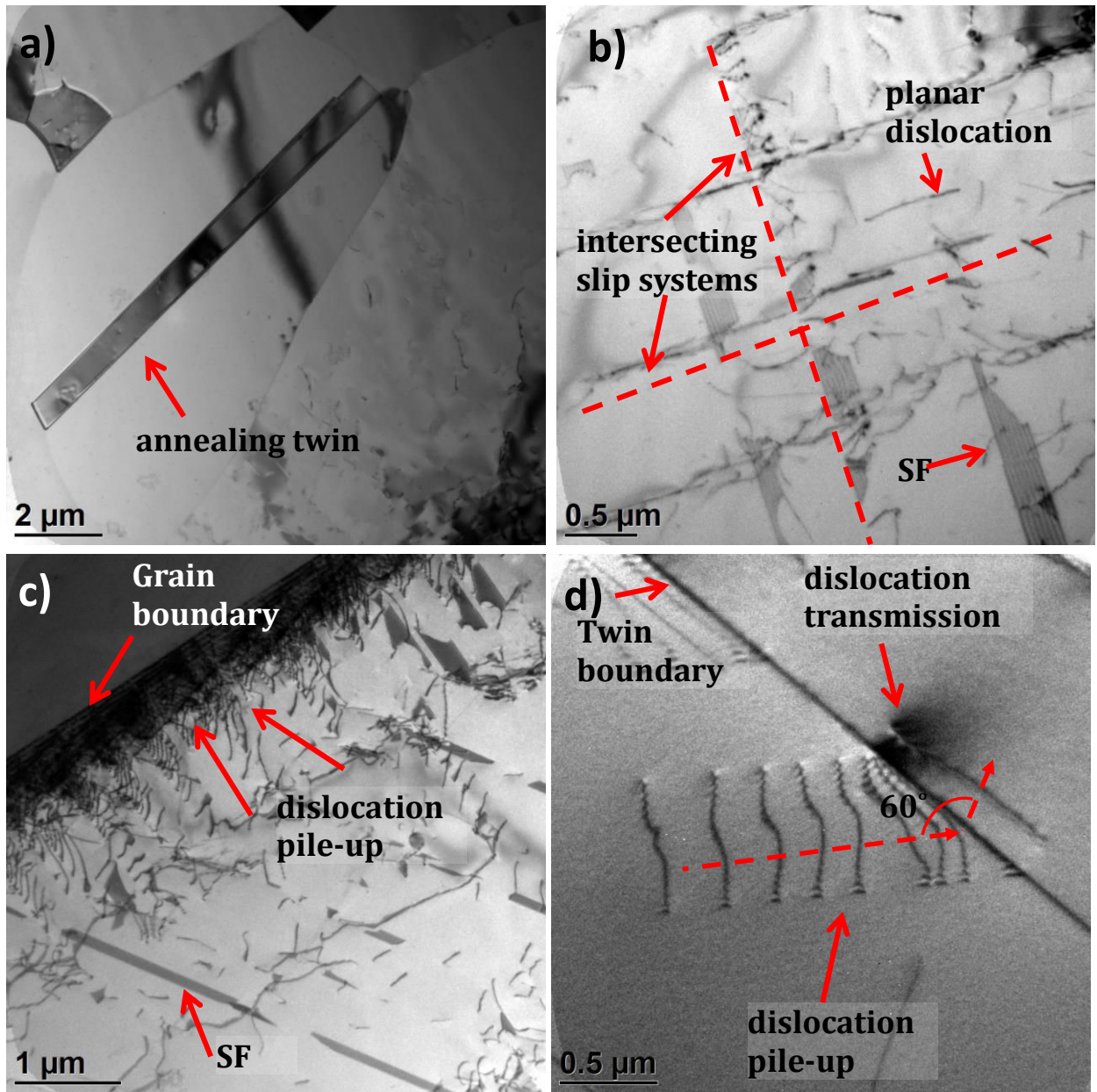


Figure 47. TEM Bright Field images of the investigated AISI 301LN steel in the as-received condition. a) Austenitic grain containing an annealing twin; b) Stacking faults; c) Dislocations pile-ups at a grain boundary; d) Dislocations pile-up passing across a twin boundary.

As mentioned in section 1.1.4, microbands consisting of interlaced stacking faults, nano-twins and hexagonal  $\epsilon$ -martensite platelets, are commonly labeled microscopic shear bands. The diffraction pattern in Figure 48d and the corresponding dark field image in Figure 48b (obtained with the  $(\bar{1}011)\epsilon$  reflection) reveal that the present shear bands are largely composed of  $\epsilon$ -martensite. Also  $\alpha'$ -martensitic nucleation at band intersections took place, as often reported in literature<sup>98,113,218</sup>.



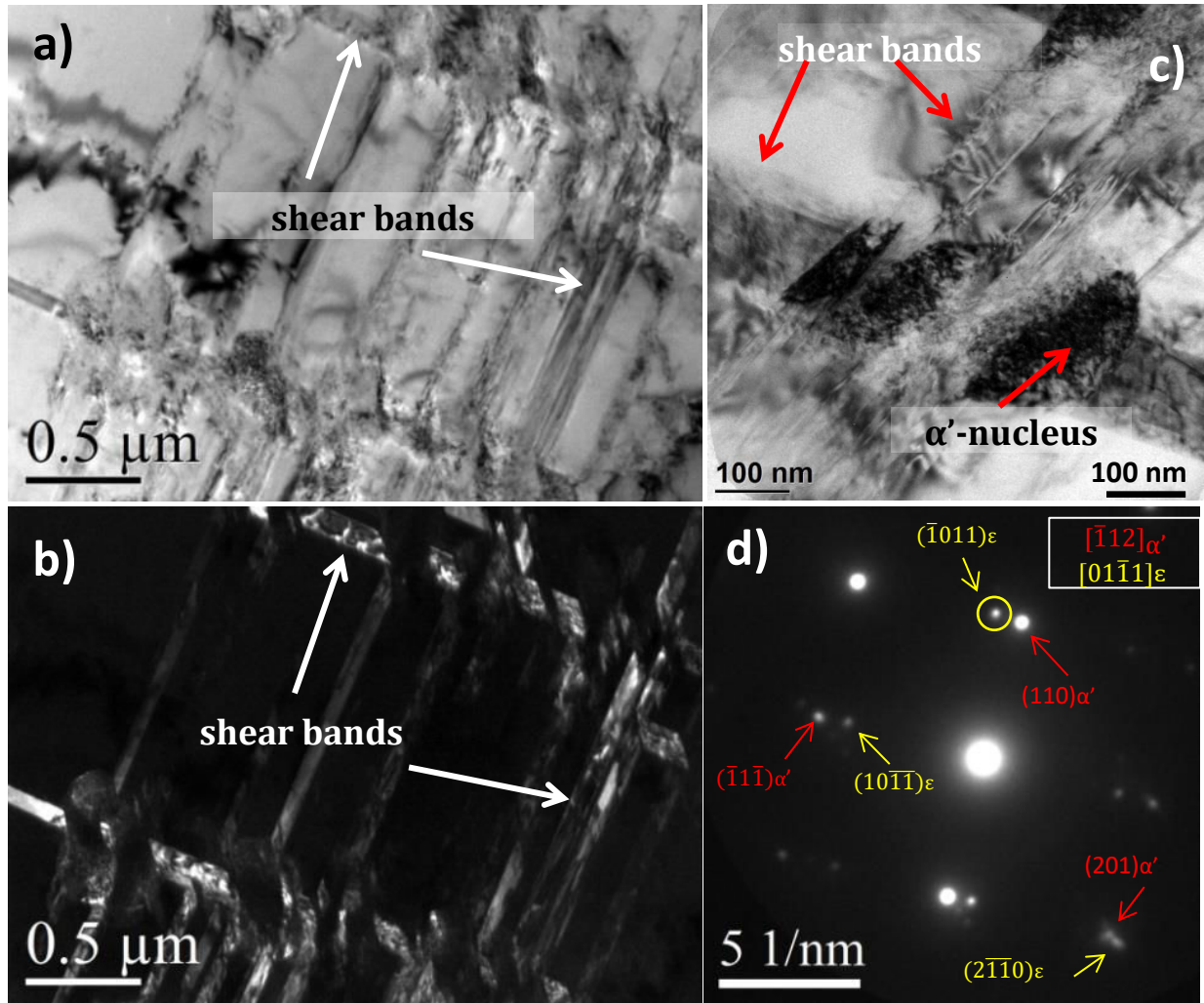
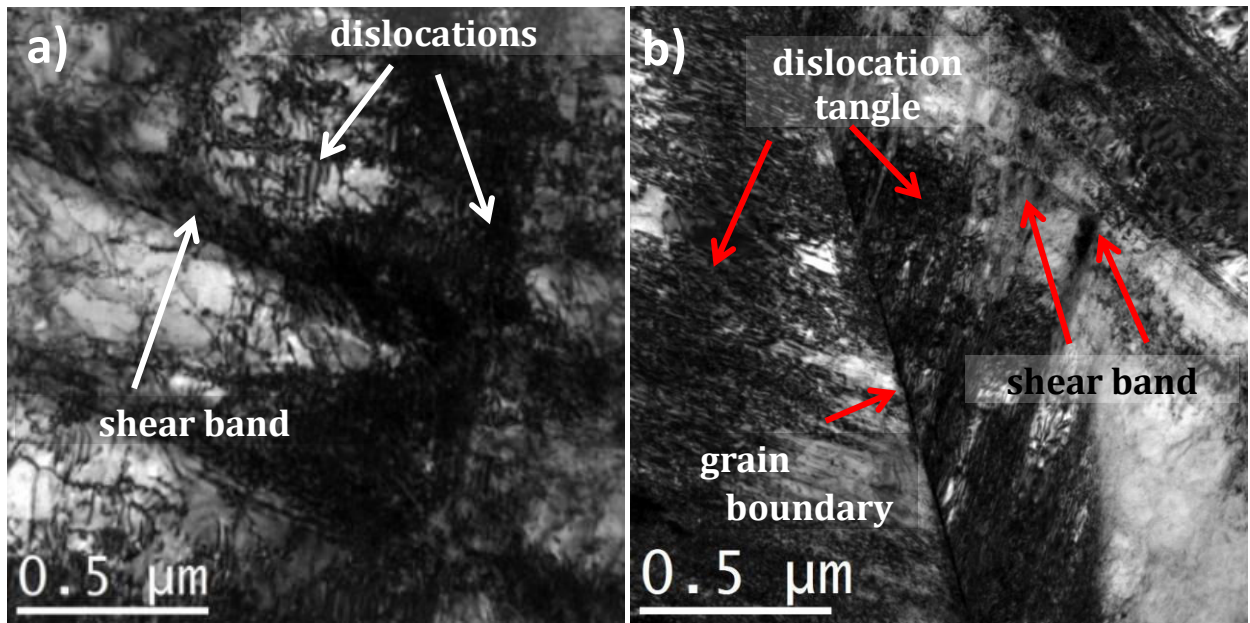


Figure 48. Deformation mechanisms in AISI 301LN steel in the skin-pass condition. a) TEM BF image of Intersecting planar defects, featuring  $\epsilon$ -martensite plates, stacking faults and microscopic shear bands with martensitic nuclei forming at the intersections; b) TEM DF image of the shear bands in a) obtained with the  $(\bar{1}011)_\epsilon$  reflection; c) TEM BF image of intersecting shear bands with  $\alpha'$ -martensite formation at the intersections; d) corresponding diffraction pattern revealing the  $\epsilon$ - and  $\alpha'$ -martensitic phase.

Figure 49 shows the dislocation substructure of the investigated steel in the skin-passed condition. High densities of tangled dislocations were observed, as well as arrangements of those dislocations in ordered slip bands. The latter is nothing different than trapping and gradual arrangement of dislocations along preexisting shear bands, as can be deduced from Figure 49a. Therefore, the distinction between shear and slip bands is vague. Figure 49b illustrated that slip bands readily initiate from grain boundaries, where the high density of piled up dislocations favors their arrangement along shear bands.



**Figure 49. Characteristic dislocation arrangement of skin-passed AISI301LN. a) Dislocations arranging along shear bands forming incipient slip bands; b) Slip band formation evolving from dislocation tangles trapped by shear bands impinging on grain boundary**

Overall, during TEM studies  $\epsilon$ -martensite plates were readily discerned, while mechanical twins were rarely observed. . Dislocation densities were higher in the proximity of grain boundaries, while in the center of the grain planar defects prevailed.

As already mentioned in Chapter 2, twinning,  $\epsilon$ -martensite formation and dislocation slip are known to be competing deformation mechanisms on austenitic steels. In the particular case of AISI 301LN grade steels,  $\epsilon$ -martensite formation is reported to be more favorable than twinning due to the low stacking fault energy of the material <sup>8,53,107</sup>, which is in good agreement with the results in the present study.



## 4 Mechanical response to nanoindentation

### 4.1 Motivation

As mentioned in section 1.2, nanoindentation is a very sensitive small-scale technique where a material is indented by a small tip and the displacement into the surface  $h$  and the corresponding load  $P$  is recorded during the loading, as well as during the unloading process. Thus, nanoindentation allows to probe the mechanical response of single grains in a polycrystalline compound locally and at small loads, and to evaluate the related mechanical anisotropy.

In the scope of this thesis, nanoindentation tests have been also performed in cyclic mode, analogous to macroscopic indentation fatigue testing. Thereby, changes in the shape of the load-penetration ( $P$ - $h$ ) curves are expected to reflect modifications in the material response with increasing the number of indentation cycles.

Therefore, for first time in steels, constant-amplitude cyclic nanoindentation tests with a sharp diamond tip were performed in order to increase the cumulative deformation in a controlled way with the number of cycles. The emerging deformation mechanisms manifested themselves in the shape of the corresponding  $P$ - $h$  curves.

The summary of the different tests conducted can be found in Table 7, while the obtained findings will be presented in the following sections.

### 4.2 Results and discussion

#### 4.2.1 Monotonic nanoindentation tests

Figure 50a represents two characteristic load-displacement (or  $P$ - $h$ ) curves obtained from monotonic nanoindentation in different grains of the annealed steel. The maximum displacements into the surface ( $h_{\max}$ ) are slightly different in spite of the same applied maximum load ( $P_{\max}$ ), according to the local variation of mechanical properties.

At the beginning of the curve, around 10 nm, a displacement burst, also known as pop-in, can be appreciated. A magnification of this trend is shown in Figure 50b, where multiple pop-ins can be clearly distinguished. The initial loading curve can be approached by the Hertz fitting, as described in section 1.2.3, which indicates that the material behavior in this region is purely elastic. It is commonly assumed

that before the occurrence of the first pop-in, no mobile dislocations are present within the activation volume surrounding the nanoindenter <sup>219</sup>. When the critical load for dislocation activation is reached, a sudden pop-in occurs indicating the elasto-plastic transition.

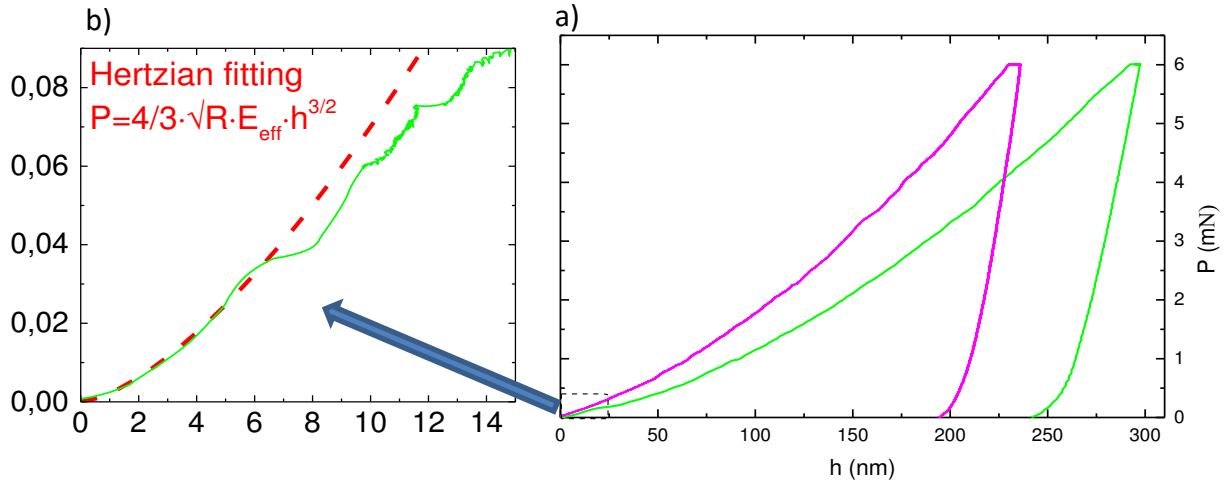


**Figure 50.** Monotonic nanoindentation in annealed AISI 301LN. a) Load-displacement curves for two indentation tests; b) Magnification of the low load range and the theoretical progression for Hertzian contact.

Preliminary tests revealed that the nanoindentation response is really complex and that the crystallographic orientation has a strong influence on the P-h curves. Trying to get a deeper understanding on the underlying deformation mechanisms, a detailed study starting from the incipient plasticity behavior and continuing with the response to cyclic deformation at higher loads was performed and will be described in the following sections.

In this regard, nanoindentation tests at small maximum indentation loads (200  $\mu\text{N}$ ) were carried out and are summarized in Figure 51. A pop-in around  $h = 5$  nm ( $P = 35$   $\mu\text{N}$ ) is clearly discernible. The inset in Figure 51a shows that the deformation remains elastic after its occurrence. The origin of this pop-in will be further discussed in section 4.2.6.

A secondary pop-in (or a set of multiple pop-ins) can be discerned around 125  $\mu\text{N}$ , corresponding to a stress about 11 GPa, which is close to  $1/(2\pi)$  of the shear modulus for the investigated steel <sup>220</sup>. The pop-in width is correlated with the critical load at which it occurs, as often observed in literature <sup>221</sup>. Since nanoindentation curves can be fitted by the Hertz equation only before the occurrence of the secondary pop-in, this phenomenon must be associated with the elasto-plastic transition. The variation in critical load for the pop-in occurrence may be related to random variations in dislocation density, as well as to different local microstructural properties. Thus, indentation tests were selectively performed in coarse grains (size around 200  $\mu\text{m}$ ) with  $\langle 001 \rangle$  and  $\langle 111 \rangle$  orientations, respectively. Figure 51b and Figure 51c illustrate the obtained results.

Figure 51b gives P-h curves corresponding to the indentations carried out within the same  $\langle 001 \rangle$  oriented grain. In all these curves, elasto-plastic transition occurs in a narrow range ( $119 \pm 8 \mu\text{N}$ ) and the corresponding pop-ins are significantly smaller than in the case of as-received condition in Figure 51a.

Analogously, Figure 51c presents the results for the  $\langle 111 \rangle$ -oriented grain. Here, with exception of one test, pop-ins appeared at an even lower load, within the band of  $87 \pm 18 \mu\text{N}$ . They were also wider and more pronounced than for  $\langle 001 \rangle$  grain, indicating that a higher amount of dislocation slip is arising during those pop-ins. Plasticity is known to initiate at free surfaces<sup>222</sup>, and thus, given that (111) is the preferential slip plane in fcc crystals, slip will occur easier in grains oriented with their (111) plane parallel to the surface, as observed elsewhere<sup>223</sup>.

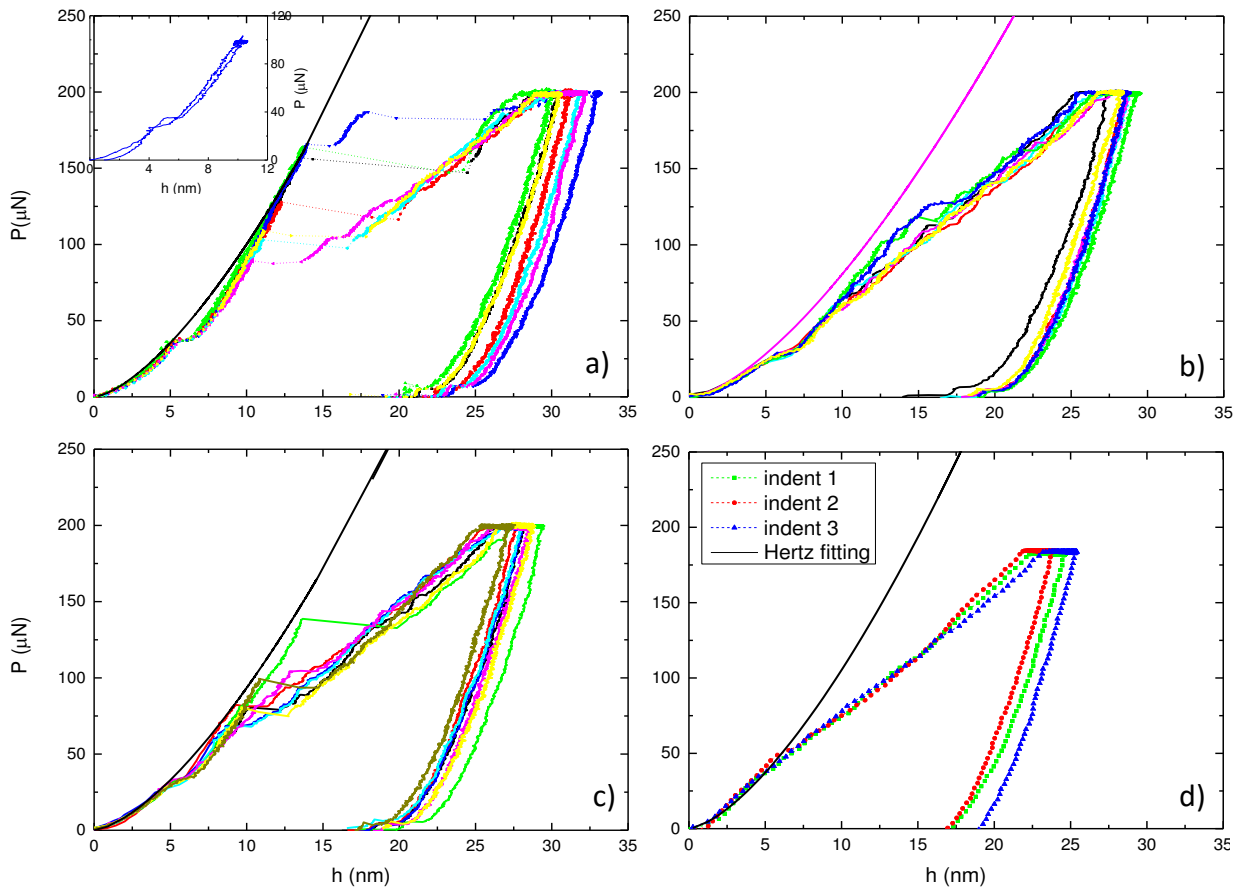


**Figure 51. Nanoindentation testing in the load range of elastoplastic transition. a) As-received annealed condition; b) Enlarged  $\langle 001 \rangle$  grain; c) Enlarged  $\langle 111 \rangle$  grain; d) Skin-passed condition.**

As a result, it can be concluded that in spite of the elasto-plastic transition being of stochastic nature<sup>223,224</sup>, crystalline anisotropy leads to a variation of the critical load for this transition. Also the grain size represents a decisive parameter for both the critical load and the width of observed pop-ins. Since grain boundaries are a known source for dislocations<sup>225</sup>, more dislocations can be activated in small grains.

However, stress fields also concentrate along grain boundaries, which is likely to hinder the activation of dislocation and consequently the critical activation load is higher.

Figure 51d illustrates the indentation behavior of the cold rolled steel. Here, the nanoindentation curve deviates from the Hertzian fitting at a penetration value corresponding to occurrence of the first pop-in (5 nm). However, pronounced pop-ins are not observed. This is in agreement with common literature findings<sup>28,173,226,227</sup>, where pre-deformed material has a high density of pre-existing dislocations within the activation volume around the nanoindenter tip, and thus can deform plastically directly from the beginning of the indentation process.

#### 4.2.2 Two-cycles nanoindentation tests

In order to achieve a better understanding on the response to nanoindentation tests of multiple cycles, beforehand tests of only two cycles were conducted. They were done at  $P_{\max} = 6$  mN, with two different test conditions: (a) without; and (b) with a holding stage at  $P_{\max}$ , as shown in Figure 52. In both cases the unloading and reloading curves do not overlap, but hysteresis occurs.

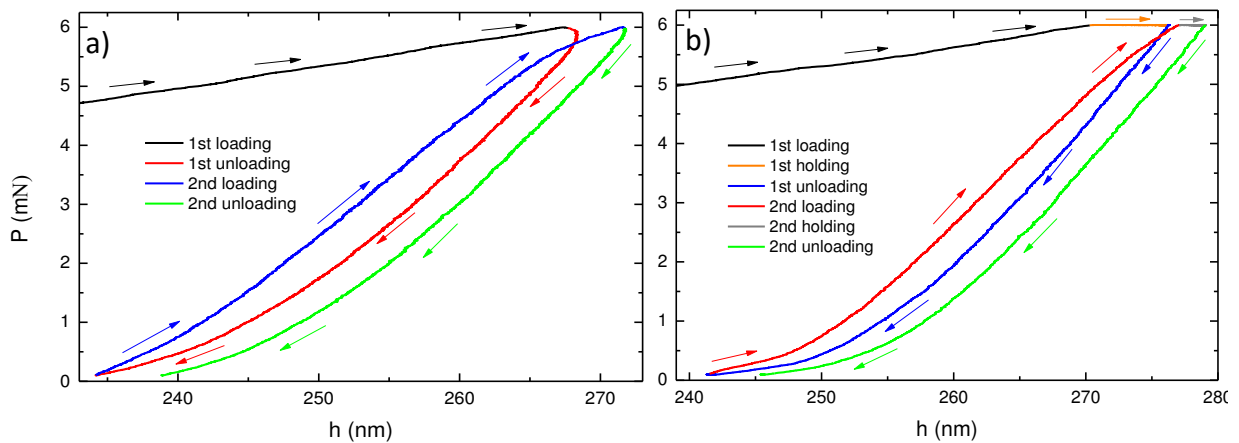


**Figure 52. Two-cycle nanoindentation test. a) P-h curve with no holding stage between the loading and unloading phases; b) P-h curve with a holding stage of 10 s between loading and unloading. Cyclic nanoindentation**

In the test without a holding stage (Figure 52a), the indenter penetration continues during the beginning of the first unloading stage, which is characteristic of materials exhibiting viscoplasticity, *i.e.* time-dependent behavior, and is known to occur also for metastable stainless steels<sup>228–232</sup>. After the reloading, the hysteresis loop remains open and  $h_{\max}$  is shifted to higher values. The later behavior is known from conventional fatigue testing and is designated as ratchet-strain accumulation. Several authors have reported that ratcheting occurs for austenitic stainless steels<sup>228,230,233–237</sup>.

Figure 52b shows that if a holding sequence of 10 s is incorporated at  $P_{\max}$  to account for the time-dependent response, no viscoplasticity can be observed during the unloading stage. However, the subsequent reloading still results in a slightly open hysteresis loop, indicating that ratcheting still occurs during the reloading. The fact that unloading and reloading cycles in Figure 52a and 52b do not overlap - as could be expected for purely elastic behavior, but form a pronounced hysteresis loop, indicates that an anelastic or reversible plastic behavior is present, which leads to energy dissipation during each cycle.

#### 4.2.3 Constant loading vs. constant displacement testing

In order to account for the above illustrated viscoplastic effect, and in agreement with common nanoindentation standards, in all of the here presented cyclic nanoindentation tests a holding stage of 10 s was incorporated following each loading sequence.

In conventional macroscopic fatigue testing, it is important to differentiate between tests performed under stress or strain control, since the material response can be different<sup>7,238–240</sup>. Therefore, in the present study, cyclic nanoindentation tests were performed both in constant loading (equivalent to stress control) and constant displacement or penetration depth mode (equivalent to strain control). Figure 53 illustrates the corresponding P-h curves.

Indentation curves corresponding to the first cycles are characteristic for ductile, work hardening metals<sup>241,242</sup>, with a high amount of irreversible plastic deformation and a small elastic recovery upon unloading; whereas during the following cycles, deformation is mostly elastic. However, the presence of hystereses is evident.

P-h curves for testing in loading mode show that  $h_{\max}$  increases continuously. Ratcheting rate diminishes with cycling, as visible from the fact that curves come closer (Figure 43b), but it does not completely cease.

Figure 43c corresponds to tests in displacement mode, where P-h curves look rather different. Here  $P_{\max}$  decreases significantly from the first to the second cycle and it keeps decreasing less sharply with continuing cycling.

Figure 54 represents both hardness and Young's modulus evolution for P-h curves depicted in Figure 53, as calculated by the Oliver-Pharr method described in Section 1.2.3.

Since the hardness depends on  $P_{\max}$  and  $h_c$  (and thus also  $h_{\max}$ ), ratcheting in both testing modes is reflected in an apparent hardness decrease. In displacement mode (Figure 54b), the marked hardness drop from the first to the second cycle is characteristic, and also the subsequent dropping rate is higher than in loading mode (Figure 54a).

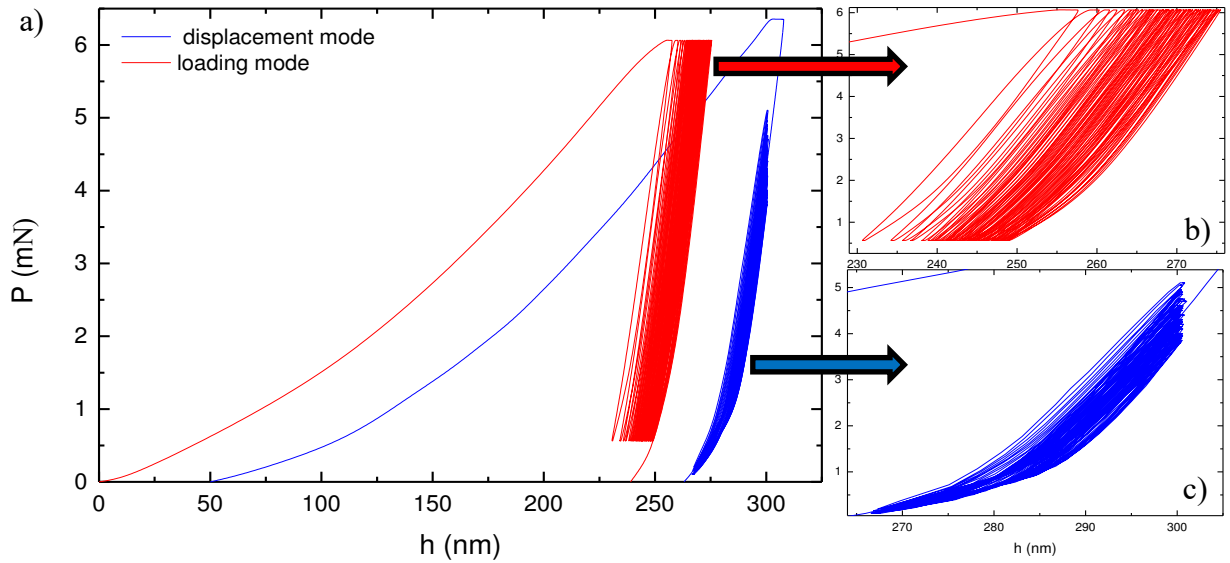


**Figure 53.** 50-cyclic nanoindentation tests. a) Representation of characteristic P-h curves for testing in loading and displacement mode; b) Magnified view of the reloading range in loading mode; and c) in displacement mode.

The observed behavior can be explained as following: in constant displacement mode, the displacement during the unloading stage can be attributed mainly to elastic recovery<sup>242</sup>. Thus, if during the next cycle reloading up to the same  $h_{\max}$  is performed, lower load would be needed to achieve  $h_{\max}$ .

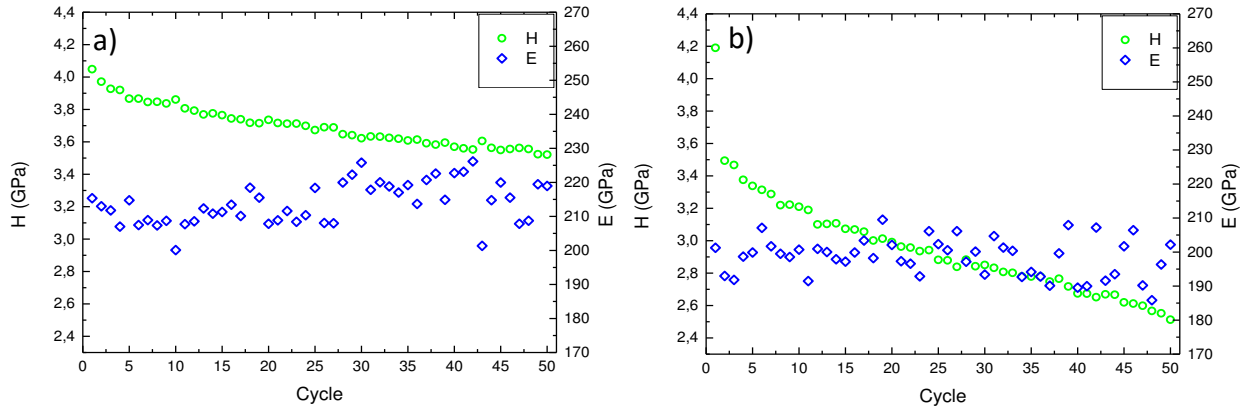


**Figure 54.** Cyclic evolution of hardness and Young's modulus for a) Loading mode; and b) Displacement mode.

On the other hand, if reloading to the same  $P_{\max}$  is applied for each cycle, every time higher  $h_{\max}$  would be achieved in reference to the preceding cycle. Thus, the indenter will penetrate deeper into the material and a part of the deformation will always be plastic. This explains why, in spite of ratcheting, the hardness decreases slower for constant loading tests.

To draw a parallel to conventional fatigue testing, nanoindentation in displacement mode can be compared to high cycle fatigue (HCF), where elastic deformation is predominant, while nanoindentation in loading mode resembles more low cycle fatigue (LCF) testing, where plastic strain is significant.

Consequently, the material is expected to respond to the latter testing condition with more and faster strain localization, as will be confirmed in section 6.2.2.

Young's modulus values are in good agreement with literature for the austenitic phase in metastable stainless steels<sup>243,244</sup>. Its cyclic evolution features some scatter, but remains basically constant in displacement mode, while in loading mode a slight cyclic increase is observed. At this point, no deeper study will be performed in this respect and the Young's modulus will be mainly used to validate the obtained results, since stability during cyclic nanoindentation testing is not self-evident.

#### 4.2.4 Tests in constant displacement mode

Testing under displacement mode has been performed for different material conditions. Figure 55 to Figure 59 show characteristic P-h curves for 100-cyclic tests, namely:

- $\langle 001 \rangle$  grains, annealed steel,  $h_{\max} = 250$  nm
- $\langle 111 \rangle$  grains, annealed steel,  $h_{\max} = 250$  nm
- $\langle 111 \rangle$  grains, annealed steel,  $h_{\max} = 500$  nm
- $\langle 111 \rangle$  grains, skin-passed steel,  $h_{\max} = 250$  nm

P-h curves are represented in subfigures a), while the second and thereafter every tenth cycle are given in amplified view in subfigures b). P-h curves of consecutive cycles have been shifted respectively 10 nm to the right.

First of all, when subfigures a) are compared, significant differences can be observed in the evolution of  $P_{\max}$ . Accordingly, while  $\langle 001 \rangle$  grains exhibit continuous cyclic softening, as discussed before, for  $\langle 111 \rangle$  orientation the initial softening is followed by a secondary hardening stage, more pronounced for high penetration tests ( $h_{\max} = 500$  nm). In the case of skin-passed samples, only a small load drop from the first to the second cycle is discernible. Thereafter the ratcheting rate is fairly low. Similar behavior was observed for differently oriented grains in SP condition.

Subfigures b), where only every tenth cycle is plotted in a magnified representation, visualize the evolution of the hysteresis loops formed between the loading and unloading part of the cyclic nanoindentation curves. In all tests performed in the annealed steel, loops broaden with cycling, whereas for the skin-passed material the opposite behavior occurs, although most of the cycles are practically elastic. Furthermore, hysteresis loops for  $\langle 111 \rangle$  oriented grains are significantly broader than for  $\langle 001 \rangle$  orientation.

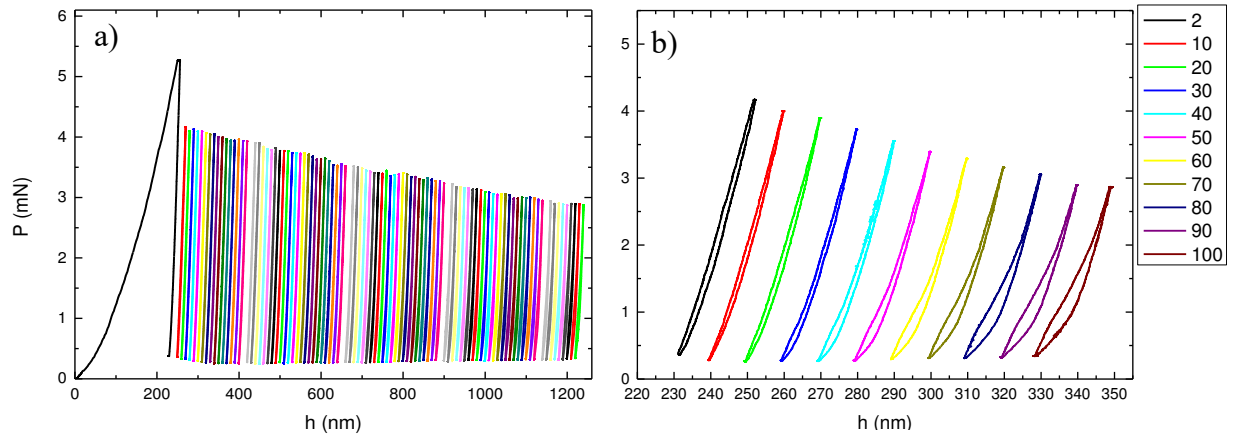


Figure 55. Cyclic evolution of P-h curves for <001> grain in annealed sample,  $h_{\max} = 250$  nm. a) General view of all cycles; b) Detailed view of every tenth cycle. Consecutive cycles are shifted 10 nm to the right.

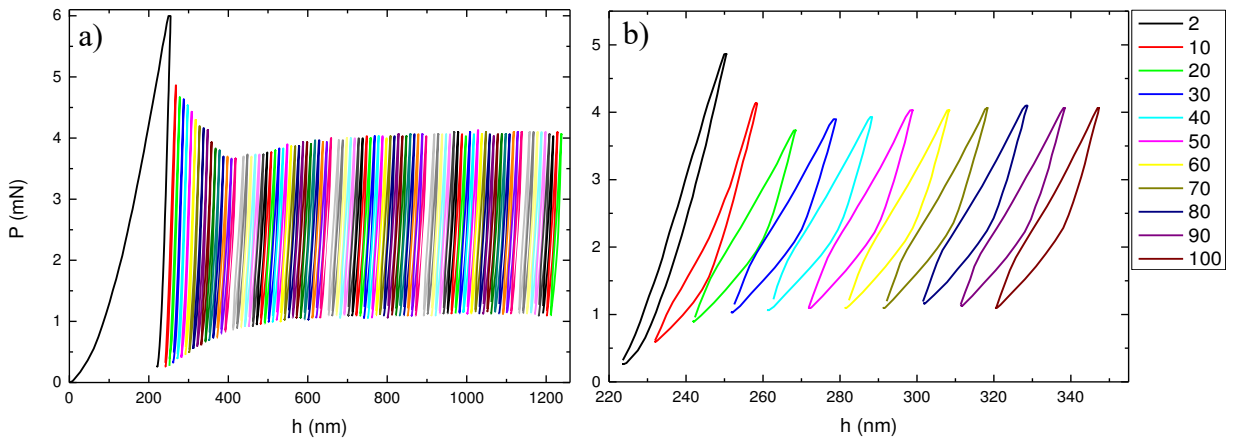


Figure 56. Cyclic evolution of P-h curves for <111> grain in annealed sample,  $h_{\max} = 250$  nm. a) General view of all cycles; b) Detailed view of every tenth cycle. Consecutive cycles are shifted 10 nm to the right.

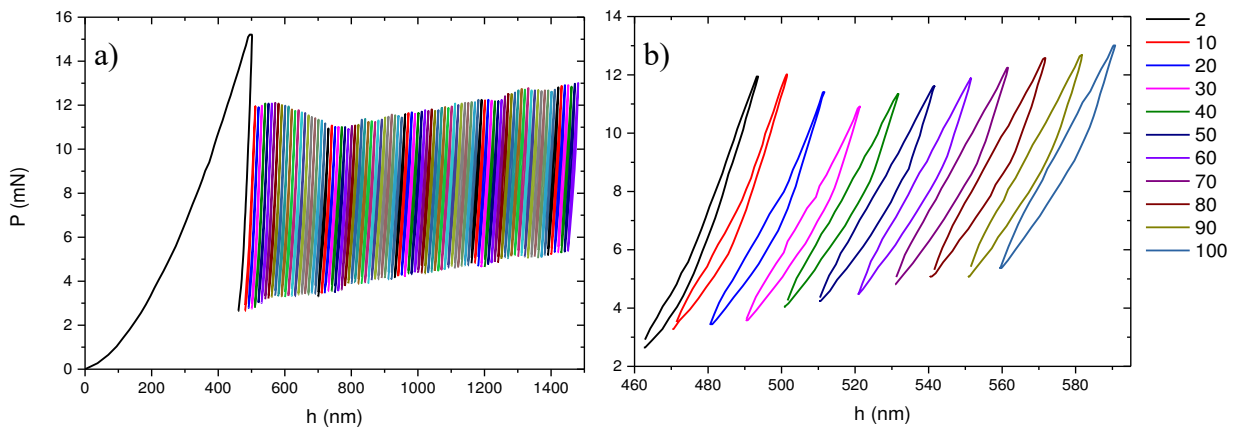
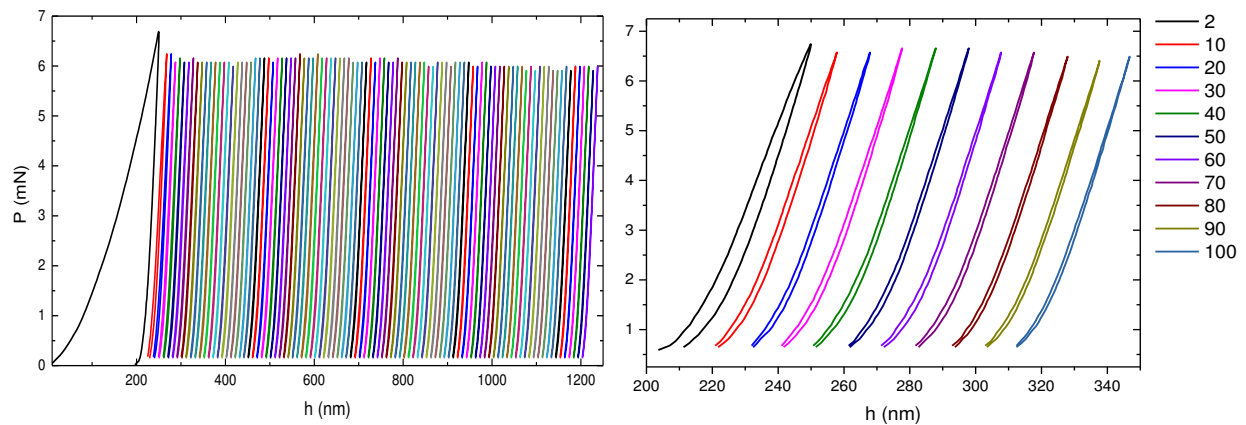
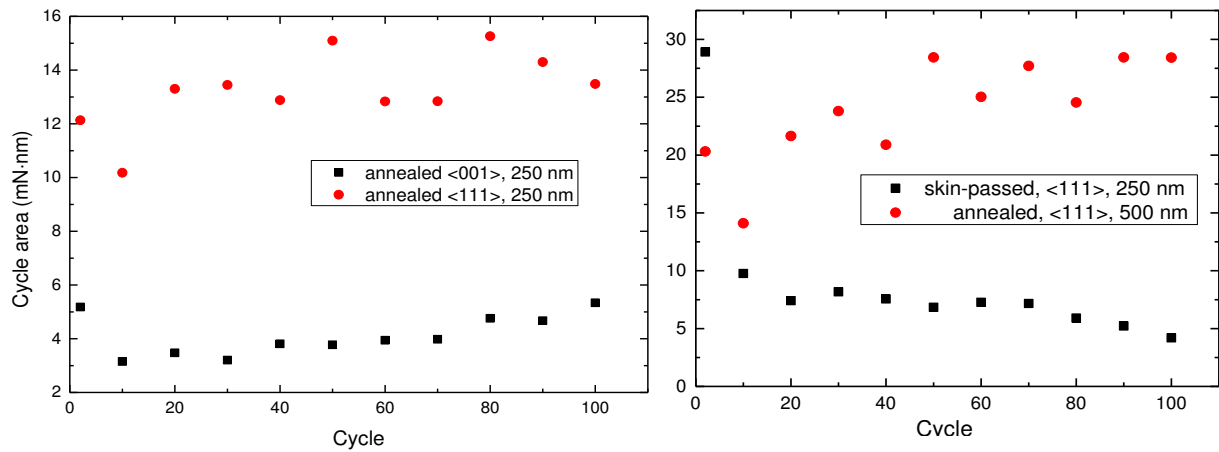


Figure 57. Cyclic evolution of P-h curves for <111> grain in annealed sample,  $h_{\max} = 500$  nm. a) General view of all cycles; b) Detailed view of every tenth cycle. Consecutive cycles are shifted 10 nm to the right.





**Figure 58.** Cyclic evolution of P-h curves for <111> grain in skin-passed sample,  $h_{\max} = 250$  nm. a) General view of all cycles; b) Detailed view of every tenth cycle. Consecutive cycles are shifted 10 nm to the right.



**Figure 59.** Evolution of the hysteresis area beginning with the 2<sup>nd</sup> indentation cycle for nanoindentation tests presented in Figure 55 to Figure 58.

In Figure 59, the area of each hysteresis loop has been plotted against the corresponding cycle number. It corresponds to the evolution of energy dispersion during the respective cycles and gives interesting insights. Thus, in all cases the hysteresis size drops from the 2<sup>nd</sup> to the 10<sup>th</sup> indentation cycle. Thereafter, it keeps dropping for the SP steel, but steadily increases for annealed conditions. Therefore, the energy is from the beginning significantly higher for <111> than for <001> oriented grains and for  $h_{\max} = 500$  nm in comparison to 250 nm. Surprisingly, the largest hysteresis occurs in the second cycle of SP material. Apparently, anelastic cyclic behavior is present, which depends on the applied strain amplitude, on the material condition, and also exhibits a significant crystalline anisotropy. This will be further discussed in Chapter 6.

Annealed metastable austenitic stainless steels are known to initially harden in response to cyclic deformation<sup>149,232,245</sup>. Both, work hardening of the austenite and phase transformation to martensite contribute to this behavior; while a softening behavior due to generation of additional mobile dislocations

and cell arrangement of dislocations takes place at elevated cycle numbers<sup>245,246</sup>. Consequently, cyclic softening, as observed in the present work is not self-evident.

The main difference between conventional fatigue testing and cyclic nanoindentation is the loading and displacement scales. The stress state induced with a Berkovich indenter is not only multiaxial, but also decreases radially with increasing distance from the nanoindenter. Thus, there is not a trivial way to compare it to the stress state created during conventional fatigue testing. The same occurs for strain, that cannot be simply estimated as the ratio between  $h_{\max}$  and the vertical grain dimension, since during indentation the applied compression is rather punctual than covering equally the whole surface of the tested grain, not to mention the strain transfer into the adjacent grains. However, it is reasonable to assume that both stress and strain ranges in nanoindentation are smaller than commonly applied within macroscopic testing.

Cyclic hardening depends strongly on maximum plastic strain<sup>231</sup> and only takes place if a threshold value of cumulative strain is reached<sup>149,152,247</sup>. So, cyclic tension tests of small strain amplitude do not lead to noticeable hardening<sup>234,247</sup>, and can even lead to cyclic softening. One of the scarce cyclic nanoindentation studies performed in metals (NiTi thin films) resulted in a similar softening behavior as here observed, which Pan *et al.*<sup>189</sup> attributed to reorganization of the defect structure. The fact that during the present study secondary hardening was found to be significantly more pronounced at higher  $h_{\max}$ , *i.e.* at higher strains, supports the assumption of a minimum strain threshold value required for cyclic hardening, while in its absence softening due to ratcheting overweighs. Furthermore, as will be shown in section 6.2.5, martensitic transformation parallel to the loading axis occurs in  $\langle 111 \rangle$ , but not  $\langle 001 \rangle$  oriented grains, while low energy dislocation arrangements leading to softening are more developed in the latter, which explains why the former exhibited secondary hardening, while the latter softened faster without any secondary hardening.

It is known that a high dislocation density increases the resistance to both viscoplastic and viscoelastic behavior, and thus lead to smaller hysteresis during cyclic tests<sup>248</sup>. For pre-strained material, as represented here by the skin-passed condition, the preexisting dislocation density is high and their mobility is strongly restricted. Thus, ratcheting and formation of wide hysteresis loops are significantly less pronounced in comparison to the annealed condition.

Moreover, softening is known to occur when prestrained materials are cyclically loaded, due to dislocation rearrangement<sup>249</sup>. However, this softening rapidly stabilizes for the skin-passed sample and no further pronounced time-dependent plasticity is observed for the following cycles. On the other hand, TEM observations in Chapter 6 will show that nanoindentation does not increase the preexisting fraction of martensite, and consequently no secondary hardening occurs for SP condition. The present findings are in agreement with Krempl<sup>229</sup>, who found that work-hardened AISI 304 reached a cyclic steady-state.

#### 4.2.5 Evaluation of elbow formation in cyclic P-h curves under loading mode

In preliminary experiments, it was observed that P-h curves exhibited a kink at low load, which is the more pronounced the lower  $P_{\min}$  is. Since in displacement mode only  $h_{\min}$ , but not  $P_{\min}$  can be controlled, testing in loading mode has been performed to further investigate this particular behavior.

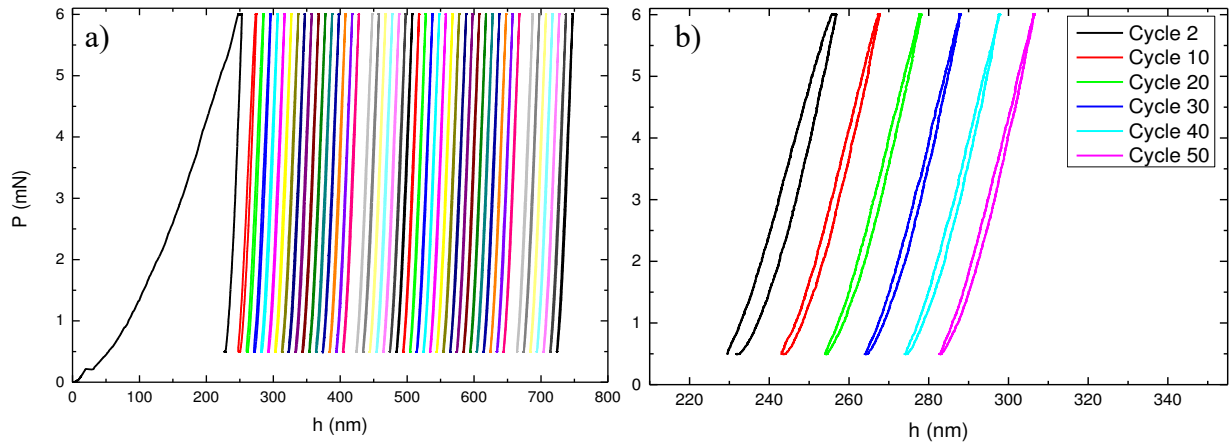


**Figure 60. Cyclic evolution of P-h curves for <001> grain in annealed sample in loading mode,  $P_{\max}=6$  mN,  $P_{\min}=0.5$  mN. a) General view of all cycles; b) Detailed view of every tenth cycle. Consecutive cycles are shifted 10 nm to the right.**

Tests were conducted for different values of  $P_{\min}$ . Figure 60 shows cyclic P-h curves in <001> oriented grains obtained in loading mode with  $P_{\min} = 0.5$  mN. The second cycle is evidently open, thereafter cycles close and P-h curves remain largely elastic, not exhibiting hysteresis broadening. However, this situation changes dramatically, when  $P_{\min}$  is decreased, as can be appreciated in Figure 61. Appreciable is a kink formation in the slope of the curves, which becomes more pronounced with increasing cycling and results in the formation of broad asymmetrically shaped hysteresis loops. Kinking becomes more pronounced for low  $P_{\min}$  values, as can be seen when comparing the sub-Figure 61a and b.

Figure 61c visualizes that kink forming and involved hysteresis occurs only if the unloading is performed until below a determined threshold  $P_{\min}$  value - approximately 0.5 mN.

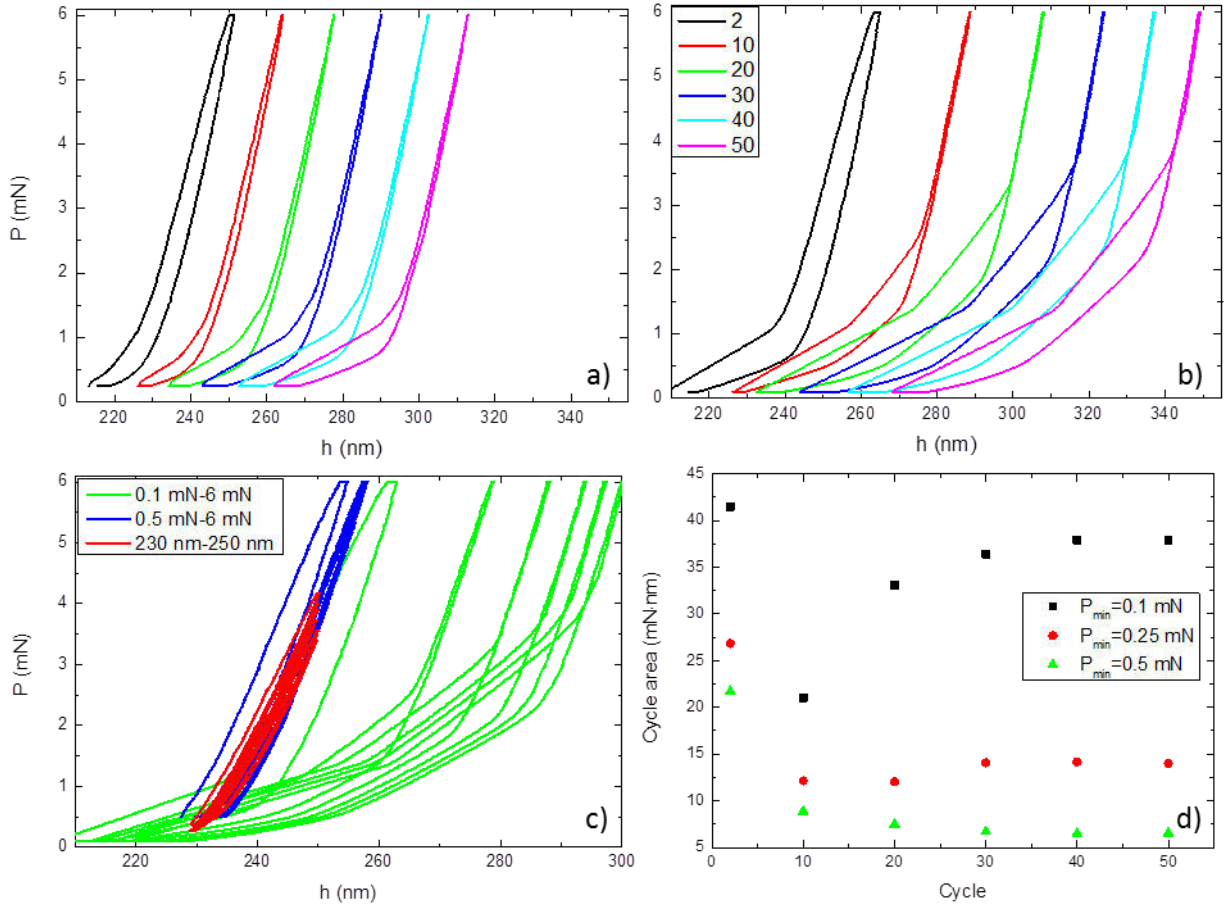


**Figure 61.** Cyclic evolution of P-h curves for different indentation conditions in <001> grains in annealed sample, detailed view of every tenth cycle. a)  $P_{\max}=6$  mN,  $P_{\min}=0.25$  mN; b)  $P_{\max}=6$  mN,  $P_{\min}=0.1$  mN; c) Combined representation of P-h curves of Figure 55b, Figure 60b and Figure 61a; d) Evolution of hysteresis areas for tests presented in Figure 60b, Figure 61a and Figure 61b. In a) and b) consecutive cycles are shifted 10 nm to the right, the P-h curves in c) are not shifted.

When increasing the number of cycles, the kink position moves to higher load values, surpassing the threshold value. Figure 61c opposes P-h curves (every tenth cycle) for loading mode with  $P_{\min} = 0.5$  mN,  $P_{\min} = 0.1$  mN and also displacement mode (test from Figure 55b) with  $h_{\min} = 230$  nm, corresponding approx. to  $P_{\min}$  of 0.5 mN, respectively. Curves are not shifted, but represented corresponding to their real cyclic displacement evolution.

Noticeably, the displacement evolution and the slope are very similar for loading mode with  $P_{\min} = 0.5$  mN and displacement mode with  $h_{\min} = 230$  nm. Also the upper part of P-h curves for  $P_{\min} = 0.1$  mN exhibits a similar slope, without changes with increasing number of cycles. However, in the latter case, the lowest part of the slope becomes less steeped and the kink position moves up, and therefore the top point of P-h curves is displaced to higher displacement values. The bottom point does not change significantly, indicating that the displacement is reversible.

Figure 61d shows the evolution of hysteresis loops for different  $P_{\min}$ . As observed in displacement mode (Figure 59), the hysteresis of the second cycle is noticeably larger than for the following ones, due to

ratcheting. Thereafter, the dissipated energy diminishes. For  $P_{\min} = 0.5$  mN, where no elbow formation occurred and the P-h slope was linear, hysteresis keeps decreasing. However, in cases where kink formation was observed, hysteresis increases progressively again. A saturation value is approached after around 40 cycles. The hysteresis loop area in loading mode, as represented in Figure 61d is significantly larger than for displacement mode (see Figure 59).

The above observed hysteresis behavior indicates that pseudo-elastic or reversible plastic behavior takes place if repetitive loading/unloading is conducted up to small  $P_{\min}$  values, while at high loads the material behaves mostly elastically.

Kinks observed in the present study are designated in literature as elbows, and they are regularly observed in nanoindentation curves of Si and other semiconductors. They have been related to reversible amorphization under load<sup>196–198</sup>, annealing treatments<sup>195</sup>, as well as to reversible phase transformation<sup>190–193</sup>. Also polymers and gold were found to exhibit elbows related to phase transformation<sup>194</sup>.

Pan *et al.*<sup>189</sup> performed cyclic nanoindentation experiments on NiTi shape memory alloys and found stress-induced martensitic transformation during the loading process, which reversed during unloading. This reversible transformation was accompanied by anelastic reloading curves with elbow formation, such as the here observed, developing the earlier, the higher the load. According to Pan *et al.*<sup>189</sup>, deformation during the first indentation cycle(s) contributes to the increase of critical stress for further slip, and phase transformation becomes more favorable during the following nanoindentation cycles. Similar behavior is plausible in the present case. The underlying deformation mechanism will be further investigated in the following section.

#### 4.2.6 Reversible phase transformation

Regularly, small serrations were observed in the P-h curves, particularly pronounced for <111>-oriented grains. Recording of the curves at high acquisition rate reveals the presence of multiple pop-ins during the loading process. Noticeably, the opposite phenomenon takes place during unloading: the occurrence of pop-outs.

Figure 62 illustrates a characteristic development of those pop-ins and pop-outs during a nanoindentation test. Figure 62a shows a cyclic P-h curve of a <111> grain tested in displacement mode, which begins as observed before: a largely plastic first indentation cycle and mostly elastic following cycles (2 to 7) featuring moderate softening. However, after a single pop-out in the unloading curve of cycle 6,  $P_{\max}$  starts decreasing faster for the following cycles, and the lower part of the unloading curve bends to an elbow during cycle 8, thus leading to an overcrossing of the loading and unloading curve. During the

following cycles the loading curve bends to an elbow, and thus the P-h curves close again. However, the hysteresis loops broaden noticeably and simultaneously the pop-ins and pop-outs emerge.

Apparently, a change of the material response to the cyclic solicitation took place during the 9<sup>th</sup> cycle. While in the first cycles the material behavior is largely elastic, the pop-ins and pop-outs going along with elbow formation indicate occurrence of anelastic behavior during the respective cycles.

After cycle number 12 and following, P-h curves do not exhibit any major shape change. However, as can be observed in Figure 62b,  $P_{\max}$  increases slowly with cycling, in agreement with previous findings for  $\langle 111 \rangle$  grains, and pop-ins and pop-outs become more pronounced.

Figure 62c represents the amplified P-h of cycle 100 and opposes it to a simulated course, where pop-ins and pop-outs are removed and the continuous parts of the curve are stitched together. Noticeably, after this procedure the P-h curve appears almost straight, with a similar unloading slope (approx. 0.14 mN/nm), as the largely elastic cycles at the beginning of the test. Moreover, it does not exhibit elbows, showing that the latter phenomenon is closely related to the pop-in formation. The inset in Figure 62c shows that the P-h curves are very stable and do not exhibit noise or scatter. Consequently, the position and shape of pop-ins can be clearly discerned. It also shows that there is no cycle opening at  $P_{\min}$ , as might appear at first glance, but instead, the last pop-out occurs only when the load is reduced to  $P_{\min}$ . As exemplary indicated for cycle 100 in Figure 62c, the sum of displacements due to pop-ins corresponds quite well to the totality of pop-outs during each cycle, indicating that the total amount of displacement is reversible in spite of the position and size of individual pop-ins and pop-out being stochastic.

However, as can be withdrawn from Figure 62d, there is a correlation between the cycle number, the average pop-in width  $\Delta h_{\text{pop-in}}$  and the total amount of displacement due to pop-ins  $\sum \Delta h_{\text{pop-in}}$ : the former increases steadily, almost doubling from 0.54 nm in cycle 10 to 0.97 in cycle 90, while the total displacement triplicates simultaneously from 8.15 to 26.11 nm.

Figure 62e represents the cyclic evolution of hysteresis loops for the first 20 cycles showing that the minimum value is achieved at cycle 6, where the onset of the reversible pop-ins was observed. Thereafter, the hysteresis area increases to values much higher than otherwise observed for similar test conditions (see Figure 59).

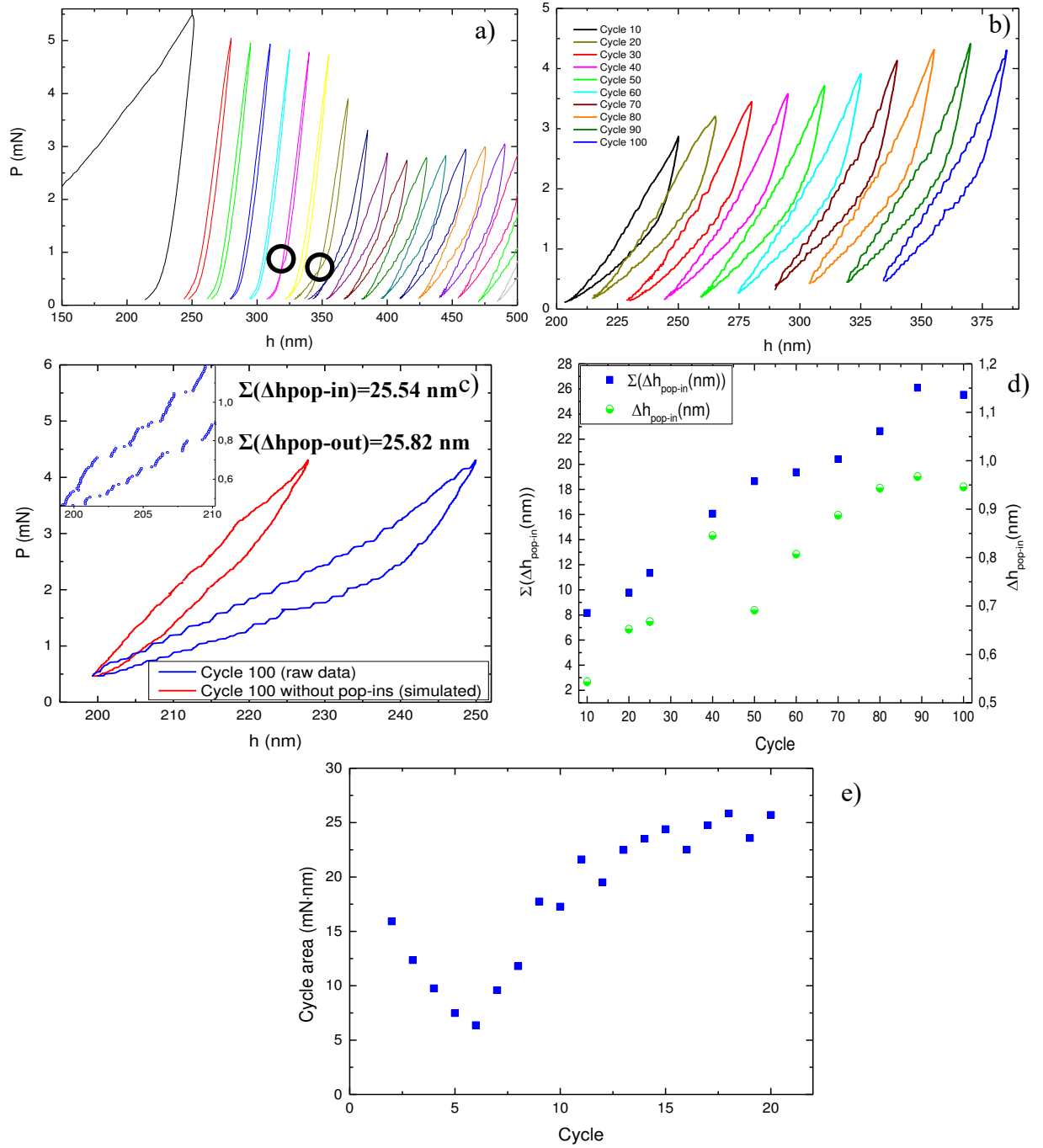


**Figure 62. Illustration of reversible pop-in formation.** a) general view of serrated P-h curve in annealed  $\langle 111 \rangle$  grain exhibiting reversible pop-ins; b) Compilation of the 2nd and thereafter every tenth cycle; c) Real and simulated "pop-in free" P-h curve of the 100th cycle; d) Evolution of hysteresis size from cycle 2 to 20 and e) Cyclic evolution of average pop-in width  $\Delta h_{pop-in}$  and total displacement during one loading phase  $\Sigma \Delta h_{pop-in}$ . In a) and b) consecutive cycles have been shifted 15 nm to the right.

As already mentioned in previous paragraphs, steels are known to exhibit anelastic behavior at room temperature, particularly during indentation loading. On the other hand, reversible  $\gamma \leftrightarrow \epsilon$  transformation under load is the most widely reported reason for occurrence of pseudoelasticity in iron-based shape

memory alloys <sup>250–253</sup>, where it is regularly observed during cyclic loading <sup>254,255</sup>. This behavior can be triggered strain-induced at room temperature, particularly in alloys with low SFE <sup>254,256,257</sup>.

Reversible pop-ins are closely related with the anelastic behavior and elbow formation previously observed. Their appearance indicates the occurrence of a displacive deformation mechanism, such as reversible dislocation gliding or reversible phase transformation, whereby taking in consideration the previous results, the latter is more plausible. Pop-ins arising beyond the elasto-plastic transition in TRIP steels have been observed by several authors in monotonic nanoindentation tests and are often attributed to phase transformation from austenite to  $\alpha'$ -martensite <sup>30,101</sup>. However, in the present case, pop-ins are reversible. Similar behavior was reported by Caër *et al.* <sup>258</sup> due to martensitic transformation in CuAlBe, but so far no reversible  $\alpha'$ -martensitic transformation had been detected in TRIP steels. This is sensible, since  $\alpha'$ -martensite is the stable phase in those steels at room temperature and can be reverted only via a thermal treatment at elevated temperatures <sup>134</sup>. However, in contrast to many other TRIP grades, the here investigated metastable stainless steel also features  $\epsilon$ -martensite, as observed in Chapter 3. Ahn *et al.* <sup>179</sup> observed the occurrence of multiple pop-ins in metastable austenitic steels and found by subsequent TEM characterization of the corresponding nanoimprints that those pop-ins correspond to the  $\gamma \rightarrow \epsilon$ -martensite transformation.

Since  $\epsilon$ -martensite can be considered as a pile-up of intrinsic stacking faults on every second (111)  $\gamma$  – plane,  $\gamma \rightarrow \epsilon$  transformation is a rather simple process. On the other hand, deformation-induced  $\epsilon$ -martensite formation in alloys with low Ni content, such as the here studied AISI 301LN, is reported to be rather unstable <sup>78</sup>. Table 9 lists the lattice parameters and the resulting distances between the closest-packed planes of the different phases occurring in the investigated material. It can be seen that the distance between the closest-packed planes in  $\epsilon$  corresponds to the one in  $\gamma$ ; while the respective distance in  $\alpha'$  is 3% smaller. As a consequence, the transformation between  $\gamma$  and  $\epsilon$  can be expected to occur easily, while  $\epsilon$  to  $\alpha'$  transformation would require a higher activation energy <sup>78</sup>. On this account, it can be postulated that during each loading cycle  $\epsilon$  formation occurs, but  $\epsilon$  does not transform to  $\alpha'$ . Moreover, it is stable only under load and reverses to  $\gamma$  during unloading. Indeed, as will be show in section 4.2.6, nanoindentation leads to the formation of thin  $\epsilon$ -martensite platelets interlaced with the surrounding highly faulted austenite. Thus, reversibility of the transformation can be expected to occur without difficulty. This might be one of the reasons why remaining  $\epsilon$ -martensite represents only a small fraction in the microstructure of austenitic stainless steels, and thus, its contribution uses to be largely ignored <sup>116</sup>.

**Table 9. Lattice parameters  $a$  and  $c$ , and distances between closest-packed planes in AISI 301LN <sup>259</sup>.**

	$\gamma$	$\alpha'$	$\epsilon$



<b>a (Å)</b>	3.61	2.86	2.54
<b>c (Å)</b>	-	-	4.16
<b>d (Å)</b>	2.08	2.02	2.08

The instability of  $\varepsilon$ -martensite formation is a phenomenon commonly exploited in shape memory alloys due to the reversible character of the former. Cyclic nanoindentation of those alloys was performed by Amini *et al.*<sup>25</sup> and resulted in the occurrence of jagged curves both during loading and unloading. The jagged shape is likely to correspond to pop-ins / pop-outs observed in the present thesis, which could not be resolved in Amini's study due to their 12 times higher loading rate. They explained the serrated shape by formation of new  $\varepsilon$ -nucleation sites and resulting stress relaxations and strain increase.

Nascimento *et al.*<sup>260</sup> tested separately  $\gamma$  and  $\varepsilon$  phases in a stainless steel with shape memory effect by nanoindentation in progressive cyclic mode. They observed that the hysteresis loops on P-h curves were wider for martensite than for austenite. This indicates a connection between hysteresis broadening and  $\varepsilon$ -phase formation.

Serrated monotonic nanoindentation curves similar to those here observed were also regularly observed for metallic glasses, being associated to the formation of shear or slip bands<sup>261–263</sup>. Albeit the deformation mechanisms in glasses are different than in crystalline metals, the findings support the hypothesis of serrations in nanoindentation curves being linked to formation of deformation bands.

Sekido *et al.*<sup>177</sup> observed multiple pop-ins corresponding to  $\varepsilon$  formation in the lower part of nanoindentation loading curve, while for the upper part the curve became continuous and the slope increased, which was found to originate from the transition in deformation mechanism from phase transformation to slip. This is similar to the curves here obtained, where the upper parts exhibit a higher slope than below the elbow and also less pop-ins. Since the slope of the upper part of the curves corresponds to the slope of the initial cycles, *i.e.* before the onset of pop-ins and serrations, it can be concluded that slip bands contribute to the anelastic cyclic behavior before the formation of  $\varepsilon$ -martensite.

According to Ahn<sup>179</sup>, the pop-in width is the projection of the slip of Shockley partial dislocations leading to  $\varepsilon$ -martensite formation. At least two stacking faults are required for the formation of an  $\varepsilon$ -band, with a respective unit displacement of around 0.1 nm, depending on the given slip system. Thus,  $\Delta h_{pop-in}$  as observed in this study corresponds to the formation of between five and ten  $\varepsilon$ -platelets.

Laplace *et al.*<sup>264</sup> detected the formation of many continuous pop-ins up to high loads, similar to the present study, and found that those pop-ins were not related to the formation of new  $\varepsilon$ -bands, but rather to

thickening of the preexisting ones, in agreement with present findings where pop-ins are more likely to increase in width than in number.

According to Amini <sup>25</sup>, the number of the nucleation sites depends on the presence of defects within the activation volume. This would explain why in the present thesis  $\epsilon$  formation occurs only after several indentation cycles and fully develops after an elevated cycle number. Once the first nucleation sites form,  $P_{\max}$  drops significantly, since deformation is eased by phase transformation.

Due to geometrical considerations <sup>179</sup>, during  $\alpha'$ -martensite formation the contraction along the indentation axis is too small to be detected as a pop-in. As will be shown in section 6.2.1,  $\alpha'$ -martensite is present in the plastic zone below the nanoindenter already after the first cycle, in spite of no pop-in due to phase transformation having occurred.

Finally, it is important to point out that the described reversible serrations were observed only for  $\langle 111 \rangle$ -oriented grains. Other authors also have reported that  $\epsilon$ -formation takes place only in austenite grains with a favorable orientation for deformation <sup>66</sup>.

### **Validation of shape memory properties**

It has been described that for Fe-Mn-Ni steels the presence of precipitates increases the shape memory characteristics <sup>265</sup> and, additionally, that only when austenite contains precipitates is susceptible to reversible  $\gamma \leftrightarrow \epsilon$  transformation under load <sup>257</sup>. The authors explained this fact because dislocation slip in obstacle free austenite is more favorable than  $\epsilon$ -martensite formation. However, the presence of precipitates changes this trend.

In the present work, no evidence of precipitation (by TEM characterization) was found. However, the high nitrogen content of AISI 301LN is known to lead to dislocation immobilization by formation of Cottrell atmospheres <sup>57</sup>. This is confirmed by the experiment described in Figure 63, where the sample was loaded and unloaded between 0 and 6 mN, in 0.6 mN steps, and a holding period of 1800 s was implemented during every step (Figure 63a).

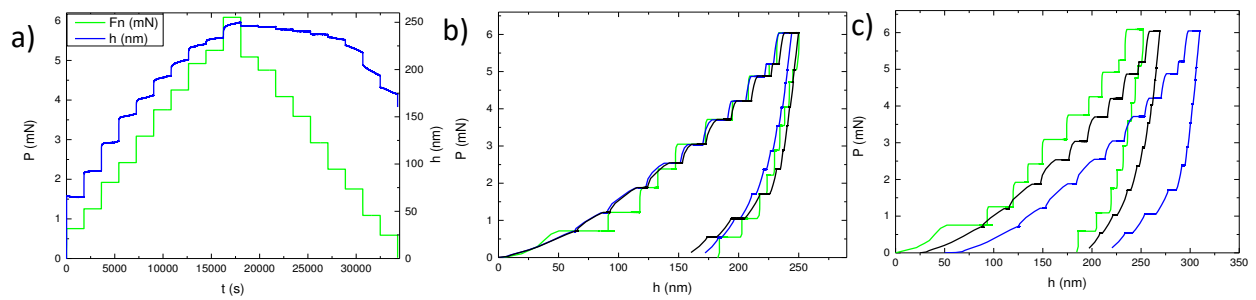


**Figure 63. Multistep nanoindentation testing with 1800 s holding periods . a) Applied load ramp and resulting displacement response; b) representative P-h curves as recorded and c) shifted 30 nm against each other.**

In agreement with the observed viscoplastic behavior,  $h$  increased noticeably during each holding step and the opposite occurred during the unloading. The exact amount of displacement at during each holding stage was not correlated to the corresponding load and was not reproducible for repeated testing. However, the total amount of displacement at full loading and full unloading is quite similar, being the maximum displacement at maximum loading  $248 \pm 3$  nm and the cumulative viscoplastic displacement  $64 \pm 2$  nm.

Interestingly, during each new loading /unloading stage the indentation slope increased significantly in comparison to the slope at the end of the previous loading segment. Apparently, dislocations became immobilized during the holding period and a significant load increase was necessary to activate them.

Since the investigated steel features a considerable N content, which contributes to dislocation pinning, it can be argued that the immobilization of dislocations during the holding stage is caused by the formation of Cottrell atmospheres. This is supported by the formation of Lüders-like bands during tensile tests of the studied steel grade <sup>266</sup>. Likely, the formation of Cottrell atmospheres in the present alloy has the same immobilization effect on dislocations as precipitates for other alloy compositions, and thus enables the development of the reversible phase transformation. Indeed, it has been reported by other authors <sup>267</sup> that load increase leads to generation of new dislocations, which first are relatively mobile, but after a holding sequence become pinned.

#### 4.2.7 Time-dependent plasticity

In the previous sections, viscoplasticity was regularly observed; nevertheless the underlying fundamental mechanisms are not discussed in detail. The following section will describe some related experiments.

Creep is known to occur during nanoindentation experiments. However, since after a hold period of 10-20 s the creep rate reduces to less than 1 nm/s, its influence is not often considered for monotonic experiments. Nevertheless, in the case of cyclic indentation, as performed in the present work, the influence of creep cannot be ignored, since the total holding time under load is considerable.

Consequently, tests have been performed to investigate time-dependent behavior during long holding stages.

Figure 64 shows nanoindentation curves with identical  $P_{\max}$  but different holding times. This plot illustrates that there is a significant increase of  $h_{\max}$ , even after a holding period of 300 s. Hence, the commonly applied holding sequence of 10 s is not sufficient to account for viscoplasticity in the investigated material, as also observed elsewhere<sup>268</sup>. Oliver and Pharr pointed out already in 1992 that time-dependent plasticity can occur in metals even after several indentation cycles and a holding interval of 100 s<sup>242</sup>.

To understand the origin of this time-dependent plasticity, studies starting from low loads, *i.e.* in the elastoplastic range, have been performed, as narrated in the following paragraphs. Subsequently, nanoindentation creep tests have been conducted in the plastic regime, *i.e.* at loads commonly applied in this study. For comparison, creep tests have been performed for macroscopic Vickers indentation.

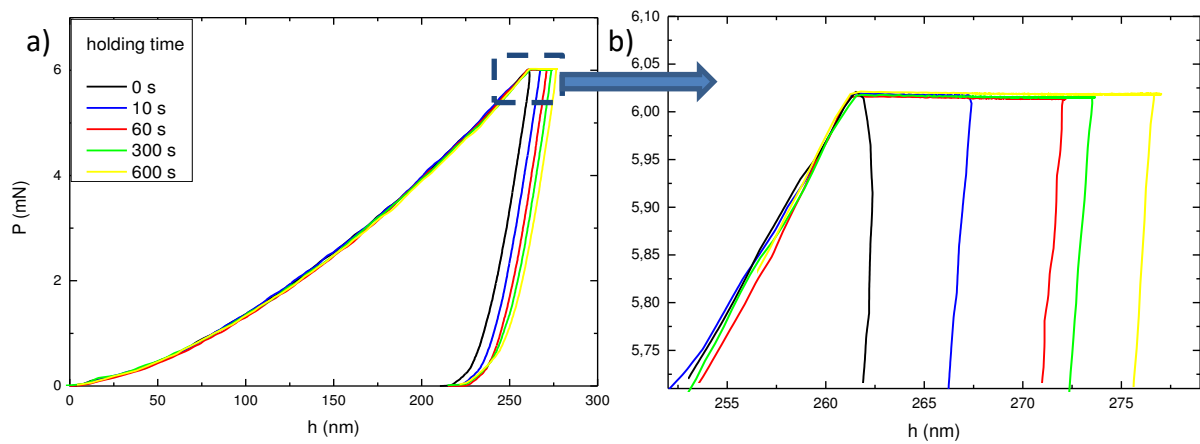


**Figure 64. Monotonic loading with different holding times. a) General view of the P-h curve, b) magnification of the holding section.**

Figure 65a and 65b correspond to nanoindentation curves in the elastoplastic transition regime, with a holding period of 60 s incorporated between the loading and the unloading stage. Thereby, the test in Figure 65a has been performed up to  $P_{\max} = 100 \mu\text{N}$ , *i.e.* below the elastoplastic transition, while Figure 65b represents the situation for  $P_{\max} = 200 \mu\text{N}$ , *i.e.* surpassing the elastoplastic transition. The latter is evidenced by the fact that secondary pop-ins appear.

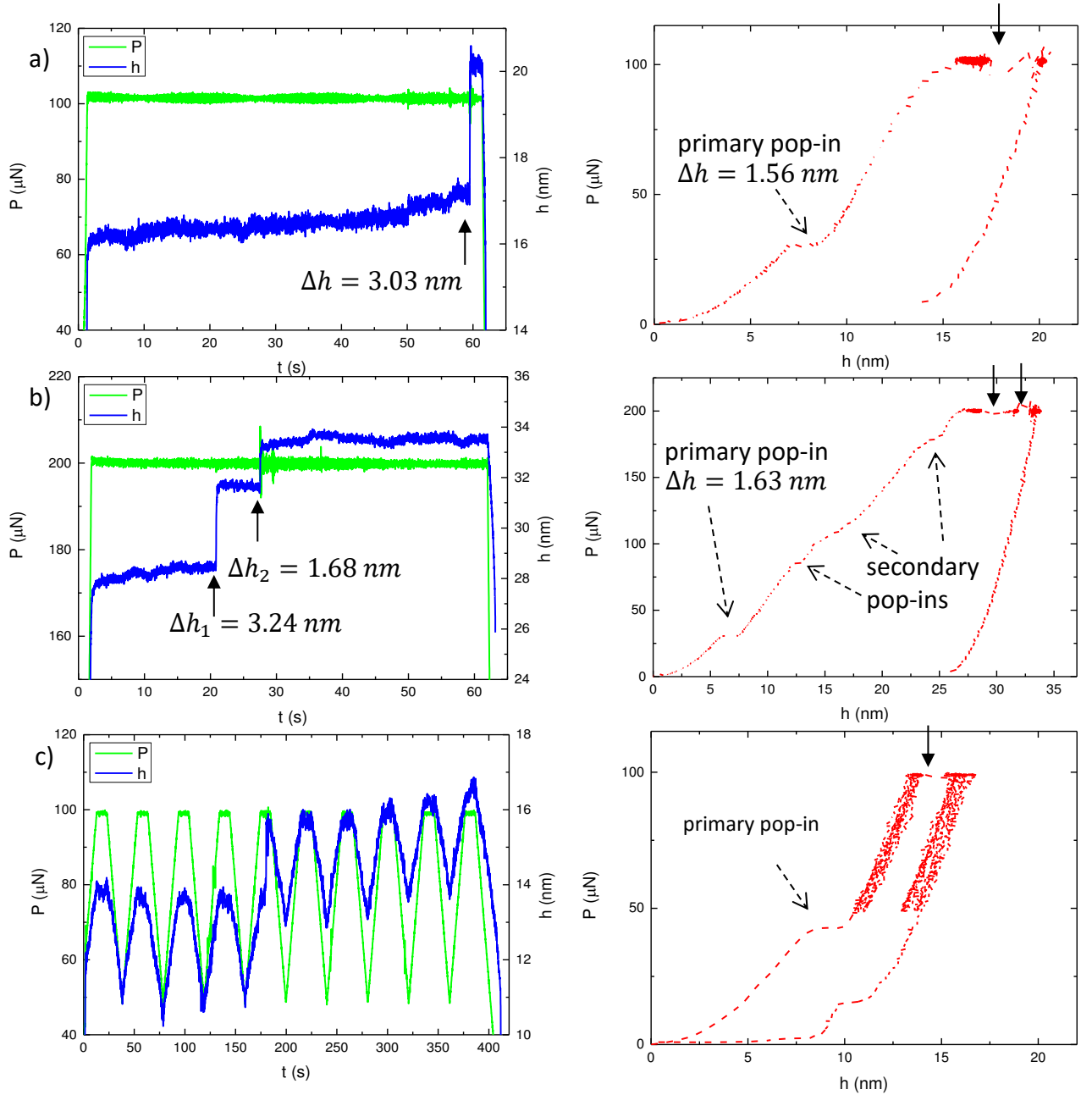


**Figure 65. Time-dependent plasticity at small loads. Sample was loaded to a)  $200 \mu\text{N}$  and b)  $100 \mu\text{N}$  and held at constant load for 60 s before unloading; c) The sample was cyclically loaded with 10 s holding stages between sequential cycles. The loading rate was 0.5 mN/min. The occurrence of pop-ins during the holding stage is indicated by vertical arrows.**

Noticeably, during the holding stage displacement jumps occurred in both cases: one jump after 58 s for  $P_{\text{max}} = 100 \mu\text{N}$  and two jumps after 18.5 and 25.5 s, respectively, for  $P_{\text{max}} = 200 \mu\text{N}$ . As can be withdrawn from Figure 65, the extent of these displacement jumps corresponds quite well to either single or double amount of the displacement burst during the first pop-in. Thus, it can be assumed that the nature of both displacements is similar.

Interestingly, the observed phenomenon comprehends an incubation process, *i.e.* can be activated during holding at constant load, whereby the incubation time depends on the applied load. It has been reported that dislocations can be activated thermally below subcritical load after prolonged holding times<sup>219,223</sup>. However, since the observed phenomenon does not lead to elastoplastic transition, it is not likely to be related to activation of dislocations. Thus, a possible explanation would be phase transformation. It is known that  $\gamma \leftrightarrow \epsilon$  transformation is opposed to  $\gamma \leftrightarrow \alpha'$  transformation<sup>269</sup>, *i.e.* the first one can occur at loads below the yield point. Indeed, reversible martensitic transformation has been detected even below the elastoplastic transition<sup>258</sup>, with the corresponding pop-ins and pop-outs, such as observed in the inset of Figure 51a.

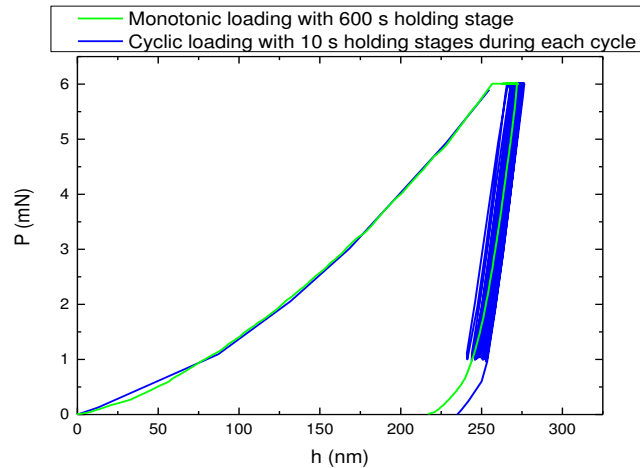
In addition to the appearance of pop-ins, a small, but continuous increase of  $h$  during the holding stage can be seen in Figure 65. Hence, the evaluation of ten different tests, with a 60 s holding period, at 50, 100 and 200  $\mu\text{N}$  of maximum indentation load, resulted in average displacements of  $0.73 \pm 0.22$  nm,  $0.98 \pm 0.50$  nm and  $2.02 \pm 0.65$  nm, respectively. Noticeably, the higher the load, the longer is the time-dependent displacement, indicating that this displacement cannot be caused by thermal drift (alone). When passing from 100 to 200  $\mu\text{N}$ , the range where most of the elasto-plastic transitions occurred,  $h$  increased noticeably. This is in good agreement with Kim *et al.*<sup>270</sup>, who observed very similar time-dependent behavior in ceramics at room temperature and also found that the latter is markedly more pronounced in the elasto-plastic rather than in the elastic regime.

Figure 65c illustrates the characteristic deformation behavior when the material is cyclically loaded between  $P_{\text{max}} = 100$   $\mu\text{N}$  and  $P_{\text{min}} = 50$   $\mu\text{N}$ . Here, a displacement jump was likewise regularly observed, preferentially occurring during holding at maximum load. The displacement jump typically occurs after longer total times than in case of monotonic loading and holding at 100  $\mu\text{N}$ , which is understandable since the average load in case of cyclic loading is lower than  $P_{\text{max}}$ . The loading-unloading curves are largely elastic, however, due to the above-mentioned steady increase of  $h(t)$ , the loops are slightly shifted against each other. No distinguished behavior for cyclic, in comparison to monotonic loading, could be observed in the here applied load range.

#### 4.2.8 Propagation of plasticity

The observed viscoplastic behavior does not necessary originate from cyclic loading, but rather from increasing holding time under load, whereby even at  $P_{\text{min}}$  between two cycles time-dependent deformation continues. However, as became clear from the obtained results, dynamic loading can be expected to lead to additional deformation mechanisms, compared to the response to monotonic indentation. This is illustrated in Figure 66, where  $P$ - $h$  curves from a 12-cycles nanoindentation test in constant load mode are superimposed to a monotonic test with a holding period of 600 s. For the former, the material was

cyclically loaded and unloaded, between 1 and 6 mN with a holding time of 10 s at maximum load, so the total test time was about 600 s. In spite of the average load being only 58% of  $P_{\max}$ , the total displacement resulting from the cyclic test was higher than for monotonic holding, confirming that an additional ratcheting component is present for cyclic loading, in addition to the viscoplasticity resulting from monotonic loading and subsequent holding.



**Figure 66. Time-dependent displacement during cyclic loading and constant holding in comparison.**

To the author knowledge, cyclic nanoindentation testing has been never performed on steels. However, for macroscopic cyclic indentation of metals, increase of plastic zone and propagation to the bulk was reported<sup>248,271</sup>, similar to here observed. However, in-depth studies on this issue have not been performed.

The aspect of plasticity propagation is enlightened in this section by presenting another interesting characteristic observed during cyclic nanoindentation: the occurrence of large, singular pop-in events, as illustrated in Figure 67. Pop-ins were observed either in the loading or unloading part of P-h curves, and occurred typically after 50 or more indentation cycles. After the pop-in, the subsequent cycles reassume their usual shape. The occurrence of a 2<sup>nd</sup> and further pop-ins could sometimes be observed after an elevated cycling number. Those pop-ins cannot be related to those at elasto-plastic transition taken place for small displacements during the first loading.

Noticeably, pop-ins occur more readily when the nanoindentation was performed in smaller grains and close to a grain boundary. The latter situation is illustrated in Figure 67. A general trend exhibits a positive correlation between the distance to the closest grain boundary and the number of cycles to the occurrence of a pop-in. Some scattering is present due to the difference in grain size and misorientation between the indented and the neighboring grain. Pop-ins could be detected for indents located further than 6  $\mu\text{m}$  or closer than 1  $\mu\text{m}$  from the grain boundary. In the microstructural characterization of the studied steel, plasticity transfer through grain boundaries was regularly observed (Chapter 3). Interestingly, this

was only the case when a pop-in was observed in the corresponding nanoindentation curve, suggesting that these two events are related.

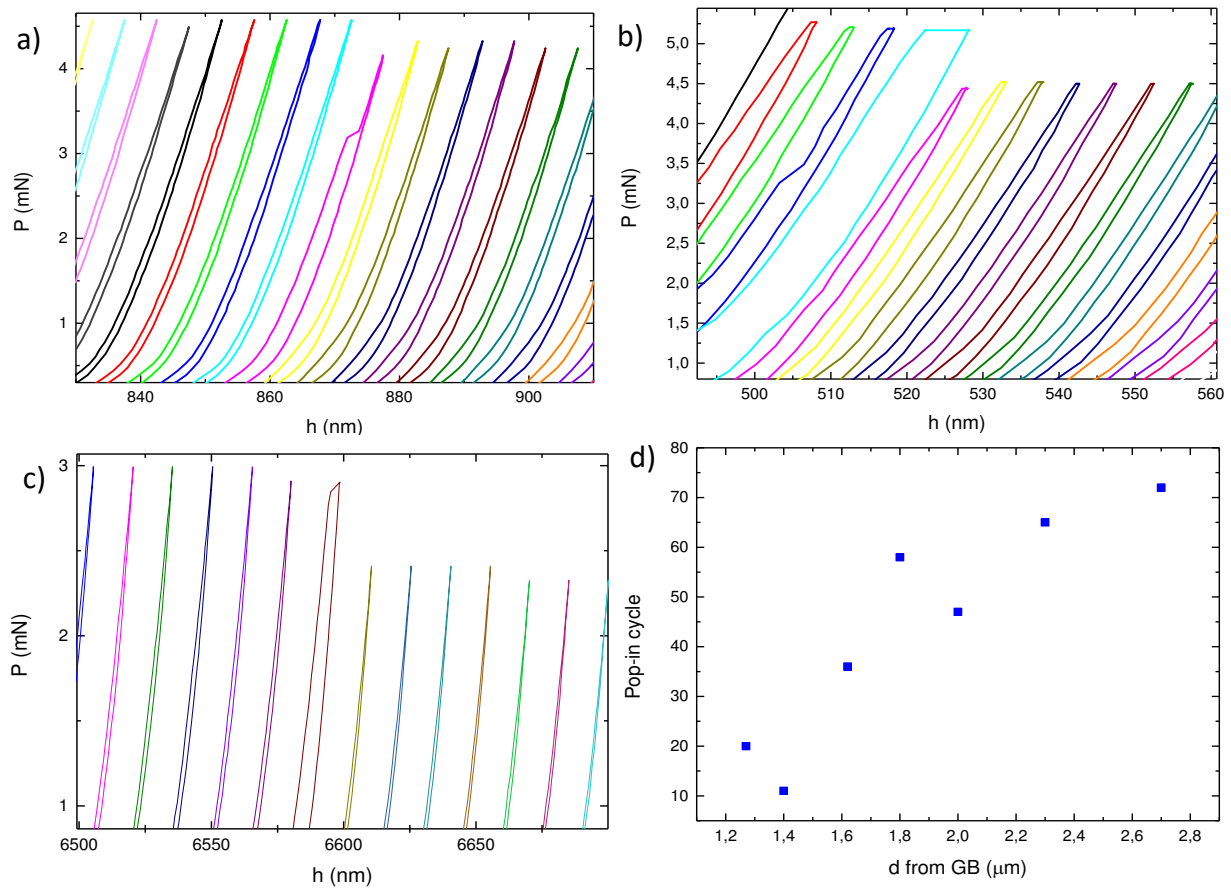


**Figure 67. Occurrence of pop-ins after prolonged cyclic nanoindentation. a)-c) Different examples of pop-ins; d) Occurrence of the first pop-in, as a function of the distance of the nanoindent from the closest grain boundary.**

It is widely reported<sup>272,273,225,274-276</sup> that nanoindentation tests in the vicinity of grain boundaries led to the occurrence of secondary pop-ins between 10 and 100 nm in width - at significantly higher loads than the elasto-plastic transition. Those pop-ins were found to be caused by dislocation pile-up at grain boundaries and subsequent slip transfer across those boundaries<sup>277</sup>.

The presence of interstitial elements, such as in the present material, is a fundamental requirement for the occurrence of pop-ins<sup>274</sup>, since the slip barrier formed by the grain boundary is believed to be caused by pinning of dislocations by Cottrell atmospheres. Once the shear stress on a slip system in the adjacent grain becomes large enough, dislocations get liberated and can move easily on the new slip system. Wang and Ngan<sup>272</sup> deduced that pop-ins occur at a critical value  $c/d$ , whereby  $c$  is the size of the plastic zone and  $d$  the distance from the center of the indentation to the grain boundary. The critical stress at which pop-in occurs is also reported to depend on the misorientation between the indented and adjacent grains<sup>274</sup>. The misorientation factor  $m'$ , which considers the geometric relationship between the



indentation axis, the active slip system in the indented grain, as well as the one in the adjacent grain, is defined as:

$$m' = \cos(\alpha) \cos(\beta) \quad (18)$$

where  $\alpha$  is the angle between the closest slip planes in the neighboring grains and  $\beta$  the angle between the closest of the slip directions lying on the closest slip planes.

On the other hand, no pop-ins were reported for indents located in the immediate proximity of a grain boundary, since in this case plasticity can be induced directly in both grains.

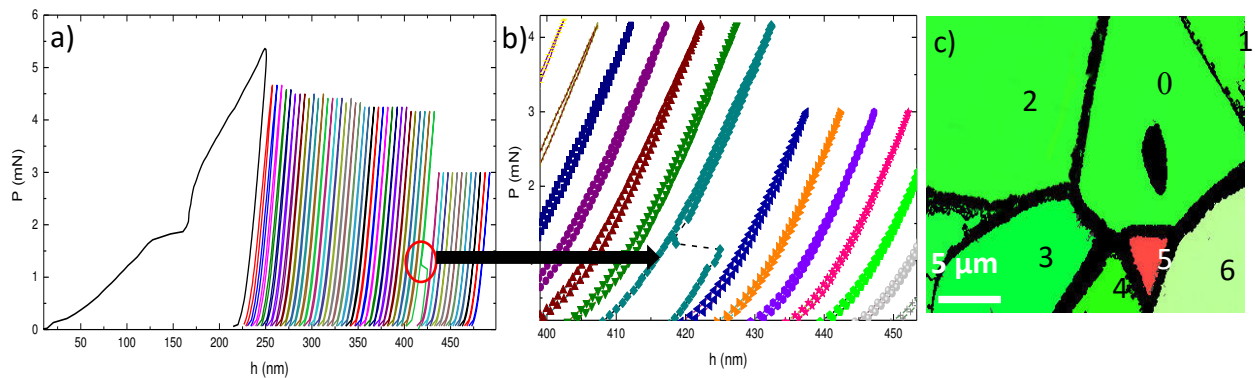


**Figure 68.** Nanoindentation test featuring a large pop-in during the first and 38<sup>th</sup> cycle. a) General representation of corresponding P-h curves (consecutive cycles shifted 10 nm to the right); b) enlarged view of pop-in in cycle 38; c) EBSD IPF map of the indentation site.

The character of the pop-in observed in the present study and the corresponding TEM results (as will be shown in section 6.2.4) let conclude that the observed phenomenon is of the same kind as in the previously mentioned literature findings, with the difference that here the applied loads are small and therefore pop-ins did not occur during the first loading cycle, but only after an elevated number of cycles.

Apparently, for the studied AISI 301LN and the implemented experimental conditions,  $P_{\max}$  usually was not enough to allow slip transmission during a single cycle. Nevertheless, the accumulation of plasticity leads to an increase of the plastic zone, so the critical  $c/d$  value can eventually be reached after multiple indentation cycles.

However, occasionally, pop-ins were detected during the first cycle, as represented in Figure 68a. Within the corresponding test, also a second pop-in was observed after 37 cycles (magnified in Figure 68b). Figure 68c gives an EBSD IPF map of the indentation site. The latter shows that the indented grain is rather small, and moreover the indentation site is close (between 4 and 5  $\mu\text{m}$  respectively) to several grain boundaries. As can be concluded from the IPF image, grains 1, 2, 3 and 4 are oriented with the same plane to the surface, as the indented grain ( $\langle 011 \rangle$ ) and thus, they are only rotated around the z-axis with regard to the latter.

Table 10 summarizes the exact orientations of the depicted grains in reference to the indentation axis and their misorientation to the indented grain. As can be deduced from the table data, the misorientation of grain 4 is close to  $54.5^\circ$ , which is one of the possible angles between two  $\{111\}$  slip planes projected onto a  $\{011\}$  surface, as is the case here. Thus, it can be assumed that in grain 4 there is a slip system lying almost equivalent to the active slip system in the indented grain. Consequently,  $m'$  is close to 1 and the critical shear stress for slip transfer is minor, being basically determined by the barrier built by the defects accumulated at the grain boundary. Therefore, it can be assumed that the critical stress for this particular case was small enough to allow slip transfer already during the first indentation cycle. The second pop-in, after 37 cycles, might be originated by slip transfer through one of the others adjacent grain boundaries.

**Table 10. Crystallographic relationship between the indented and the adjacent grains.**

<b>Grain</b>	<b>0</b>	<b>1</b>	<b>2</b>	<b>3</b>	<b>4</b>	<b>5</b>	<b>6</b>
<b>Misorientation</b>	0	59.82	58.5	30.3	53.4	59.9	47.5
<b>&lt;hkl&gt;</b>	<178>	<304>	<304>	<101>	<506>	<129>	<135>

## 4.3 Appendix /Supplementary: Verification of equipment stability

### 4.3.1 Creep & thermal drift study

Since pronounced creep leading to cyclic softening in steels at room temperature might be considered a surprising result, drift corrected creep measurements were conducted, as described in this section, in order to reassure the validity of the results.

The outcome is illustrated in Figure 69: sample was first loaded to 0.6 mN and hold for 1800 s; subsequently, P was increased to 6 mN and held for another 1800 s before complete unloading (Figure 69a). Although from the results in section 4.2.7 time-dependent behavior is expected to occur even at low loads, it can be assumed that at higher loads, where the dislocation activation volume under the indenter tip is bigger, the resulting time-dependent displacement will be significantly larger. Thus, dislocation slip at 0.6 mN, in comparison to 6 mN, is considered to be negligible at prolonged holding times, and the corresponding time evolution of  $h$  at 0.6 mN can be subtracted from the one for 6 mN, imputing its origin mainly to thermal drift. Assuming that the direction and rate of thermal drift were the same for holding at 0.6 and 6 mN, the resulting curve is considered as the drift-corrected time-dependent displacement at 6 mN. Thus, Figure 69b illustrates a characteristic evolution for  $\Delta h$  at 0.6 mN and 6 mN. Noticeably, a small negative thermal drift was present, as can be concluded from the slope at 0.6 mN of the curves at prolonged holding times. The slope of  $h$  at 6 mN was slightly positive; indicating that for higher loads there is a continuous displacement increase, even for high loads.

In Figure 69c, drift-corrected curves for three different tests are plotted in one graph. These curves were largely reproducible. For comparison, ex-situ creep measurements have been also performed with Vickers indentation for two different loads and ten different holding times. Just as observed for the non-drift-corrected curves by Kim *et al.*<sup>270</sup>, all curves are of parabolic nature and exhibit a transient and a steady state regime. In the present study, the amount of the total displacement during the transient regime and the slope in the steady-state regime are very similar for all curves, with the only difference in the slope of the transient regime and thus, the instant of the onset of the steady-state.

The evolution of the time-dependent displacement becomes clear in Figure 69d, where the creep strain rates are calculated as:

$$\dot{\epsilon} = \frac{d(\Delta h/h)}{dt} \quad 278,279,$$

The transition from transient to steady state occurs between 150 and 450 s.

Results for Vickers indentation are in good agreement with those from nanoindentation, with the only difference of the transition between different creep regimes being less marked. Thus, the time-dependent behavior observed within this study is confirmed to be a physical phenomenon and not an artifact caused by thermal drift.

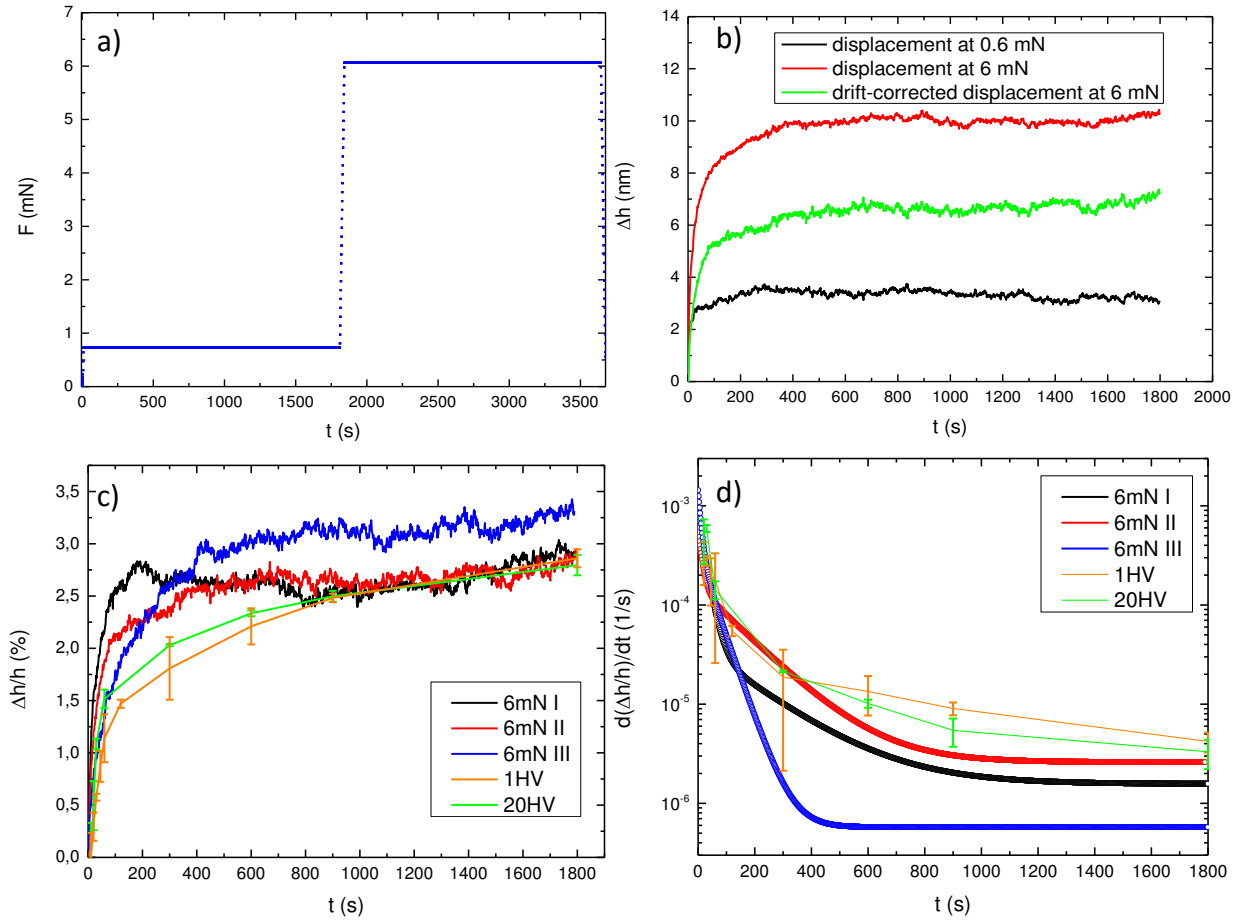


Figure 69. Nanoindentation creep measurements a) Applied loading ramp; b) total displacement  $\Delta h(t)$  evolution at 0.6 mN and 6 mN, as well as the difference between the two; c) relative displacement  $\Delta h/h(t)$  evolution for three drift-corrected creep tests at 6 mN, as well as the displacements averaged from respectively three test sets for Vickers indentation at 1HV and 20 HV respectively; d) relative creep rate estimated from c). Initial  $h_{max}$  was around 250 nm.

#### 4.3.2 Cyclic evolution of mechanical properties

Another critical issue is the maintenance of the contact area and indenter tip geometry during the cyclic nanoindentation experiments. Figure 70 represents the cyclic evolution of the unloading slope  $\frac{\partial P}{\partial h}$  at  $h = h_{max}$ , which corresponds to the contact stiffness  $S$ , for the experiments represented in Figure 54. As mentioned in section 1.2.3,  $S$  is related to the effective Young's modulus via the contact area  $A_c$  and the geometry shape factor  $\beta$ .  $\beta$  is calculated from the corresponding  $S$ ,  $E_{eff}$  and  $A_c$  values, and is plotted in Figure 70 as well.

The calculated  $\beta$  values are in good agreement with the expected value for a Berkovich tip<sup>280–282</sup> and remain stable both in displacement and loading modes. On the contrary,  $S$  is only constant for

displacement mode, but not in loading mode. Since the Young's modulus is an intrinsic material property, *i.e.* should remain constant, and  $\beta$  was also confirmed to be constant, the evolution in  $S$  can be only due to the evolution in the contact area. This confirms that the contact area only changes in loading mode, due to the cyclically increasing  $h_c$  values, while in displacement mode, where  $h_c$  remains constant, the same is true for the contact area and contact stiffness.

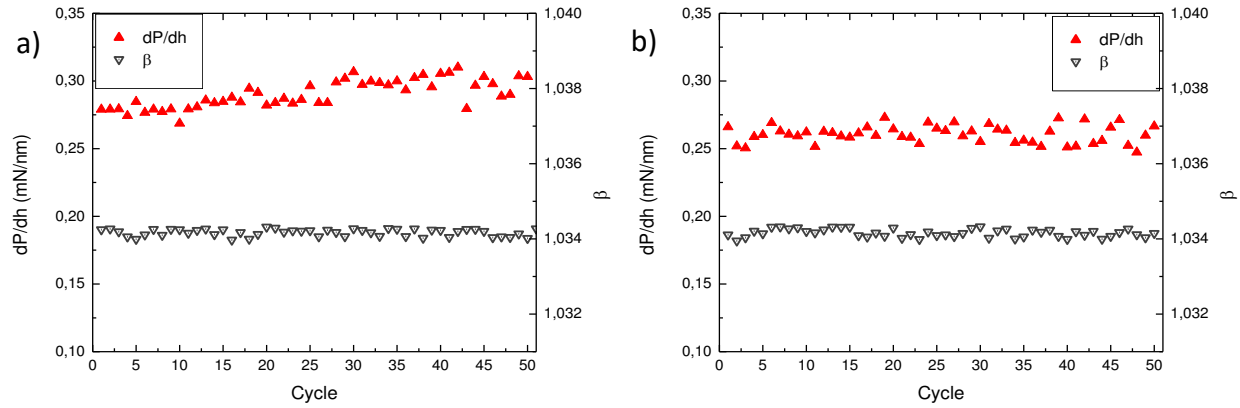


Figure 70. Cyclic evolution of contact stiffness and  $\beta$  corresponding to a) Figure 54a and b) Figure 54b.

## 4.4 Conclusions

This chapter has confirmed that it is possible to use cyclic nanoindentation as a tool to induce gradual deformation and strain accumulation in a selective way. Moreover, the measurement accuracy has been validated.

It was found that the AISI 301LN steel shows a pronounced time-dependent deformation behavior at room temperature. One of the origins for this behavior is viscoplasticity, caused by dislocation mobility and thermally assisted phase transformation when holding prolonged time under load; the other origin is ratcheting, due to cyclic loading. The accompanying strain accumulation can lead to plasticity transmission into adjacent grains, whereby the misorientation factor plays an important role.

The material exhibited crystalline anisotropy both, during the elastoplastic transition and within the plastic range. Accordingly, secondary hardening occurred only for selected grain orientations. Signs for formation of  $\alpha'$ -martensite are given, though it was not accompanied by detectable pop-ins due to variant selection and resulting minor displacement parallel to the z-axis. Thus,  $\alpha'$ -martensitic transformation cannot be detected through evaluation of nanoindentation curves alone.

On the other hand, nanoindentation cycling resulted in pronounced anelasticity due to reversible  $\gamma \leftrightarrow \epsilon$  transformation under load, such as happens for shape-memory alloys. It is somewhat surprising, since to

the author knowledge only Mn-based austenitic stainless steels (series 200) are known to possess these properties. This is reasonable, taking into account that steels with a chemical composition as AISI 301 exhibit a much smaller fraction of  $\epsilon$ -martensite than high Mn-grades.

Thus, shape memory effect might be too weak to be detected by conventional cyclic loading techniques. However, cyclic nanoindentation is a suitable technique to further investigate this behavior. It was found that the investigated steel exhibits a dislocation pinning effect, favoring phase transformation over dislocation slip. Moreover, its lattice parameters facilitate reversible  $\gamma \leftrightarrow \epsilon$  transformation, rather than a  $\gamma \rightarrow \alpha'$  or  $\epsilon \rightarrow \alpha'$  transformation.

It was further confirmed that pre-straining stabilizes the material against further deformation.

From the experimental point of view, the evaluation of P-h curves was enabled analyzing the following criteria:

- Time-dependent behavior under constant load / displacement.
- Cyclic evolution of load /hardness.
- Evaluation of P-h curve shape and hysteresis loops.
- Evaluation of three different types of pop-ins: i) elasto-plastic transition at low loads, ii) Reversible pop-ins and pop-outs related to phase transformation, throughout a large part of P-h curves, iii) Large pop-ins occurring occasionally, correlated with plasticity transmission to neighboring grains.

## 5 Characterization of surface deformation

### 5.1 Motivation

In the previous chapter, it became clear that the mechanical response of the studied material is sensitive to the test conditions during the nanoindentation experiments. Thus, the next evident step is the examination of micro- and substructural changes arising from the imposed deformation.

Typically, substructural arrangements formed during nanoindentation are studied by means of TEM with lamellae lifted-out by FIB from the center of the residual imprint and perpendicular to the specimen surface. On the other hand, the deformation mechanisms activated below the indenter tip parallel to the loading axis, are expected to be different than those at the free surface, surrounding the nanoindent. The latter has been investigated by SEM and AFM<sup>18,283,284</sup>. However, the limitations of these characterization techniques do not allow unambiguous phase identification, which is of high importance for metastable steels given to the deformation-induced martensitic transformation. Misra *et al.*<sup>173</sup> studied the deformation parallel to the surface by preparation of thin foils by electrolytic thinning. Nevertheless, this method does not allow the extraction of TEM samples from the immediate surface layer, but rather from an inner material layer parallel to the surface, and thus, it is not suitable for study of defects, such as slip traces emerging at the surface.

Thus, within this chapter, surface deformation resulting from nanoindentation has been studied, as a preceding step before continuing with the characterization of deformation within the bulk of the indented grain (Chapter 6). For this purpose, a TEM lamella was extracted directly from the surface surrounding a residual imprint resulting from cyclic nanoindentation, such as explained in section 2.1. The study was conducted in the following sequence: first, local deformation induced by nanoindentation was observed by EBSD; in the second section, surface deformation induced by monotonic and cyclic indentation for two different crystallographic grain orientations were compared by means of FESEM; the third subsection is devoted to the TEM study of the two types of martensite induced by deformation in metastable austenitic stainless steels; and in the last part of this chapter, HRTEM was applied for a deeper study of the fine structure of  $\epsilon$ -martensite.

## 5.2 Results and discussion

### 5.2.1 General aspect of residual nanoimprints

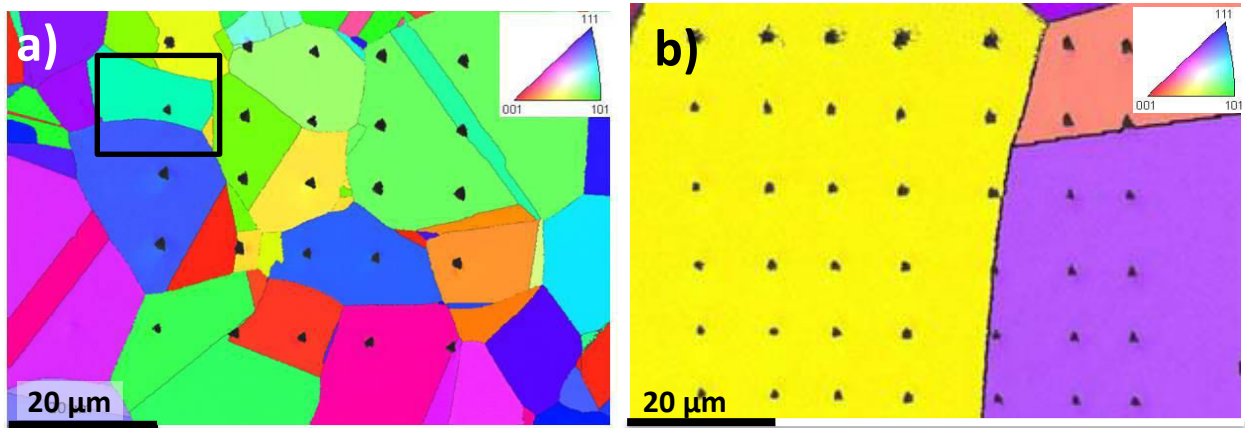


Figure 71. Indentation matrices in annealed samples. a) SG and b) CG condition, located on areas previously mapped and represented in Figure 45a and b, respectively.

Figure 71 represents EBSD IPF maps of annealed SG and CG samples, showing the same areas as in Figure 45a and b after performance of nanoindentation tests. The corresponding maps did not reveal significant differences in the steel microstructure compared to the mapping previous to the nanoindentation: neither formation of twins nor martensitic transformation were discerned.

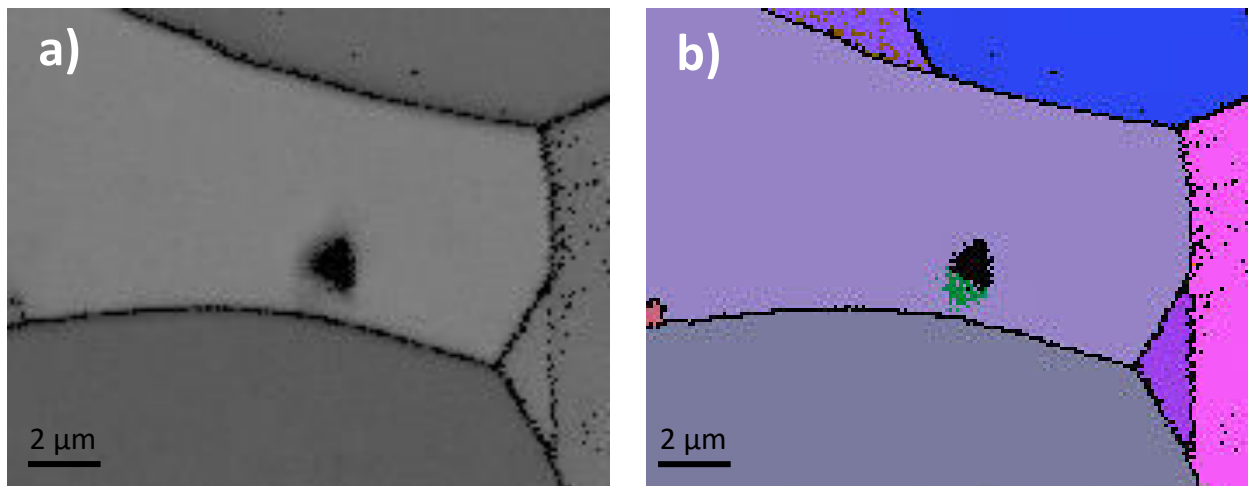


Figure 72. Close view of an indent in Figure 1c. a) EBSD Band Contrast map showing modified contrast around the residual imprint; b) All-Euler EBSD map exhibiting lattice rotation at one edge of the indent.

However, at a closer view, the dark contrast in the band contrast (BC) image indicates the presence of strain accumulation at the immediate surroundings of the indents, as highlighted in Figure 72a.



Furthermore, the Euler Angle image (Figure 72b) reveals the presence of lattice rotations, with misorientations around  $1^\circ$ . Misorientation is confined to a region of nearby  $1\ \mu\text{m}$  from the indent center, giving a clue of the approximate dimensions of the plastic zone surrounding the nanoindents. Lattice rotation due to strain accommodation is a phenomenon frequently observed after indentation loading, whose origin is in the generation of Geometrically Necessary Dislocations (GNDs) under the indenter tip<sup>12,27,285</sup>.

### 5.2.2 Surface deformation patterns induced by nanoindentation

It is well established that for fcc metals, there are four possible  $\{111\}$  slip planes, containing each three possible  $\langle 110 \rangle$  slip directions, thus leading to twelve glide systems. For uniaxial monotonic strain, usually only the glide system with the highest Schmid factor is activated. But when fcc metals are subjected to macroscopic cyclic deformation, several glide systems can be simultaneously activated<sup>283,286,287</sup>. At the surface, activation of slip planes can be characterized by the study of the corresponding slip traces. Within this section, the respective behavior for cyclic nanoindentation has been studied.

Figure 73 shows SEM images of residual imprints from monotonic and cyclic nanoindentation tests in grains oriented with their  $\langle 001 \rangle$  and  $\langle 111 \rangle$  directions parallel to the indentation axis. For each case, parallel lines surrounding the imprints are clearly observed at the surface. The presence of the slip traces is directly related to the crystallographic orientation of the indented grain<sup>145</sup>, and their direction is given by the intersection of the respective slip planes with the surface plane. Thus, for  $\langle 001 \rangle$  oriented grains, if the surface plane is defined as (001), simple mathematical calculations result in the plane being cut by the planes (111),  $(\bar{1}11)$ ,  $(1\bar{1}1)$  and  $(\bar{1}\bar{1}1)$  along the directions  $[\bar{1}10]$ ,  $[\bar{1}\bar{1}0]$ ,  $[110]$  and  $[1\bar{1}0]$ , leading to a 4-fold symmetry arrangement<sup>288</sup>. Analogously, looking parallel to the  $\langle 111 \rangle$  direction, the surface plane (111) is cut by the planes  $(\bar{1}11)$ ,  $(1\bar{1}1)$  and  $(11\bar{1})$  along the directions  $[01\bar{1}]$ ,  $[10\bar{1}]$  and  $[1\bar{1}0]$ , forming angles of  $60^\circ$  to each other, leading to a 3-fold symmetry arrangement.

According to the explanations above, Figure 73 reveals that for  $\langle 001 \rangle$  oriented grains slip traces build a square around the imprint, intersecting at angles of  $90^\circ$ ; whereas for  $\langle 111 \rangle$  grains, three slip directions trace an equilateral triangle. This corresponds to the theoretical prediction, suggesting that due to the complex stress field caused by nanoindentation, apparently all the possible slip systems were simultaneously activated and for the applied load multiple slip took place in all four test conditions. These results are in agreement with the nanoindentation behavior of fcc metals modeled with finite element analysis by Liu *et al.*<sup>241</sup>. The latter also observed that the residual imprints are shallower for grains

oriented along  $\langle 001 \rangle$  than for ones along  $\langle 111 \rangle$  and also more material pile-up around the imprints occurs for the former.

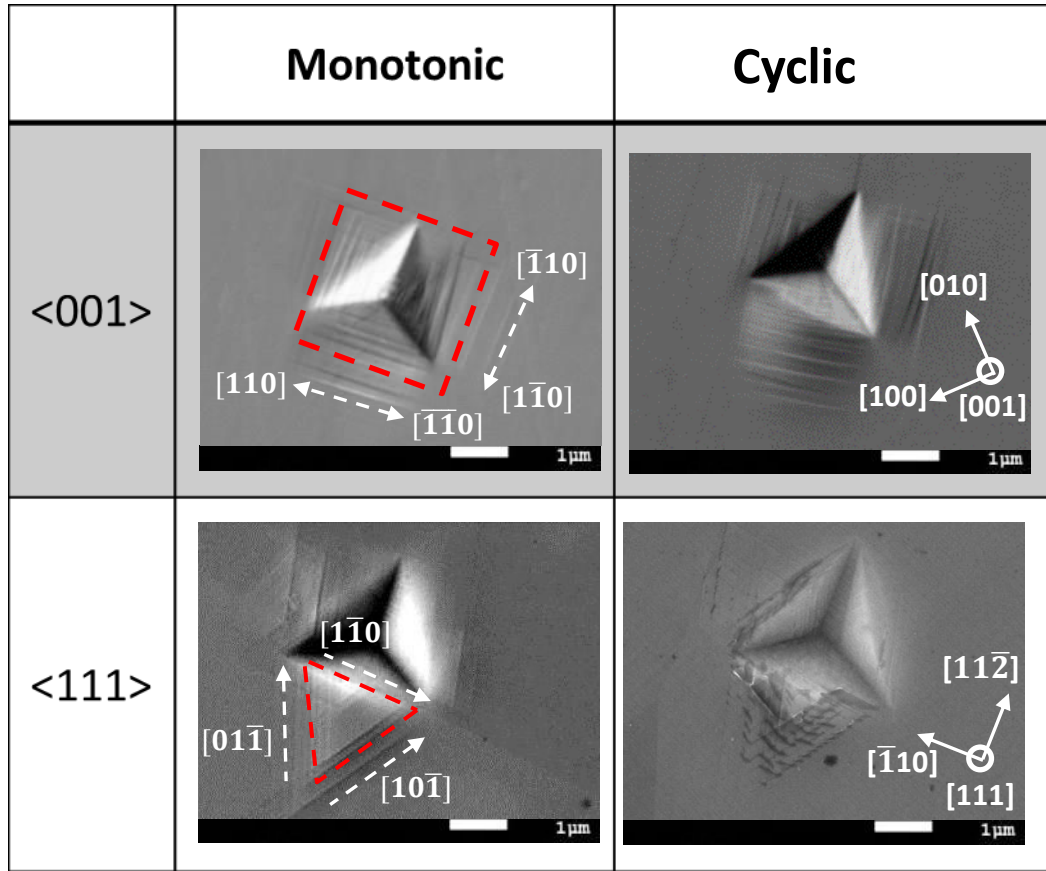


**Figure 73.** SEM images of the deformed nano-indentated grains along  $\langle 001 \rangle$  and  $\langle 111 \rangle$  directions revealing slip band traces. The 4-fold and 3-fold symmetries of the traces are marked for  $\langle 001 \rangle$  and  $\langle 111 \rangle$ , respectively.

Comparing the deformation pattern for single and cyclic indentations, there are some evident differences. For grains oriented along  $\langle 001 \rangle$ , the density and extension of the slip lines are somewhat increased and noticeable material pile-up appears at the edges of the imprint – in agreement with Liu’s study. In the case of grains oriented along  $\langle 111 \rangle$ , small particle-like features are formed at the intersections of the slip lines.

In order to analyze the influence of grain boundaries on the surface deformation, an imprint induced by cyclic indentation along the  $\langle 111 \rangle$  direction and close to a grain limit was selected, as can be observed in the EBSD Inverse Pole Figure (IPF) map in Figure 74a. A FESEM view of this selected imprint is shown in Figure 4b, where two intersecting sets of slip plane traces (labeled I and II) can be distinguished. These traces initiate at the edge of the indent and, in case of set II, impinge on and interact with the adjacent grain boundary. At the intersection of the two activated slip systems, and close to edge of the residual imprint, small granular particles are visible, which will be studied more in detail in the following.

### 5.2.3 Characterization of underlying defects

In order to gain a deeper understanding on the main deformation mechanisms activated by nanoindentation, TEM characterization was performed. The white dashed square in Figure 74a and b indicates the shape and position of the plan view TEM lamella, which was prepared following the previously described procedure, illustrated in Figure 43.

A BF image of the corresponding thin foil is depicted in Figure 75a, while Figure 75b illustrates the DF image for the austenitic phase. Moreover, the diffraction pattern is given in Figure 77d.

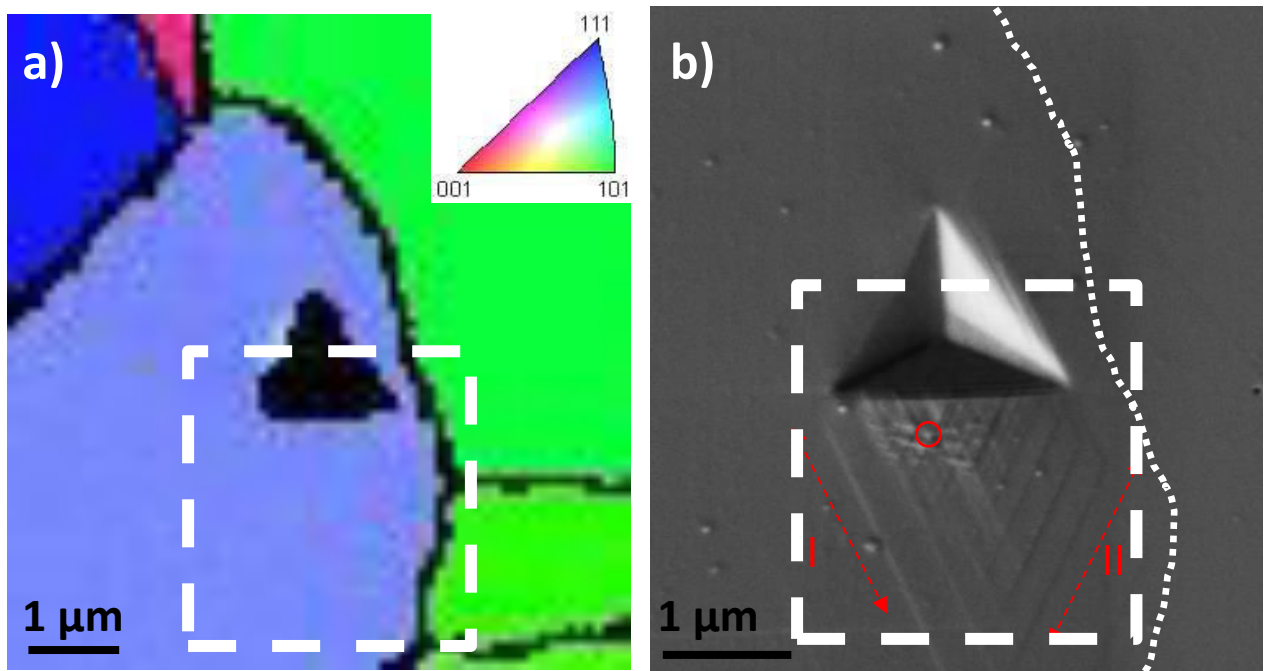


**Figure 74. a) EBSD IPF map and b) SEM image of the area around the residual imprint along  $\langle 111 \rangle$  direction. The white dotted line traces the approximate position of the grain boundary and the small circle highlight exemplary a particle formed at the intersection of slip plane traces.**

A high density of dislocations piled up at the grain boundary is discernible and leads to the illumination of the austenitic phase in the DF image (right hand of Figure 75b).

Figure 75a shows the presence of thick irregular deformation bands emerging from the residual imprint, and fine parallel ones at a longer distance. Figure 76 shows a magnified view of the latter, located in an area relatively far from both the nanoindentation and the grain boundary (labeled Area A, as marked in Figure 75b). DF image in Figure 76b was obtained with the  $\epsilon$ -martensitic reflection in Figure 77d, revealing that those thin bands contain  $\epsilon$ -martensite.

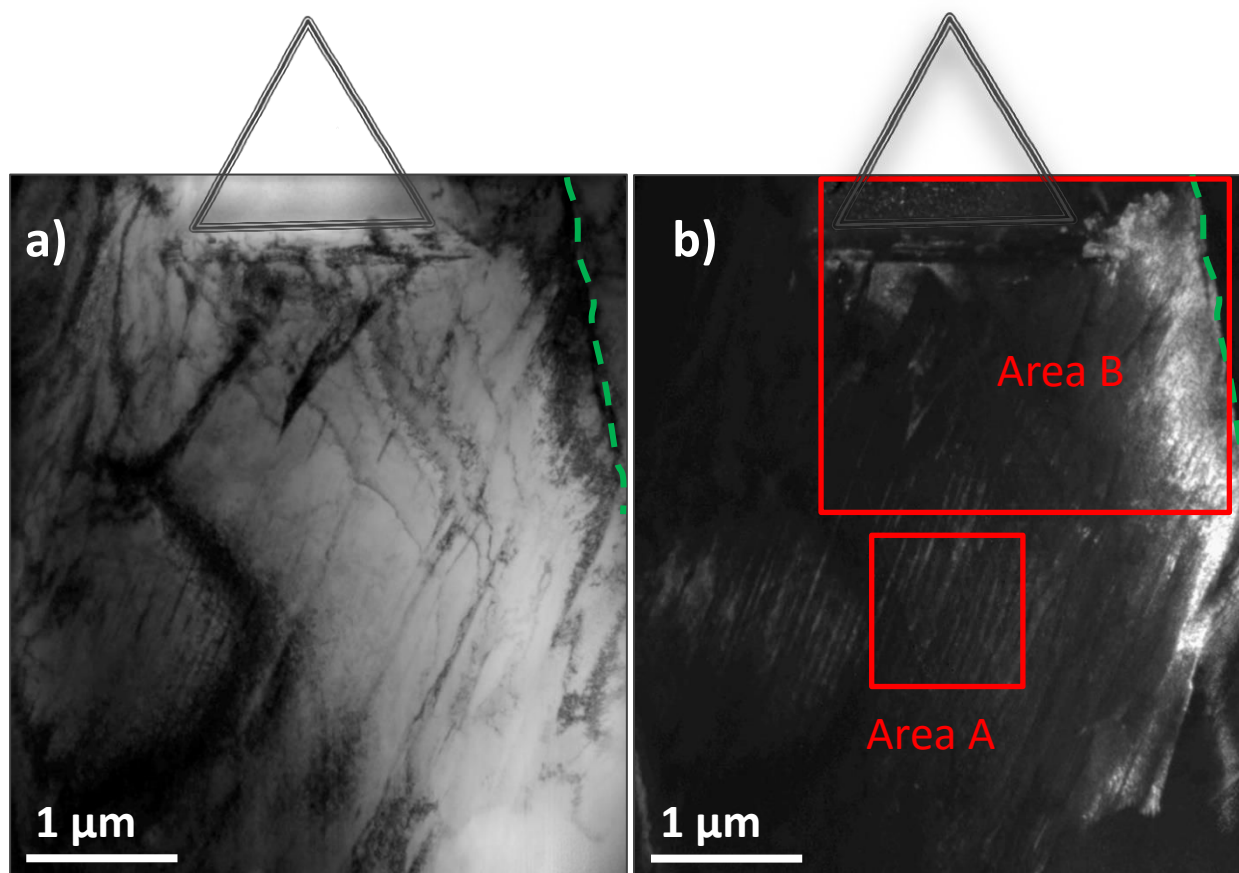


Figure 75. a) TEM BF and b) DF images of the lamella extracted from the area marked by the rectangle frame in Figure 74 a and b. The position of the nanoindenter is outlined by triangles, while the grain boundary is traced with dashed lines.

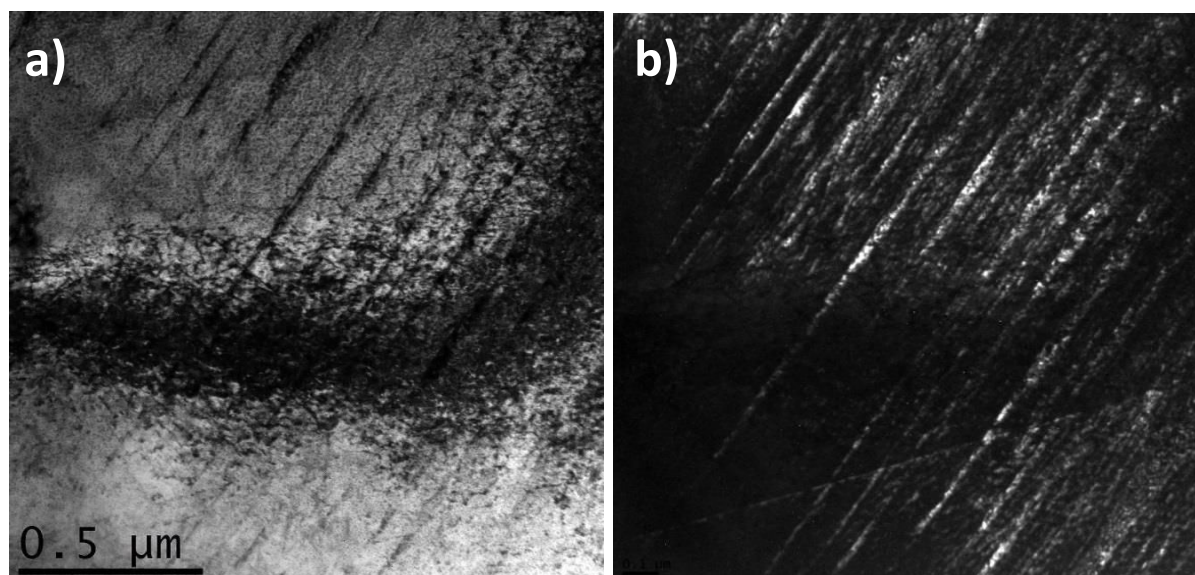
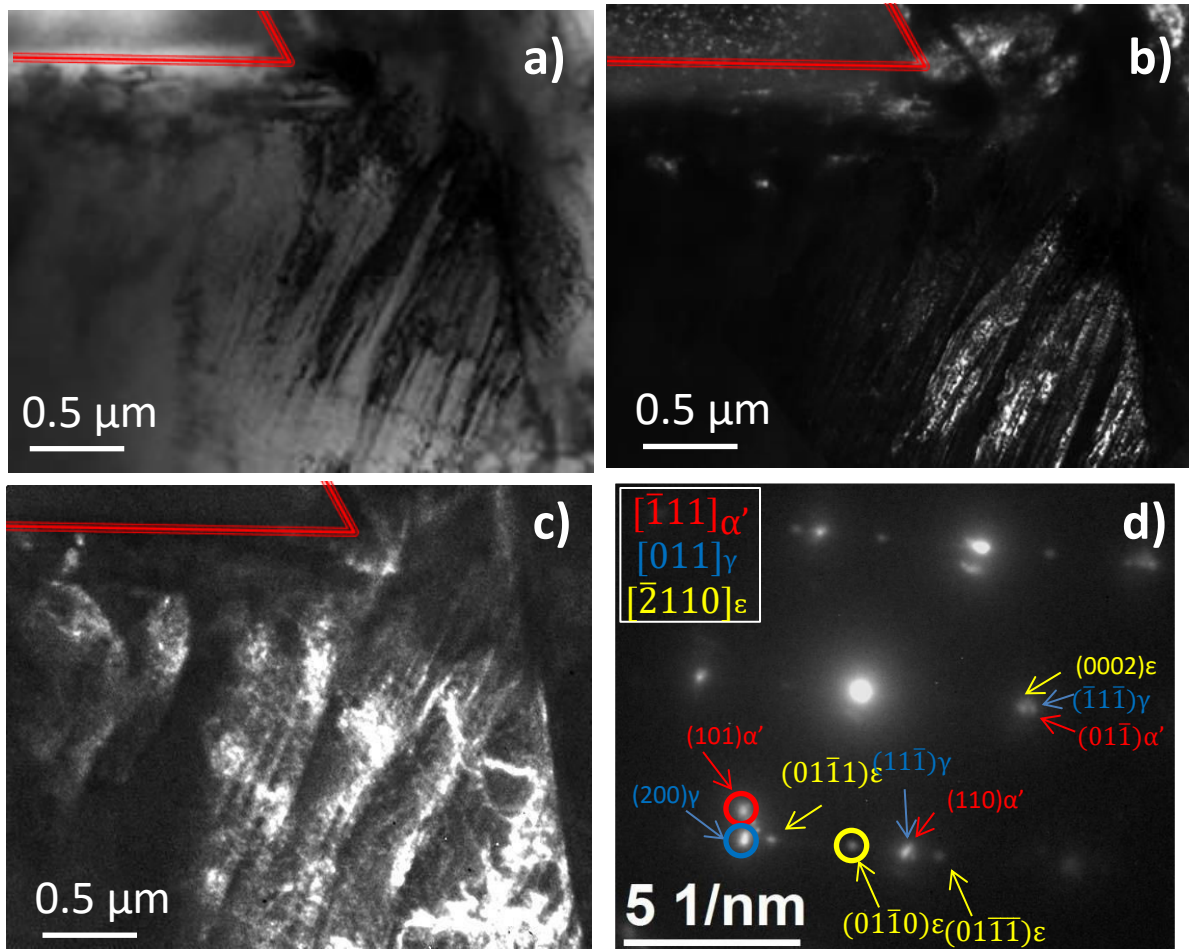


Figure 76. a) BF and b) DF images of the deformation bands from Area A In Figure 75 .

Figure 77a and b represent a magnified view of Area B from Figure 76. Several irregularly shaped, thick shear bands adjacent to the grain boundary can be seen. TEM diffraction indicates that these bands are of the same nature as the ones observed in Figure 76, but due to the higher stress field near the grain boundary their extension is more advanced. Their position and distribution correspond to the traces of the slip system II, observed in Figure 74b. Thus, it can be concluded that the traces observed by FESEM are rather shear band traces, than dislocation slip traces. Along these shear bands, also  $\alpha'$ -martensitic clusters were detected (Figure 77c). Their nature will be discussed in more detail in subsection 5.2.5.



**Figure 77.** Magnified view of Area B in Figure 5. a) BF and b) austenite DF images, revealing thick shear bands emerging at the grain boundary; c) corresponding  $\alpha'$ -martensite DF; d) associated diffraction pattern. The DF images in Figure 75b, Figure 76b and Figure 77c are obtained with the encircled reflections of the respective phases. The boundary of the residual imprint is outlined in a)-c).

$\epsilon$ -martensite was not observed by EBSD because platelets need to reach a certain minimum width to be detectable with this technique<sup>76</sup>. This would also explain the presence on non-indexable bands in the SP material (Section 3.2), which from their shape reassemble shear bands. Therefore, TEM investigation is required to characterize  $\epsilon$ -martensite platelets. Moreover, due to their very fine size, high resolution TEM (HRTEM) has been employed in the present work.



$\epsilon$ -martensite platelets at larger distances from the residual imprint (Figure 75 and Figure 76) were straight and parallel, as is commonly observed in literature <sup>68,80,81</sup>, while the bundles parallel to the edge of the residual imprint are obviously curved. Material pile-up, as well as lattice rotations, as found in section 0, likely lead to these distortions.

#### 5.2.4 Fine structure characterization

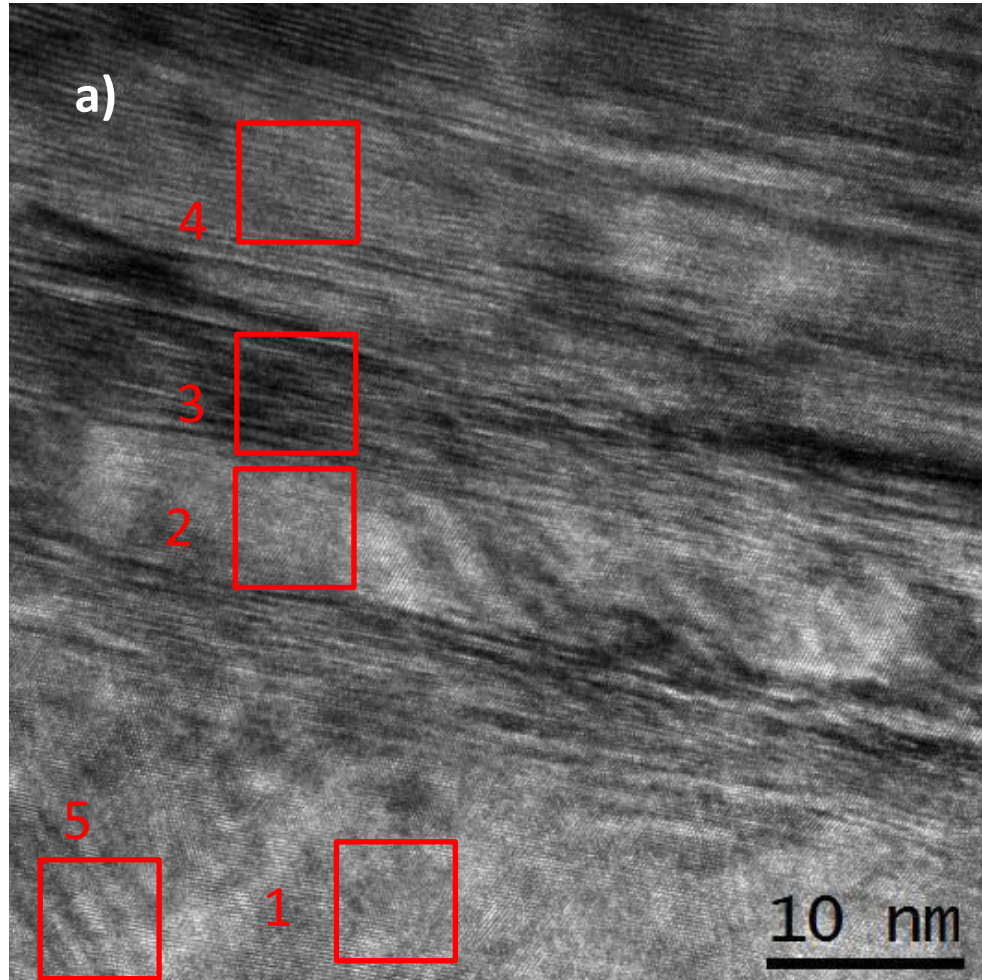
It is commonly found that stress-induced  $\epsilon$ -martensite presents a lamellar substructure, consisting of  $\epsilon$  and  $\gamma$  alternating bands <sup>289</sup>, where  $\epsilon$ -bands get wider when increasing strain. Figure 78a shows HRTEM images of the fine bands structure marked with a rectangle in Figure 79c and Figure 79d, whereas Figure 78b corresponds to the austenite matrix, surrounding  $\epsilon$ -martensite with a largely regular lattice. On the contrary, the band in Figure 78c gives a streaky diffraction pattern, due to its thinness and also to the presence of irregular stacking sequences.

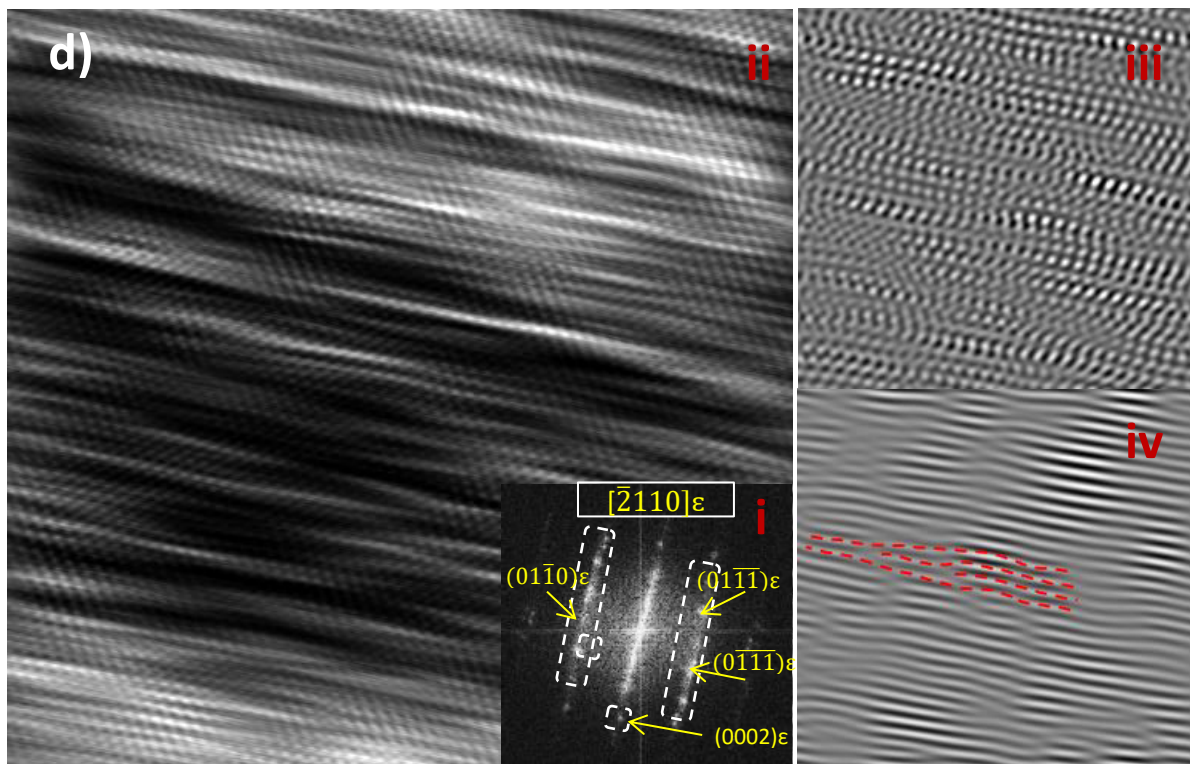
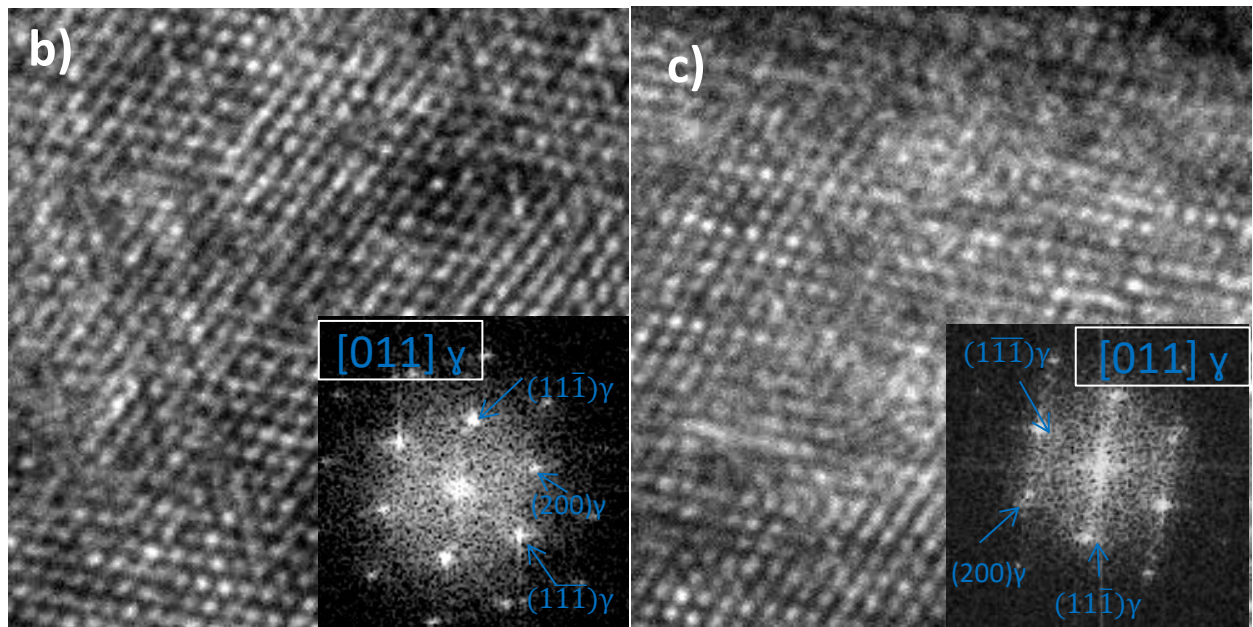
With the inserted corresponding FFT, Figure 78d and Figure 78e, present the structure of two adjacent  $\epsilon$ -platelets, respectively. Thereby, the first one (Figure 78d) is thinner than the second one (Figure 78e). Both of them adopt Shoji-Nishiyama OR with the surrounding austenite. Thin platelets are fairly irregular, as can be concluded from their streaky appearance and from the numerous stacking faults and dislocations visible in the corresponding inset-image.

Digital Micrograph® filtering masks, as outlined in the Figure 78di, were applied to remove low and high frequency noises and to highlight the symmetry of the lattices (Figure 78diii). The forbidden (0001) $\epsilon$  reflections were also excluded from the filtering masks, since they lead to a decreased contrast on every second plane. A filtered image obtained only with one set of planes, *i.e.* (0002) $\epsilon$ , shows the additional inserted planes (traced with red lines), corresponding to the presence of dislocations (Figure 78diiv). This deformed internal substructure supports the assumption of  $\epsilon$ -platelets evolving from austenitic deformation bands. Indeed,  $\gamma$  is widely known to transform to  $\epsilon$  by formation of intrinsic stacking faults (ISFs) on every second plane <sup>68,290,291</sup>. Thus, a deformed substructure, with a higher density of preexisting ISFs, is more likely to undergo this  $\gamma \Rightarrow \epsilon$  transformation. However, the thicker  $\epsilon$ -platelet exhibits a more regular lattice and a clearer diffraction pattern. Mechanically induced  $\epsilon$ -bands are known to nucleate and grow simultaneously from different sites in the austenitic matrix <sup>289,290</sup>. Apparently, this phase gains on stability during the growing <sup>203</sup>.

Finally, Figure 78f exhibits another set of very thin periodic structures, which resemble nanoscopic austenitic twins. Indeed, the atomic lattices reveal unambiguously the presence of approximately 1 nm thick austenitic twinned bands. Therefore, it can be concluded that the shear bands observed in this work

are of mixed nature, a stacking sequence of fine austenitic bands, austenitic nano-twins and  $\epsilon$ -martensite platelets. The presence of austenitic bands interlaced with  $\epsilon$ -phase explains why shear bands can be illuminated in the DF image with both  $\gamma$  and  $\epsilon$ -martensite diffraction reflections. As previously mentioned, due to the low SFE of the present alloy, twinning is less favorable than  $\epsilon$ -band formation, hence the observed twinned sequences are restricted to only a few atomic layers.







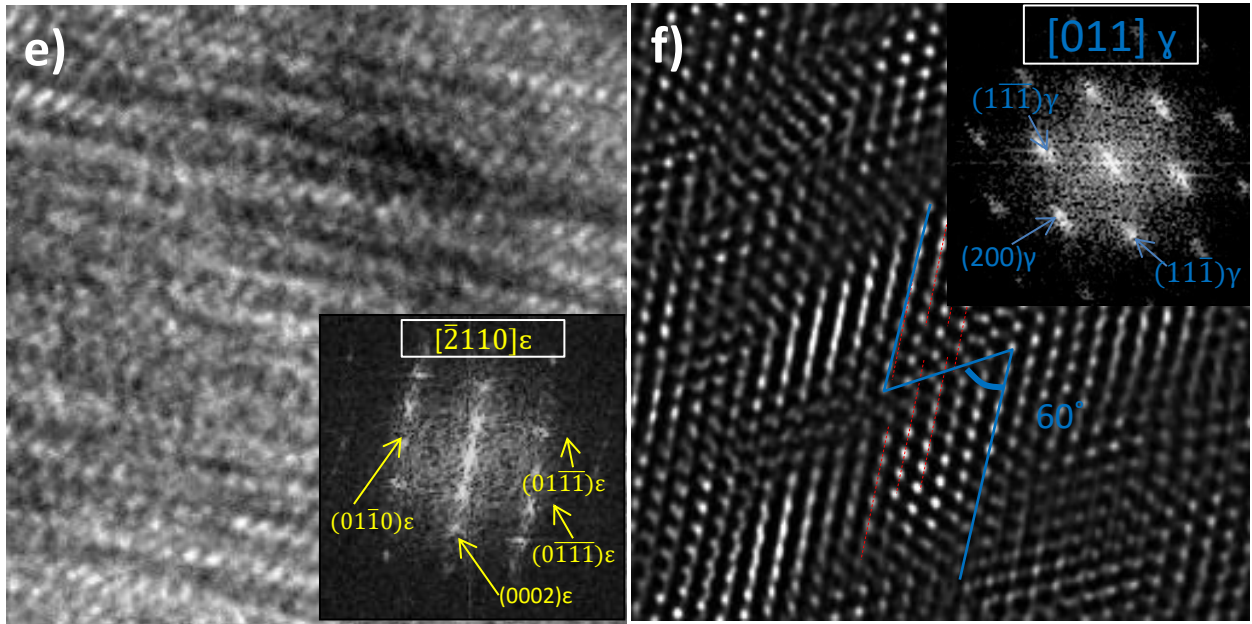


Figure 78. HRTEM analysis of the bands composition a) observed area contains five different structures marked by rectangles b) Zone 1 – wide austenitic area c) Zone 2 – defected narrow austenitic band d) Zone 3 – thin  $\epsilon$ -martensite platelet e) Zone 4 – wider  $\epsilon$ -martensite platelet f) austenitic nano-twins.

### 5.2.5 $\alpha'$ -martensite formation

Continuing with the analysis of the surface region beside the residual imprint edge shown in Figure 80a, two different areas can be distinguished, marked as regions A and B. At the right side of the nanoindent, adjacent to the grain boundary (Region B), the presence of granular particles can be observed at the shear band intersections. Indexation of electron diffraction pattern in Figure 77d indicates that they are of  $\alpha'$ -martensitic nature (Figure 80b). A comparison with a FESEM image (taken from the surface before the lift-out of the TEM lamella) shows that their position, size and distribution coincide with the particles previously observed at the intersection of shear band traces.

The second structure can be observed in the central region, below the residual imprint (Region A). Here, polygonal martensitic patches are present (Figure 80c). They seem to have coalesced from single nuclei, due to the high density of those in the central region. Those patches are separated by heavily deformed shear bands belonging to the slip system II (Figure 78d). It is worth mentioning that the martensitic transformation was *spatially* asymmetric: no martensitic nuclei were observed at the left side of the residual imprint, which is on the far side from the grain boundary.

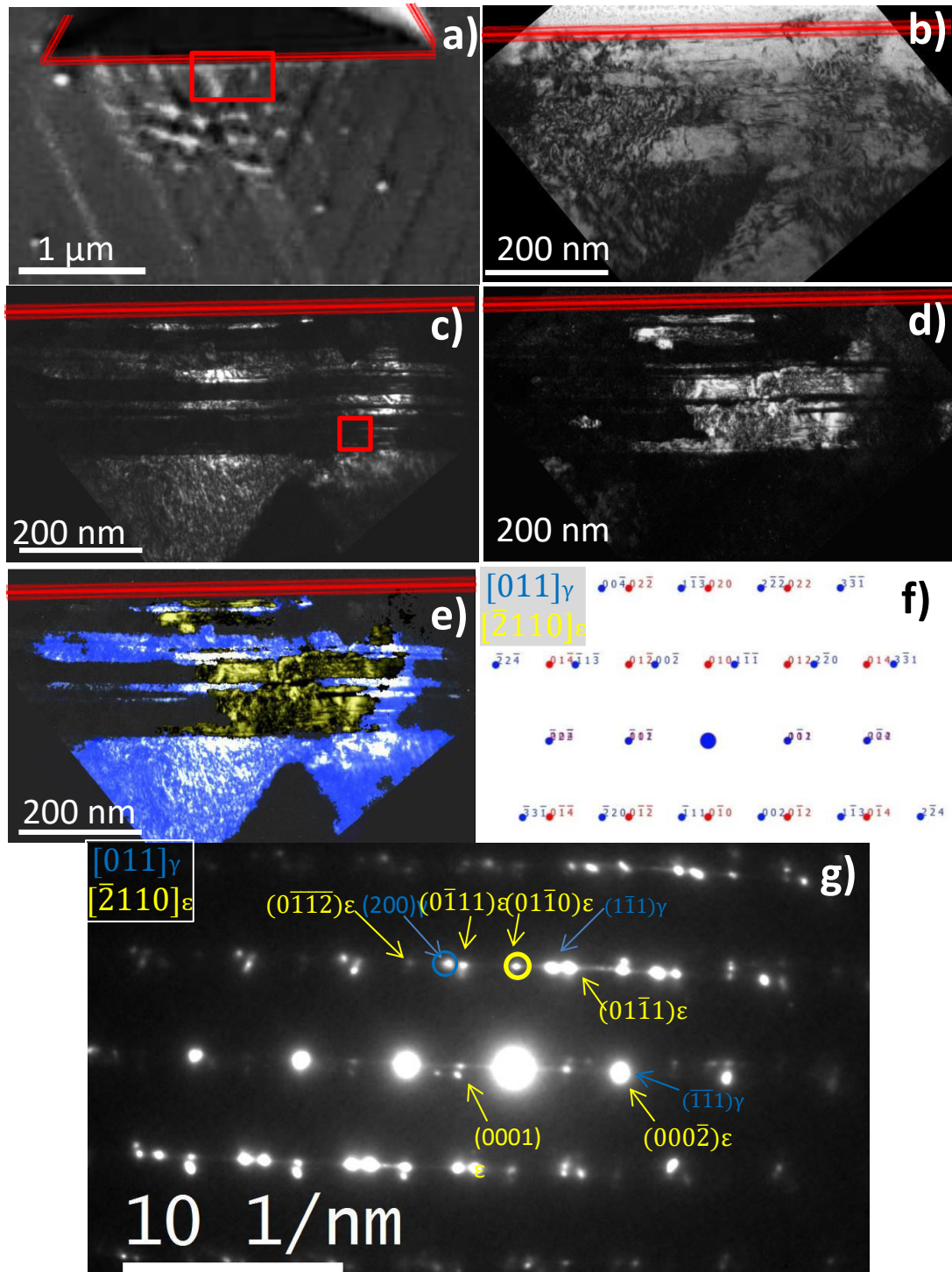


Figure 79. Deformation band at the edge of the residual imprint. The edge of the nanoindent is marked by a triple line. a) Magnified SEM image of the lower edge of the residual imprint, b) BF image of the area within the red frame drawn in a); c) DF image obtained with the  $(020)\gamma$  reflection; d) DF image obtained with the  $(01\bar{1}0)\epsilon$  reflection; e) composed image where both phases become visible; f) Simulated composite diffraction pattern with  $(111)_\gamma \parallel (0002)_\epsilon$ ; g) Observed composite diffraction where forbidden  $(0001)_\epsilon$  reflection is present due to multiple diffraction.

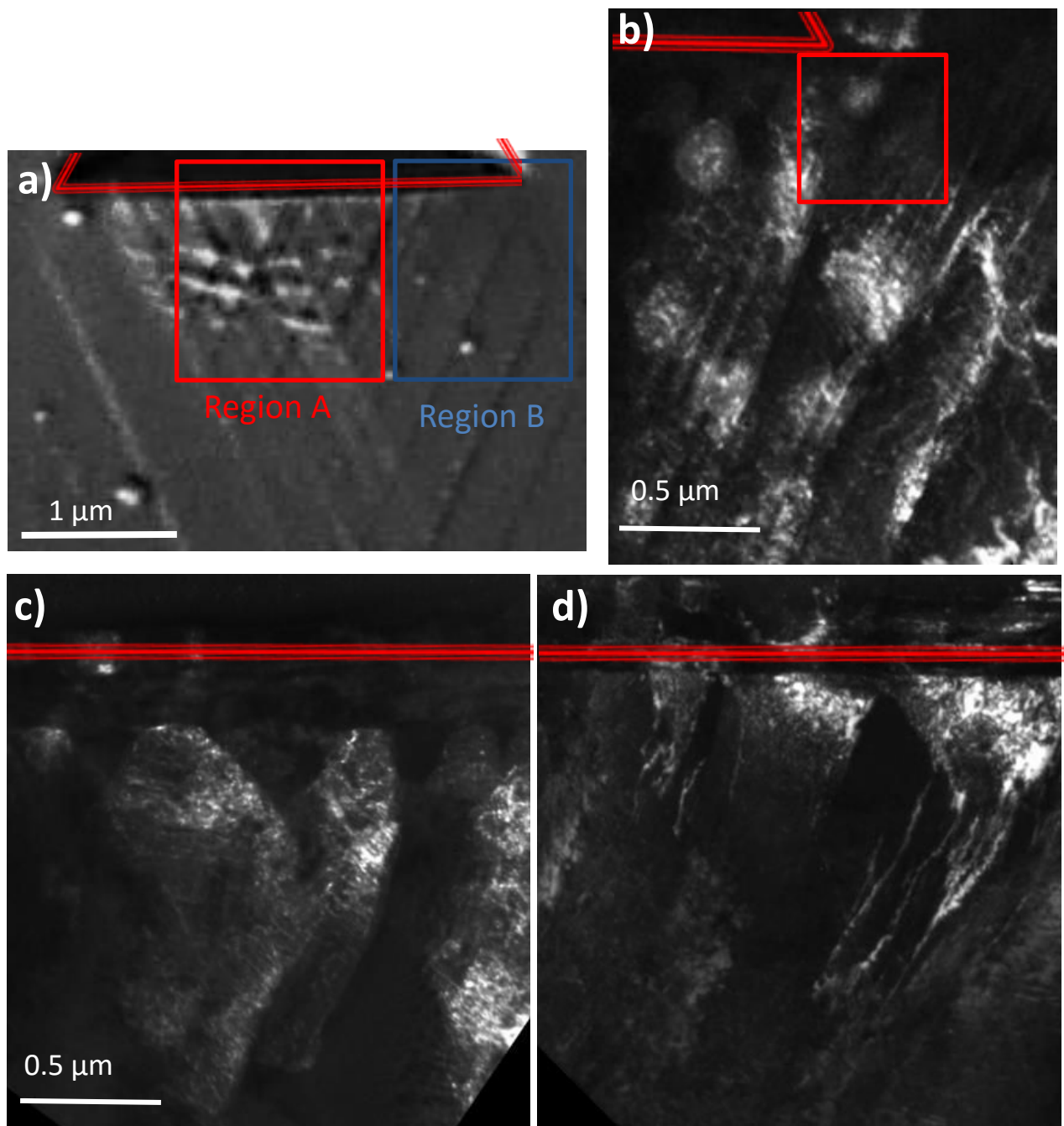


Figure 80. a) Magnified view of the region of interest. a) SEM image including Region A at the center and B at the edge of the nanoindent; b) TEM DF image of Region B obtained with the  $(01\bar{1})\alpha'$  diffraction reflection (the rectangle marks the area which will be observed more in detail in Figure 81); c) DF image of region A obtained with the  $(01\bar{1})\alpha'$  diffraction reflection; d) DF image of region A obtained with the  $(020)\gamma$  reflection. The course of the residual imprint is traced by a triple line.



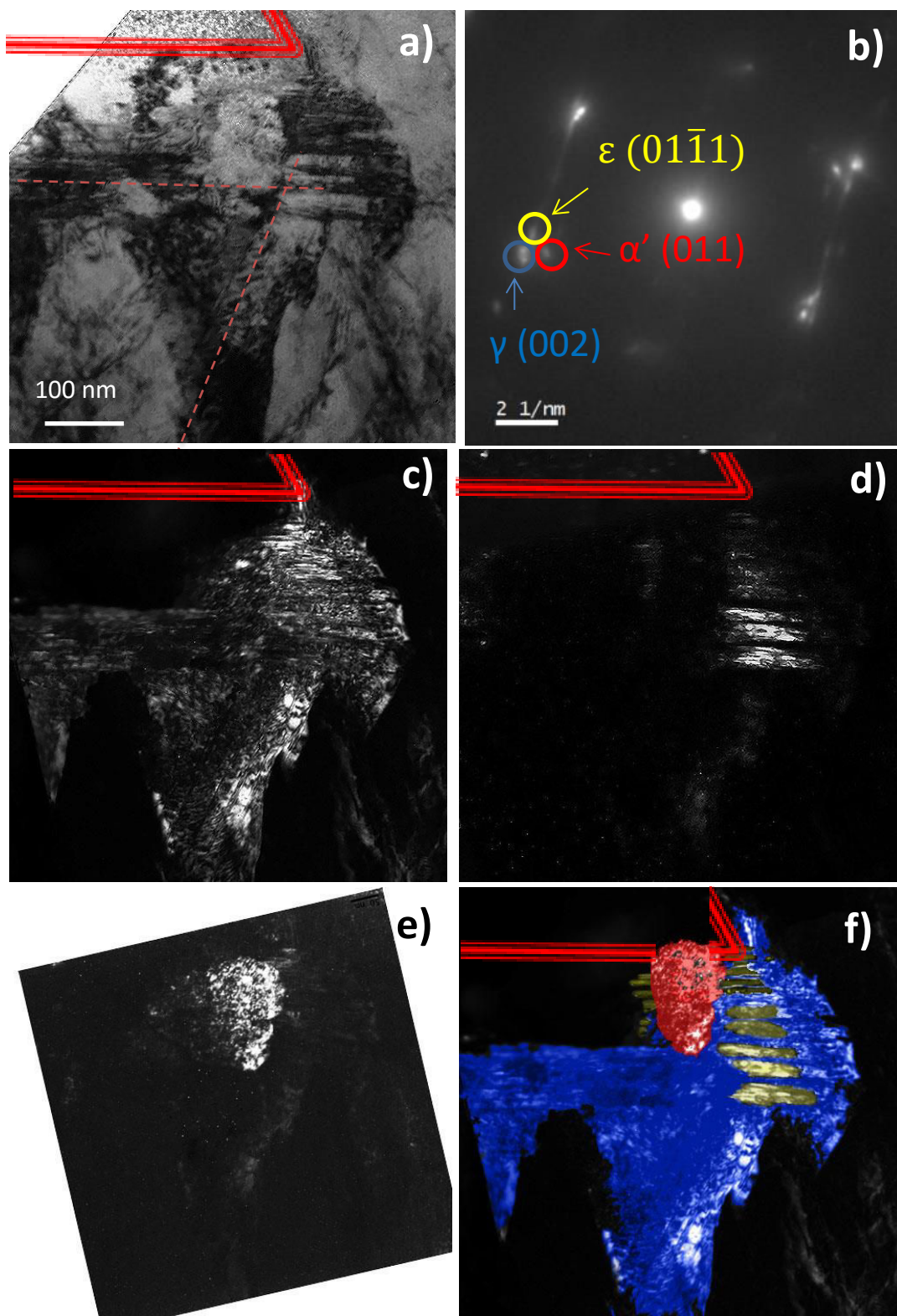


Figure 81. a) magnified TEM BF image of an  $\alpha'$ -martensite nucleus at a shear band intersection. The slip planes corresponding to the observed shear bands are marked by dashed lines; b) corresponding diffraction pattern; c) DF image obtained with  $\gamma$ , d) with  $\epsilon$  and e) with  $\alpha'$ -reflections, respectively; f) superposed DF image. The nanoindent edge is traced by a triple line.

One of the smallest martensitic nuclei, located at the corner of the residual imprint (marked zone in Figure 80b), was observed more in detail. Figure 81 reveals the intersection of two microscopic shear bands, where the one parallel to the indent edge consists of interlaced  $\gamma$  and  $\varepsilon$  bands, while the band emerging from the edge of the nanoindent (slip system 2) is less regularly shaped and contains a high density of tangled dislocations. Due to the localized stress state, those bands are particularly wide and deformed in the immediate surroundings of the residual imprint, thinning down with increasing distance from the latter. Thin bands parallel to the inserted reference lines are discernible. An  $\alpha'$ -martensitic feature, around 180 nm long and 100 nm wide, is present at the intersection of the shear bands. Thereby, the  $\alpha'$  and the austenite phase surrounding it, extend slightly over the edge of the residual imprint. This circumstance is likely to be induced by the volume expansion involved in  $\gamma \rightarrow \alpha'$  transformation<sup>47,48</sup>. The hydrostatic pressure in the bulk material hinders this expansion<sup>292</sup>. Shear activated during nanoindentation might promote martensitic transformation<sup>30,172</sup>, however the additional compressive stress further restricts the volume expansion<sup>293</sup>. Therefore, martensitic transformation, in the bulk, goes along with deformation and distortion<sup>218</sup>. On the contrary, near the surface the material is less constrained<sup>218,294</sup>, as observed in the present study. These results are in agreement with that of Wu *et al.*<sup>295</sup>, who found martensite forming in austenitic micropillars is virtually dislocation free, due to the absence of constraint, while in the bulk counterpart the dislocation density of martensite is high<sup>100,114,218,296</sup>. The fact that the  $\alpha'$ -particle extends over the edge of the residual imprint implies that it apparently formed during or after the retraction of the indenter tip, promoted by the corresponding stress relaxation.

The nucleation of  $\alpha'$ -embryos at shear band intersections and its growth by coalescence with other nuclei are in good agreement with the widely known deformation mechanisms in metastable austenitic stainless steels under macroscopic deformation<sup>98,113,218</sup>, and also coincide with the observations for skin-passed condition in Section 3.2. On the other hand, a certain minimum strain accumulation is required for martensite nucleation<sup>144,205,297</sup>. So, monotonic nanoindentation tests on AISI 301 with an applied load of 1 mN did not result in martensite formation on the sample surface<sup>298</sup>.

### 5.2.6 Correlation between applied characterization techniques

Comparing the results obtained by EBSD considering the crystallographic orientation and location of grain boundaries, with those from FESEM regarding surface topography and also TEM observations regarding phase composition, the following points can be conjectured:

1. The surface traces observed by FESEM could be assigned to shear bands corresponding to the respective active slip systems, while the spherical particles, at slip traces intersections, correspond actually to  $\alpha'$ -martensite nuclei.
2.  $\alpha'$ -martensite nuclei preferentially form in  $\langle 111 \rangle$  oriented grains. This can be explained by the geometry of the shear band traces. As observed in Figure 73, for  $\langle 001 \rangle$  grains traces are parallel to the edges of the residual imprint, which results in different slip systems activated to each edge. Then, the respective deformation bands intersect far away from the nanoindent. For  $\langle 111 \rangle$  grains, three different slip directions are activated, forming a triangle. As a consequence, shear band traces intersect centrally at the indent edge, where the stress field, as well as the density of shear bands, is the highest. Consequently, martensitic nucleation is easily induced under these conditions.
3. For the applied load range, martensite embryos appear only after cyclic nanoindentation, but not for single indentation. This is in agreement with the knowledge of macroscopically deformed materials requiring a strain accumulation to create the necessary defect structure for the incubation of  $\alpha'$ -martensite.
4. Martensite nuclei, as here observed, have a rather spherical shape; while martensitic embryos formed in the bulk use to be polyhedral type <sup>98</sup>. It is reasonable to assume that at the free surface, where the phase transformation is not spatially confined, a semi-spherical shape might result energetically more favorable, given the lowest interface surface energy for the spherical shape.

### 5.3 Conclusions

Mechanical testing by nanoindentation has not only the advantage of providing a high-precision small scale technique, which can be employed selectively, it also creates regions of higher and lower strain, due to the radially decreasing stress field. This in turn allows to draw conclusions about the evolution of deformation.

Therefore, the performed surface characterization after cyclic nanoindentation testing revealed that planar defects, such as austenitic nano-twins, SFs and  $\epsilon$ -martensite platelets, form collectively microscopic shear bands in the surroundings of the residual imprint. On the other hand, twins in this low SFE alloy are apparently not stable enough to grow to important sizes.  $\epsilon$ -martensitic platelets were found interlaced with austenitic bands forming fine composite bands.  $\alpha'$ -martensite formation was observed in fine details at shear band intersections, where embryos gradually coalesce, thus growing to bigger particles.

The selective placement of nanoindentations, *i.e.* in grains with different crystallographic orientation, allow to draw conclusions about crystallographic anisotropy of  $\alpha'$ -martensite nucleation. Furthermore, the

influence of grain boundaries became obvious by the asymmetric deformation pattern. So, the highest density and thickness of the shear bands is located in the vicinity of the grain boundaries and also the presence of dislocations was mainly confined to pile-ups at the grain boundaries.

The free surface allows the volume expansion accompanying the phase transformation, thus no strong deformation or distortion was present in the  $\alpha'$ -martensite phase and its surroundings. Consequently, fine details, such as  $\epsilon$ -martensite platelets and incipient  $\alpha'$ -martensite nuclei, could be clearly distinguished. Thus, the surface provides a convenient observation site for tracking deformation dynamics, particularly in combination with cyclic nanoindentation, a suitable tool for inducing deformation progressively.

## 6 Characterization of subsurface deformation

### 6.1 Motivation

After studying the deformation mechanisms on the surface surrounding the residual imprint, the consistent progression is examining their counterpart within the volume affected by the nanoindentation. As it was outlined in section 1.3.1, one of the most convenient techniques for subsurface characterization of metallic alloys is TEM. For this purpose, cross section lamellae were extracted parallel to the loading axis and cutting through the central point of the residual imprint. To make the results comparable regarding the geometrical orientation of the slip planes with respect to the viewing plane, the cut was performed in such a way that the cross section area was perpendicular to  $[0\bar{1}1]$  direction.

Thereby, the following aspects were accessed:

- 1) **Deformation mechanisms induced by monotonic nanoindentation:** to reduce the number of involved parameters, initially only grains with the same crystallographic orientation were investigated, namely those oriented with their  $\langle 111 \rangle$  axis perpendicular to the sample surface, and thus parallel to the indentation axis. Nanoindentations were performed in selected, not confined locations, *i.e.* with the distance to the closest grain boundary significantly larger than the dimension of the plastic strain field induced by the nanoindentation.
- 2) **Cyclic evolution of deformation:** cyclic nanoindentation was performed under the same conditions as above, in order to study the influence of repeated loading on the deformation substructure.
- 3) **Effect of testing mode:** as became clear in Chapter 4, testing in loading and displacement modes generates different material responses. Thus, in the next step of the present study, TEM lamellae originating from cyclic nanoindentation testing, in both in constant displacement and constant loading modes were compared, in order to establish the connection to conventional cyclic deformation testing.
- 4) **Influence of the deformation constraints:** this is accessed as a function of the proximity to grain boundaries. Therefore, reference to large (annealed CS), flat (annealed CS) and small grains (annealed SG) has been made. The plastic zone radius  $R_p$  corresponding to a nanoimprint is assumed to be less than twelvefold of  $h_{\max}^{299-301}$ , so in the present case  $R_p$  would be lower than 3  $\mu\text{m}$ . Accordingly, the term “large grain” refers to grains where the nanoindentation could be placed at more than 2  $R_p$  from the closest grain boundary. “Flat



grain” comprehends grains where only the lateral distances to the closest grain boundary are above  $2 R_p$ , while the grain is vertically confined. And finally, in “small grains” all distances from the indentation location to grain boundaries are below  $2 R_p$ . Furthermore, transmission of plasticity as observed in confined grains, will be discussed.

- 5) **Crystalline anisotropy:** In Chapter 4, it was confirmed that the studied material exhibits an important crystalline anisotropy. The influence of this factor is further studied in the present chapter by comparing deformation substructures in  $\langle 111 \rangle$  and  $\langle 001 \rangle$  oriented small grains.
- 6) **Effect of prestrain:** work hardening influence was analyzed by indenting  $\langle 111 \rangle$ -oriented grains from skin-passed samples and comparing the resulting deformation substructures to the counterpart from annealed condition.
- 7) **Plasticity transmission through grain boundaries:** pop-ins observed in Chapter 4 were attributed to plasticity transmission through grain boundaries. Now, the corresponding deformation substructure has been evaluated, in order to verify this assumption.

## 6.2 Results and discussion

### 6.2.1 Monotonic nanoindentation

Figure 82 shows TEM images of the cross section of the indented area after a monotonic nanoindentation test in a large austenitic  $\langle 111 \rangle$  grain. A residual imprint can be observed (Figure 82a), surrounded by an area with a moderate dislocation density and bending contours. However, at higher magnification and appropriate diffraction contrast, a martensitic grain with a size of around  $0.02 \mu\text{m}^2$  was found directly under the residual imprint, as illustrated in Bright Field (BF) and Dark Field (DF) images corresponding to Figure 82b and c, respectively. Otherwise, no evidence of deformation could be discerned and the rest of the grain remained fully austenitic.

High plastic deformation is known to develop directly under the indenter tip<sup>276,301–303</sup>. Following Gan<sup>304</sup>, the plastic zone directly ahead of the indenter tip will be called Indenter Penetration Zone (IPZ).

Kysar *et al.*<sup>305</sup> performed an extensive study of the density and distribution of dislocations induced by nanoindentation and found that the highest slip activity takes place directly at the IPZ and perpendicular to the flanks of the imprint. These results were also confirmed by simulation studies<sup>306</sup>.

Rester *et al.*<sup>29</sup> investigated the cross sections of nanoindentations in Cu by EBSD and TEM. They concluded that the local misorientation surrounding the residual imprint can lead to the formation of a

nanograin at the IPZ. Considering the lattice rotation observed in Figure 72b, it is reasonable to assume that, in the present case, the high deformation in the IPZ represents a favorable site for martensitic transformation. The shape and growth direction of the martensitic grain resembles the subgrain from Rester's study<sup>29</sup>.

Formation of austenitic subgrains resulting from nanoindentation has also been reported for different fcc metals<sup>27,304,307,308</sup>. However, here the subgrain is clearly martensitic, as confirmed by indexing the corresponding TEM diffraction pattern. This martensitic transformation induced by nanoindentation has been observed in different austenite containing steels<sup>28,30,101,309</sup>.

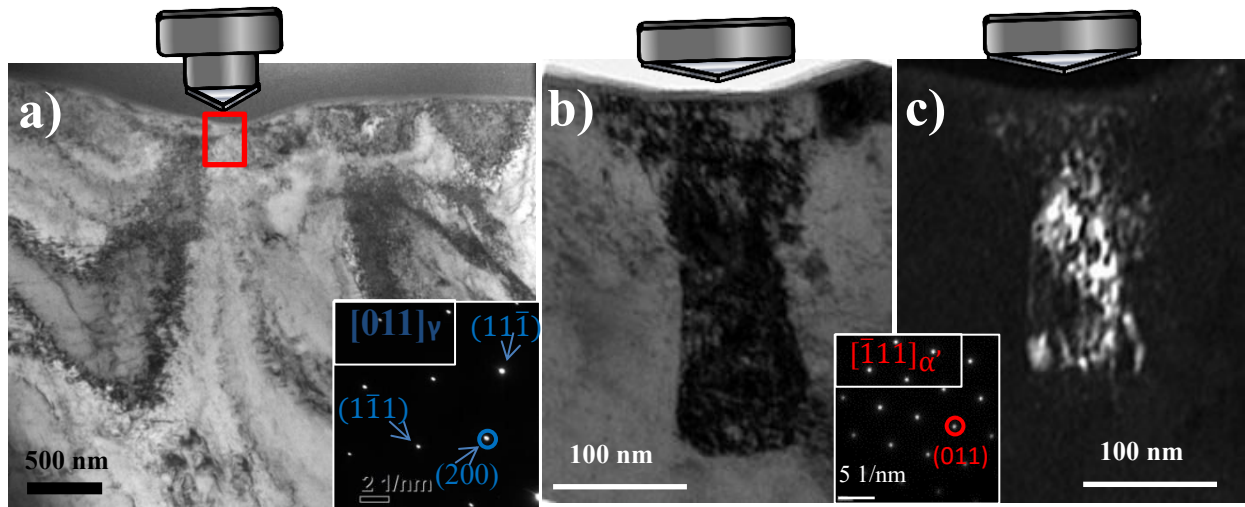


**Figure 82.** Residual imprint after monotonic nanoindentation testing in large  $\langle 111 \rangle$  oriented grain of 250 nm maximal displacement into the surface. a) TEM BF general image; b) and c) TEM BF and DF images of martensitic particle emerged under the imprint, respectively. Corresponding diffraction patterns are given in the insets of a) and b/c).

## 6.2.2 Deformation in weakly confined grains

Figure 83 illustrates the substructure resulting from a 50 cycles indentation test in a large  $\langle 111 \rangle$  grain. A martensitic feature surrounds the residual imprint (Figure 83b), similar to the case of monotonic nanoindentation. However, the total size of this martensitic area is around  $0.05 \mu\text{m}^2$ , which is larger than in case of single nanoindentation. Moreover, the formation of an extended shear band underneath is clearly discernible in DF condition (Figure 83c). Indeed, the martensitic particle seems to constitute the upper part of this shear band. Shear bands formation, emerging from residual nanoimprints, was also observed by Lloyd *et al.*<sup>27</sup>. On the other hand, Gan<sup>304</sup> found that wedge indentation in Cu crystals resulted in subgrain formation in the IPZ, while thereunder formation of slip bands occurred. This is in good agreement with the present observations.

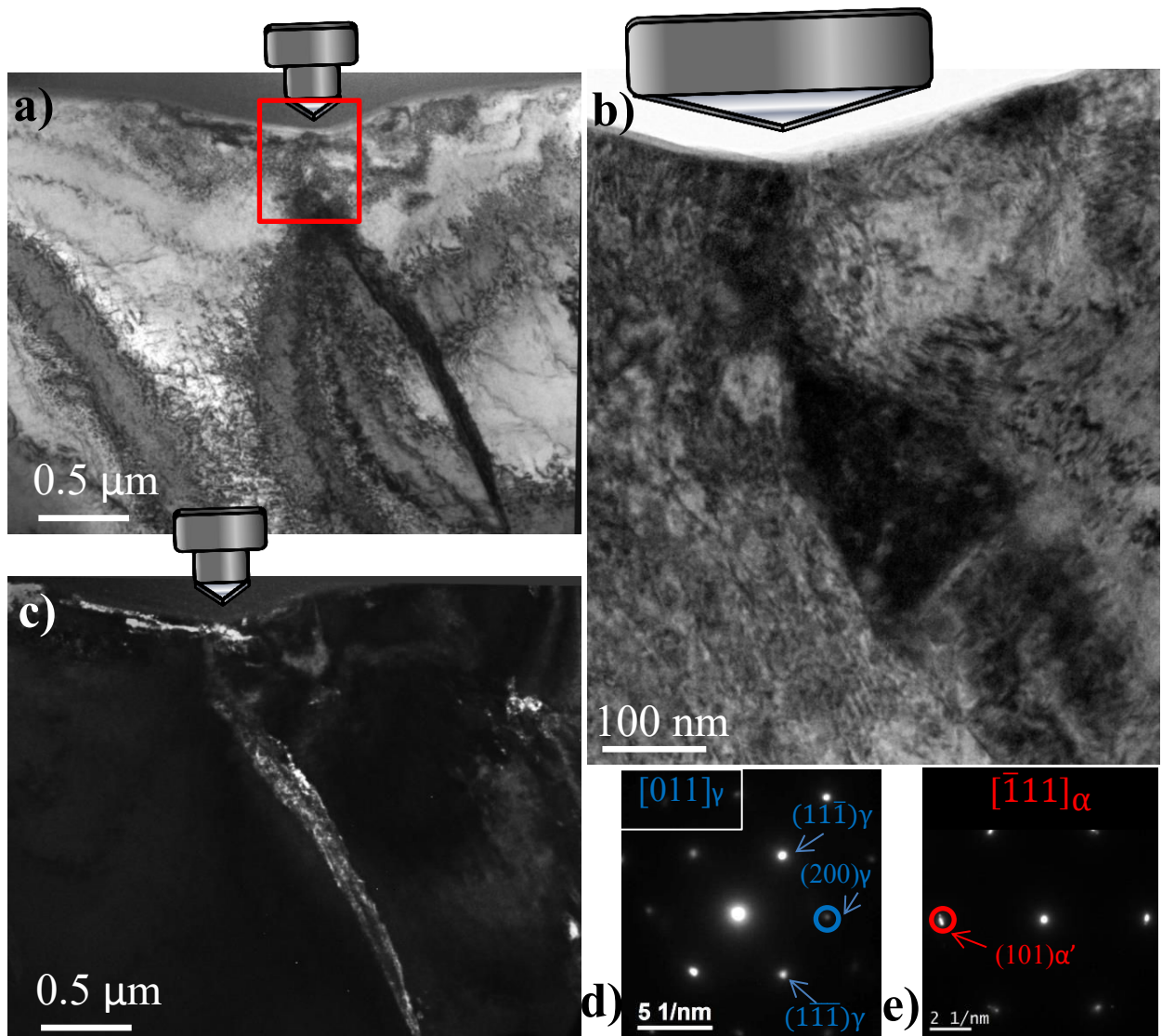
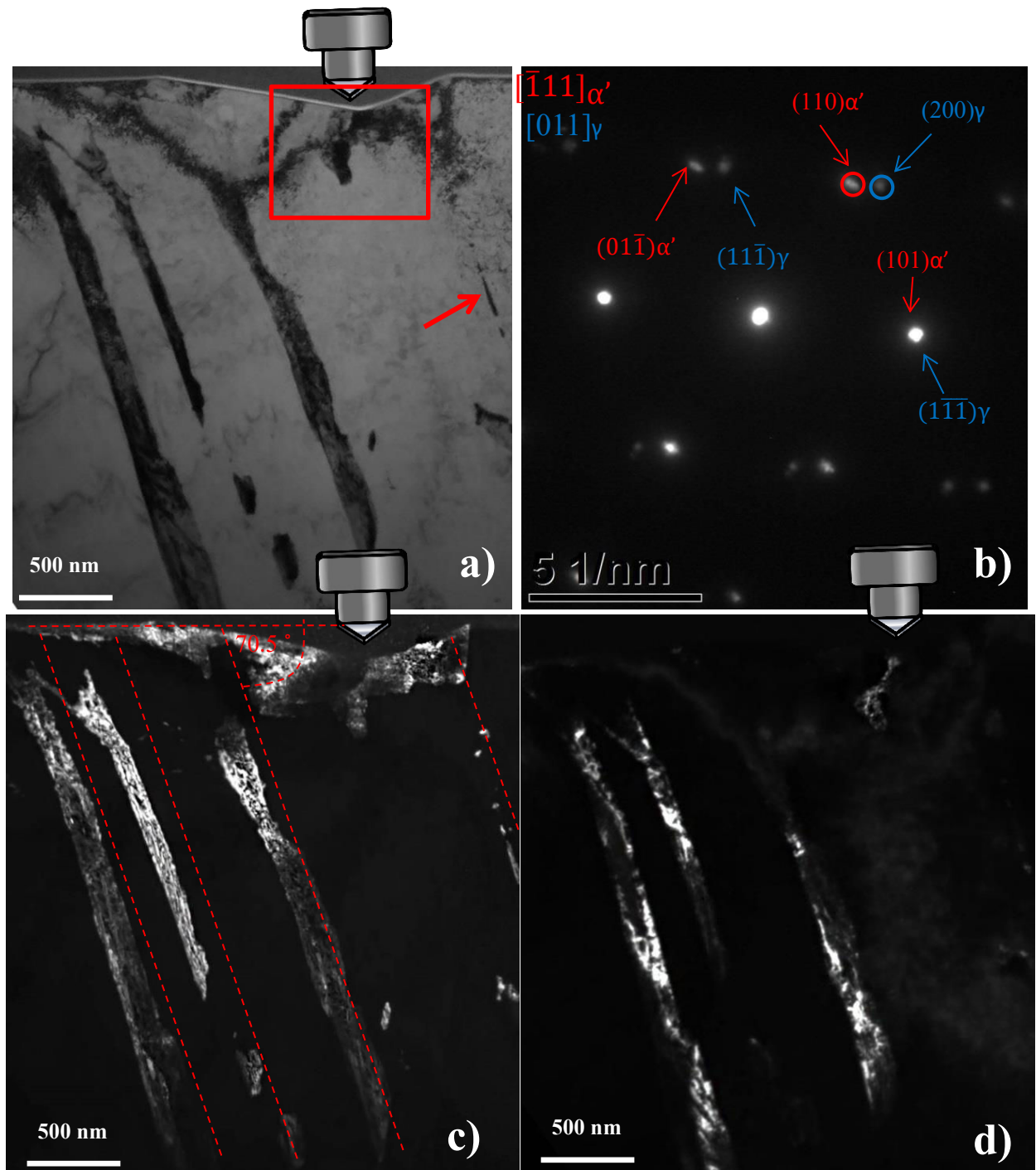


Figure 83. TEM imaging of the substructure surrounding the nanoindentation after cyclic nanoindentation in displacement mode. a) General overview; b) Enlarged view of the framed area in a) visualizing the darker martensite phase; c) DF image of a) illuminating a shear band; d) Diffraction pattern corresponding to c); e) Diffraction pattern corresponding to b).

#### Comparison of substructural arrangements resulting from testing in loading or in displacement mode:

As mentioned in Chapter 4, in conventional fatigue testing different results can be obtained whether tests are conducted under stress or under strain control. For that reason, in an analogous manner, cyclic nanoindentation tests have been carried out both, in constant loading and also in constant penetration mode. Subsequently, the resulting substructural features have been compared.



**Figure 84.** Cross section of residual imprint after 50 cycles of nanoindentation in constant load mode. a) TEM BF image; b) Diffraction pattern from the surrounding of a shear band; c) Corresponding DF image illuminating shear bands; d) DF image of  $\alpha'$ -martensite laths forming inside of shear bands.

Figure 84 represents TEM images of a  $\langle 111 \rangle$  grain indented in loading mode. Three thick shear bands formed under the obtuse flank of the indenter, as well as a thin one under the acute flank (marked by an arrow), can be discerned in Figure 84a and c, opposed to a single band observed for testing in

displacement mode. This lets conclude that, on one hand, cumulative deformation in loading mode is significantly higher than in displacement mode and, on the other hand, this deformation is asymmetrically distributed. The former is reasonable for cyclic softening materials, where the strain increases with the number of cycles when testing at constant load. Noticeably, it is in good agreement with the cyclic evolution of P-h curves, as observed in Chapter 4. The latter can be explained by the asymmetry of the left and right flank of the Berkovich indenter producing a different stress state on each side, as discussed by Miura *et al.*<sup>300</sup>.

All shear bands are parallel to each other and form an angle of  $70.5^\circ$  to the surface plane. Given that the surface plane was (111) and the viewing direction  $[0\bar{1}1]$ , it can be concluded that shear bands lie on the  $(11\bar{1})$  slip plane.

Another interesting finding is that the thick shear bands have partially transformed to martensite, as revealed by the diffraction pattern (Figure 84b) and also by the corresponding martensite DF image (Figure 84d).

Martensite is in Kurdjumov-Sachs relationship<sup>92</sup> to the shear bands with:

$$(111)_\gamma \parallel (011)_\alpha \quad \text{and} \quad [01\bar{1}]_\gamma \parallel [11\bar{1}]_\alpha ,$$

indicating that the martensitic phase evolved from austenite.

The faulty stacking sequence in shear bands is apparently favorable for  $\alpha'$ -martensite formation. This is consistent with the results of Talonen and Hänninen, who found that shear bands and martensite formation are linked<sup>8</sup>. As reported by several authors<sup>76,98–100</sup>, blocked-shaped martensite structures form by nucleation and coalescence of  $\alpha'$ -martensite embryos within a single shear band.

The second shear band located at the left side of the residual imprint (Figure 84) is discontinuous, which may be understood assuming that it has a limited thickness perpendicular to the surface and besides it is likely undulated. Thus, when a cross section cut is performed, some bent parts will not lie on the observed area. This circumstance was used to compare two band sections, similar in size, but one being completely austenitic and the other mostly martensitic. Figure 85 opposes the corresponding microstructures.

The non-transformed shear band has a streaky appearance, due to the many thin defect bands it is composed of. On the other site, the martensitic part is highly deformed, featuring a high density of dislocations. This is consistent with the knowledge about strain-induced martensite produced by macroscopic deformation<sup>114,296</sup>.

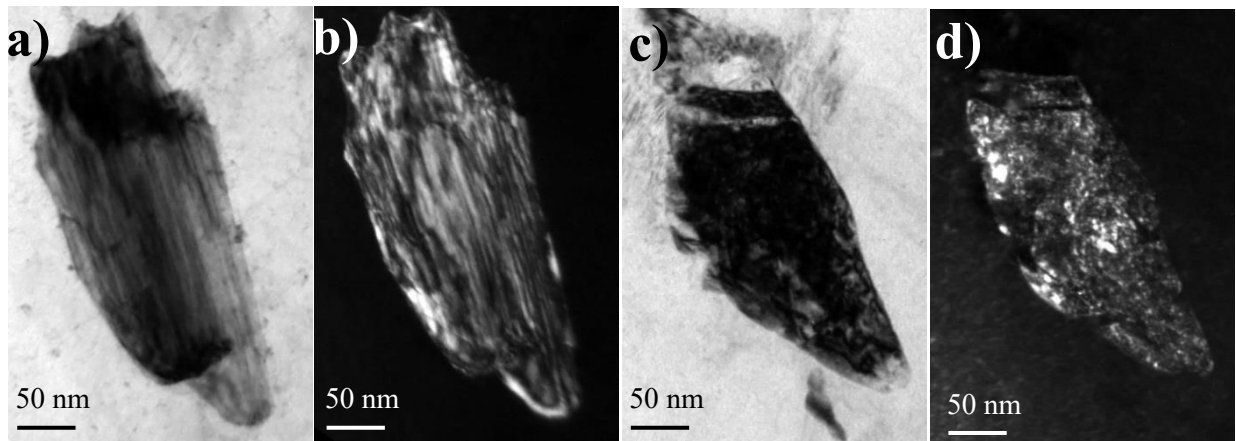


**Figure 85.** Comparison of a), b) austenitic, and c), d) martensitic, shear band sections. a) and c) are BF TEM images, whereas b) and d) are DF TEM images of the corresponding phases obtained with the respective diffraction reflections marked in Figure 84b.

A closer observation of the IPZ reveals the presence of an irregular martensitic area directly under the nanoimprint. It has a size of approx.  $0.12 \mu\text{m}^2$ , being thus significantly larger than for displacement mode testing, and consists of several nanograins arranged in a zigzag shape.

The diffraction pattern in Figure 86b shows the presence of at least four differently oriented nanograins, with a maximum total misorientation of  $18^\circ$ . As indicated by the auxiliary lines in Figure 86c, the first fragment of this martensitic area is aligned almost parallel to the surface. A second fragment lies on the  $(1\bar{1}\bar{1})$  slip plane, whereas the third one follows the other  $(11\bar{1})$  slip plane. It seems that directly under the nanoimprint the shear stress induced by nanoindentation is large enough to activate the martensitic transformation on the  $(111)$  slip plane, while at increasing depth either  $(11\bar{1})$  or  $(\bar{1}\bar{1}\bar{1})$  slip planes have the highest Schmid factor, depending on the local lattice rotation.

Some lattice rotation can also be observed for the two martensitic fragments after cycling in displacement mode (Figure 83b); however, it is less significant than in loading mode. Similar behavior was observed by Kim *et al.*<sup>310</sup>, who found that martensite formation under a nanoindent occurs in form of several blocks with different variants. They postulated that a sequential transformation takes place, with the resulting increase of misorientation and change of stress field when each new block is formed. Also Takaki *et al.*<sup>311</sup> observed rotations in the diffraction pattern, similar to the here presented, likely due to crystallographic distortion during deformation.



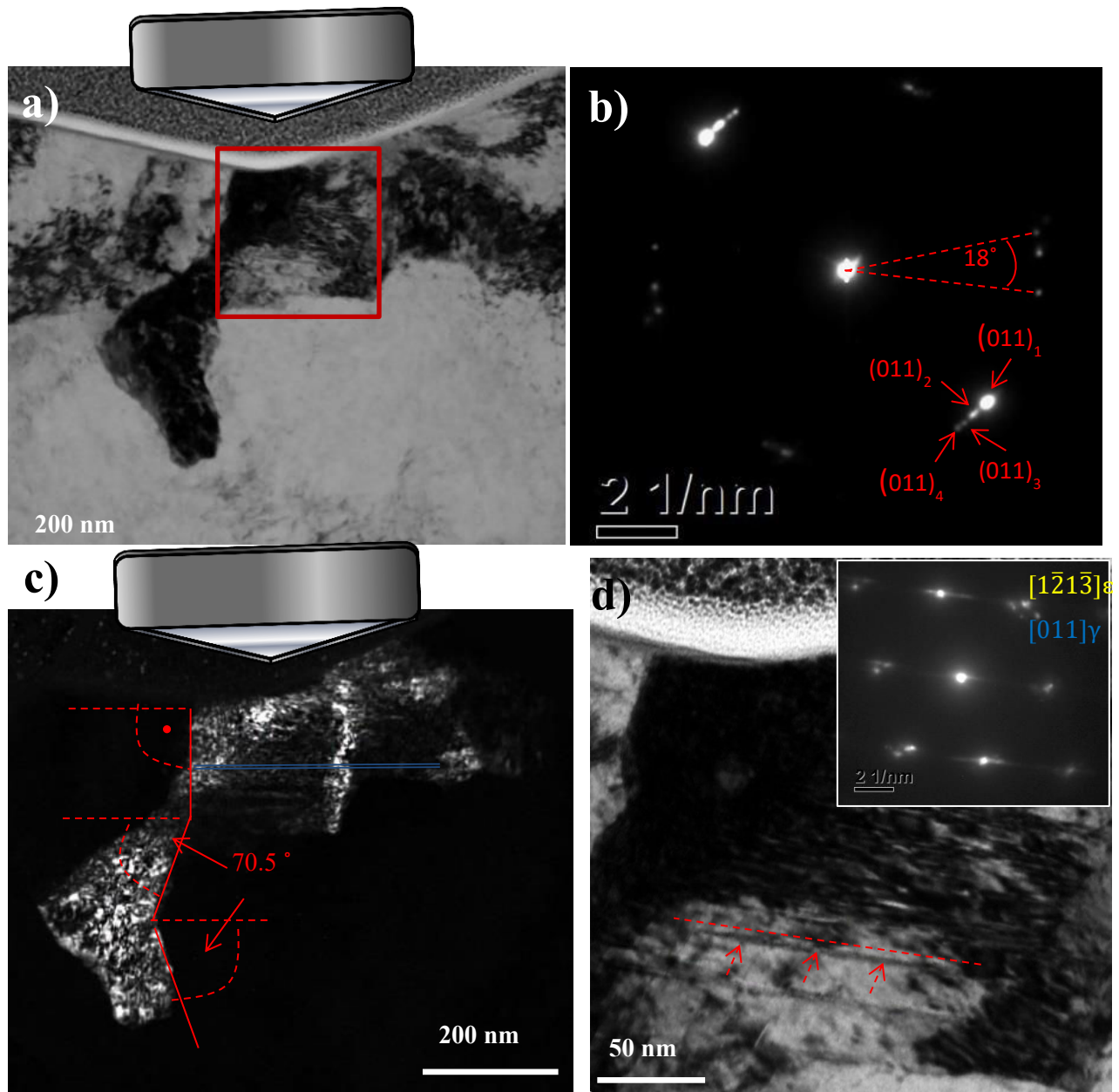


**Figure 86.** Magnified view of martensitic particle formed under the nanoindenter tip. a) BF TEM image; b) Corresponding diffraction pattern; c) DF TEM image illuminating the martensitic phase; d) Magnified image of the area framed in a) with the corresponding diffraction pattern. A dashed line and arrows point out at a nanoscopic bundle.

Additionally, directly under the surface and in the immediate surroundings of the residual imprint, a shear band section parallel to the surface is present, lying evidently on the (111) plane. This circumstance can be better appreciated in Figure 86d, which shows a magnified image of the area immediately under the nanoimprint. It reveals the presence of fine nanoscopic bundles, dispersed between the martensitic phase and parallel to the growth direction of the latter. The corresponding diffraction pattern in the inset reveals the presence of austenitic and  $\epsilon$ -martensitic phase, whereby the arrangement in thin bands leads to the

appearance of streaks. In Chapter 5, those bundles were found to be interlaced nanoscopic deformation twins and  $\varepsilon$ -martensite platelets, bundles forming along the (111) slip planes, at the edge of the nanoindentation imprint. Since on the surface those nanoscopic bands were found to serve as  $\alpha'$ -martensite nucleation sites, it can be assumed that the observed  $\alpha'$ -particles under the nanoindenter originate from nuclei forming and coalescing within those fine bands.

Shearing on the (111) plane is unusual, since from Schmid's law it can be expected that the slip plane lying perpendicular to the load axis has a Schmid factor of 0, and consequently, it is not likely to be activated. However, nanoindentation represents a special situation, where the shear stresses are multiaxial and the surface curvature and lattice rotations change the local orientation of slip planes.

To conclude, the activated deformation mechanisms are similar for nanoindentation under both testing modes, *i.e.* loading and displacement. However, for the former case the amount of cumulative deformation, after the same number of indentation cycles, is higher. As it has been observed by other authors for cyclic macroindentation<sup>248</sup>, under constant load mode  $h_{\max}$  can increase with each cycle due to time-dependent behavior, thus leading to a growth of the plastic zone. Therefore, not only the lattice rotations are expected to be larger<sup>308</sup>, resulting in a bigger martensite area, but also more shear bands and a more dislocations will be emitted from the nanoindenter tip, contributing to slip bands formation.

Comparing Figure 83 and 84, it becomes clear that the formation of shear bands must precede the apparition of martensite laths. This is in agreement with Sabooni *et al.*<sup>99</sup>, who observed that to have martensite laths, in case of macroscopic deformation (*i.e.* cold rolling), a minimum cumulative strain was necessary. Das *et al.*<sup>312</sup> arrived to the same conclusion after investigating the martensite content as a function of the number of fatigue cycles.

Moreover, the character of the shear bands determines the shape and morphology of martensite laths, in agreement with literature<sup>292</sup>. In the present study, martensite laths were not observed after 50 nanoindentation cycles in displacement mode, where the cumulative strain was apparently too low, while in loading mode the critical amount of strain was reached.

### 6.2.3 Deformation in uniaxially confined grains

Figure 87 shows the substructure generated after 50 nanoindentation cycles under displacement mode in a  $\langle 111 \rangle$  oriented "flat grain" with a boundary located parallel to the surface, approximately 4  $\mu\text{m}$  beneath. That grain exhibited a high dislocation density. However, instead of shear bands on  $(\bar{1}\bar{1}1)$  or  $(1\bar{1}\bar{1})$  slip systems, the presence of a thick bundle of shear bands on (111) plane along the grain boundary (*i.e.* parallel to the grain boundary and to the surface) was discerned (Figure 87b). As revealed by the DF TEM image in Figure 87c, those shear bands are interlaced with martensitic lamellae. Apparently, strain



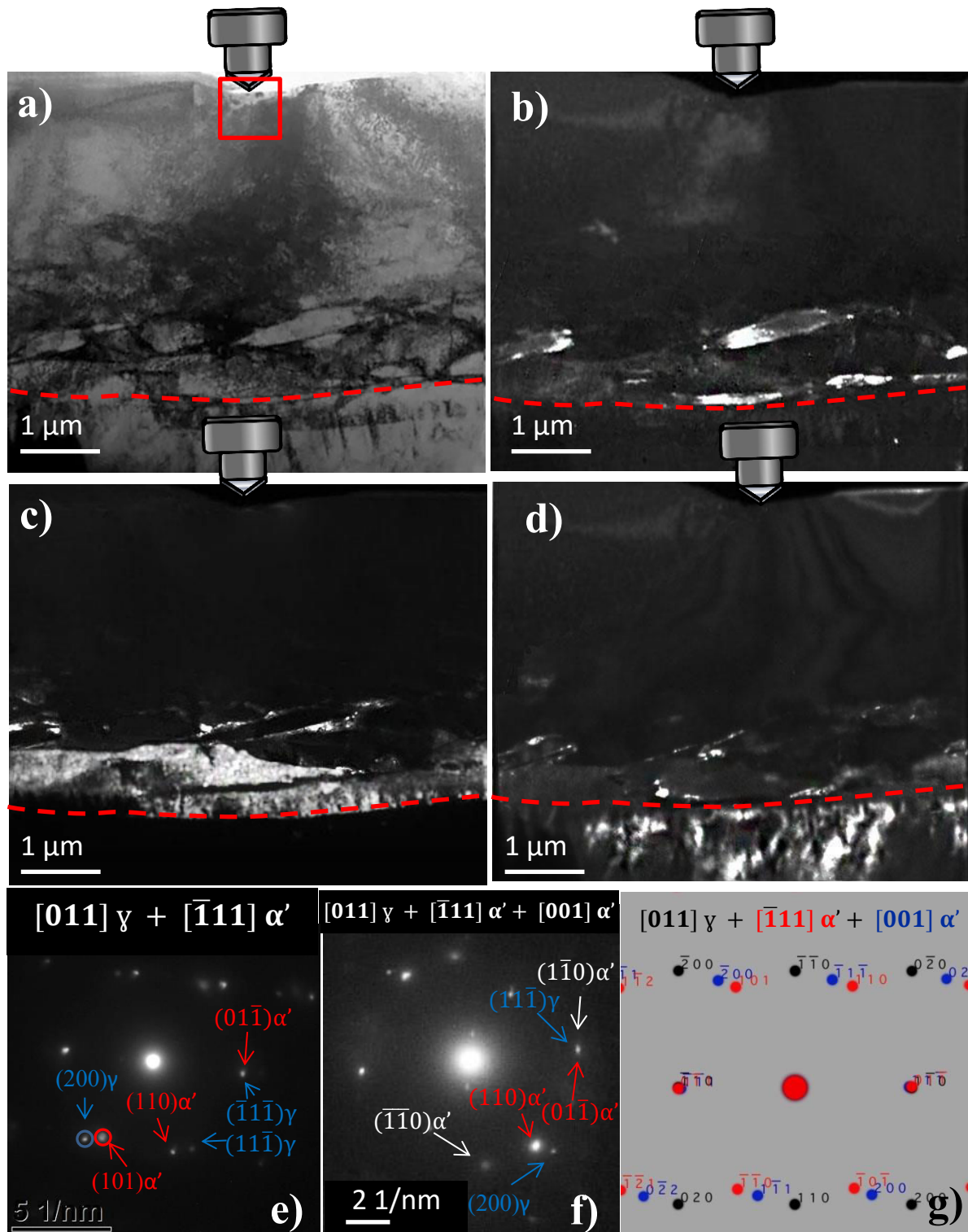
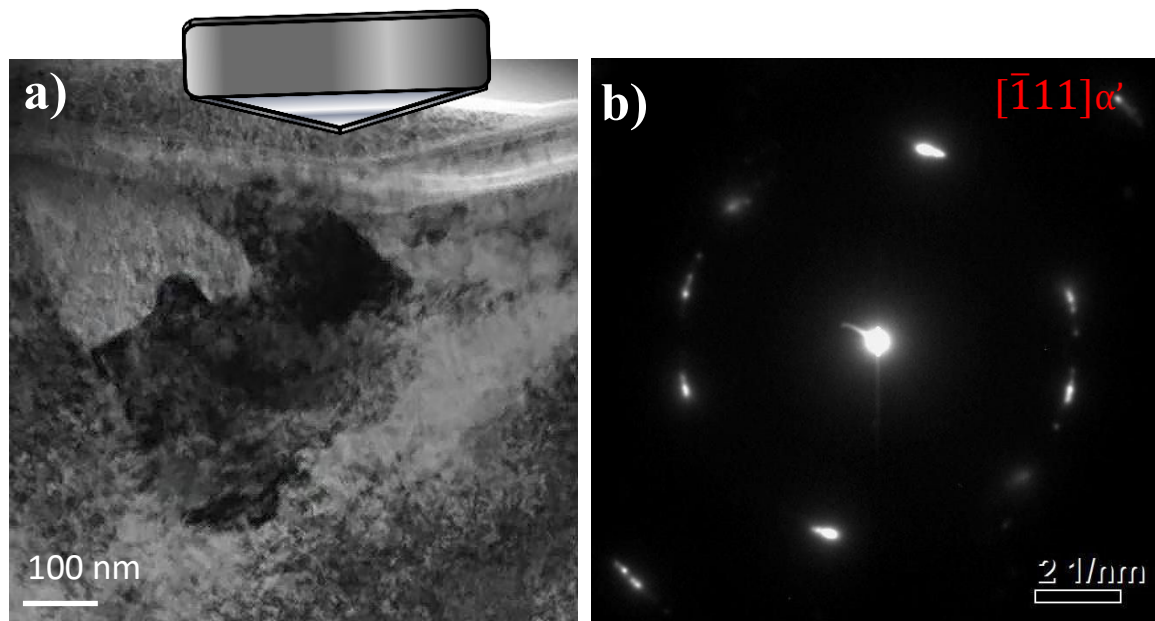


Figure 87. Cross section of a nanoimprint in a “flat”  $\langle 111 \rangle$  oriented grain. a) BF TEM image of the cross section; b) Corresponding DF image illuminating shear bands; c) DF image revealing the presence of martensite laths; e) DF image of deformed austenitic phase at the far side of the grain boundary; f) Diffraction pattern corresponding to b) and c); g) Diffraction pattern corresponding to d); h) simulated diffraction pattern corresponding to g).

accumulation due to dislocation pile-up, at the grain boundary, has reached the critical value for shear band formation on planes adjacent to the boundary and also has contributed to  $\alpha'$ -martensitic transformation within those shear bands<sup>313,314</sup>.

As already mentioned, the plastic zone produced by nanoindentation expands no more than twelve times the maximum indentation depth. This is less than 3  $\mu\text{m}$  under the testing conditions here applied, whereas the grain boundary was 4  $\mu\text{m}$  below the indentation location. Therefore, it may be postulated that dislocation pile-up at the grain boundary leads to an intensification of the local stress field, which interacts with the stress field induced by the nanoindenter, resulting in an increase of the effective size of the plastic zone.



**Figure 88. Magnified view of the martensitic phase formed in the IPZ. a) BF TEM image; b) Corresponding Diffraction pattern.**

In the case of single indentations, similar deformation features, *i.e.* shear bands partly transformed to martensitic lamellae, were not observed at grain boundaries located at comparable distances. For that reason, it becomes clear that a sufficient amount of dislocation pile-up generated by repeated nanoindentation must precede their formation. This is analogous to the behavior in large grains, where the formation of shear bands occurred only after sufficient cumulative strain. The difference is that, in the latter case, shear bands emerged directly from the IPZ, while for the flat grain dislocations released from the nanoindenter tip created stress fields by piling-up at the boundary after passing through the entire grain. Thus, the presence of grain boundaries affects the deformation behavior resulting from cyclic nanoindentation.

On the other hand, if the IPZ is observed at a magnified view, a martensitic area is discerned (Figure 88a). Analogously to the situations commented in the previous subsection, this martensitic area consists of several nanograins arranged in zigzag bands. The multiple reflections in the corresponding diffraction pattern (Figure 88b) indicate that those nanograins are rotated against each other. The total size of the martensitic area was  $0.06 \mu\text{m}^2$ , which is comparable to the case of testing of large grains. Thus, it can be concluded that the confinement of the grain in one direction alters significantly the deformation behavior in the interior of the grain, but does not affect appreciably the martensitic transformation in the IPZ.

#### 6.2.4 Transmission of plasticity through grain boundaries

The study of plasticity propagation is of high interest, since damage evolution at grain boundaries is controlled by slip transfer<sup>315,316</sup> and the slip band-grain boundary intersections are preferred crack nucleation sites<sup>3</sup>. Therefore, slip transfer is an important factor regarding cyclic stress response<sup>317</sup>. Furthermore, in case of metastable stainless steels, the interaction between martensitic phase and grain boundaries has important consequences<sup>313,318</sup>. This feature could be accessed by cyclic.

As already observed for the as-received material in section 3.2 (see Figure 47), dislocation pile-up at grain boundaries is a common feature. With increasing cumulative strain, pile-ups grow<sup>104,105</sup> and cause stress fields at the grain boundary, protruding also into the neighboring grain<sup>319</sup>. When strain surpasses a threshold value, dislocations can be emitted from the grain boundary into the adjacent grain<sup>320</sup>. This can be corroborated by Figure 87d.

Figure 89 shows a magnified view of a grain boundary. A string of particles parallel to that boundary is present and the corresponding diffraction pattern (Figure 87g) reveals their martensitic nature. More precisely, two martensitic systems can be distinguished: one is oriented in Kurdjumov-Sachs (K-S) relationship with the surrounding austenite matrix, while the other has its [001] zone axis parallel to the austenitic [011] axis, *i.e.* in Nishiyama-Wassermann (N-W) orientation relationship (OR)<sup>72</sup>.

DF images obtained with the diffraction reflections marked in Figure 87g are presented in Figure 89c and 89d. Martensite in K-S orientation with austenite grows in the direction of the observed shear bands, whereas N-W oriented martensite seems to be in a more incipient development state, exhibiting thin and short needles. From these observations, it is reasonable to postulate that K-S type martensite nucleated from shear bands, as observed before, while N-W martensite possibly emerges from the grain boundary-shear band intersection, which is also a common martensite formation site in stainless steels<sup>99,312,321</sup>.

K-S and N-W OR are regularly observed simultaneously in austenite-martensite transformations in steels<sup>322,323</sup>, while several factors, such as chemical composition<sup>324–326</sup>, prevalence of certain types of dislocations<sup>327</sup>, or thermomechanical history<sup>328</sup>, are decisive to establish the final predominant OR. Moreover, martensite morphology is linked to the OR type<sup>329</sup>. Thus, K-S is known to be preferential for

lath martensite<sup>330–334</sup>, as observed in this study, while N-W is reported for lenticular martensite<sup>72,335</sup>. Other authors<sup>324,336</sup> found that in metastable stainless steels OR changes from K-S to N-W with proceeding deformation, which agrees well with the previous statement, since  $\alpha'$  nucleation at the grain boundary is observed only after slip transfer, *e.g.* occurs later than nucleation within intersections of shear bands and subsequent lath formation.

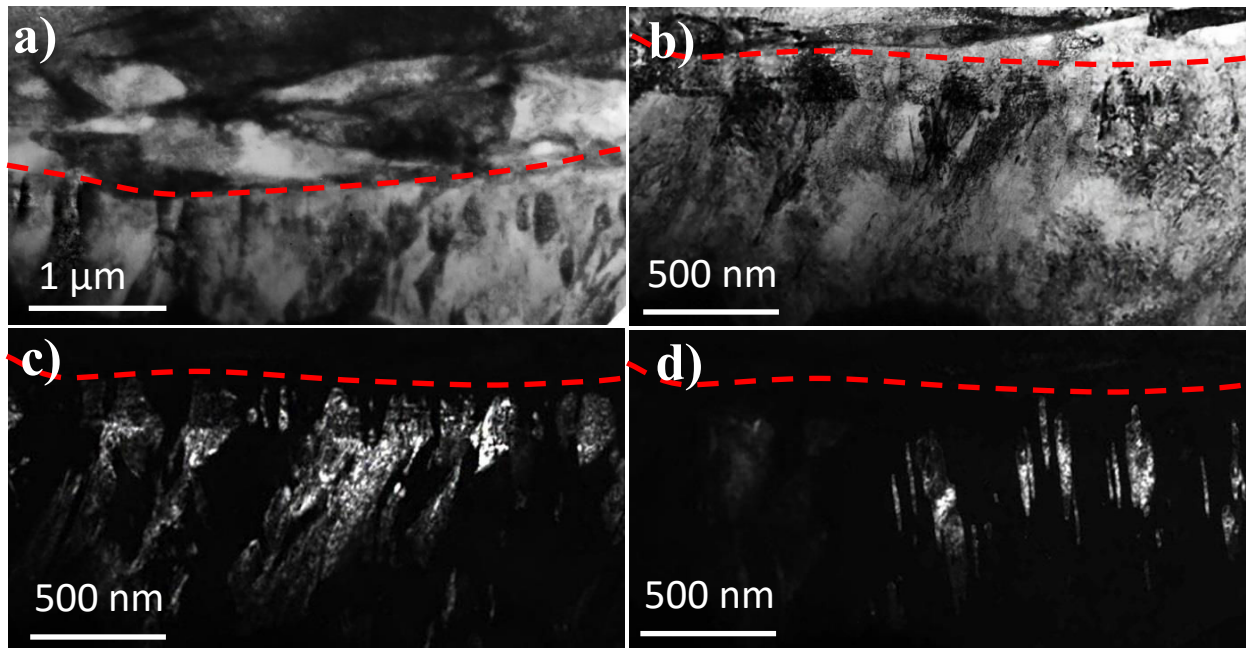


Figure 89. View of the grain boundary region in Figure 87. a) General view; b) Magnification of the far side of the grain boundary; c) Corresponding DF image of  $[111]$  oriented martensite; d) DF image illuminating  $[001]$  oriented martensite. The corresponding diffraction pattern is Figure 87g. The approximate position of the grain boundary is marked by dotted lines.

### 6.2.5 Deformation in strongly confined grains and crystalline anisotropy

So far, only  $\langle 111 \rangle$  oriented grains have been investigated in order to reduce the number of involved parameters. However, austenitic stainless steels are known to exhibit an important crystalline anisotropy<sup>284</sup>, which was confirmed in Chapter 4. Therefore, in the following subsections substructural arrangements in  $\langle 111 \rangle$  and  $\langle 001 \rangle$  small grains subjected to cyclic nanoindentation under constant penetration mode are compared.

#### Small $\langle 111 \rangle$ oriented grains:

Figure 90 illustrates the deformation substructure obtained in a small  $\langle 111 \rangle$  grain. An almost vertical martensitic area of approximately  $0.75 \mu\text{m}^2$ , protruding from the residual imprint towards the subjacent grain boundary, is clearly visible. It is composed of many misoriented nanograins adopting a zigzag shape. These nanograins appear illuminated in the DF image (Figure 90d) with  $\alpha'$ -martensitic reflection in the corresponding diffraction pattern (Figure 90e). This diffraction pattern further reveals a weak

reflection corresponding to  $\varepsilon$ -martensite, suggesting that, as already observed before, a shear band is forming the backbone of the particle. Indeed, the presence of some thin sections of remaining shear bands can be seen in Figure 90c.

An interesting question is why for the small grain only remainders of shear bands are present, while in all the previous cyclic tests formation of well-developed shear bands was observed. An explanation can be found regarding the FIB image in Figure 90b. Here, a cross section at the edge of the indent is imaged before the extraction of the TEM lamella from the center of the residual imprint. Two fold can be seen in the figure. First, a band inclined close to  $70.5^\circ$  to the surface (corresponding to  $(11\bar{1})$  slip plane) emerges directly under the nanoimprint. Its position corresponds to the martensitic phase observed under the center of the nanoimprint in Figure 90a. Furthermore, the presence of additional bands can be observed on the right side of the nanoimprint, at the grain boundary. As it will be explained in detail in Chapter 7, FIB contrast gives comprehensive information about the microstructure of stainless steels. Thus, a region with a dark contrast can be attributed to the martensitic phase, due to its lower density and thus easier ion channeling. Analogously, regions with bright contrast can be assigned to deformed austenite due to the lower channeling depth. Accordingly, the observed bands are likely originated from shear bands, which transform to martensitic laths. The region at the edge of the imprint is less deformed than around its center, so the degree of martensitic transformation, as well as distortion of the band through lattice rotations is expected to be lower there. Thus, in agreement with the previous findings, the formation of shear bands in the plasticity zone precedes the gradual transformation of the deformed volume to martensite. With increasing deformation, the shear band under the residual imprint was “consumed” by  $\alpha'$ -martensite transformation, and become difficult to discern.

Figure 91 shows more in detail the transformed core under the nanoindenter, which is embedded in an austenitic region of high dislocation density (Figure 91a), extended until the lateral grain boundary. Interestingly, concentric rings of particularly large dislocation densities are apparently emerging from the martensitic area. The magnified image, in Figure 91b, shows that between those rings planar dislocation arrangement on two slip systems without significant interference is given, while towards the core of the ring the dislocations significantly increase in number and become tangled.

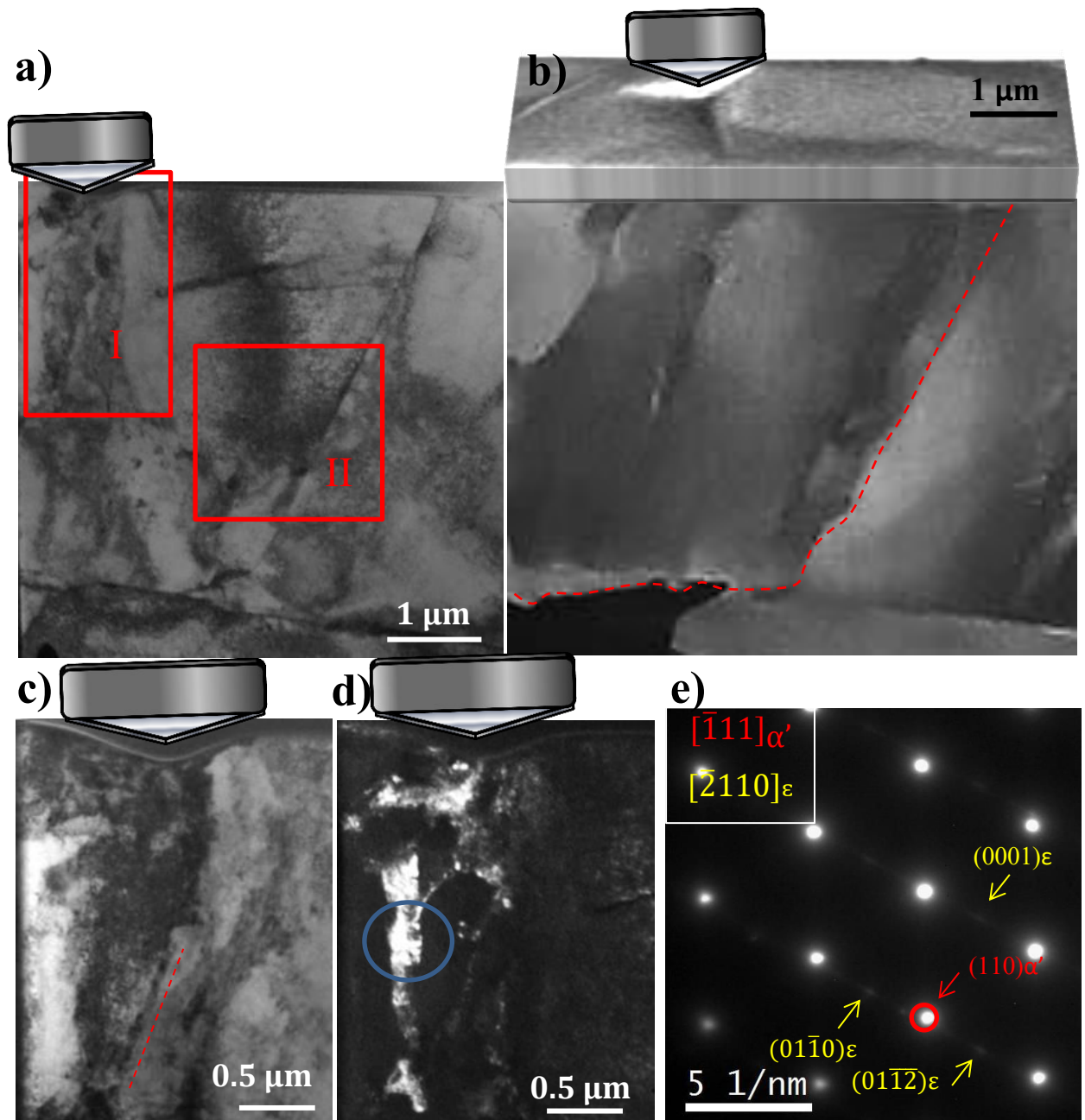


Figure 90. TEM images from a cross section lamella corresponding to a small  $\langle 111 \rangle$  oriented grain after cyclic nanoindentation testing. a) BF TEM image of the indented grain; b) corresponding FIB image from the material cross section recorded before the extraction of the TEM lamella, the approximate position of the grain boundary is framed by dashed lines; c) Magnification of the region of frame I (the presence of small shear bands located is marked by a dashed line); d) corresponding DF TEM image illuminating the martensitic phase; e) Diffraction pattern obtained from the area encircled in d).



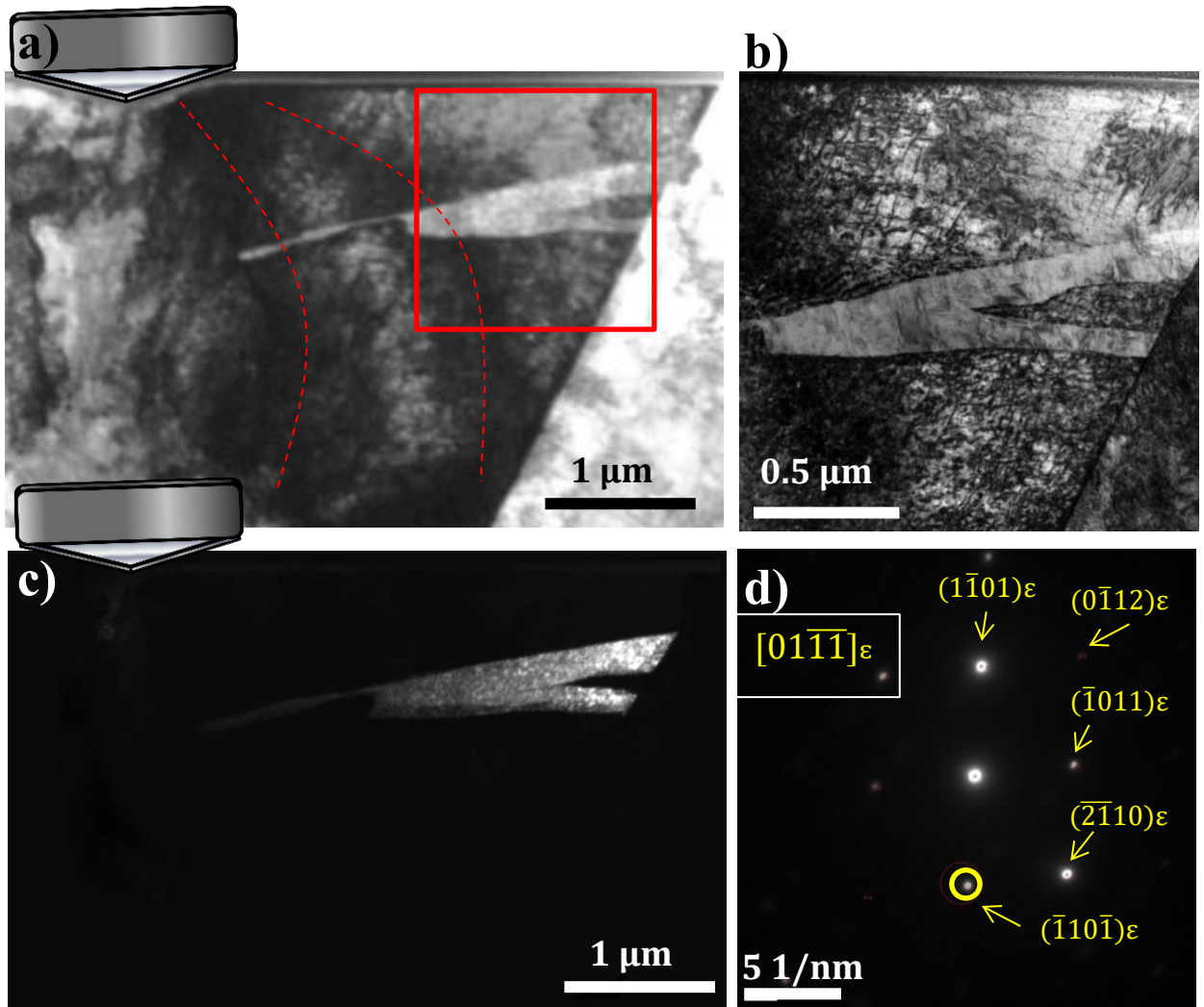


Figure 91. Area of high dislocation density surrounding the martensite under the residual imprint. a) TEM BD image, concentric rings of high dislocation density are marked by dashed lines; b) Magnified view of the area inside the rectangle frame in a); c) DF image illuminating the shear band emerging from the grain boundary; d) Corresponding diffraction pattern.

Apparently, with every new nanoindentation cycle a new wave of dislocations is generated from the vertical martensitic feature and emitted concentrically into the lateral directions. This is sensible, since the martensitic transformation is associated with the generation of Geometrically Necessary Dislocations (GNDs) in order to accommodate the strain between the austenitic and martensitic phase<sup>172,218,337–339</sup>. Thus, gradual phase transformation during cyclic indentation will lead to gradual generation of new dislocations.

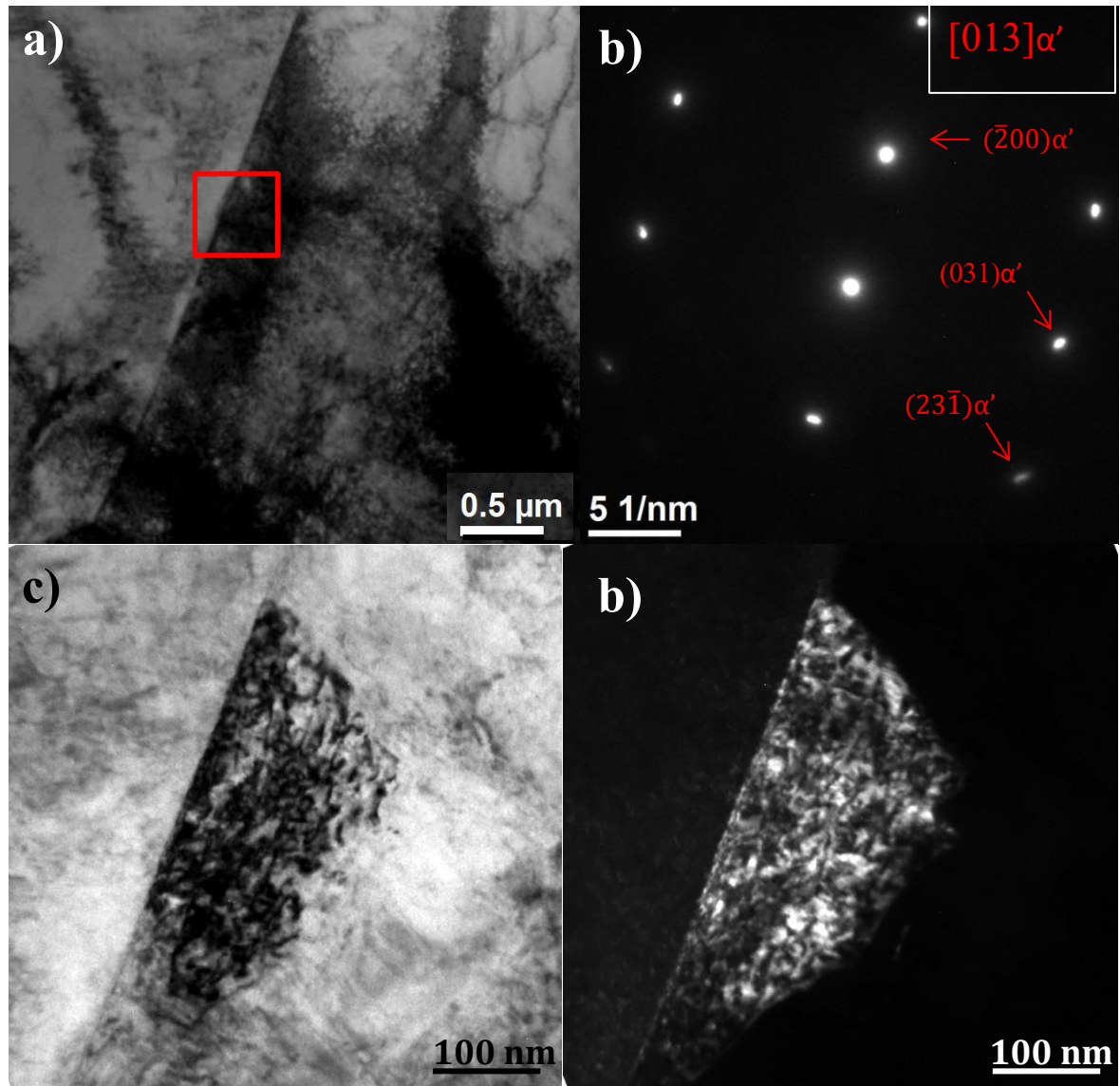


Figure 92. TEM characterization of the lateral grain boundary. a) Magnified view of the region in frame II in Figure 90a showing transmitted dislocations; b) Diffraction pattern from the region marked in a); c) and d) BF and DF TEM images respectively of the region marked in a) obtained with an  $(200)\alpha'$  diffraction reflection in b)

The dislocation density is significantly higher as compared to the case of large grains, since the spatial confinement does not permit an unrestricted flow of dislocations into the surroundings. Furthermore, the emergence of a shear band (Figure 91a,c,d) from the adjacent grain boundary can be observed. This shear band does not follow the course of the grain boundary, but rather lies on the  $\{111\}$  plane, approx. 1 μm below the sample surface. Since in the indented grain the closest horizontal boundary is located at a larger distance from the indentation site than the closest vertical one, apparently the shear stress situation is such that the formation of the observed shear band is favored. However, the shear band parallel to the grain boundary which was observed at the edge of the residual imprint in Figure 90b, can no longer be seen under the center of the nanoimprint.



Figure 92 evidences the plasticity transmission through the grain boundary. As previously mentioned the initially planar arrangement of dislocations on two intersecting systems, in the indented grain evolves to a dense dislocations forest. On the other hand, dislocations protruding from the far side of the grain boundary into the adjacent grain are rather irregular and tangled, as can be observed in Figure 92a. Figure 92b and 92c show the presence of a martensitic particle located directly at the grain boundary. Due to absence of any confinement inside of the band, its shape is irregular and diffuse. Martensite formation in stainless steels is also known to occur from dislocation pile-up at grain boundaries<sup>97</sup>, which is apparently the mechanism followed in the present case.

Actually, if there is no plasticity concentration in form of bands in the indented grain, band structure will not be induced in the adjacent grain. Instead, rather unorganized dislocations, such as those present in the indented grain, will be transferred across the grain boundary. It was reported<sup>116</sup> that  $\alpha'$ -martensite formation in small fine grains is more influenced by the presence of grain boundaries and thus, occurs less crystallographic and more irregular in shape than in coarse grains. This explains quite well the martensite formation at the grain boundary observed in Figure 92.

#### **Small $\langle 001 \rangle$ oriented grains:**

As illustrated in Figure 93,  $\langle 001 \rangle$  grain exhibits substructural features quite different from the ones observed in  $\langle 111 \rangle$  grain. Distinguishable is the presence of many slip bands emerging from the grain boundary (Figure 93a), more than those observed for any  $\langle 111 \rangle$  oriented grain. DF imaging (Figure 93c), obtained with the corresponding diffraction pattern in Figure 93b, reveals that the underlying shear bands have partially transformed to martensitic laths. While tangled dislocations are present between slip bands, also formation of incipient cell arrangement throughout the grain is present (Figure 93d), opposed to the disordered dislocation tangles in small  $\langle 111 \rangle$  grains.

Furthermore, a flat martensitic region appears around the imprint, which expands parallel to the surface. A higher magnification (Figure 94) reveals two well-defined and differently oriented block-shaped martensitic regions, at the left and right sides of the imprint, respectively (Figure 94d and e), while the region immediately surrounding the imprint is heavily deformed. Both particles lie in the represented tilt condition with their  $[\bar{1}11]$  zone axis parallel to the beam direction; however, they are rotated against each other (as well, as the correspondent diffraction patterns in Figure 94b and Figure 94c). The total size of both martensitic blocks is around  $3.9 \mu\text{m}^2$ , significantly larger than in case of  $\langle 111 \rangle$  grain.

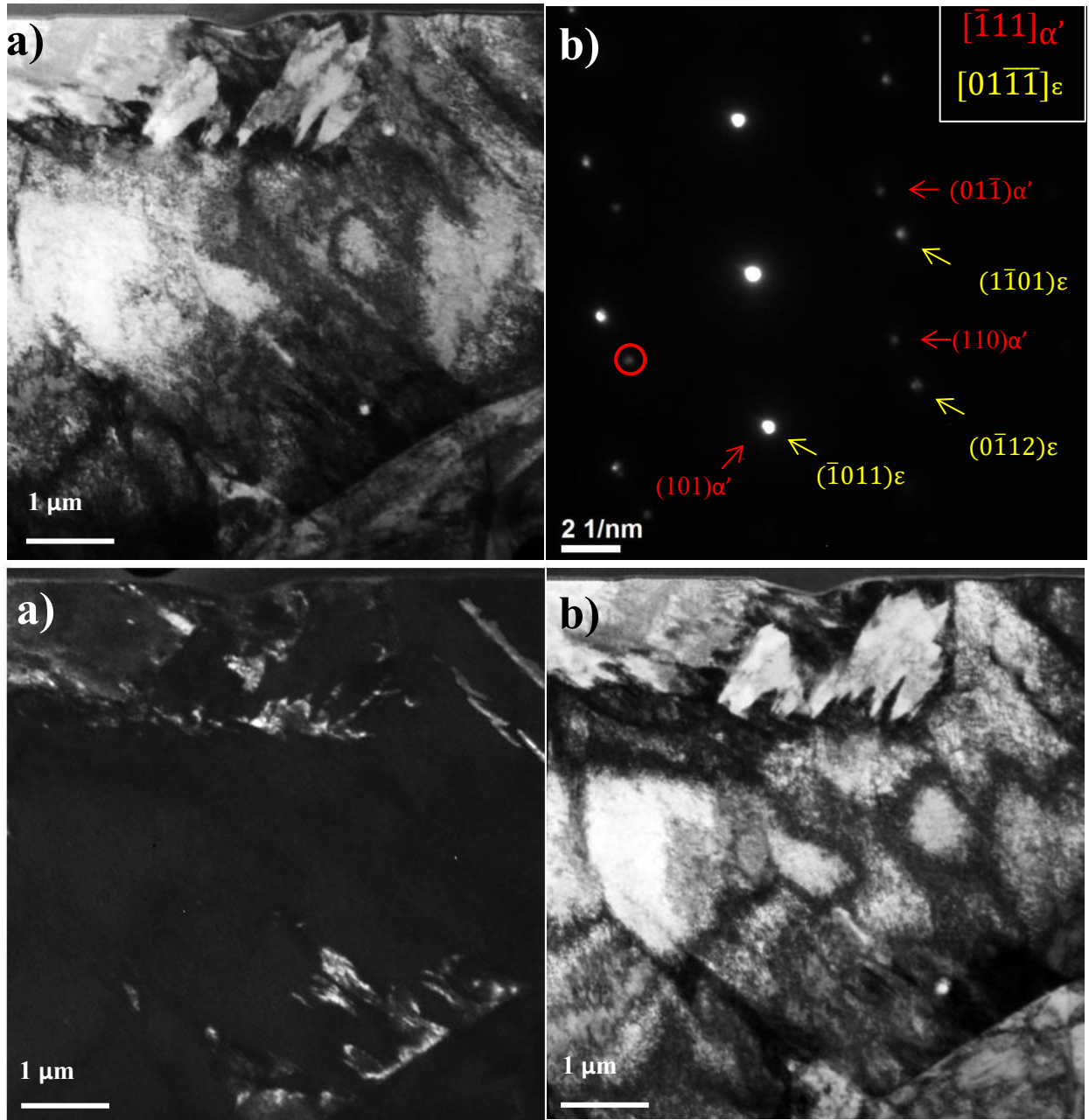


**Figure 93.** TEM characterization of the cross section of an imprint after 50 nanoindentation cycles in a  $\langle 001 \rangle$  oriented grain. a) General BF TEM image of the indented grain showing the presence of shear bands and martensite laths; b) corresponding diffraction pattern; c)  $\alpha'$ -martensite DF image of the indented grain; d) BF TEM image of the same region under slightly different diffraction conditions revealing the presence of dislocation cells.

The diffraction pattern (Figure 94c) reveals the presence of intersecting shear bands between the two martensitic areas, as well as surrounding the right one. The orientations of these shear bands correspond to the growth directions of the respective martensitic phases. This is in agreement with the previous observations of shear band formation preceding the growth of the martensitic phase for  $\langle 111 \rangle$  oriented grains.

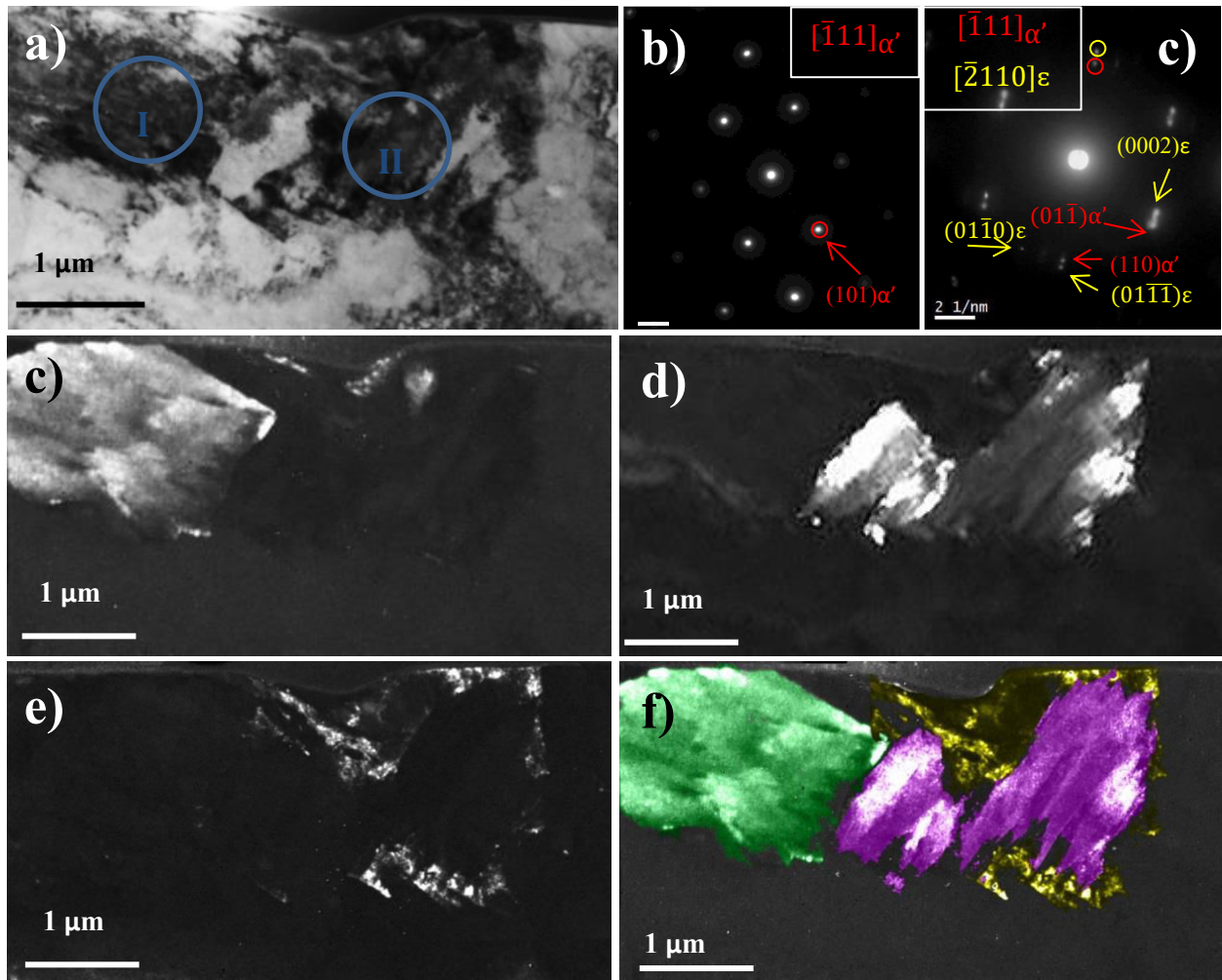


Figure 94. Close view of the deformed region surrounding the nanoimprint. a) BF TEM image; b) and c) diffraction patterns from encircled regions I and II in a) respectively; d) and e) DF obtained with encircled  $\alpha'$ -reflections in b) and c) respectively; f) DF TEM image of shear bands framing the  $\alpha'$ -martensitic area obtained with the encircled  $\epsilon$ -reflection in b); g) Combined DF TEM image illustrating the whole martensitic region in the IPZ.

Based on all these observations about the deformation mechanisms activated by nanoindentation in  $\langle 111 \rangle$  and  $\langle 001 \rangle$  oriented grains, two important differences can be outlined, which are separately addressed in the following subsections. They concern:

1. The shape and size of the martensitic regions in the IPZ;
2. The dislocation arrangements.

### Comparison of martensitic structures:

In order to understand why in  $\langle 111 \rangle$  grains the martensitic phase grows almost vertically, whereas in  $\langle 001 \rangle$  grains its development is horizontal, and moreover, none of them follows a crystallographic

direction, it is necessary to consider the anisotropy of the plastic zone as a function of the relationship between the indentation axis and the slip planes.

Alcalá *et al.*<sup>340,341</sup> performed analyses of the plastic deformation below nanoindenters in Cu. Their results are represented in Figure 95, where the simulation shows that for fcc materials plastic flow is favored parallel to the indentation axis for  $\langle 111 \rangle$  oriented grains, while for  $\langle 001 \rangle$  grains it is flattened in vertical direction, but prolonged parallel to the surface plane. This is related to the respective spatial distribution of slip systems in each case. This shape difference between the plastic zones for  $\langle 111 \rangle$  and  $\langle 001 \rangle$  grains is in good agreement with the observations of the present study (compare Figure 90d and Figure 94g to Figure 95, leading to the conclusion that the formation of martensitic subgrains under the nanoindenter is directly related to the shape of the plastic zone under the nanoindenter). The zigzag shape observed for the martensitic areas, following alternately one or other active slip plane, is consistent with this explanation. On the other hand, Alcalá's model was developed for Cu and Al-Cu crystals, but for AISI 301LN stainless steel a more pronounced elongation and flattening in  $\langle 111 \rangle$  and  $\langle 001 \rangle$  grains, respectively, is expected, due to its higher yield stress.

Plasticity analysis by Alcalá *et al.*<sup>340,341</sup> was carried out for a stable material, *i.e.* no susceptible to phase-transformation, so care must be taken when comparing the results, especially when evaluating cyclic deformation behavior, due to the hardening involved with phase transformation. However, the scarcely pronounced hardness difference between work-hardened austenite and martensite allows a qualitative comparison.

Worth mentioning is the asymmetry observed for the  $\langle 001 \rangle$  grain, where martensite formation was more expanded to the left than to the right side of the indent. This is due to the asymmetry of the Berkovich indenter, as discussed before, and differences between the size of plastic zones at both flanks were observed also by other authors<sup>300</sup>. Apart from this asymmetry, Alcalá *et al.*<sup>340,341</sup> found that plastic zones for Berkovich indentations do not differ much from those produced by spherical indenters. Thus, the growth direction of martensite under the nanoindenter can be considered as the result of shear stresses on multiple slip systems activated by nanoindentation.

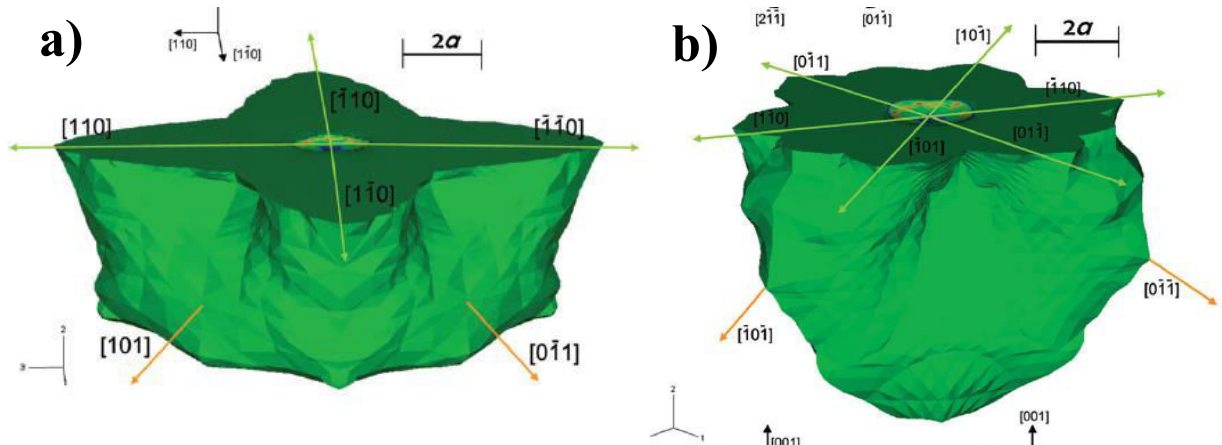


**Figure 95.** Calculated shape of plastic zones under nanoimprints in Cu for: a)  $\langle 001 \rangle$  oriented; and b)  $\langle 111 \rangle$  oriented indented grains<sup>340</sup>. Reproduced with kind permission of <http://www.tandfonline.com>.

Another point to mention is the significant size difference between martensitic areas in  $\langle 111 \rangle$  and  $\langle 001 \rangle$  grains. The volume expansion going along with  $\gamma \rightarrow \alpha'$  transformation creates hydrostatic pressure and hinders the phase transformation in the bulk, while on the surface the material is less confined and can expand. Indeed, the formation of martensite under compressive stress is not very favorable<sup>292,293,342</sup>. This explains why the flat oriented martensitic phase in the IPZ of  $\langle 001 \rangle$  grains reaches a significantly higher dimension than the vertically oriented martensite in  $\langle 111 \rangle$  grains. Also other authors found that in austenitic stainless steels, grains with the  $\langle 001 \rangle$  direction parallel to the loading axis are oriented more favorable for phase transformation<sup>343,344</sup>.

### Comparison of dislocation arrangements:

Multiple slip was observed for both  $\langle 111 \rangle$  and  $\langle 001 \rangle$  oriented grains, in agreement with literature results<sup>213,214</sup>. In small grains, opposed to large ones, dislocation density is higher and there are more barriers to slip, and as a result multiple slip is activated at an earlier stage of deformation<sup>345</sup>. Nevertheless, the difference is how dislocations are arranged.

In conventional macroscopic fatigue testing of austenitic stainless steels, different stages can be distinguished as a function of their characteristic dislocation substructures<sup>146–148</sup>. In the first stage, planar arrangements are typically observed. At later stages, the increasing dislocation density can lead, in crystals oriented for multiple slip, first to the formation of tangles and later to substructural arrangements such as veins and channels and also cells<sup>346,347</sup>. Consequently, it can be concluded that for the same level of strain accumulation,  $\langle 001 \rangle$  grains reach a further cyclic deformation stage than  $\langle 111 \rangle$  grains.

In order to understand the origin of this difference, nanohardness measurements were performed in CG (coarse grain) samples. Hardness values of randomly placed 10 x 10 nanoindentation matrices, with

$h_{\max} = 250$  nm and 500 nm, respectively, were calculated from the load-displacement data according to the Oliver-Pharr method<sup>156</sup>. In addition, 25 indentations were carried out selectively in grains with  $\langle 111 \rangle$  and  $\langle 001 \rangle$  orientations. Table 11 summarizes the results.

**Table 11. Comparison of nano-hardness values for different crystallographic orientations and maximum displacements.**

$h_{\max}$ (nm)	$\underline{H}$ [GPa]	$H_{\langle 111 \rangle}$ [GPa]	$H_{\langle 001 \rangle}$ [GPa]	$H_{\langle 111 \rangle}/H_{\langle 001 \rangle}$
250	$3.67 \pm 0.31$	$3.81 \pm 0.26$	$3.46 \pm 0.14$	1.10
500	$3.24 \pm 0.24$	$3.33 \pm 0.13$	$3.01 \pm 0.08$	1.11

It becomes clear that, in spite of the size effect characteristic for nanoindentation testing<sup>165</sup>, for both  $h_{\max}$  values  $\langle 111 \rangle$  grains were found to be approx. 10% harder than  $\langle 001 \rangle$  grains. This anisotropy is in agreement with the established behavior for fcc metals<sup>348</sup>, where  $\langle 111 \rangle$  always exhibits the highest Taylor factor and  $\langle 001 \rangle$  the lowest<sup>213,284</sup>, with the corresponding consequences on yield stress and hardness. Lower hardness values correspond to less slip resistance<sup>349</sup>. Thus, slip is easily activated in  $\langle 001 \rangle$  grains, leading to the formation of a higher number of shear bands and a faster development of characteristic fatigue dislocation arrangements. Furthermore, there might be a correlation between the higher martensite fraction and the earlier development of dislocation cells arrangement. In this sense, Das concluded that the barrier effect created by the presence of martensite accelerates the generation of dislocations and triggers the growth of dislocation cells<sup>313</sup>.

The dislocation configuration is known to be determined by the SFE<sup>245,345</sup>, the strain amplitude<sup>249,345,350</sup> and the crystallographic orientation<sup>246,351</sup>. As for the latter, most studies of fatigue properties of fcc materials, concentrate only on the difference between crystallographic orientations for single and multiple slip<sup>213,352</sup>.  $\langle 001 \rangle$  and  $\langle 111 \rangle$  are both multiple slip orientations<sup>213,352</sup>, and thus, according to literature reports, both should have a similar deformation behavior. However, the present study shows that for materials undergoing phase transformation, there is a significant difference in the behavior of the two orientations<sup>213</sup>. Therefore, detailed studies of dislocation arrangements, as a function of grain orientation, are of utmost importance in order to develop alloys with favorable mechanical properties.

## 6.2.6 Plasticity evolution

Figure 96 shows the microstructure of a small  $\langle 111 \rangle$  oriented grain after 200 nanoindentation cycles with  $h_{\max} = 250$  nm. A highly deformed austenitic phase, exhibiting a high dislocation density, extends widely to both sides of the residual imprint, as well as vertically until the grain boundary (Figure 96b). The



diffraction pattern corresponding to the IPZ (inset in Figure 96c) shows randomly distributed  $\alpha'$ -martensite reflections, superposed with a ring-like pattern.

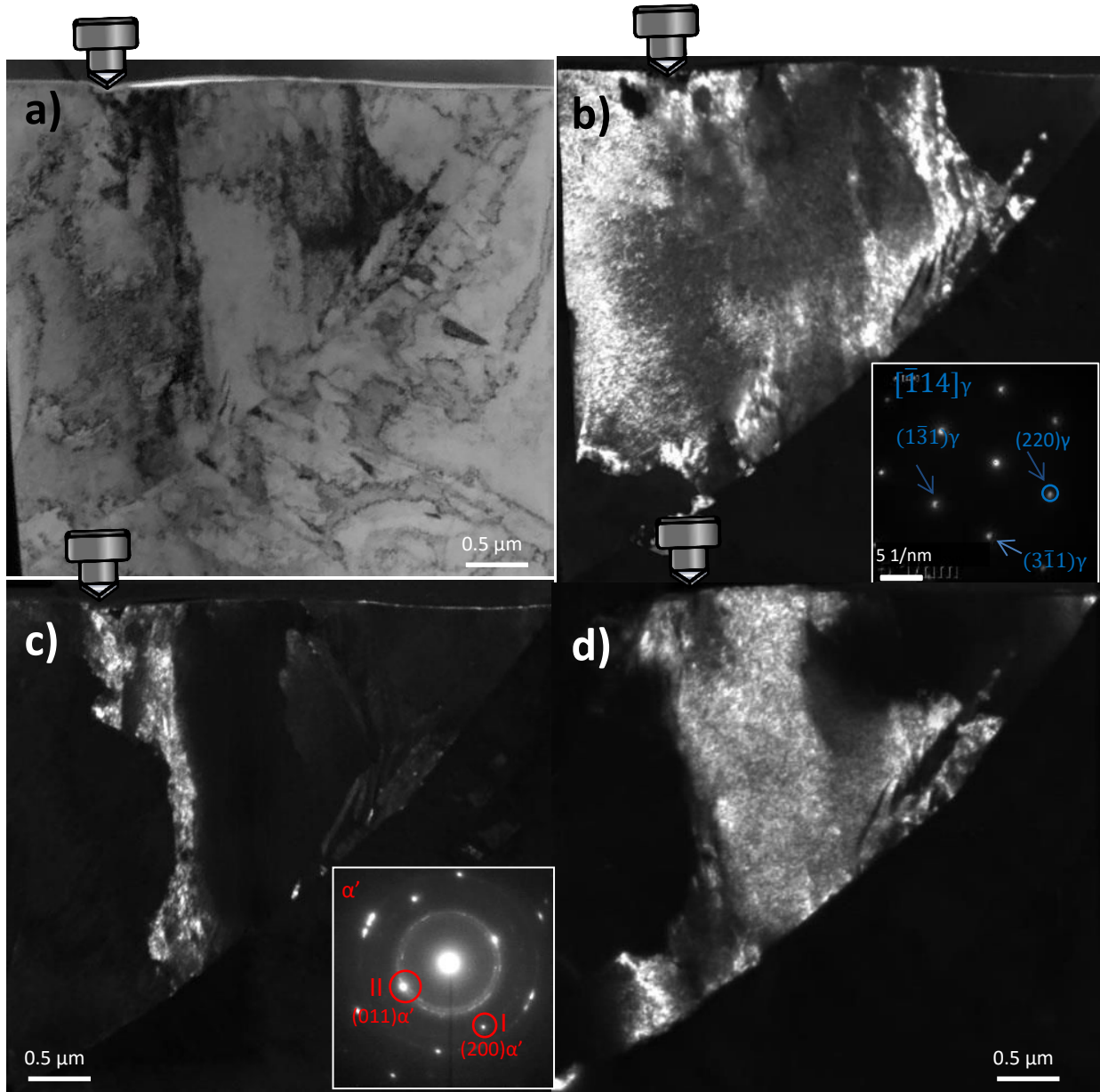


**Figure 96.** Small  $\langle 111 \rangle$  oriented grain after 200 nanoindentation cycles. a) TEM BF image; b) corresponding DF TEM image illuminating the austenitic plasticity zone; c) DF image of martensitic particle formed under the nanoindenter obtained from the diffraction reflection I of the diffraction pattern in the inset; and d) Dislocation cell-type martensite TEM DF image obtained with the diffraction reflection II.

If a single reflection is chosen, as in case of Figure 96c, the corresponding DF image shows a well-defined martensitic particle protruding vertically until the grain boundary, such as observed after 50 cycles. However, selection of a ring section leads to a diffuse DF image (Figure 96d), where a large area surrounding the axis from the center of the nanoimprint to the grain boundary is illuminated.

The diffuse martensitic zone has the characteristics of dislocation cell-type martensite, *i.e.* a martensite type which develops from break-up of a martensite lath due to severe deformation<sup>99,101,311,353–355</sup>. It can be recognized by a high dislocation density leading to the diffuse appearance and also exhibits ring-like diffraction patterns due to the strong distortions and lattice rotations, both as here observed. Dislocation cell-type martensite coexists with lath-type martensite, whereby the fraction of the former becomes higher with increasing deformation. Indeed, small areas of dislocation cell-type martensite were also observed in the flat and small grains after 50 cycles of nanoindentation. However, their presence was less clear than in the case of 200 cycles. Thus, it is obvious that strain accumulation during cyclic nanoindentation tests leads to similar deformation mechanisms as conventional macroscopic low cycle fatigue testing.

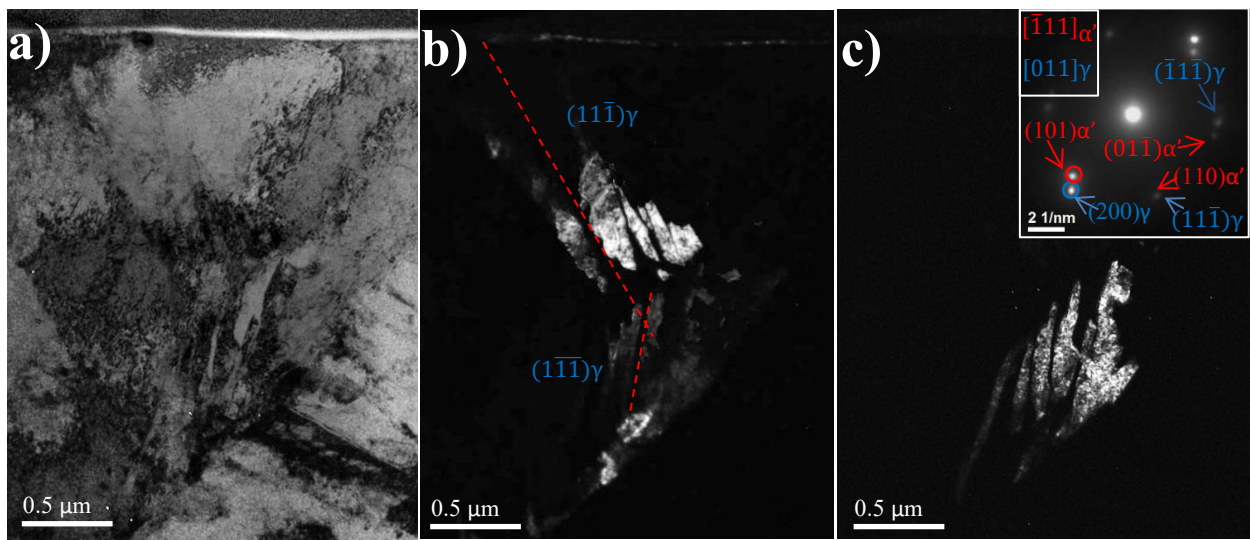


**Figure 97. Deformation band system at the grain boundary. a) BF TEM image; b) DF image obtained with the  $\gamma$  {200} diffraction reflection; and c) DF TEM image obtained with the  $\alpha'$  {200} diffraction reflection.**

As can be discerned in Figure 96c, the martensitic phase spreads along the grain boundary. Deformation mechanisms activated in the zone close to the grain boundary are illustrated more in detail in Figure 97. A set of shear bands protrudes on the  $(11\bar{1})$  slip plane below the residual imprint towards the grain boundary (Figure 97b). However, when the bands almost reach the grain boundary, they reorient to the  $(1\bar{1}1)$  slip plane and the reoriented part is largely transformed to martensite (Figure 97c). The latter is expected, since after previous findings, stress concentration directly at the grain boundary is larger than in the center of the grain and thus, the martensitic transformation takes place earlier in the vicinity of grain boundaries. Concerning the change in the shear bands direction, while in the surrounding of the nanoindenter tip the active slip plane with the highest Schmid is determined by its angle with the flanks of the former, at the grain boundary slip planes more parallel to the latter are preferred, as already observed in the case of the flat grain (Section 6.2.3).



Figure 98 corresponds to the deformation substructure at the other side of the grain boundary. Noticeably, significant plasticity transfer took place, resulting in a high dislocation density (Figure 98a) and formation of slip bands partially transformed to martensite, as can be concluded from the corresponding diffraction pattern given in Figure 98b.

Comparing the results to the findings in Section 6.2.1 and 6.2.2, it becomes clear that significant martensite formation occurs only after high cumulative strain (which augments with decreasing grain size and increasing the number of cycles). This is in agreement with literature reports for macroscopic properties of stainless steels <sup>356</sup>.

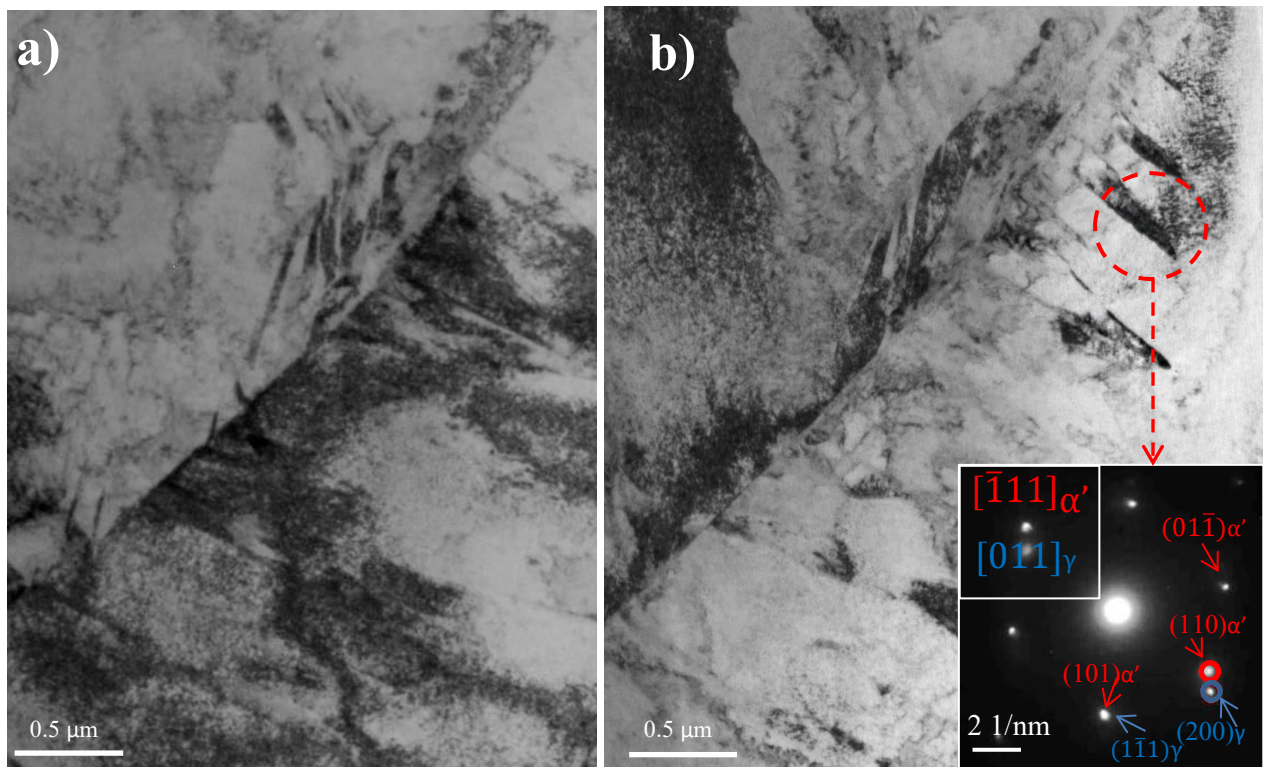


Figure 98. BF TEM images of the grain boundary region corresponding to different tilt angles. b) Includes a diffraction pattern, as obtained from the area marked by a circle.

### 6.2.7 Evolution of deformation for prestrained condition

To achieve an understanding of the influence of predeformation, the cyclic indentation behavior of skin-passed steel was studied. For this purpose, a small grain oriented close to  $\langle 111 \rangle$  was chosen. Resulting substructural characteristics are illustrated in Figure 99. As can be derived from this figure, the whole grain exhibits a regular system of intersecting shear bands, with  $\alpha'$ -martensite forming at the

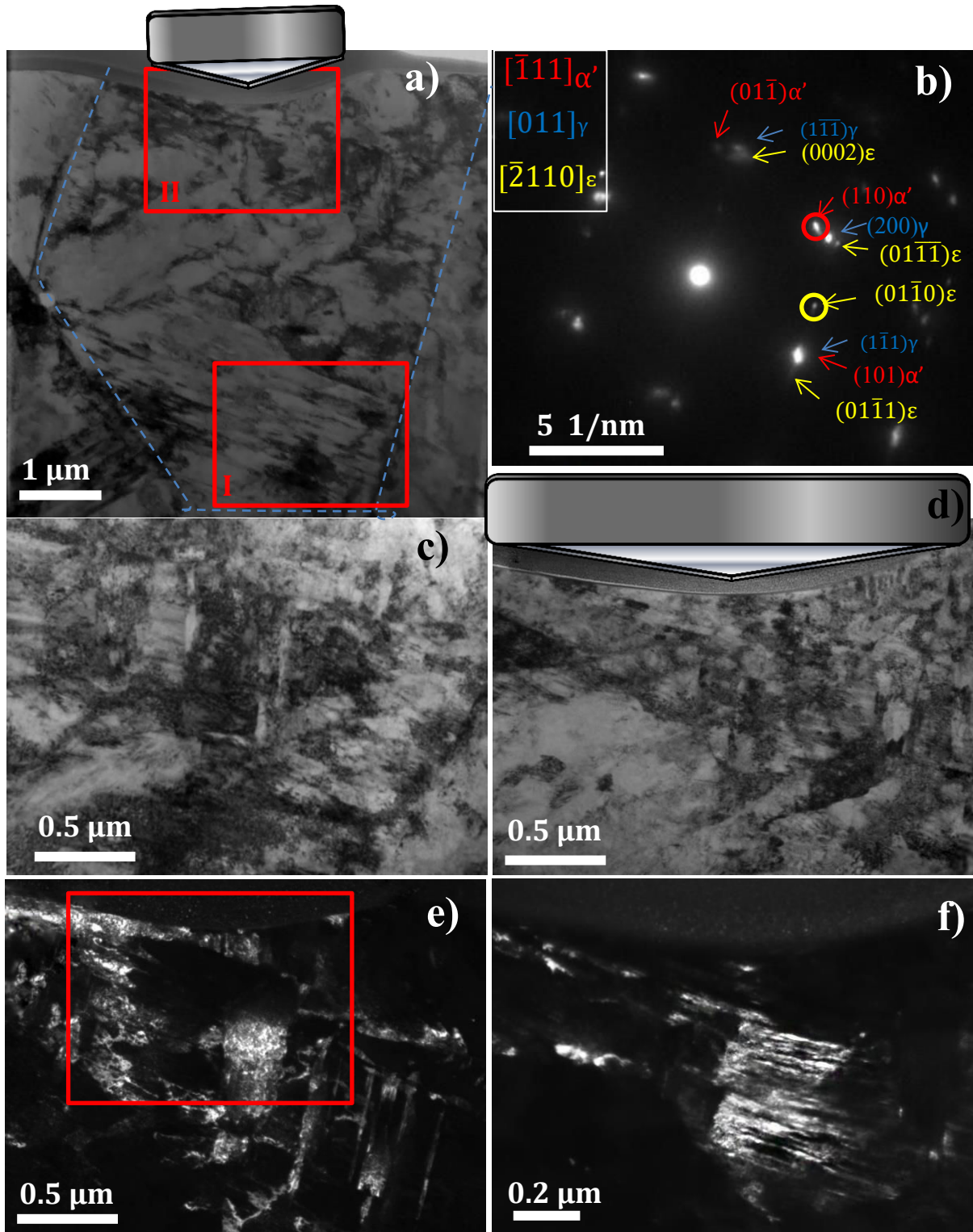


Figure 99. 50-cyclic nanoindentation test in a small grain of a skin-passed sample. a) BF TEM image of the indented grain with the approximate position of grain boundaries marked with a dashed line; b) Diffraction pattern obtained in region II, as marked in a); c) amplified BF TEM image of region I in a); d) amplified BF image of region II in a); e) and f) DF TEM images obtained with the  $\alpha'$ - and  $\epsilon$ -martensite diffraction reflections encircled in b).

intersections. Comparing the deformation substructure in the bulk of the grain (Figure 99b) and one in the IPZ (Figure 99d-f), no substantial differences can be observed. Thus, there is no evidence for additional deformation arisen from the nanoindentation testing. The only exception is the shape of the shear bands, which at closer look appear slightly curved, following the shape of the residual imprint, rather than being ideally straight as in region I. Therefore, it is reasonable to assume that those shear bands existed already before the indentation experiments, and bent during the latter due to emerging lattice rotations. TEM results indicate that pre-hardening of the sample by skin-passing inhibits further deformation by nanoindentation. This is in agreement with the characteristics of the corresponding load-displacement curves, as it was discussed in Chapter 4.

## 6.3 Conclusions

Selected austenitic grains were deformed by nanoindentation and subsequently investigated by TEM. Substructural arrangements produced by monotonic loading, as well as their evolution with increasing cumulative strain induced by cyclic indentation, have been studied. It was demonstrated that parameters such as loading mode, grain size and crystallographic orientation have an important influence on the deformation behavior.

The main findings are summarized in the following:

1. Deformation behavior resulting from nanoindentation can be divided in local, *i.e.* directly related to the large shear stresses immediately in the IPZ, and general, *i.e.* extending over the whole indented grain. The former is given mainly for monotonic indentation, as well as cyclic indentation in large grains; it leads to nanoindentation-specific features, such as local lattice rotations, nanoscopic shear bands and subsequent formation of martensitic particles. On the other hand, the latter behavior was rather predominant in cyclically deformed small grains, where the spatial confinement led to a rather homogeneous plasticity distribution within the indented grain. Therefore, deformation mechanisms comparable to those known from conventional deformation tests were activated. They were governed by the stress localization at grain boundaries and cyclically evolving arrangements of dislocations.
2. Cyclic nanoindentation leads to a gradual accumulation and propagation of plasticity, analogous to conventional macroscopic fatigue testing. As a consequence, the transition from lamellar to dislocation cell-type martensite can take place. Likewise, slip transfer into adjacent grains and subsequent martensite formation was observed.
3. Within the investigated strain range, dislocation structures after 50 cycles resembled in many ways those found in other fcc metals, while martensitic transformation (dislocation cell-type)

became important only at elevated cycle numbers. However, for the investigated steel, in contrast to many other fcc materials, the prevalence of microscopic shear bands largely determines the deformation behavior, starting from the first indentation cycle.

4. It was found that strain localization, as well as evolution of dislocation arrangements, accelerated dramatically with decreasing grain size.
5. Testing in loading mode led to a higher cumulative deformation compared to displacement mode, which is sensible, taking into account the softening behavior observed in Chapter 4.
6. Prestrain, such as given in case of the skin-pass condition, goes along with work hardening. The latter inhibits the propagation of deformation induced by nanoindentation. This explains the observed stability of P-h curves for the prestrained condition.
7. Crystalline anisotropy manifested itself through different phase transformation and dislocation arrangements. Particularly interesting is that crystalline anisotropy was found not only between grains oriented for single slip and multiple slip, as widely reported, but also between two different “hard” orientations, both oriented for multiple slip. Thus, for  $\langle 001 \rangle$  grains, the local plastic deformation was rather extended along the surface, while for  $\langle 111 \rangle$  grains it propagated into the bulk. Also, small  $\langle 001 \rangle$  grains featured dislocation cells after 50 cycles, while in  $\langle 111 \rangle$  grains dislocations were still tangled at this stage. These differences in microstructure explain the dissimilitude in mechanical properties observed for  $\langle 001 \rangle$  and  $\langle 111 \rangle$  grains, as found in Chapter 4: it is reasonable to assume that the martensitic phase formed under the nanoindenter tip increases the penetration resistance for successive cycles, while flat shaped martensite positioned at the sides of the indented area is not directly probed during the loading of the IPZ. Thus, here no secondary hardening takes place.
8. Comparing the observed deformation mechanisms to those present at the surface, as studied in Section 5.3, in the interior of the grain dislocation slip was clearly an important mechanism, while at the surface only incipient formation of slip bands was observed.

In conclusion, within the present chapter it was shown that, in spite of the complex stress fields given by nanoindentation, the onset, growth and transmission of plasticity triggered by cyclic nanoindentation can be related to similar deformation mechanisms as those known from conventional cyclic deformation tests. However, nanoindentation allows to investigate those mechanisms with a higher spatial selectivity and precision, as well as higher temporal resolution.

## 7 Supplementary subsurface characterization and 3D reconstruction

### 7.1 Motivation

The results in Chapters 5 and 6 confirmed the unquestionable convenience of the TEM technique. However, the latter also has a large inconvenience, namely the time, effort and cost involved in the preparation and study of TEM lamellae, as well as the limited size of the latter. The occurrence of preparation artifacts, such as bending of the lamellae, is another drawback. The latter is particularly an issue for metastable steels, since martensitic transformation involves a volume expansion between 2 and 4%, and thus an accumulation of residual stresses due to the confinement of this expansion. The extraction of the lamella allows the release of the accumulated stress, leading to bending of the lamella.

On this account, an alternative approach has been applied in the present thesis for the subsurface characterization of nanoindentations, as will be described in this chapter. Namely, Focused Ion Beam (FIB) microscopy has been used to perform Scanning Ion Microscopy (SIM) imaging, as well as 3D-tomography, in order to access the phase transformation and the plastic zone in the area surrounding residual nanoindentation imprints. The latter is usually performed by a FIB/FESEM combination (FIB sectioning and FESEM imaging) and has been successfully used for different materials, *e.g.* to study crack propagation in cemented carbides<sup>357</sup>. However, for the microstructural characterization of the here studied steel, the contrast of Electron Channeling Contrast Imaging (ECCI)<sup>358</sup> is not suitable to clearly distinguish different microstructural features<sup>14,284</sup>, while SIM provides a significantly stronger contrast<sup>359,360</sup>. Thus, FIB/FIB tomography was the advanced characterization method chosen for the present investigation.

In detail, three cases were considered:

- For comparison, first, the surface and cross section of a SP sample were characterized by FIB.
- Subsequently, the cross section of a residual imprint after a monotonic nanoindentation test was observed.
- And finally, the cross section of the residual imprint after a cyclic nanoindentation test was characterized, and the deformation substructure was reconstructed in 3D by FIB/FIB tomography.

Thereby, the here studied cross sections of nanoindentations are the same which were characterized by TEM in sections 6.2.1 and 6.2.6, whereat FIB characterization was actually performed before the lift-out of the corresponding TEM lamella.

## 7.2 Results and discussion

Figure 100 shows the substructure of the skin-passed sample, as observed by SIM. A large area of the sample surface was imaged in Figure 100a. In agreement with the observations in Chapter 3, a heterogeneous microstructure with different prominent features was present.

The magnified view of a selected grain in Figure 100b highlights the presence of distinctive parallel bands. A cross section of this grain, following the line indicated in the figure, was prepared and is represented in Figure 100c. It reveals that the above-mentioned bands protrude as some tenths of nanometers thick plates into the bulk, rather than being only a surface feature. A second system of those bands crosses the first ones at an angle close to  $70.5^\circ$ . Small particles with a dark contrast can be observed at the intersections of the bands, as well as inside of single bands. Those bands and particles resemble the shear bands and  $\alpha'$ -martensitic nuclei, similar to the ones observed by TEM, EBSD and FESEM in chapters 3 and 5. This was confirmed by subsequent extraction of a thin foil from the cross section.

Figure 100d shows the corresponding TEM BF image obtained from the area marked by the rectangle in Figure 100c. Bands and particles observed with SIM are well preserved after the extraction of the TEM thin foil. SAED is shown in the inset between Figure 100e and f. It exhibits simultaneously  $\alpha'$ -martensitic and austenitic reflections. The corresponding TEM DF images (Figure 100e for austenite and Figure 100f for  $\alpha'$ -martensite), allow an unambiguous identification of the observed features. Figure 100f also illustrates the gradual formation of martensitic laths inside of the austenitic shear bands, whereby similar structures can be observed in the SIM image in Figure 100c as dark contrasted, thickened bands (left side of the image). Thus, an excellent agreement is found between TEM and SIM imaging.

SIM images are created by the channeling of ions, which depends on the material density<sup>361</sup>. Since martensite has a lower density than austenite, ions can channel deeper before interacting with atoms and inducing the emission of secondary electrons (SEs). Secondary electrons produced deeper in the bulk are in turn less likely to reach the surface and then be detected. This explains why martensite appears darker in SIM images.



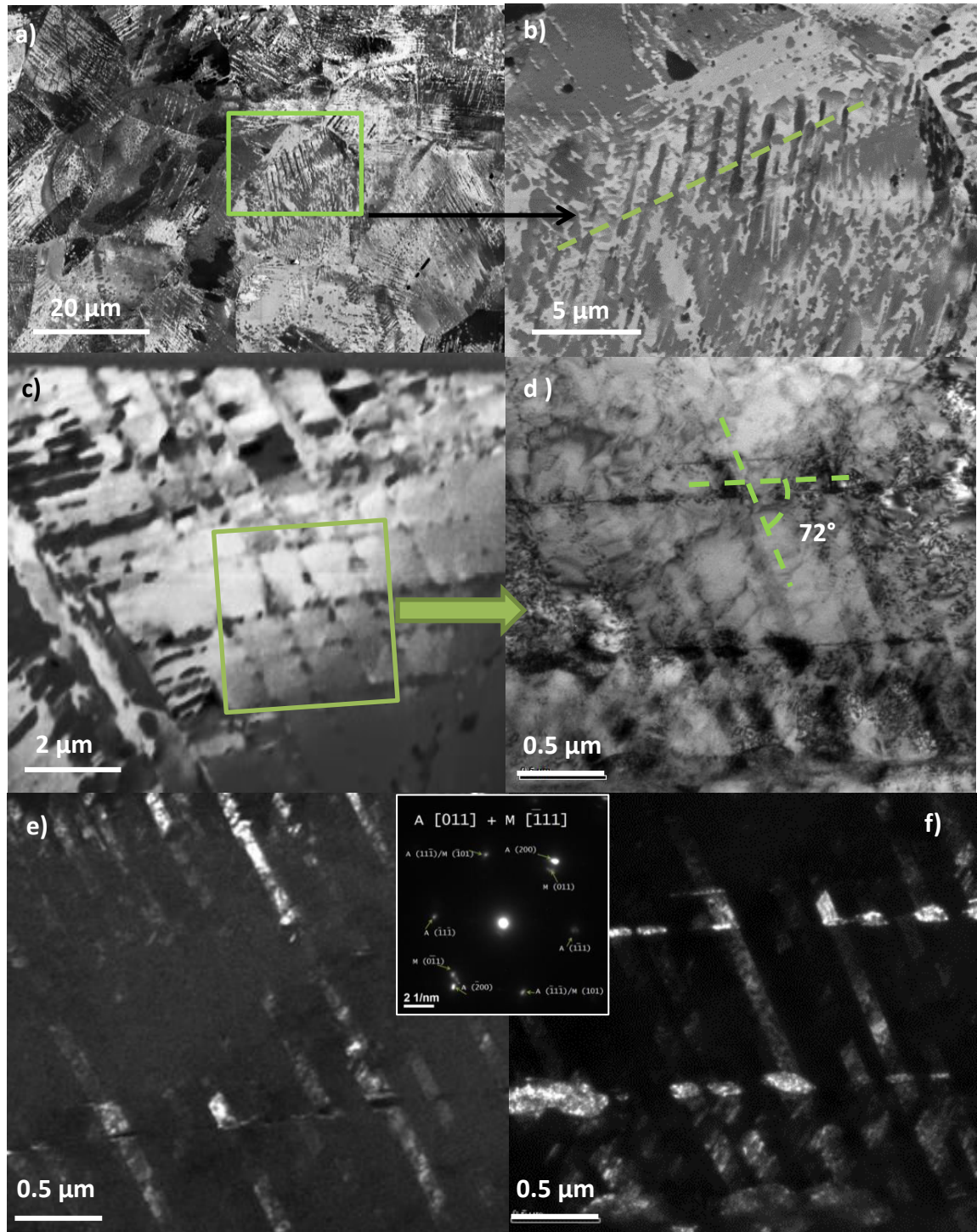


**Figure 100.** Characterization of the deformation structure in a SP sample by SIM. a) FIB image of the surface of a skin-passed sample; b) FIB image corresponding to a magnification of the area marked by the square in Figure 1a; c) SIM image of the cross-section obtained following the discontinuous line of Figure 1b; d) Bright field TEM image corresponding to the area marked by the square in Figure 1c; e) Dark field TEM image of austenite; f) Dark field TEM image of martensite, the correspondent diffraction pattern is shown in the inset between e) and f), where the phases are indexed using A for austenite and M for  $\alpha'$ -martensite.

After confirming the agreement between FIB and TEM images for macroscopically deformed samples, the next step was the characterization of the damage induced by monotonic nanoindentation. This was performed in austenitic grains oriented parallel to the  $\langle 111 \rangle$  axis, namely, the same grains, whose cross section was observed in Section 6.2.1 by TEM. Figure 101 shows the corresponding SIM image. It exhibits a rather homogenous microstructure with little pronounced deformation features. However, a small, dark grey patch can be observed directly under the imprint, surrounded by a more diffuse, lighter grey, large area. Comparing the location, shape and size of these features to the ones in section 6.2.1 (see Figure 82), and considering the contrast code established above, it can be concluded that the dark patch corresponds to the  $\alpha'$ -martensitic nanograin, while the surrounding diffuse zone represents the deformed austenitic matrix, featuring a high dislocation density.

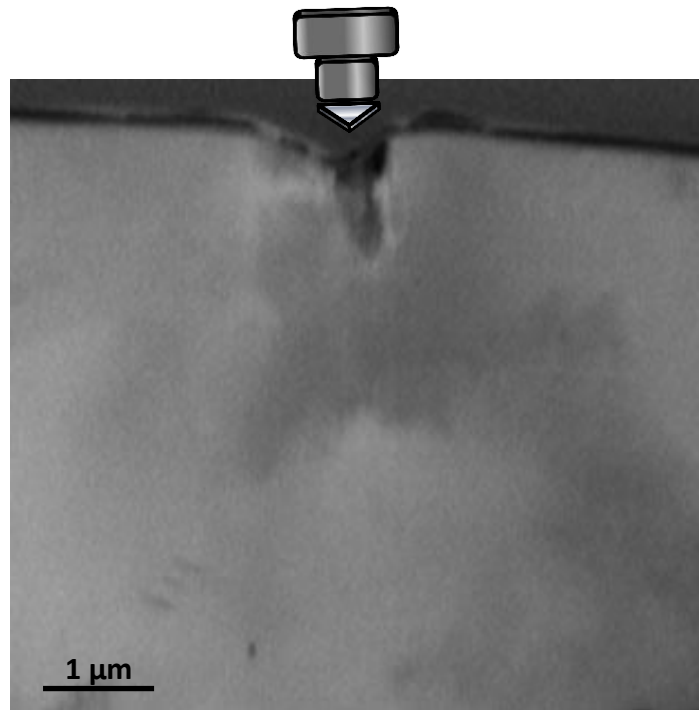


**Figure 101.** Cross section of a residual imprint after monotonic nanoindentation. The cross section was imaged by SIM previously to the lift-out of the corresponding TEM lamella (see Figure 82).

The main part of the study in this chapter concerns the deformation induced by cyclic nanoindentation, as presented in the following paragraphs.

Figure 102 represents in detail the microstructure of the austenitic  $\langle 111 \rangle$  oriented small grain subjected to 200 nanoindentation cycles, before the corresponding TEM lamella was extracted and observed in Chapter 6.2.6. So, Figure 102a shows the location of the residual imprint, as accessed by EBSD, while Figure 102b represents the corresponding FESEM image. The nanoindentation was placed



asymmetrically with respect to the center of the indented grain, allowing to access the influence of grain boundaries.

Noticeably, the indented grain is strongly confined, with its dimensions being rather small in comparison to the size of the residual imprint. In agreement with observations for other  $\langle 111 \rangle$  oriented grains in Chapter 5,  $\alpha'$ -martensite embryos nucleate at the shear band intersections at the sample surface surrounding the residual imprint. A selected series of cross-sections milled through the imprint, (as marked by dashed lines in Figure 102b) is represented in Figure 102c to 102f. Unlike in the case of monotonic indentation, after 200 indentation cycles, the whole austenitic grain shows a highly deformed substructure in the SIM image, which expands around the residual imprint and along the grain boundary. Auxiliary lines are tracing the different contrast for clarity.

Figure 102c shows that even relatively far from the center of the residual imprint (section corresponding to line 1 in Figure 102b), inhomogeneous contrast is observed and two different areas can be distinguished in the austenite grain. The sectioning of the imprint was performed until its center, as illustrated in Figure 102f corresponding to line 4 in Figure 4b.

The closer to the indentation center, the more pronounced becomes the presence of a dark martensitic zone. This zone grows from the center of the residual imprint, with an angle close to  $70.5^\circ$  (thus, parallel to a  $\{111\}$  slip plane), towards the closest grain boundary. Furthermore, dark contrast bands can be observed parallel adjacent to this grain boundary (see Figure 102e).

A dashed rectangle in Figure 102d marks to the location, where TEM lamella was extracted, namely the TEM lamella already presented in section 6.2.6 (see Figure 96). Comparing SIM images with TEM BF and DF images, and considering the previous findings, it can be stated that the dark-contrasted phase growing from the residual imprint towards the grain boundary is dislocation cell-type martensite, while the band parallel to the grain boundary is a martensitic lath evolved from a shear band. Figure 102e and f show that those two separate martensitic structures eventually meet and grow together. Moreover, the bright regions surrounding the martensitic phase in Figure 102 (marked by dashed lines), correspond to the deformed austenitic phase, as observed in Figure 96b. This phase exhibits a high dislocation density and can be considered as part of the plasticity zone resulting from the cumulative deformation.

Interestingly, SIM images give a better contrast and definition of the deformed microstructure, compared to TEM, especially for the dislocation cell-type martensite.

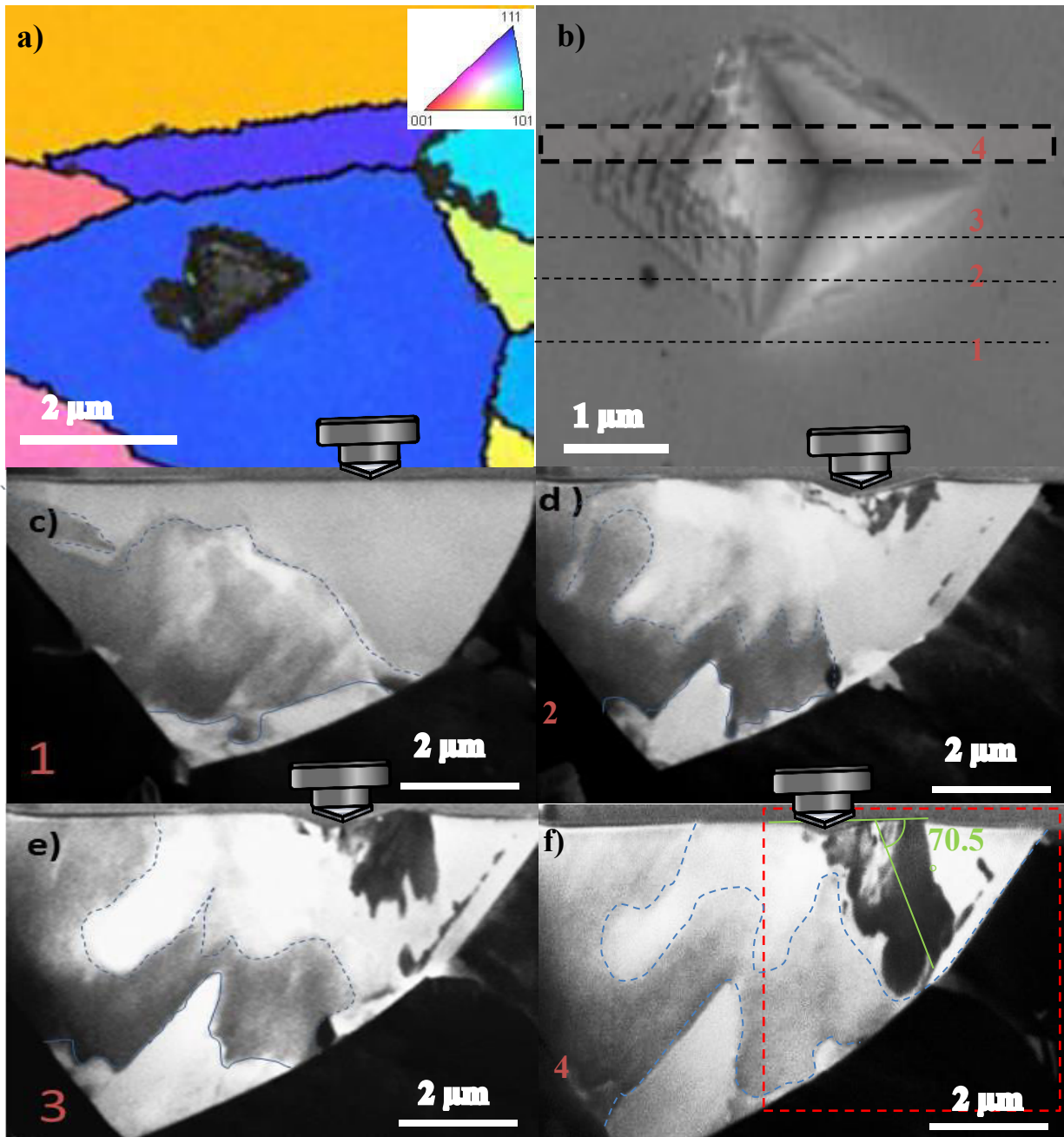
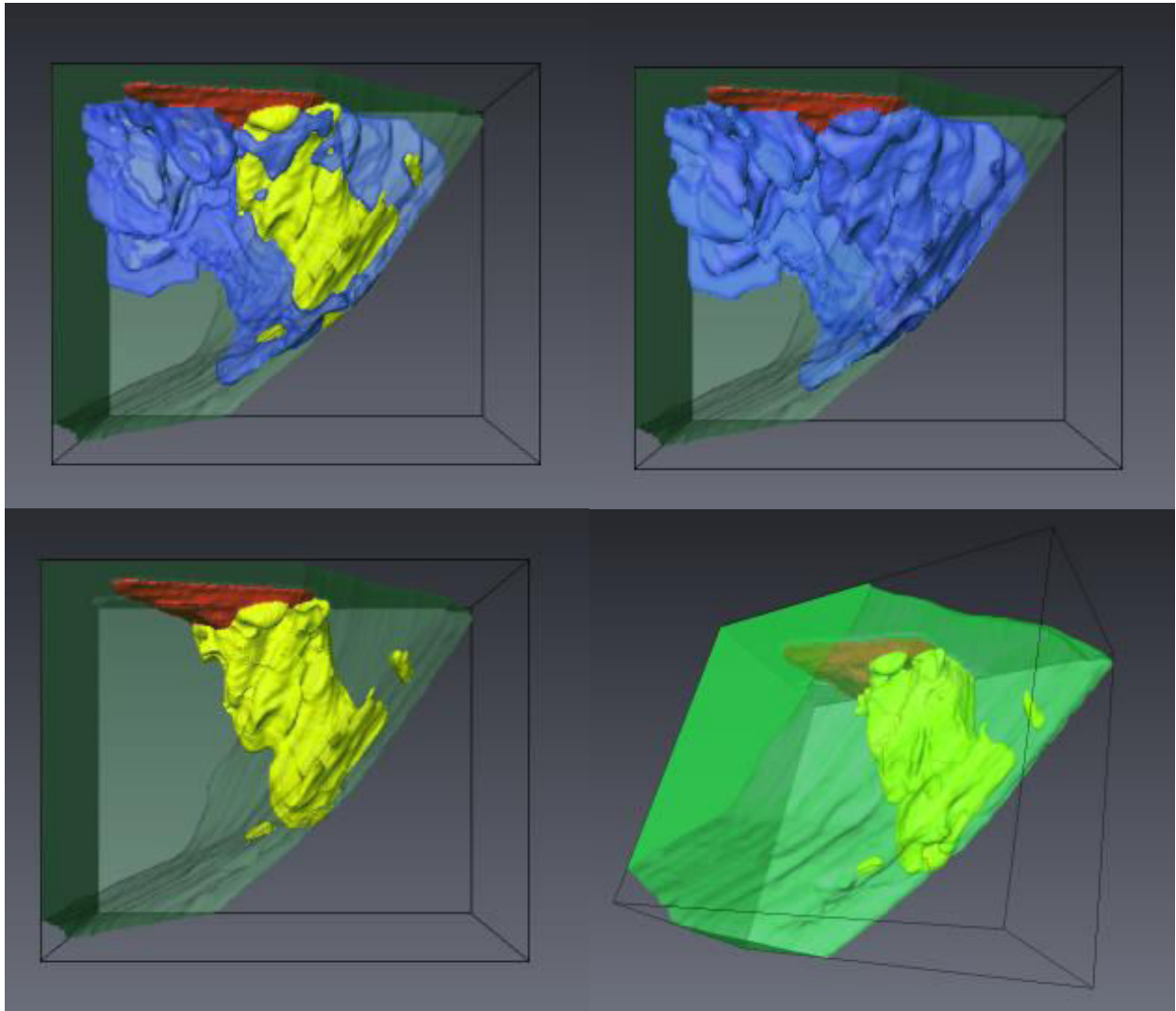


Figure 102. Cross section of a residual imprint after cyclic nanoindentation. a) EBSD IPF mapping, confirming that the imprint lies inside a  $\langle 111 \rangle$  oriented grain; b) FESEM surface image with auxiliary lines indicating the position of the cross sections represented in the figures below; c)-f) SIM images of the respective sections 1-4, auxiliary lines separate areas of different contrast.



**Figure 103. 3D tomographic reconstruction of the cross-sections under the nanoimprint produced by the cyclic indentation. Color code: Green – indented austenitic grain - red: residual imprint; yellow – martensitic grain; blue – deformation zone surrounding the martensitic grain.**

In order to achieve a better understanding of the dimensions of the plastic zone, a 3D reconstruction was carried out with a total of 72 sections of the imprint produced by the cyclic indentation. Figure 103 shows several images taken from the reconstructed volume. It is evident that the growth of the martensitic area occurs at the expense of the austenitic plastic zone, indicating that austenite deformation precedes the martensitic transformation, rather than being a competing process. Tomography visualizes particularly well that both the growth of the martensitic phase towards the grain boundary and the dissemination of both, martensitic and deformed austenitic structures, along the grain boundary.

Interestingly, in this particular case, martensite did not grow strictly vertically to the bulk of the grain, as was observed in Figure 96 and as would correspond to a superposition of several activated slip systems

under the nanoindenter tip, but instead only one slip system is active in the IPZ, namely the one which promotes the growth towards the closest grain boundary.

Resuming and comparing the deformation evolving during cyclic nanoindentation of spatially confined grains, the following kinetics can be assumed for the  $\alpha'$ -martensite:

1. Formation of  $\alpha'$ -martensitic nanoparticle in the IPZ below the nanoindenter.
2. Growth of this martensitic feature along the slip plane oriented towards the closest grain boundary.
3. Simultaneous formation of  $\alpha'$ -martensitic laths at the grain boundary, on slip planes lying most parallel to the grain boundary.
4. Coincidence and coalescence of the two features.

The process outlined above is in good correspondence with the change of the active slip system at the grain boundary, as observed in Figure 97.

### 7.3 Conclusion

Through three examples (macroscopic deformation by skin-pass, monotonic nanoindentation and cyclic nanoindentation) the usefulness of SIM imaging technique has been highlighted for the characterization of substructural evolution when metastable austenitic steels are deformed. The contrast provided by this technique can be directly related to  $\gamma \rightarrow \alpha'$  phase transformation, and to the accumulation of plastic deformation, allowing a detailed characterization of the surface, as well as of the bulk.

Compared to other advanced characterization techniques, such as EBSD for surface characterization and TEM for the bulk, SIM results being faster, easier and more cost efficient compared to the traditional techniques. Besides, especially in the case of sectional tomography, it can provide more complete information about the microstructural transformation in 3D. This makes FIB not only a powerful technique for sample preparation on small scale, but also for contrast-enhanced imaging.

## 8 Closing Discussion

Some of the main points to be highlighted within the present thesis are resumed in the following:

It has been shown that, as a function of austenitic grain size and crystallographic orientation, different dislocation arrangements are produced in metastable stainless steels when subjected to nanoindentation testing. Moreover, martensitic transformation is influenced by both factors. Thus,  $\alpha'$ -martensite was found to be closely related to the orientation relationship between active slip planes and loading axis. Also, all deformation mechanisms and plasticity transmission showed to be highly influenced by the stress localization at grain boundaries.

Reversible  $\epsilon$ -martensitic transformation, known from shape-memory alloys, has not been reported so far for stainless steels. Apparently, the chemical composition of the present alloy, especially the enrichment with nitrogen, promotes this characteristic. Within this thesis, it was found to occur after a certain number of nanoindentation cycles. This indicates that some dislocation organization must occur to facilitate the reversible phase transformation, as reported in literature<sup>189</sup>.

The nonlinearity at lower indentation loads, leading to the formation of elbows, is also in good agreement with reported literature for reversible phase transformation, as narrated in section Chapter 1.3.3. Also  $\epsilon$ -martensitic transformation was found to be anisotropic, since it followed the SN relationship and as a consequence, formed with preference in grains oriented appropriately with respect to the loading axis. This fact was evidenced by the hysteresis loop size recorded during cyclic nanoindentation tests, which was wider for grains oriented favorably for  $\epsilon$ -martensitic transformation. The reversible transformation behavior is likely originating from the fact that  $\epsilon$ -martensite plates formed under the applied loads had an average thickness below 1 nm, as determined in chapter 4, and thus, were not stable enough to persist after unloading. It is also worth mentioning that phase-transformation related pop-ins were found to originate from  $\epsilon$ -martensite, while  $\alpha'$ -martensite formation was not reflected in the P-h curves.

The viscoplastic behavior, as observed in section 4.2.2 is in agreement with the results of Misra et al. represented in curve in Figure 28 (Chapter 1). Thereby, viscoplastic behavior (discernible from the buckling of the unloading curve) took place only for indentation of austenite, but not for martensite. Thus, it can be concluded that the nanoindentation response observed within the present thesis results from austenite, and even after an elevated number of indentation cycles a large part of the material probed by the nanoindenter remains austenitic. In conventional macroscopic fatigue testing, softening behavior is known to occur in annealed stainless steels due to low energy dislocation arrangements<sup>245,246</sup>. This mechanism was also unambiguously observed by TEM in Chapter 6 within the present study. From this point of view, cyclic nanoindentation can be considered as a technique to analyze local fatigue behavior.

P-h curves showed that softening usually prevails over the hardening induced by phase transformation, whereas secondary hardening only occurred for certain crystallographic orientations (*i.e.*  $\langle 111 \rangle$ ), when martensite was formed and grew vertically under the residual imprint.

Also related to the cyclic softening, a time-dependent behavior was discerned: some researchers<sup>229,233,362–364</sup> found rate-dependence in AISI 304 and 316 stainless steels at room temperature. At low imposed strain, this behavior led to a cyclic softening, which prevailed over the cyclic hardening<sup>234</sup>. These results might be surprising for a metastable stainless steel, which can be expected to exhibit distinctive hardening behavior<sup>231</sup>. The key to explain the observed behavior is the small strain amplitude applied in the present study, while hardening is commonly recognized to occur when surpassing a certain minimum strain. Furthermore, it was shown that prestrain stabilizes the steel against further phase transformation going along with cyclic softening or hardening behavior.

Thus, nanoindentation provides the possibility to study the deformation behavior in a smaller strain range as by macroscopic testing techniques. On the other side, nanoindentation also allows working at significantly higher loads than those here applied. For understanding of the observed phenomena, the following two points must be considered:

On one hand, opposite to  $\gamma \rightarrow \alpha'$ ,  $\gamma \rightarrow \epsilon$ -martensite transformation implies a volume contraction<sup>365,366</sup>. Consequently, tensile deformation promotes  $\alpha'$ -martensite and suppresses  $\epsilon$ -martensite formation, while for compressive deformation the opposite is the case<sup>365</sup>. Thus, it is known that the pseudo-elastic response of established shape memory alloys is much more pronounced for nanoindentation than for tensile testing<sup>187</sup>. Accordingly, the onset of  $\alpha'$ -transformation is shifted in case of nanoindentation (predominantly compressive) to higher strain values as compared to typical macroscopic forming processes, such as cold rolling<sup>365</sup>. This explains why within the present study shear band formation was readily observed, whereas  $\alpha'$ -martensitic transformation was still in its initial state.

On the other hand, it is also known that  $\epsilon$ -martensitic transformation leads to softening<sup>367,368</sup>. This circumstance agrees very well with the softening observed below the kink, in case of elbow formation, as observed in Chapter 2. This low-slope region below the kink is where the majority of pop-ins related to reversible  $\epsilon$ -transformation has been detected. On the other hand, since TEM characterization revealed that at least some part of the formed  $\epsilon$ -martensite stabilized in form of shear bands and remained after unloading, the formation of those shear bands might contribute, together with dislocation motion, to the observed softening behavior.

The observed softening behavior also explains why deformation features were different when cycling in loading or displacement mode: in loading mode, the displacement or penetration depth increases with increasing cycles, leading to a significant accumulated strain, while in displacement mode the imposed deformation is mostly in the elastic (or pseudoelastic) range.

## 9 Final Conclusions

In the present thesis, deformation behavior of single austenitic grains in a polycrystalline metastable stainless steel has been accessed by nanoindentation. This instrumented testing technique has shown not only the advantage of providing a high-precision at small scale, but also, it can be employed selectively to investigate deformation mechanisms with a higher precision, and spatial resolution than conventional testing techniques.

Therefore, different specific test conditions, both for monotonic (*i.e.* only one indentation) and cyclic (*i.e.* repeated indentations at the same location) tests, were selected. Analysis of the obtained loading-unloading (P-h) curves, and their correlation with the substructural features discerned mainly by TEM, allowed to obtain the following insights concerning deformation mechanisms in metastable austenitic stainless steels:

- Qualitatively similar deformation mechanisms to those known from conventional macroscopic testing can be also induced by nanoindentation.
- Deformation behavior resulting from nanoindentation can be divided in local, *i.e.* directly related to the large shear stresses immediately in the IPZ, and general, *i.e.* extending over the whole indented grain.
- Nanoindentation-specific deformation structure comprehends local lattice rotations, nanostructured shear bands and subsequent formation of martensitic particles.
- General deformation structure comprehends homogeneous dislocation arrangement within the interior of the grain, formation of planar defects at preferential sites (*e.g.* grain boundaries) and plasticity transmission through grain boundaries.
- Both, general and nanoindentation-specific deformation, were highly anisotropic, depending on the crystallographic orientation of each grain.
- Mechanical response to indentation and the resulting deformation substructures are strongly dependent on volume confinement (determined by grain size and shape).
- AISI 301LN was found to deform at the onset of plasticity mainly by formation of shear bands. Other deformation structures, such as low energy dislocation arrangements or  $\alpha'$ -martensitic transformation occurred in succession.
- Reversible  $\varepsilon$ -martensite transformation takes places under nanoindentation loading.
- $\alpha'$ -martensite embryos nucleating at shear band intersections were observed to coalesce.

- Three types of pop-ins can be obtained from P-h curves, due to elastoplastic transmission,  $\gamma \leftrightarrow \epsilon$  transformation and transmission of plasticity across the grain boundaries, respectively.

On the other hand, also conclusions concerning the advanced characterization techniques can be drawn:

- Cyclic nanoindentation is a powerful tool for monitoring the evolution of deformation mechanisms insitu, while TEM is a powerful tool for characterization of the resulting deformation structure. The combination of deformation by nanoindentation and subsequent characterization by TEM carried out for different experimental conditions, allowed an ex-situ reconstruction of the underlying fundamental principles.
- It was shown that there is a good correspondence between the data recorded by the nanoindentation equipment and the related microstructure. Thus, from the sole analysis of the P-h curves, important information about dynamics of deformation, influence of grain boundaries, plasticity transfer and crystalline anisotropy can be gathered without any need for further time and cost-consuming characterization of the tested material.
- It was also confirmed by correlation between cyclic nanoindentation P-h curves and TEM studies that pop-ins at high loads (or elevated number of cycles), indeed correspond to transmission of plasticity.
- It is important to characterize both the surface and the bulk deformation substructures to obtain an integral understanding of the deformation behavior.
- The usefulness of the SIM imaging technique has been highlighted for the characterization of substructural evolution. Compared to other advanced characterization techniques, such as EBSD for surface characterization and TEM for the bulk, SIM results faster, easier and more cost efficient. In the case of sectional tomography, it can provide more complete information about the microstructural transformation in three dimensions.



## 10 Future Outlook

The present thesis comprehends an innovative approach regarding small-scale investigation of deformation mechanisms in metallic materials. No relevant basic studies were carried out before regarding cyclic nanoindentation in phase transforming steels, so this thesis can be considered as an introduction to this field. Certainly, many aspects need to be studied more in depth.

From the crystallographic point of view, only two directions, both oriented for multiple slip, were compared within the study of the crystalline anisotropy. For a more in-depth study, the deformation in other directions, especially in grains oriented for single slip, as well as the presence of crystalline anisotropy in prestrained steels, should be researched, more in detail.

On the other hand, due to the restricted possibility of TEM lamella preparation by FIB, being the latter a relatively expensive and time consuming method, only few selected deformation structures were studied. A more detailed study of the deformation evolution within the few first cycles can provide valuable information.

Also worth studying is the deformation for nanoindentations placed on the grain boundary, impacting simultaneously two contiguous grains, selected in relation with both their size and their crystallographic orientation.

The present work was carried out with a Berkovich indenter since preliminary studies revealed that a spherical tip did not produce a sufficiently large stress concentration to induce martensitic transformation. However, for materials where stress localization generated by a spherical tip is sufficient to achieve the desired material deformation, a corresponding study would certainly be of interest in order to investigate the strain-stress behavior.

It is also important to keep in mind that in nanoindentation creep tests, opposed to tensile creep tests, the contact area changes significantly with  $\Delta h$ . Thus, not only the strain, but also the stress evolve during the creep test. So, with increasing penetration depth the stress, and consequently the creep rate, decreases. Would the contact area stay constant, the creep strain can be expected to be higher than observed in this study. Thus, a set of reference tests with a flat punch should be carried out to determine the real creep behavior.

## 11 Bibliography

1. Misra, R. D. K. *et al.* Nanograined/Ultrafine-Grained Structure and Tensile Deformation Behavior of Shear Phase Reversion-Induced 301 Austenitic Stainless Steel. *Metall. Mater. Trans. A* **41**, 2162–2174 (2010).
2. Lamb, S. *Handbook of Stainless Steels and Nickel Alloys. Materials and Corrosion* (CASTI Publishing Inc., 2001). doi:10.1002/maco.200490050
3. Hamada, A. S., Karjalainen, L. P., Surya, P. K. C. V. & Misra, R. D. K. Fatigue behavior of ultrafine-grained and coarse-grained Cr–Ni austenitic stainless steels. *Mater. Sci. Eng. A* **528**, 3890–3896 (2011).
4. Karjalainen, L. Some strengthening methods for austenitic stainless steels. *Steel Res. Int.* **79**, (2008).
5. Spencer, K., Embury, J. D., Conlon, K. T., Véron, M. & Bréchet, Y. Strengthening via the formation of strain-induced martensite in stainless steels. *Mater. Sci. Eng. A* **387–389**, 873–881 (2004).
6. Rosen, A., Jago, R. & Kjer, T. Tensile properties of metastable stainless steels. *J. Mater. Sci.* **7**, 870–876 (1972).
7. Taheri, S., Hauet, A., Taleb, L. & Kpodekon, C. Micro-macro investigations about the fatigue behavior of pre-hardened 304L steel. *Int. J. Plast.* **27**, 1981–2004 (2011).
8. Talonen, J. & Hänninen, H. Formation of shear bands and strain-induced martensite during plastic deformation of metastable austenitic stainless steels. *Acta Mater.* **55**, 6108–6118 (2007).
9. Hedström, P. Deformation and martensitic phase transformation in stainless steels. (Luleå University of Technology, 2007).
10. Field, J. & Swain, M. Determining the mechanical properties of small volumes of material from submicrometer spherical indentations. *J. Mater. Res.* (1995).
11. Oliver, W. C. & Pharr, G. M. Measurement of hardness and elastic modulus by instrumented indentation: Advances in understanding and refinements to methodology. *J. Mater. Res.* **19**, 3–20 (2011).
12. Zaafarani, N., Raabe, D., Singh, R. N., Roters, F. & Zaefferer, S. Three-dimensional investigation of the texture and microstructure below a nanoindent in a Cu single crystal using 3D EBSD and crystal plasticity finite element simulations. *Acta Mater.* **54**, 1863–1876 (2006).
13. Diop, M. in *Nanoindentation in Materials Science* (InTech, 2012). doi:10.5772/50997
14. Roa, J. J. *et al.* Deformation of polycrystalline TRIP stainless steel micropillars. *Mater. Sci. Eng. A* **647**, 51–57 (2015).
15. Li, X. & Bhushan, B. Development of a nanoscale fatigue measurement technique and its application to ultrathin amorphous carbon coatings. *Scr. Mater.* **47**, 473–479 (2002).
16. Pfetting-Micklich, J. *et al.* On the crystallographic anisotropy of nanoindentation in pseudoelastic NiTi.

*Acta Mater.* **61**, 602–616 (2013).

17. Stinville, J. C., Tromas, C., Villechaise, P. & Templier, C. Anisotropy changes in hardness and indentation modulus induced by plasma nitriding of 316L polycrystalline stainless steel. *Scr. Mater.* **64**, 37–40 (2011).
18. Wang, Y., Raabe, D., Klüber, C. & Roters, F. Orientation dependence of nanoindentation pile-up patterns and of nanoindentation microtextures in copper single crystals. *Acta Mater.* **52**, 2229–2238 (2004).
19. Moharrami, N., Oila, A. & Bull, S. J. Extracting mechanical properties of copper coatings on oxidized silicon substrates by nanoindentation. *J. Phys. D. Appl. Phys.* **47**, 315104 (2014).
20. De Diego-Calderón, I., Santofimia, M. J., Molina-Aldareguia, J. M., Monclús, M. A. & Sabirov, I. Deformation behavior of a high strength multiphase steel at macro- and micro-scales. *Mater. Sci. Eng. A* **611**, 201–211 (2014).
21. Molnarova, M., Gavendova, P., Kvačák, T. & Kovác, F. NANOHARDNESS TESTING OF MULTIPHASE C-Mn-Si STEEL. *Chem. List.* **106**, 495–522 (2012).
22. Furnémont, Q., Kempf, M., Jacques, P. J. & Go, M. On the measurement of the nanohardness of the constitutive phases of TRIP-assisted multiphase steels. *Mater. Sci. Eng. A* **328**, 26–32 (2002).
23. Basu, S., Barsoum, M. W., Williams, A. D. & Moustakas, T. D. Spherical nanoindentation and deformation mechanisms in freestanding GaN films. *J. Appl. Phys.* **101**, 083522 (2007).
24. Skrzypczak, M., Guerret-Piecourt, C., Bec, S., Loubet, J.-L. & Guerret, O. Use of a nanoindentation fatigue test to characterize the ductile–brittle transition. *J. Eur. Ceram. Soc.* **29**, 1021–1028 (2009).
25. Amini, A., Cheng, C., Kan, Q., Naebe, M. & Song, H. Phase Transformation Evolution in NiTi Shape Memory Alloy under Cyclic Nanoindentation Loadings at Dissimilar Rates. *Sci Rep* **3**, 3412 (2013).
26. Saka, H. & Nagaya, G. Plan-view transmission electron microscopy observation of a crack tip in silicon. *Philos. Mag. Lett.* **72**, 251–255 (1995).
27. Lloyd, S. J. *et al.* Observations of nanoindents via cross-sectional transmission electron microscopy: a survey of deformation mechanisms. *Proc. R. Soc. A Math. Phys. Eng. Sci.* **461**, 2521–2543 (2005).
28. Qiao, X., Han, L., Zhang, W. & Gu, J. Nano-indentation investigation on the mechanical stability of individual austenite in high-carbon steel. *Mater. Charact.* **110**, 86–93 (2015).
29. Rester, M., Motz, C. & Pippan, R. The deformation-induced zone below large and shallow nanoindentations: A comparative study using EBSD and TEM. *Philos. Mag. Lett.* **88**, 879–887 (2008).
30. Ahn, T.-H. *et al.* Investigation of strain-induced martensitic transformation in metastable austenite using nanoindentation. *Scr. Mater.* **63**, 540–543 (2010).
31. ASM International. *ASM Handbook Vol 1 Properties and Selection Irons, Steels and High Performance Alloys. Fonderie* **1**, (ASM International, 2005).
32. Cobb, H. M. *The History of Stainless steel. ASM International* (ASM International, 2010).

doi:10.1016/S0026-0657(10)80254-1

33. Streicher, M. A. *Austenitic and Ferritic Stainless Steels. Uhlig's Corrosion Handbook: Third Edition* (John Wiley & Sons, 2000).
34. Schaeffler, A. L. Constitution diagram for stainless steel weld metal. *Met. Prog.* **56**, 680–680B (1949).
35. Davis, J. R. *ASM Speciality Handbook: Stainless Steels*. (ASM International, 1994).
36. Leffler, B. *Stainless steels and their properties*. (1996).
37. Eichelman, G. J. & Hull, F. C. The effect of composition on the temperature of spontaneous transformation of austenite to martensite in 18-8 type stainless steel. *Trans. ASM* **45**, 77–104 (1953).
38. Peterson, S., Mataya, M. & Matlock, D. The formability of austenitic stainless steels. *JOM* 54–58 (1997).
39. Llewellyn, D. T. Work hardening effects in austenitic stainless steels. *Mater. Sci. Technol.* **13**, 389–400 (1997).
40. Marshall, P. *Austenitic stainless steels: microstructure and mechanical properties*. (Elsevier Applied Science, 1984).
41. De Cooman, B. C. Structure-properties relationship in TRIP steels containing carbide-free bainite. *Curr. Opin. Solid State Mater. Sci.* **8**, 285–303 (2004).
42. Petrov, R., Kestens, L., Wasilkowska, A. & Houbaert, Y. Microstructure and texture of a lightly deformed TRIP-assisted steel characterized by means of the EBSD technique. *Mater. Sci. Eng. A* **447**, 285–297 (2007).
43. Furnémont, Q., Lacroix, G., Godet, S., Conlon, K. T. & Jacques, P. J. Critical Assessment of the Micromechanical Behaviour of Dual Phase and Trip-Assisted Multiphase Steels. *Can. Metall. Q.* **43**, 35–42 (2004).
44. Breedis, J. F. Martensitic transformations in iron-chromium- nickel alloys. *Trans. AIME* **230**, 1583–1596 (1964).
45. Silva, P., Abreu, H. & Albuquerque, V. Cold deformation effect on the microstructures and mechanical properties of AISI 301LN and 316L stainless steels. *Mater. Des.* (2011).
46. Pla-Ferrando, R., Sánchez-Caballero, S., Selles, M. a & Martínez, a V. TWIP/TRIP steels. Future trends in automotive industries. *Ann. ORADEA Univ.* **X**, 23–26 (2011).
47. Santofimia, M.J. , Zhao, L.b , Sietsma, J. Volume change associated to carbon partitioning from martensite to austenite. in *7th International Conference on Processing and Manufacturing of Advanced Materials, THERMEC'2011* **706-709**, 2290–2295 (Materials Science Forum, 2012).
48. Perdahcioğlu, E., Geijselaers, H. & Groen, M. Influence of plastic strain on deformation-induced martensitic transformations. *Scr. Mater.* **58**, 947–950 (2008).
49. Zackay, V., Parker, E. R., Fahr, D. & Busch, R. The enhancement of ductility in high-strength steels. *Trans. ASM* **60**, 252–259 (1967).

50. Kim, Y. H., Kim, K. Y. & Lee, Y. D. Nitrogen-Alloyed, Metastable Austenitic Stainless Steel for Automotive Structural Applications. *Mater. Manuf. Process.* **19**, 51–59 (2004).
51. Lo, K. H., Shek, C. H. & Lai, J. K. L. Recent developments in stainless steels. *Mater. Sci. Eng. R Reports* **65**, 39–104 (2009).
52. Nanga-Nyongha, S. Comportement et transformations martensitiques de deux aciers inoxydables austénitiques: effets de la température, de la vitesse et du chargement. (Mécanique [physics.med-ph]. ' Ecole Nationale Supérieure des Mines de Paris, 2008. Fran, cais., 2008).
53. Karaman, I., Sehitoglu, H., Maier, H. J. & Chumlyakov, Y. I. Competing mechanisms and modeling of deformation in austenitic stainless steel single crystals with and without nitrogen. *Acta Mater.* **49**, 3919–3933 (2001).
54. Karaman, I., Sehitoglu, H., Chumlyakov, Y. I., Maier, H. J. & Kireeva, I. V. Extrinsic stacking faults and twinning in Hadfield manganese steel single crystals. *Scr. Mater.* **44**, 337–343 (2001).
55. Lee, E. H. *et al.* On the origin of deformation microstructures in austenitic stainless steel: Part I - Microstructures. *Acta Mater.* **49**, 3269–3276 (2001).
56. Hull, D. & Bacon D. J. *Dislocations*. (Oxford Press, 1989).
57. H.Cottrell, A. *Dislocations and Plastic Flow in Crystals*. (Oxford Univ. Press, 1953). doi:10.1126/science.119.3095.551
58. Li, B., Yan, P. F., Sui, M. L. & Ma, E. Transmission electron microscopy study of stacking faults and their interaction with pyramidal dislocations in deformed Mg. *Acta Mater.* **58**, 173–179 (2010).
59. Carpenter, H. C. . & Tamura, S. Experiments on the Production of Large Copper Crystals. *Proc. R. Soc. London A* **113**, 28–43 (1926).
60. Christian, J. & Mahajan, S. Deformation twinning. *Prog. Mater. Sci.* **39**, 1–157 (1995).
61. Talonen, J., Nenonen, P., Pape, G. & Hänninen, H. Effect of Strain Rate on the Strain-Induced Austenite-Martensite Transformation and Mechanical Properties of Austenitic Stainless Steels. *Metall. Mater. Trans. A* **36**, 421–432 (2005).
62. Tsakiris, V. & Edmonds, D. V. Martensite and deformation twinning in austenitic steels. *Mater. Sci. Eng. A* **273-275**, 430–436 (1999).
63. Byun, T. ., Lee, E. . & Hunn, J. . Plastic deformation in 316LN stainless steel – characterization of deformation microstructures. *J. Nucl. Mater.* **321**, 29–39 (2003).
64. Misra, R. D. K., Zhang, Z., Jia, Z., Somani, M. C. & Karjalainen, L. P. Probing deformation processes in near-defect free volume in high strength–high ductility nanograined/ultrafine-grained (NG/UFG) metastable austenitic stainless steels. *Scr. Mater.* **63**, 1057–1060 (2010).
65. Remy, L. Kinetics of f.c.c. deformation twinning and its relationship to stress-strain behaviour. *Acta Metall.*

- 26, 443–451 (1978).
66. Hedström, P., Lienert, U., Almer, J. & Odén, M. Elastic strain evolution and  $\varepsilon$ -martensite formation in individual austenite grains during in situ loading of a metastable stainless steel. *Mater. Lett.* **62**, 338–340 (2008).
  67. Venables, J. A. The martensite transformation in stainless steel. *Philos. Mag.* **7**, 35–44 (1962).
  68. Fujita, H. & Ueda, S. Stacking faults and fcc ( $\gamma$ )  $\rightarrow$  hcp ( $\epsilon$ ) transformation in 188-type stainless steel. *Acta Metall.* **20**, 759–767 (1972).
  69. Brooks, J. W., Loretto, M. H. & Smallman, R. E. In situ observations of the formation of martensite in stainless steel. *Acta Metall.* **27**, 1829–1838 (1979).
  70. Redjaïmia, A. Les défauts de la structure cristalline Métal réel Défauts de structure. 2013–2014 (2014).
  71. Fang, X. F. & Dahl, W. Strain Hardening and Transformation Mechanism of Deformation-Induced Martensite Transformation in Metastable Austenitic Stainless Steels. **141**, 189–198 (1991).
  72. Nishiyama, Z., Fine, M. E., Meshii, M. & Wayman, C. M. Martensitic transformation. 480 (1978).
  73. Rémy, L. & Pineau, A. Twinning and strain-induced f.c.c.  $\rightarrow$  h.c.p. transformation on the mechanical properties of CoNiCrMo alloys. *Mater. Sci. Eng.* **26**, 123–132 (1976).
  74. Olson, G. B. & Cohen, M. Kinetics of strain-induced martensitic nucleation. *Metall. Trans. A* **6**, 791–795 (1975).
  75. Kumar, B. R. *et al.* Deformation-induced transformation textures in metastable austenitic stainless steel. *Mater. Sci. Eng. A* **429**, 205–211 (2006).
  76. Martin, S., Wolf, S., Martin, U., Krüger, L. & Jahn, a. Investigations on martensite formation in CrMnNi-TRIP steels. *ESOMAT 2009 - 8th Eur. Symp. Martensitic Transform.* **05022**, 1–7 (2009).
  77. Hedström, P., Lienert, U., Almer, J. & Odén, M. Stepwise transformation behavior of the strain-induced martensitic transformation in a metastable stainless steel. *Scr. Mater.* **56**, 213–216 (2007).
  78. Blanc, G. & Tricot, R. Transformations martensitiques dans les aciers inoxydables austénitiques Fe-Cr-Ni. *Rev. la Métallurgie* **70**, 257–514 (1973).
  79. Cina, B. A transitional h.c.p phase in the  $\gamma \rightarrow \alpha$  transformation in certain Fe-base alloys. *Acta Metall.* **6**, 748–762 (1958).
  80. Lagneborg, R. The martensite transformation in 18% Cr-8% Ni steels. *Acta Metall.* **12**, 823–843 (1964).
  81. Lee, T. H., Shin, E., Oh, C. S., Ha, H. Y. & Kim, S. J. Correlation between stacking fault energy and deformation microstructure in high-interstitial-alloyed austenitic steels. *Acta Mater.* **58**, 3173–3186 (2010).
  82. Lee, T.-H., Ha, H.-Y., Hwang, B., Kim, S.-J. & Shin, E. Effect of Carbon Fraction on Stacking Fault Energy of Austenitic Stainless Steels. *Metall. Mater. Trans. A* **43**, 4455–4459 (2012).

83. Solomon, N. & Solomon, I. Deformation induced martensite in AISI 316 stainless steel. *Rev. Metal.* **46**, 121–128 (2010).
84. Nohara, K., Ono, Y. & Ohashi, N. Composition and Grain Size Dependencies of Strain-induced Martensitic Transformation in Metastable Austenitic Stainless Steels. *Tetsu-to-Hagane* **63**, 772–782 (1977).
85. Sjöberg, J. INFLUENCE OF ANALYSIS ON PROPERTIES OF STAINLESS SPRING STEEL. *WIRE* **23**, 155–158 (1973).
86. Olson, G. B. A mechanism for the strain-induced martensitic transformations\* nucleation of. *J. LessCommon Met.* **28**, 107–118 (1972).
87. Olson, G. B. & Cohen, M. Stress-assisted isothermal martensitic transformation: Application to TRIP steels. *Metall. Trans. A* **11**, 1907–1914 (1982).
88. Lecroise, F. & Pineau, a. Martensitic Transformations Induced By Plastic-Deformation in Fe-Ni-Cr-C System. *Metall. Trans.* **3**, 387–396 (1972).
89. Suzuki, T. *et al.* Plastic deformation and martensitic transformation in an iron-base alloy. *Scr. Metall.* **10**, 353–358 (1976).
90. Bunshah, R. & Mehl, R. Rate of propagation of martensite. *Trans. AIME* **197**, 1251–1258 (1953).
91. Bhadeshia, H. K. D. H. Martensite in steels. *Mater. Sci. Metall.* 1–12 (2002).
92. Kurdjumov, G. & Sachs, G. Z. Over the mechanisms of steel hardening. *Z. Phys.* **64**, 325 (1930).
93. Pawlak, S. Austenite stability in the high strength metastable stainless steels. *J. Achiev. Mater. Manuf. Eng.* **22**, 2–5 (2007).
94. Humbert, M., Petit, B., Bolle, B. & Gey, N. Analysis of the  $\gamma \rightarrow \epsilon \rightarrow \alpha'$  variant selection induced by 10% plastic deformation in 304 stainless steel at -60°C. *Mater. Sci. Eng. A* **454-455**, 508–517 (2007).
95. Venables, J. The martensite transformation in stainless steel. *Philos. Mag.* **7**, 35–44 (1961).
96. Murr, L. E., Staudhammer, K. P. & Hecker, S. S. Effects of Strain State and Strain Rate on Deformation-Induced Transformation in 304 Stainless Steel: Part II. Microstructural Study. *Metall. Trans. A* **13**, 627–635 (1982).
97. Brooks, J. W., Loretto, M. H. & Smallman, R. E. Direct observations of Martensite Nuclei in Stainless steel. *Acta Metall.* **27**, 1839–1847 (1979).
98. Staudhammer, K., Murr, L. & Hecker, S. Nucleation and evolution of strain-induced martensitic (bcc) embryos and substructure in stainless steel: a transmission electron microscope study. *Acta Metall.* **31**, 267–274 (1983).
99. Sabooni, S., Karimzadeh, F., Enayati, M. H. & Ngan, a. H. W. The role of martensitic transformation on bimodal grain structure in ultrafine grained AISI 304L stainless steel. *Mater. Sci. Eng. A* **636**, 221–230 (2015).

100. Seol, J. B., Jung, J. E., Jang, Y. W. & Park, C. G. Influence of carbon content on the microstructure, martensitic transformation and mechanical properties in austenite/-martensite dual-phase Fe-Mn-C steels. *Acta Mater.* **61**, 558–578 (2013).
101. Misra, R. D. K., Venkatsurya, P., Wu, K. M. & Karjalainen, L. P. Ultrahigh strength martensite–austenite dual-phase steels with ultrafine structure: The response to indentation experiments. *Mater. Sci. Eng. A* **560**, 693–699 (2013).
102. Lee, W. S. & Lin, C. F. Morphologies and characteristics of impact-induced martensite in 304L stainless steel. *Scr. Mater.* **43**, 777–782 (2000).
103. Sun, B. L. Adams, W. E. King, S. Observations of lattice curvature near the interface of a deformed aluminium bicrystal. *Philos. Mag. A* **80**, 9–25 (2000).
104. Bilby, B. & Eshelby, J. D. in *Fracture, an advanced treatise* 99–182 (1968).
105. Tanaka, K. & Mura, T. A Dislocation Model for Fatigue Crack Initiation. *J. Appl. Mech.* **48**, 97–103 (1981).
106. Wo, P. C. & Ngan, A. H. W. Investigation of slip transmission behavior across grain boundaries in polycrystalline Ni3Al using nanoindentation. *J. Mater. Res.* **19**, 189–201 (2004).
107. Gutierrez-Urrutia, I. & Raabe, D. Dislocation and twin substructure evolution during strain hardening of an Fe–22wt.% Mn–0.6wt.% C TWIP steel observed by electron channeling contrast imaging. *Acta Mater.* **59**, 6449–6462 (2011).
108. Allain, S., Chateau, J. P., Bouaziz, O., Migot, S. & Guelton, N. Correlations between the calculated stacking fault energy and the plasticity mechanisms in Fe-Mn-C alloys. *Mater. Sci. Eng. A* **387-389**, 158–162 (2004).
109. Brofman, P. J. & Brofman, P.J., Ansell, G. S. On the Effect of Carbon on the Stacking Fault Energy of Austenitic Stainless Steels. *Metall. Trans. A* **9A**, (1978).
110. Bracke, L. & Mertens, G. Influence of phase transformations on the mechanical properties of high-strength austenitic Fe-Mn-Cr steel. ... *Mater. Trans. A* (2006).
111. Schramm, R. E. & Reed, R. P. Stacking fault energies of seven commercial austenitic stainless steels. *Metall. Trans. A* **6**, 1345–1351 (1975).
112. Mirzadeh, H. & Najafizadeh, a. Correlation between processing parameters and strain-induced martensitic transformation in cold worked AISI 301 stainless steel. *Mater. Charact.* **59**, 1650–1654 (2008).
113. Suzuki, T., Kojima, H., Suzuki, K., Hashimoto, T. & Ichihara, M. An experimental study of the martensite nucleation and growth in 18/8 stainless steel. *Acta Metall.* **25**, 1151–1162 (1977).
114. Talonen, J. Effect of strain-induced  $\alpha'$ -martensite transformation on mechanical properties of metastable austenitic stainless steels. (Helsinki University of Technology, 2007).
115. Chatterjee, S., Wang, H.-S., Yang, J. R. & Bhadeshia, H. K. D. H. Mechanical stabilisation of austenite. *Mater. Sci. Technol.* **22**, 641–644 (2006).



116. Maréchal, D. Linkage between mechanical properties and phase transformations in a 301LN austenitic stainless steel. (THE UNIVERSITY OF BRITISH COLUMBIA, 2011).
117. Hamada, A. S., Karjalainen, L. P., Misra, R. D. K. & Talonen, J. Contribution of deformation mechanisms to strength and ductility in two Cr-Mn grade austenitic stainless steels. *Mater. Sci. Eng. A* **559**, 336–344 (2013).
118. Gavriljuk, V. . *et al.* Grain boundary strengthening in austenitic nitrogen steels. *Mater. Sci. Eng. A* **271**, 14–21 (1999).
119. Stoltz, R. E. & Vander Sande, J. B. The effect of nitrogen on stacking fault energy of Fe-Ni-Cr-Mn steels. *Metall. Trans. A* **11**, 1033–1037 (1980).
120. Fujikura, M., Takada, K. & Ishida, K. EFFECT OF MANGANESE AND NITROGEN ON MECHANICAL-PROPERTIES OF FE-18 PERCENT CR-10 PERCENT NI STAINLESS-STEELS. *Trans. Iron Steel Inst. Japan* **15**, 565–469 (1975).
121. Yakubtsov, I. A., Ariapour, A. & Perovic, D. D. Effect of nitrogen on stacking fault energy of f.c.c. iron-based alloys. *Acta Mater.* **47**, 1271–1279 (1999).
122. Masumura, T. *et al.* The difference in thermal and mechanical stabilities of austenite between carbon- and nitrogen-added metastable austenitic stainless steels. *Acta Mater.* **84**, 330–338 (2015).
123. Vogt, J.-B. Effective Stresses and Microstructure in Cyclically Deformed 316L Austenitic Stainless Steel : Effect of Temperature and Nitrogen Content. *Fatigue Fract. Eng. Mater. Struct.* **16**, 555–564 (1993).
124. Maeng, W. & Kim, M. Comparative study on the fatigue crack growth behavior of 316L and 316LN stainless steels: effect of microstructure of cyclic plastic strain zone at crack tip. *J. Nucl. Mater.* **282**, 32–39 (2000).
125. Prasad Reddy, G. V., Sandhya, R., Sankaran, S. & Laha, K. On the Relationship Between Cyclic Deformation Behavior and Slip Mode in 316LN Stainless Steel with Varying Nitrogen Content. *Trans. Indian Inst. Met.* **69**, 303–308 (2016).
126. Prasad Reddy, G. V., Sandhya, R., Sankaran, S. & Mathew, M. D. Low Cycle Fatigue Behavior of 316LN Stainless Steel Alloyed with Varying Nitrogen Content. Part I. *Metall. Mater. Trans. A* 1–11 (2014). doi:10.1007/s11661-014-2429-4
127. Bai, Y. *et al.* Improvement of fatigue properties in type 304 stainless steel by annealing treatment in nitrogen gas. *Mater. Sci. Eng. A* **607**, 578–588 (2014).
128. Brofman, P.J., Ansell, G. S. On the Effect of Fine Grain Size on the Ms Temperature in Fe-27Ni-O.025C Alloys. *Metall. Mater. Trans. A* **14**, 2–4 (1983).
129. Jimenez-Melero, E. *et al.* Martensitic transformation of individual grains in low-alloyed TRIP steels. *Scr. Mater.* **56**, 421–424 (2007).
130. Barsoum, M. W., Murugaiah, A., Kalidindi, S. R., Zhen, T. & Gogotsi, Y. Kink bands, nonlinear elasticity and nanoindentations in graphite. *Carbon N. Y.* **42**, 1435–1445 (2004).

131. Jun, J.-H. & Choi, C.-S. Variation of stacking fault energy with austenite grain size and its effect on the MS temperature of  $\gamma \rightarrow \epsilon$  martensitic transformation in Fe–Mn alloy. *Mater. Sci. Eng. A* **257**, 353–356 (1998).
132. Misra, R. D. K. *et al.* Interplay between grain structure, deformation mechanisms and austenite stability in phase-reversion-induced nanograined/ultrafine-grained austenitic ferrous alloy. *Acta Mater.* **84**, 339–348 (2015).
133. Shrinivas, V., Varma, S. K. & Murr, L. E. Deformation-induced martensitic characteristics in 304 and 316 stainless steels during room-temperature rolling. *Metall. Mater. Trans. A* **26**, 661–671 (1995).
134. Mateo, A., Zapata, A. & Fargas, G. Improvement of mechanical properties on metastable stainless steels by reversion heat treatments. *IOP Conf. Ser. Mater. Sci. Eng.* **48**, 012001 (2013).
135. Di Schino, A. & Kenny, J. M. Grain size dependence of the fatigue behaviour of a ultrafine-grained AISI 304 stainless steel. *Mater. Lett.* **57**, 3182–3185 (2003).
136. Choi, I.-C., Yoo, B.-G., Kim, Y.-J. & Jang, J. Indentation creep revisited. *J. Mater. Res.* **27**, 3–11 (2012).
137. Jin, J.-E., Jung, Y.-S. & Lee, Y.-K. Effect of grain size on the uniform ductility of a bulk ultrafine-grained alloy. *Mater. Sci. Eng. A* **449-451**, 786–789 (2007).
138. Hall, E. O. The Deformation and Ageing of Mild Steel: III Discussion of Results. *Proc. Phys. Soc. Sect. B* **64**, 747 (1951).
139. Petch, N. J. The Cleavage Strength of Polycrystals. *J. Iron Steel Inst* **174**, 25 – 28 (1953).
140. Kashyap, B. P. & Tangri, K. On the Hall-Petch relationship and substructural evolution in type 316L stainless steel. *Acta Metall. Mater.* **43**, 3971–3981 (1995).
141. Rajasekhara, S., Ferreira, P. J., Karjalainen, L. P. & Kyröläinen, a. Hall–Petch Behavior in Ultra-Fine-Grained AISI 301LN Stainless Steel. *Metall. Mater. Trans. A* **38**, 1202–1210 (2007).
142. Sinclair, C. W., Proudhon, H. & Mithieux, J. D. Work Hardening in a Fine Grained Austenitic Stainless Steel. *Mater. Sci. Forum* **539-543**, 4714–4719 (2007).
143. Hedström, P., Lindgren, L. & Almer, J. Load partitioning and strain-induced martensite formation during tensile loading of a metastable austenitic stainless steel. *Metall. Mater. Trans. A* (2009).
144. Hecker, S. S., Stout, M. G., Staudhammer, K. P. & Smith, J. L. Effects of Strain State and Strain Rate on Deformation-Induced Transformation in 304 Stainless Steel: Part I. Magnetic Measurements and Mechanical Behavior. *Metall. Trans. A* **13**, 619–626 (1982).
145. Villechaise, P., Sabatier, L. & Girard, J. C. On slip band features and crack initiation in fatigued 316L austenitic stainless steel: Part 1: Analysis by electron back-scattered diffraction and atomic force microscopy. *Mater. Sci. Eng. A* **323**, 377–385 (2002).
146. Obrtlík, K., Kruml, T. & Polák, J. Dislocation structures in 316L stainless steel cycled with plastic strain amplitudes over a wide interval. *Mater. Sci. Eng. A* **187**, 1–9 (1994).

147. Mateo, A. *et al.* Cyclic deformation behaviour of superduplex stainless steels. *Mater. Sci. Eng. A Structural Mater. Prop. Microstruct. Process.* **314**, 176–185 (2001).
148. Mateo, A., Llanes, L., Iturgoyen, L. & Anglada, M. Cyclic stress-strain response and dislocation substructure evolution of a ferrite-austenite stainless steel. *Acta Mater.* **44**, 1143–1153 (1996).
149. Bayerlein, M., Christ, H. J. & Mughrabi, H. Plasticity-induced martensitic transformation during cyclic deformation of AISI 304L stainless steel. *Mater. Sci. Eng. A* **114**, (1989).
150. Baudry, G. & Pineau, A. Influence of strain-induced martensitic transformation on the low-cycle fatigue behavior of a stainless steel. *Mater. Sci. Eng.* **28**, 229–242 (1977).
151. Chanani, G. R., Antolovich, S. D. & Gerberich, W. W. Fatigue crack propagation in TRIP steels. *Metall. Trans.* **3**, 2661–2672 (1972).
152. Hong, S. G., Lee, S. B. & Byun, T. S. Temperature effect on the low-cycle fatigue behavior of type 316L stainless steel: Cyclic non-stabilization and an invariable fatigue parameter. *Mater. Sci. Eng. A* **457**, 139–147 (2007).
153. Müller-Bollenhagen, C., Zimmermann, M. & Christ, H.-J. Very high cycle fatigue behaviour of austenitic stainless steel and the effect of strain-induced martensite. *Int. J. Fatigue* **32**, 936–942 (2010).
154. Stolarz, J., Baffie, N. & Magnin, T. Fatigue short crack behaviour in metastable austenitic stainless steels with different grain sizes. *Mater. Sci. Eng. A* **319-321**, 521–526 (2001).
155. Roth, I., Kübbeler, M., Krupp, U., Christ, H.-J. & Fritzen, C.-P. Crack initiation and short crack growth in metastable austenitic stainless steel in the high cycle fatigue regime. *Procedia Eng.* **2**, 941–948 (2010).
156. Oliver, W. C. & Pharr, G. M. An improved technique for determining hardness and elastic modulus using load and displacement sensing indentation experiments. (1992).
157. Anton Paar. *The Ultra Nanoindentation Tester: New generation of thermal drift free indentation.* (2016).
158. Pharr, G. M. Measurement of mechanical properties by ultra-low load indentation. *Mater. Sci. Eng. A* **253**, 151–159 (1998).
159. Li, X., Diao, D. & Bhushan, B. Fracture mechanisms of thin amorphous carbon films in nanoindentation. *Acta Mater.* **45**, 4453–4461 (1997).
160. Fischer-Cripps, A. A review of analysis methods for sub-micron indentation testing. *Vacuum* **58**, 569–585 (2000).
161. Hertz, H. R. Miscellaneous papers. *Macmillan Co. Ltd* **92**, 156–171 (1896).
162. Herbert, E. ., Pharr, G. ., Oliver, W. ., Lucas, B. . & Hay, J. . On the measurement of stress–strain curves by spherical indentation. *Thin Solid Films* **398-399**, 331–335 (2001).
163. Shim, S., Bei, H., George, E. P. & Pharr, G. M. A different type of indentation size effect. *Scr. Mater.* **59**, 1095–1098 (2008).

164. Johnson, K. L. Contact Mechanics. *Journal of the American Chemical Society* **37**, 1–17 (1985).
165. Nix, W. & Gao, H. Indentation size effects in crystalline materials: a law for strain gradient plasticity. *J. Mech. Phys. Solids* **46**, (1998).
166. Fleck, N. A., Hutchinson, J. W. & Fleck. A Phenomenological Theory for Strain Gradient Effects in Plasticity. *J. Mech. Phys. solids* **185**, 185–192 (2001).
167. Stelmashenko, N. A., Walls, M. G., Brown, L. M. & Milman, Y. V. Microindentations on W and Mo oriented single crystals: An STM study. *Acta Metall. Mater.* **41**, 2855–2865 (1993).
168. Schuh, C. A., Mason, J. K. & Lund, A. C. Quantitative insight into dislocation nucleation from high-temperature nanoindentation experiments. *Nat. Mater.* **4**, 617–21 (2005).
169. Kim, Y.-J. *et al.* Martensitic phase transformation and pop-in in compression of austenitic steel nanoplates observed in situ by transmission electron microscopy. *Mater. Lett.* **75**, 107–110 (2012).
170. Bei, H., Gao, Y., Shim, S., George, E. & Pharr, G. Strength differences arising from homogeneous versus heterogeneous dislocation nucleation. *Phys. Rev. B* **77**, 060103 (2008).
171. Kang, S., Jung, Y.-S., Yoo, B.-G., Jang, J. & Lee, Y.-K. Orientation-dependent indentation modulus and yielding in a high Mn twinning-induced plasticity steel. *Mater. Sci. Eng. A* **532**, 500–504 (2012).
172. He, B., Huang, M., Liang, Z. & Ngan, A. Nanoindentation investigation on the mechanical stability of individual austenite grain in a medium Mn Transformation-Induced Plasticity Steel. *Scr. Mater.* **69**, 215–218 (2013).
173. Misra, R. D. K., Venkatsurya, P. K. C., Somani, M. C. & Karjalainen, L. P. Nanoscale Deformation Behavior of Phase-Reversion Induced Austenitic Stainless Steels: The Interplay Between Grain Size from Nano-Grain Regime to Coarse-Grain Regime. *Metall. Mater. Trans. a-Physical Metall. Mater. Sci.* **43A**, 5286–5297 (2012).
174. Misra, R. D. K. *et al.* Nanoscale deformation experiments on the strain rate sensitivity of phase reversion induced nanograined/ultrafine-grained austenitic stainless steels and comparison with the coarse-grained counterpart. *Mater. Sci. Eng. A* **548**, 161–174 (2012).
175. Misra, R. D. K. *et al.* Nanomechanical insights into the deformation behavior of austenitic alloys with different stacking fault energies and austenitic stability. *Mater. Sci. Eng. A* **528**, 6958–6963 (2011).
176. Misra, R. D. K. *et al.* Nanograined/ultrafine-grained structure and tensile deformation behavior of shear phase reversion-induced 301 austenitic stainless steel. *Metall. Mater. Trans. A Phys. Metall. Mater. Sci.* **41**, 2162–2174 (2010).
177. Sekido, K. *et al.* Nanoindentation/atomic force microscopy analyses of  $\epsilon$ -martensitic transformation and shape memory effect in Fe–28Mn–6Si–5Cr alloy. *Scr. Mater.* **65**, 942–945 (2011).
178. Taylor M.A. Plastic strain in metals. 307–325 (1938).

179. Ahn, T.-H., Lee, S. B., Park, K.-T., Oh, K. H. & Han, H. N. Strain-induced  $\epsilon$ -martensite transformation during nanoindentation of high-nitrogen steel. *Mater. Sci. Eng. A* **598**, 56–61 (2014).
180. Packard, C. E., Witmer, L. M. & Schuh, C. A. Hardening of a metallic glass during cyclic loading in the elastic range. *Appl. Phys. Lett.* **92**, 0–3 (2008).
181. Packard, C. E., Homer, E. R., Al-Aqeeli, N. & Schuh, C. a. Cyclic hardening of metallic glasses under Hertzian contacts: Experiments and STZ dynamics simulations. *Philos. Mag.* **90**, 1373–1390 (2010).
182. Packard, C. E. E., Franke, O., Homer, E. R. R. & Schuh, C. a. A. Nanoscale strength distribution in amorphous versus crystalline metals. *J. Mater. Res.* **25**, 2251–2263 (2010).
183. Basu, S. & Barsoum, M. Deformation micromechanisms of ZnO single crystals as determined from spherical nanoindentation stress–strain curves. *J. Mater. Res.* 1–8 (2007). doi:10.1557/JMR.2007.0305
184. Barsoum, M. W., Zhen, T., Kalidindi, S. R., Radovic, M. & Murugaiah, a. Fully reversible, dislocation-based compressive deformation of Ti<sub>3</sub>SiC<sub>2</sub> to 1 GPa. *Nat. Mater.* **2**, 107–111 (2003).
185. Basu, S., Barsoum, M. W. & Kalidindi, S. R. Sapphire: A kinking nonlinear elastic solid. *J. Appl. Phys.* **99**, (2006).
186. Amini, A., Cheng, C. & Asgari, A. Combinational rate effects on the performance of nano-grained pseudoelastic Nitinol. *Mater. Lett.* **105**, 98–101 (2013).
187. Zhang, H. S. & Komvopoulos, K. Nanoscale Pseudoelasticity of Single-crystal Cu-Al-Ni shape-memory Alloy Induced by Cyclic Nanoindentation. *J. Mater. Sci.* **41**, 5021–5024 (2006).
188. Arciniegas, M., Gaillard, Y., Peña, J., Manero, J. M. & Gil, F. J. Thermoelastic phase transformation in TiNi alloys under cyclic instrumented indentation. *Intermetallics* **17**, 784–791 (2009).
189. Pan, G. *et al.* Superelasticity of TiNi thin films induced by cyclic nanoindentation deformation at nanoscale. *Mater. Sci. Eng. A* **600**, 8–11 (2014).
190. Gogotsi, Y. & Domnich, V. Cyclic nanoindentation and Raman microspectroscopy study of phase transformations in semiconductors. *J. Mater. ...* 871–879 (2000).
191. Oliver, D. J., Bradby, J. E., Ruffell, S., Williams, J. S. & Munroe, P. Nanoindentation-induced phase transformation in relaxed and unrelaxed ion-implanted amorphous germanium. *J. Appl. Phys.* **106**, 093509 (2009).
192. Rao, R., Bradby, J. E., Ruffell, S. & Williams, J. S. Nanoindentation-induced phase transformation in crystalline silicon and relaxed amorphous silicon. *Microelectronics J.* **38**, 722–726 (2007).
193. Jang, J. Il, Lance, M. J., Wen, S. & Pharr, G. M. Evidence for nanoindentation-induced phase transformations in germanium. *Appl. Phys. Lett.* **86**, 1–3 (2005).
194. Naimi-Jamal, M. R. & Kaupp, G. Quantitative evaluation of nanoindents: Do we need more reliable mechanical parameters for the characterization of materials? *Zeitschrift fuer Met. Res. Adv. Tech.* **96**, 1226–

- 1236 (2005).
195. Lian, D. & Lin, P. L. Berkovich nanoindentation on single SiGe epitaxial films. *Microelectron. Reliab.* **56**, 66–72 (2016).
  196. Domnich, V., Gogotsi, Y. & Dub, S. Effect of phase transformations on the shape of the unloading curve in the nanoindentation of silicon. *Appl. Phys. Lett.* **76**, 2214 (2000).
  197. Huang, H. & Yan, J. New insights into phase transformations in single crystal silicon by controlled cyclic nanoindentation. *Scr. Mater.* **102**, 35–38 (2015).
  198. Chang, L. & Zhang, L. C. Deformation mechanisms at pop-out in monocrystalline silicon under nanoindentation. *Acta Mater.* **57**, 2148–2153 (2009).
  199. Fang, T.-H., Chang, W.-J., Lin, C.-M. & Chang, C.-C. Cyclic Nanoindentation of Semiconductor and Metal Thin Films. *Int. J. Mod. Phys. B* **23**, 5639–5647 (2009).
  200. Misra, R. D. K., Zhang, Z., Venkatasurya, P. K. C., Somani, M. C. & Karjalainen, L. P. The effect of nitrogen on the formation of phase reversion-induced nanograined/ultrafine-grained structure and mechanical behavior of a Cr-Ni-N steel. *Mater. Sci. Eng. A* **528**, 1889–1896 (2011).
  201. Xiao, L. *et al.* Lattice-parameter variation with carbon content of martensite. I. X-ray-diffraction experimental study. *Phys. Rev. B* **52**, 9970–9978 (1995).
  202. Petein, A. On the interactions between strain-induced phase transformation and mechanical properties in Mn-Si-Al steels and Ni-Cr austenitic steels. (Université Catholique de Louvain, 2007).
  203. Nascimento-Borges, F. C. Iron Based Shape Memory Alloys: Mechanical and Structural Properties, Shape Memory Alloys - Processing, Characterization and Applications. *Shape Mem. Alloy. – Process. Charact. Appl.* 116–128 (2013).
  204. Tavares, S. S. M., Neto, J. M., da Silva, M. R., Vasconcelos, I. F. & de Abreu, H. F. G. Magnetic properties and  $\alpha'$  martensite quantification in an AISI 301LN stainless steel deformed by cold rolling. *Mater. Charact.* **59**, 901–904 (2008).
  205. Angel, T. Formation of Martensite in Austenitic Stainless Steel. *J. Iron Steel Inst.* **177**, 165–174 (1954).
  206. Choi, J.-Y. & Jin, W. Strain induced martensite formation and its effect on strain hardening behavior in the cold drawn 304 austenitic stainless steels. *Scr. Mater.* **36**, 99–104 (1997).
  207. Jacques, P. On the physics and mechanics of phase transformations in TRIP-assisted multiphase steels. (Université catholique de Louvain, 1998).
  208. Basa, A., Thaulow, C. & Barnoush, A. Chemically Induced Phase Transformation in Austenite by Focused Ion Beam. *Metall. Mater. Trans. A* (2013). doi:10.1007/s11661-013-2101-4
  209. Johnson, E., Johansen, A., Sarholt-Kristensen, L. & Graabaek, L. Mossbauer and TEM Study of Martensitic Transformations in Ion Implanted 17/7 Stainless Steel. *Nucl. Instruments Methods Phys. Res. Sect. B* **19**,

- 171–176 (1987).
210. Knipling, K. E., Rowenhorst, D. J., Fonda, R. W. & Spanos, G. Effects of focused ion beam milling on austenite stability in ferrous alloys. *Mater. Charact.* **61**, 1–6 (2010).
  211. Gotte, L., Mendez, J., Villechaise, P. & Violan, P. Effect of the grain size on low cycle fatigue of copper polycrystals. *Fatigue '96. Sixth Int. Fatigue Congr.* **1**, 167–172 (1996).
  212. Llanes, L., Rollett, A. D., Laird, C. & Bassani, J. L. Effect of grain size and annealing texture on the cyclic response and the substructure evolution of polycrystalline copper. *Acta Metall. Mater.* **41**, 2667–2679 (1993).
  213. Mineur, M., Villechaise, P. & Mendez, J. Influence of the crystalline texture on the fatigue behavior of a 316L austenitic stainless steel. *Mater. Sci. Eng. A* **286**, 257–268 (2000).
  214. Morrison, D. J. Influence of Grain-Size and Texture on the Cyclic Stress-Strain Response of Nickel. *Mater. Sci. Eng. a-Structural Mater. Prop. Microstruct. Process.* **187**, 11–21 (1994).
  215. Carstensen, J. V. & Pedersen, O. B. Texture and grain-size effects on cyclic plasticity in copper and copper-zinc. *Mater. Sci. Eng. A* **234-236**, 497–500 (1997).
  216. Altenberger, I., Scholtes, B., Martin, U. & Oettel, H. Cyclic deformation and near surface microstructures of shot peened or deep rolled austenitic stainless steel AISI 304. *Mater. Sci. Eng. A* **264**, 1–16 (1999).
  217. Kruml, T., Polák, J. & Degallaix, S. Microstructure in 316LN stainless steel fatigued at low temperature. *Mater. Sci. Eng. A* **293**, 275–280 (2000).
  218. Olson, G. B. & Cohen, M. Annual Reviews. *Annu. Rev. Mater. Sci.* **11**, 415–430 (1981).
  219. Page, T. F., Oliver, W. C. & McHargue, C. J. The deformation behavior of ceramic crystals subjected to very low load (nano)indentations. *J. Mater. Res.* **7**, 450–473 (1992).
  220. Oila, A. & Bull, S. J. Atomistic simulation of Fe-C austenite. *Comput. Mater. Sci.* **45**, 235–239 (2009).
  221. Mao, W. G., Shen, Y. G. & Lu, C. Nanoscale elastic-plastic deformation and stress distributions of the C plane of sapphire single crystal during nanoindentation. *J. Eur. Ceram. Soc.* **31**, 1865–1871 (2011).
  222. Horstemeyer, M. F., Baskes, M. I. & Plimpton, S. J. Length scale and time scale effects on the plastic flow of fcc metals. *Acta Mater.* **49**, 4363–4374 (2001).
  223. Li, T. L., Gao, Y. F., Bei, H. & George, E. P. Indentation Schmid factor and orientation dependence of nanoindentation pop-in behavior of NiAl single crystals. *J. Mech. Phys. Solids* **59**, 1147–1162 (2011).
  224. Ngan, A. H. W., Zuo, L. & Wo, P. C. Size dependence and stochastic nature of yield strength of micron-sized crystals: a case study on Ni<sub>3</sub>Al. *Proc. R. Soc. A Math. Phys. Eng. Sci.* **462**, 1661–1681 (2006).
  225. Ohmura, T., Tsuzaki, K. & Yin, F. X. Nanoindentation-induced deformation behavior in the vicinity of single grain boundary of interstitial-free steel. *Mater. Trans.* **46**, 2026–2029 (2005).
  226. Barnoush, A., Welsch, M. T. & Vehoff, H. Correlation between dislocation density and pop-in phenomena in

- aluminum studied by nanoindentation and electron channeling contrast imaging. *Scr. Mater.* **63**, 465–468 (2010).
227. Barnoush, A. Correlation between dislocation density and nanomechanical response during nanoindentation. *Acta Mater.* **60**, 1268–1277 (2012).
  228. Yoshida, F. Uniaxial and biaxial creep-ratcheting behavior of SUS304 stainless steel at room temperature. *Int. J. Press. Vessel. Pip.* **44**, 207–223 (1990).
  229. Krempl, E. An experimental study of room-temperature rate-sensitivity, creep and relaxation of AISI type 304 stainless steel. *J. Mech. Phys. Solids* **27**, 363–375 (1979).
  230. Ohno, N. & Abdel-Karim, M. Uniaxial Ratchetting of 316FR Steel at Room Temperature— Part II: Constitutive Modeling and Simulation. *J. Eng. Mater. Technol.* **122**, 35 (2000).
  231. Kang, G., Ohno, N. & Nebu, A. Constitutive modeling of strain range dependent cyclic hardening. *Int. J. Plast.* **19**, 1801–1819 (2003).
  232. Chaboche, J. L. & Rousselier, G. On the Plastic and Viscoplastic Constitutive Equations - Part II: Applications of Internal Variable Concepts to the 316 Stainless Steel. *J. Press. Vessel Technol.* **105**, 159–164 (1983).
  233. Kujawski, D., Kallianpur, V. & Krempl, E. An experimental study of uniaxial creep, cyclic creep and relaxation of aisi type 304 stainless steel at room temperature. *J. Mech. Phys. Solids* **28**, 129–148 (1980).
  234. Mima, Y. & Ohno, N. Uniaxial Ratchetting of 316FR Steel at Room Temperature — Part I : Experiments. **122**, 29–34 (2000).
  235. Krempl, E. & Ruggles, M. B. The interaction of cyclic hardening and ratchetting for AISI type 304 stainless steel at room temperature-II. Modeling with the viscoplasticity theory based on overstress. *J. Mech. Phys. Solids* **38**, 587–597 (1990).
  236. Ruggles, M. B. & Krempl, E. The Influence of Test Temperature on the Ratchetting Behavior of Type 304 Stainless Steel. *J. Eng. Mater. Technol.* **111**, 378 (1989).
  237. Ellis, J. R., Robinson, D. N. & Pugh, C. E. Time Dependence in Biaxial Yield of Type 316 Stainless Steel at Room Temperature. *J. Eng. Mater. Technol.* **105**, 250 (1983).
  238. Figueroa, J. C., Bhat, S. P., De la Veaux, R., Murzenski, S. & Laird, C. The cyclic stress-strain response of copper at low strains-I. Constant amplitude testing. *Acta Metall.* **29**, 1667–1678 (1981).
  239. Llanes, L. & Laird, C. EFFECT OF LOADING MODE ON THE CYCLIC RESPONSE AND THE ASSOCIATED SUBSTRUCTURE OF POLYCRYSTALLINE COPPER IN THE HIGH-CYCLE REGIME. *Fatigue Fract. Eng. Mater. Struct.* **16**, 165–179 (1993).
  240. Llanes, L. & Laird, C. Substructure evolution of copper polycrystals under different testing conditions: conventional strain control and ramp loading. *Mater. Sci. Eng. A* **161**, 1–12 (1993).



241. Liu, Y. *et al.* Orientation effects in nanoindentation of single crystal copper. *Int. J. Plast.* **24**, 1990–2015 (2008).
242. Oliver, W. & Pharr, G. An improved technique for determining hardness and elastic modulus using load and displacement sensing indentation experiments. *J. Mater. Res.* **7**, 1564–1583 (1992).
243. Berrahmoune, M. R. Transformation martensitique et rupture différée dans l'acier austénitique instable 301In. (École Nationale Supérieure d'Arts et Métiers, 2006).
244. Weidner, A., Hangen, U. D. & Biermann, H. Nanoindentation measurements on deformation-induced  $\alpha'$ -martensite in a metastable austenitic high-alloy CrMnNi steel. *Philos. Mag. Lett.* **94**, 522–530 (2014).
245. Raman, S. G. S. & Padmanabhan, K. A. Influence of martensite formation and grain size on room temperature cycle fatigue behaviour of AISI 304LN austenitic stainless steel. **10**, 614–620 (1994).
246. Niewczas, M. Latent hardening effects in low cycle fatigue of copper single crystals. *Philos. Mag.* **6435**, 1–32 (2012).
247. Glage, A., Weidner, A. & Biermann, H. Effect of austenite stability on the low cycle fatigue behavior and microstructure of high alloyed metastable austenitic cast TRIP-steels. *Procedia Eng.* **2**, 2085–2094 (2010).
248. Yang, F., Peng, L. & Okazaki, K. Cyclic indentation in aluminum. *J. Mater. Sci.* **42**, 4513–4520 (2007).
249. Laird, C., Charsley, P. & Mughrabi, H. Low energy dislocation structures produced by cyclic Deformation. *Mater. Sci. Eng. A* **81**, 433–450 (1986).
250. Sawaguchi, T. *et al.* Mechanism of reversible transformation-induced plasticity of Fe–Mn–Si shape memory alloys. *Scr. Mater.* **59**, 826–829 (2008).
251. Kajiwar, S. & Kikuchi, T. Shape memory effect and related transformation behavior in FeNiC alloys. *Acta Metall. Mater.* **38**, 847–855 (1990).
252. Li, C. L., Cheng, D. J. & Jin, Z. H. Influence of deformation temperature on shape memory effect of Fe–Mn–Si–Ni–Cr alloy. *Mater. Sci. Eng. A* **325**, 375–379 (2002).
253. Koohdar, H., Nili-ahmadabadi, M., Habibi-parsa, M. & Ghasemi-nanesa, H. Investigating on the reverse transformation of martensite to austenite and Pseudoelastic behavior in Ultrafine-Grained Fe-10Ni-7Mn ( wt %) Steel processed by heavy cold rolling. **829**, 25–29 (2014).
254. Sawaguchi, T., Kikuchi, T. & Kajiwar, S. The pseudoelastic behavior of Fe–Mn–Si-based shape memory alloys containing Nb and C. *Smart Mater. Struct.* **14**, S317–S322 (2005).
255. Baruj, A., Bertolino, G. & Troiani, H. E. Temperature dependence of critical stress and pseudoelasticity in a Fe–Mn–Si–Cr pre-rolled alloy. *J. Alloys Compd.* **502**, 54–58 (2010).
256. Wang, X. & Zhang, C. Pseudoelastic behavior in an Fe–Mn–Si–Ni–Co shape memory alloy. *J Mater. Sci. Lett.* **17**, 1795–1796 (1998).
257. Koohdar, H. R., Nili-Ahmadabadi, M., Habibi-Parsa, M. & Jafarian, H. R. Development of pseudoelasticity

- in Fe-10Ni-7Mn (wt%) high strength martensitic steel by intercritical heat treatment and subsequent ageing. *Mater. Sci. Eng. A* **621**, 52–60 (2015).
258. Caër, C., Patoor, E., Berbenni, S. & Lecomte, J.-S. Stress induced pop-in and pop-out nanoindentation events in CuAlBe shape memory alloys. *Mater. Sci. Eng. A* **587**, 304–312 (2013).
  259. Petein, A. On the interactions between strain-induced phase transformations and mechanical properties in Mn-Si-Al steels and Ni-Cr austenitic steels Chapter VI : Influence of Strain- induced Phase Transformations on the Mechanical Properties of Fe-Ni-Cr and Fe-Mn-Si.
  260. Nascimento, F. C., Bueno, J. C., Lepienski, C. M., Otubo, J. & Mei, P. R. Determinação das propriedades mecânicas da martensita-eps; por indentação instrumentada em ligas inoxidáveis com memória de forma. *Rem Rev. Esc. Minas* **63**, 39–44 (2010).
  261. Golovin, Y. I., Ivolgin, V. I., Khonik, V. a & Kitagawa, K. Serrated plastic flow during nanoindentation of a bulk metallic glass. *Scr. Mater.* **45**, 947–952 (2001).
  262. Huang, H., Zhang, J., Shek, C.-H. & Yan, J. Effects of pre-compression deformation on nanoindentation response of Zr65Cu15Al10Ni10 bulk metallic glass. *J. Alloys Compd.* (2016). doi:10.1016/j.jallcom.2016.03.057
  263. Yoo, B.-G., Kim, J.-Y. & Jang, J. Influence of Indenter Geometry on the Deformation Behavior of Zr60Cu30Al10 Bulk Metallic Glass during Nanoindentation. *Mater. Trans.* **48**, 1765–1769 (2007).
  264. Laplanche, G., Pfetzinger-Micklich, J. & Eggeler, G. Sudden stress-induced transformation events during nanoindentation of NiTi shape memory alloys. *Acta Mater.* **78**, 144–160 (2014).
  265. Kubo, H., Nakamura, K., Farjami, S. & Maruyama, T. Characterization of Fe-Mn-Si-Cr shape memory alloys containing VN precipitates. *Mater. Sci. Eng. A* **378**, 343–348 (2004).
  266. Nanga, S., Pineau, A., Tanguy, B. & Santacreu, P. 17th European Conference on Fracture Strain Induced Martensitic Transformations in two Austenitic Stainless Steels : Macro-Micro Behaviour 17th European Conference on Fracture. 1373–1380 (2008).
  267. Ahn, T.-H., Oh, C.-S., Lee, K., George, E. P. & Han, H. N. Relationship between yield point phenomena and the nanoindentation pop-in behavior of steel. *J. Mater. Res.* **27**, 39–44 (2012).
  268. Chudoba, T. & Richter, F. Investigation of creep behaviour under load during indentation experiments and its influence on hardness and modulus results. *Surf. Coatings Technol.* **148**, 191–192 (2001).
  269. R. Abeyaratne, J. K. K. *Evolution of phase transitions A Continuum theory*. (Cambridge University Press, 2006).
  270. Kim, Y.-J., Choi, I.-C., Lee, J.-A., Seok, M.-Y. & Jang, J. Strain-dependent transition of time-dependent deformation mechanism in single-crystal ZnO evaluated by spherical nanoindentation. *Philos. Mag.* **95**, 1896–1906 (2014).
  271. Li, J. C. M. & Chu, S. N. G. Impression Fatigue. *Scr. Metall.* **13**, 1021–1026 (1979).

272. Wang, M. G. & Ngan, A. H. W. Indentation strain burst phenomenon induced by grain boundaries in niobium. *J. Mater. Res.* **19**, 2478–2486 (2004).
273. Soer, W. A., Aifantis, K. E. & Hosson, J. T. M. De. Incipient plasticity during nanoindentation at grain boundaries in body-centered cubic metals. **53**, 4665–4676 (2005).
274. Britton, T. B., Randman, D. & Wilkinson, A. J. Nanoindentation study of slip transfer phenomenon at grain boundaries. *J. Mater. Res.* **24**, 607–615 (2009).
275. Ohmura, T. & Tsuzaki, K. Plasticity initiation and subsequent deformation behavior in the vicinity of single grain boundary investigated through nanoindentation technique. *J. Mater. Sci.* **42**, 1728–1732 (2007).
276. Yang, B. & Vehoff, H. Dependence of nanohardness upon indentation size and grain size - A local examination of the interaction between dislocations and grain boundaries. *Acta Mater.* **55**, 849–856 (2007).
277. Tsurekawa, S., Chihara, Y., Tashima, K., Ii, S. & Lej??ek, P. Local plastic deformation in the vicinity of grain boundaries in Fe-3 mass% Si alloy bicrystals and tricrystal. *J. Mater. Sci.* **49**, 4698–4704 (2014).
278. Maier, V., Merle, B., Göken, M. & Durst, K. An improved long-term nanoindentation creep testing approach for studying the local deformation processes in nanocrystalline metals at room and elevated temperatures. *J. Mater. Res.* **28**, 1177–1188 (2013).
279. Bower, A. F., Fleck, N. A., Needleman, A. & Ogbonna, N. Indentation of a power law creeping solid. *Proc. R. Soc. London Ser. A Math. Phys. Sci.* **441**, 97–124 (1993).
280. Pharr, G. M., Oliver, W. C. & Brotzen, F. R. On the generality of the relationship among contact stiffness, contact area, and elastic-modulus during indentation. *J. Mater. Res.* **7**, 613–617 (1992).
281. Oliver, W. C. & Pharr, G. M. Measurement of hardness and elastic modulus by instrumented indentation: Advances in understanding and refinements to methodology. *J. Mater. Res.* **19**, 3–20 (2004).
282. King, R. B. Elastic analysis of some punch problems for a layered medium. *Int. J. Solids Struct.* **23**, 1657–1664 (1987).
283. Villechaise, P., Mendez, J. & Violan, P. Cyclic behaviour and surface slip features in  $\langle 111 \rangle$  oriented copper single crystals. *Acta Metall. Mater.* **39**, 1683–1691 (1991).
284. Roa, J. J., Fargas, G., Mateo, A. & Jiménez-Piqué, E. Dependence of nanoindentation hardness with crystallographic orientation of austenite grains in metastable stainless steels. *Mater. Sci. Eng. A* **645**, 188–195 (2015).
285. Dahlberg, C. F. O., Saito, Y., Öztö, M. S. & Kysar, J. W. Geometrically necessary dislocation density measurements associated with different angles of indentations. *Int. J. Plast.* **54**, 81–95 (2014).
286. Villechaise, P., Mendez, J. & Violan, P. Analysis of [100] slip traces in  $\langle 111 \rangle$  -oriented copper crystals cyclically strained at room temperature. *Mater. Sci. Eng. A* **141**, L9–L13 (1991).
287. Marinelli, M.-C. *et al.* Activated slip systems and microcrack path in LCF of a duplex stainless steel. *Mater.*

- Sci. Eng. A* **509**, 81–88 (2009).
288. Chang, S. C. & Chen, H. C. The determination of F.C.C. crystal orientation by indentation. *Acta Metall. Mater.* **43**, 2501–2505 (1995).
  289. Bergeon, N., Guenin, G. & Esnouf, C. Characterization of the stress-induced  $\epsilon$  martensite in a Fe–Mn–Si–Cr–Ni shape memory alloy: microstructural observation at different scales, mechanism of formation and growth. *Mater. Sci. Eng. A* **238**, 309–316 (1997).
  290. Yang, J. H. & Wayman, C. M. Self-accommodation and shape memory mechanism of  $\epsilon$ -martensite—I. Experimental observations. *Mater. Charact.* **28**, 23–35 (1992).
  291. Byun, T. S. On the stress dependence of partial dislocation separation and deformation microstructure in austenitic stainless steels. *Acta Mater.* **51**, 3063–3071 (2003).
  292. Cakmak, E., Choo, H., Kang, J.-Y. & Ren, Y. Relationships Between the Phase Transformation Kinetics, Texture Evolution, and Microstructure Development in a 304L Stainless Steel Under Biaxial Loading Conditions: Synchrotron X-ray and Electron Backscatter Diffraction Studies. *Metall. Mater. Trans. A* **46**, 1860–1877 (2015).
  293. Patel, J. R. & Cohen, M. Criterion for the action of applied stress in the martensitic transformation. *Acta Metall.* **1**, 531–538 (1953).
  294. Miller, A., Estrin, Y. & Hu, X. Z. Magnetic force microscopy of fatigue crack tip region in a 316L austenitic stainless steel. *Scr. Mater.* **47**, 441–446 (2002).
  295. Wu, S. Z., Liang, Z. Y., He, B. B. & Huang, M. X. Martensitic transformation in micron-sized Fcc single crystals. *Metall. Mater. Trans. A Phys. Metall. Mater. Sci.* **45**, 4731–4736 (2014).
  296. Bhadeshia, H. K. D. H. & Honeycombe, R. W. K. *Steels: Microstructure and Properties: Microstructure and Properties*. (Elsevier, Butterworth-Heinemann, 2006).
  297. Iwamoto, T., Tsuta, T. & Tomita, Y. Investigation on deformation mode dependence of strain-induced martensitic transformation in TRIP steels and modelling of transformation kinetics. *Int. J. Mech. Sci.* **40**, 173–182 (1998).
  298. Hausild, P., Nohava, J. & Pilvin, P. Characterisation of strain-induced martensite in a metastable austenitic stainless steel by nanoindentation. *Strain* **47**, 129–133 (2011).
  299. Murakami, Y. & Itokazu, M. Elastic-plastic analysis of triangular pyramidal indentation. *Int. J. Solids Struct.* **34**, 4005–4018 (1997).
  300. Miura, T., Fujii, K., Fukuya, K. & Takashima, K. Influence of crystal orientation on hardness and nanoindentation deformation in ion-irradiated stainless steels. *J. Nucl. Mater.* **417**, 984–987 (2011).
  301. Chen, J. & Bull, S. J. On the relationship between plastic zone radius and maximum depth during nanoindentation. *Surf. Coatings Technol.* **201**, 4289–4293 (2006).

302. Chiu, Y. L. & Ngan, A. H. W. A TEM investigation on indentation plastic zones in Ni<sub>3</sub>Al(Cr,B) single crystals. *Acta Mater.* **50**, 2677–2691 (2002).
303. Zaafarani, N., Raabe, D., Roters, F. & Zaefferer, S. On the origin of deformation-induced rotation patterns below nanoindents. *Acta Mater.* **56**, 31–42 (2008).
304. Gan, Y. X. Analysis of stress and deformation states in wedge indented face-centered cubic single crystals. *Mater. Sci. Eng. A* **485**, 589–600 (2008).
305. Kysar, J. W., Saito, Y., Oztop, M. S., Lee, D. & Huh, W. T. Experimental lower bounds on geometrically necessary dislocation density. *Int. J. Plast.* **26**, 1097–1123 (2010).
306. Reuber, C., Eisenlohr, P., Roters, F. & Raabe, D. Dislocation density distribution around an indent in single-crystalline nickel: Comparing nonlocal crystal plasticity finite-element predictions with experiments. *Acta Mater.* **71**, 333–348 (2014).
307. Rester, M., Motz, C. & Pippan, R. Microstructural investigation of the deformation zone below Nano-Indents in Copper. in *Mater. Res. Soc. Symp. Proc.* **1049**, 6427–6435 (2008).
308. Kiener, D., Durst, K., Rester, M. & Minor, a. M. Revealing deformation mechanisms with nanoindentation. *JOM-JOURNAL Met.* **61**, 14–23 (2009).
309. Park, H. S., Han, J. C., Lim, N. S. & Park, C. G. Nano-scale observation on the transformation behavior and mechanical stability of individual retained austenite in CMnSiAl TRIP steels. *Mater. Sci. Eng. A* **627**, 262–269 (2015).
310. Kim, Y., Ahn, T. H., Suh, D. W. & Han, H. N. Variant selection during mechanically induced martensitic transformation of metastable austenite by nanoindentation. *Scr. Mater.* **104**, 13–16 (2015).
311. Takaki, S., Tomimura, K. & Ueda, S. Effect of pre-cold-working on diffusional reversion of deformation induced martensit in metastable austenitic stainless steel. *ISIJ Int.* **34**, 522–527 (1994).
312. Das, A. Magnetic properties of cyclically deformed austenite. *J. Magn. Magn. Mater.* **361**, 232–242 (2014).
313. Das, A., Sivaprasad, S., Chakraborti, P. C. & Tarafder, S. Connection between deformation-induced dislocation substructures and martensite formation in stainless steel. *Philos. Mag. Lett.* **91**, 664–675 (2011).
314. Das, A., Sivaprasad, S., Chakraborti, P. C. & Tarafder, S. Morphologies and characteristics of deformation induced martensite during low cycle fatigue behaviour of austenitic stainless steel. *Mater. Sci. Eng. A* **528**, 7909–7914 (2011).
315. Reed-Hill, R. E. & Abbaschian, R. *Physical Metallurgy Principles*. Stamford, CT (PWS Publishing Company, 2015).
316. Bayerlein, M. & Mughrabi, H. The formation of wither tongue- or ribbon-like extrusions in fatigued copper polycrystals. *Acta Metall. Mater.* **39**, 1645–1650 (1991).
317. Das, A. Dislocation configurations through austenite grain misorientations. *Int. J. Fatigue* **70**, 473–479

- (2015).
318. Yun, J. Y. *et al.* Effect of strain-induced  $\epsilon$  and  $\alpha'$ -martensitic transformation on cavitation erosion resistance in austenitic Fe-Cr-C-Mn alloys. *Wear* **338-339**, 379–384 (2015).
  319. Guo, Y. *et al.* Measurements of stress fields near a grain boundary: Exploring blocked arrays of dislocations in 3D. *Acta Mater.* **96**, 229–236 (2015).
  320. Zhang, L., Ohmura, T., Shibata, A. & Tsuzaki, K. Characterization of local deformation behavior of Fe-Ni lenticular martensite by nanoindentation. *Mater. Sci. Eng. A* **527**, 1869–1874 (2010).
  321. Manganon, P. L. & Thomas, G. The martensite phase in 304 stainless steel. *Met. Trans.* **1**, 1577–1586 (1970).
  322. Wenk, H. R., Huensche, I. & Kestens, L. In-situ observation of texture changes during phase transformations in ultra-low-carbon steel. *Metall. Mater. Trans. A Phys. Metall. Mater. Sci.* **38**, 261–267 (2007).
  323. Sato, H. & Zaefferer, S. A study on the formation mechanisms of butterfly-type martensite in Fe-30% Ni alloy using EBSD-based orientation microscopy. *Acta Mater.* **57**, 1931–1937 (2009).
  324. Mine, Y., Hirashita, K., Matsuda, M. & Takashima, K. Martensite formation in hydrogen-containing metastable austenitic stainless steel during micro-tension testing. *Metall. Mater. Trans. A Phys. Metall. Mater. Sci.* **42**, 3567–3571 (2011).
  325. RAY, R. & JONAS, J. TRANSFORMATION TEXTURES IN STEELS. *Int. Mater. Rev.* **35**, 1–36 (1990).
  326. Brückner, G., Gottstein, G. & Köntges, A. Microstructure and texture development during the phase transformation in an Fe-Ni-Co-Ti shape memory alloy. *Steel Res.* **70**, 188–192 (1999).
  327. Jonas, J. J., He, Y. & Godet, S. The possible role of partial dislocations in facilitating transformations of the Nishiyama-Wassermann type. *Scr. Mater.* **52**, 175–179 (2005).
  328. Durlu, T. N. Effects of high austenitizing temperature and austenite deformation on formation of martensite in Fe-Ni-C alloys. *J. Mater. Sci.* **36**, 5665–5671 (2001).
  329. Maki, T. Microstructure and Mechanical Behaviour of Ferrous Martensite. *Mater. Sci. Forum* **56-58**, 157–168 (1990).
  330. Chilton, J. M., Barton, C. J. & Speich, G. R. Martensite Transformation in Low-Carbon Steels. *J. Iron Steel Inst.* **Feb**, 184–193 (1970).
  331. Schoen, F. J., Nilles, J. L. & Owen, W. S. Crystallographic aspects of Fe-Ni and Fe-Ni-C dilute alloy martensites. *Metall. Trans.* **2**, 2489–2494 (1971).
  332. Wakasa, K. & Wayman, C. M. Crystallography and morphology of ferrous lath martensite. *Metallography* **14**, 49–60 (1981).
  333. Kelly, P. M., Jostsons, A. & Blake, R. G. The orientation relationship between lath martensite and austenite in low carbon, low alloy steels. *Acta Metall. Mater.* **38**, 1075–1081 (1990).

334. Zhang, M. X. & Kelly, P. M. Accurate orientation relationship between ferrite and austenite in low carbon martensite and granular bainite. *Scr. Mater.* **47**, 749–755 (2002).
335. Fearon, E. O. & Bevis, M. The macromorphology, micromorphology, habit planes and orientation relationships associated with martensite crystals formed in a range of iron 30-34 per cent nickel alloys. *Acta Metall.* **22**, 991–1002 (1974).
336. Yang, H. Y., Li, J. & Yang, P. The change of orientation relationships between austenite and alpha'-martensite during deformation in high manganese trip steel. *Acta Metall. Sin. (English Lett.)* **28**, 289–294 (2015).
337. Korzekwa, D. A., Matlock, D. K. & Krauss, G. Dislocation substructure as a function of strain in a dual-phase steel. *Metall. Trans. A* **15**, 1221–1228 (1984).
338. Kim, D. H. *et al.* Microtexture development during equibiaxial tensile deformation in monolithic and dual phase steels. *Acta Mater.* **59**, 5462–5471 (2011).
339. Sarosiek, A. M. & Owen, W. S. On the importance of extrinsic transformation accommodation hardening in dual-phase steels. *Scr. Metallurgica* **17**, 227–231 (1983).
340. Alcalá, J., Esqué-de los Ojos, D. & Očenášek, J. Continuum crystal plasticity analyses of the plastic flow features underneath single-crystal indentations. *Philos. Mag.* **91**, 1050–1069 (2011).
341. Esqué-De Los Ojos, D., Očenášek, J. & Alcalá, J. Sharp indentation crystal plasticity finite element simulations: Assessment of crystallographic anisotropy effects on the mechanical response of thin fcc single crystalline films. *Comput. Mater. Sci.* **86**, 186–192 (2014).
342. Stringfellow, R. G., Parks, D. M. & Olson, G. B. A constitutive model for transformation plasticity accompanying strain-induced martensitic transformations in metastable austenitic steels. *Acta Metall. Mater.* **40**, 1703–1716 (1992).
343. Tao, K. *et al.* In situ neutron diffraction study of grain-orientation-dependent phase transformation in 304L stainless steel at a cryogenic temperature. *J. Appl. Phys.* **100**, (2006).
344. Oliver, E. C., Withers, P. J., Daymond, M. R., Ueta, S. & Mori, T. Neutron-diffraction study of stress-induced martensitic transformation in TRIP steel. *Appl. Phys. A Mater. Sci. Process.* **74**, 1143–1145 (2002).
345. Breedis, J. . Influence of dislocation substructure on the martensitic transformation in stainless steel. *Acta Metall.* **13**, 239–250 (1965).
346. Shimano, H. *et al.* Analysis of partially pulsating fatigue process on carbon steel with microstructural observation. *Mater. Sci. Eng. A* **651**, 83–88 (2016).
347. Kuhlmann-Wilsdorf, D. & Laird, C. Dislocation behavior in fatigue. *Mater. Sci. Eng.* **27**, 137–156 (1977).
348. Sauzay, M. & Jourdan, T. Polycrystalline microstructure, cubic elasticity, and nucleation of high-cycle fatigue cracks. *Int. J. Fract.* **141**, 431–446 (2006).

349. Vachhani, S. J. & Kalidindi, S. R. Grain-scale measurement of slip resistances in aluminum polycrystals using spherical nanoindentation. *Acta Mater.* **90**, 27–36 (2015).
350. Huang, H. L. A study of dislocation evolution in polycrystalline copper during low cycle fatigue at low strain amplitudes. **342**, 38–43 (2003).
351. Mecke, K., Blochwitz, C. & Kremling, U. The Development of the Dislocation Structures during the Fatigue Process of FCC Single Crystals. *Cryst. Res. Technol.* **17**, 1557–1570 (1982).
352. Steckmeyer, A., Sauzay, M., Weidner, A. & Hieckmann, E. Micromechanical modelling of the cyclic stress-strain behaviour of nickel polycrystals. *Int. J. Fatigue* **40**, 154–167 (2012).
353. Viswanathan, G. B., Lee, E., Maher, D. M., Banerjee, S. & Fraser, H. L. Direct observations of dislocation substructures formed by nano-indentation of the  $\alpha$ -phase in an  $\alpha/\beta$  titanium alloy. *Mater. Sci. Eng. A* **400–401**, 463–466 (2005).
354. Misra, R. D. K. *et al.* On the Significance of Nature of Strain-Induced Martensite on Phase-Reversion-Induced Nanograined/Ultrafine-Grained Austenitic Stainless Steel. *Metall. Trans. A* **41**, 3–12 (2009).
355. Rajasekhara, S., Karjalainen, L. P., Kyröläinen, A. & Ferreira, P. J. Microstructure evolution in nano/submicron grained AISI 301LN stainless steel. *Mater. Sci. Eng. A* **527**, 1986–1996 (2010).
356. Das, A. Slip System Activity During Cyclic Plasticity. *Metall. Mater. Trans. A* **45**, 2927–2930 (2014).
357. Tarrago, J. M. *et al.* Fracture and Fatigue Behaviour of Cemented Carbides: 3-D FIB Tomography of Crack-microstructure Interactions. *Int. J. Powder Metall.* **50**, 254–266 (2014).
358. Gutierrez-Urrutia, I., Zaefferer, S. & Raabe, D. Electron channeling contrast imaging of twins and dislocations in twinning-induced plasticity steels under controlled diffraction conditions in a scanning electron microscope. *Scr. Mater.* **61**, 737–740 (2009).
359. Uchic, M. D., Groeber, M. A., Dimiduk, D. M. & Simmons, J. P. 3D microstructural characterization of nickel superalloys via serial-sectioning using a dual beam FIB-SEM. *Scr. Mater.* **55**, 23–28 (2006).
360. Ingemarsson, L. *et al.* Oxidation behavior of a Mo(Si,Al)<sub>2</sub> composite at 900–1600 °C in dry air. *J. Mater. Sci.* **48**, 1511–1523 (2013).
361. Orloff, J. High-resolution focused ion beams. *Rev. Sci. Instrum.* **64**, 1105 (1993).
362. Kang, G., Gao, Q. & Yang, X. A visco-plastic constitutive model incorporated with cyclic hardening for uniaxial/multiaxial ratcheting of SS304 stainless steel at room temperature. *Mech. Mater.* **34**, 521–531 (2002).
363. Yamada, H. & Li, C.-Y. Stress relaxation and mechanical equation of state in austenitic stainless steels. *Metall. Trans.* **4**, 2133–2136 (1973).
364. Albertini, C. & Montagnani, M. Dynamic uniaxial and biaxial stress-strain relationships for austenitic stainless steels. *Nucl. Eng. Des.* **57**, 107–123 (1980).



- 365. Lebedev, A. A. & Kosarchuk, V. V. Influence of phase transformations on the mechanical properties of austenitic stainless steels. *Int. J. Plast.* **16**, 749–767 (2000).
- 366. Bannykh, O. A., Koveneristyi, Y. K. Steels for operation at low temperatures. *Metall. Moscow* 13 (1969).
- 367. Reed, R. P. & Horiuchi, T. *Austenitic Steels at Low Temperatures. Aging* **7**, (1983).
- 368. Pavlov, I. M., Bannykh, O. A., Mekhed, G. I. & Chulanov, O. B. *Plastic Deformation of Metals and Alloys*. (Nauka, 1979).

# Abstract

## Keywords:

Metastable austenitic stainless steels, Phase transformation, Cyclic nanoindentation, Plastic deformation mechanisms, Transmission electron microscopy (TEM), Focused ion beam (FIB), Scanning ion microscopy (SIM), Crystalline anisotropy, Grain size, Plasticity transmission

Metastable austenitic stainless steels feature an abundance of different deformation mechanisms, which contribute to the distinguished mechanical properties of these alloys. However, these properties are known to depend on the local microstructure and also are highly anisotropic. Furthermore, deformation is expected to be different for the bulk and the surface of a sample. In this sense, a discrete study is not trivial.

The present work aims at investigation of the main deformation mechanisms and their gradual evolution, by employing controlled deformation of individual austenite grains via monotonic and cyclic nanoindentation. The corresponding loading–unloading curves have given extensive information about underlying mechanical properties, which could be related to an exhaustive reconstruction of the deformation substructure, both in surface and bulk, by different small scale characterization techniques.

Amongst others, features such as time-dependent deformation, reversible phase transformation under load, crystalline anisotropy and grain size influences, besides plasticity transmission and fatigue behavior have been found and analyzed.

## Resumen

### Palabras claves:

Aceros inoxidables austeníticos metaestables, Transformación de fase, Indentación cíclica, Mecanismos de deformación plástica, Microscopía electrónica de transmisión (MET), FIB, SIM, Anisotropía cristalina, Tamaño de grano, Transferencia de plasticidad

Los aceros inoxidables austeníticos metaestables pueden experimentar una amplia gama de mecanismos de deformación diferentes, los cuales contribuyen a sus extraordinarias propiedades mecánicas. Sin embargo, estas propiedades dependen de la microestructura y son altamente anisotrópicas. Además, la deformación es diferente en la superficie y en el interior de una muestra. Por lo tanto, un estudio detallado no resulta trivial. El objetivo de este trabajo es el estudio de los principales mecanismos de deformación, así como de su desarrollo gradual. Para ello se han realizado ensayos de nanoindentación, tanto monotónica como cíclica, los cuales han permitido la deformación controlada de granos austeníticos preseleccionados.

Las curvas de carga y descarga de los ensayos de nanoindentación han proporcionado amplia información sobre el comportamiento mecánico del acero, la cual se ha podido correlacionar con la reconstrucción detallada de las subestructuras de deformación, tanto a nivel superficial como en el interior, la cual se ha llevado a cabo mediante técnicas de caracterización a escala microscópica.

Entre otros, se encontraron y estudiaron fenómenos como las transformaciones de fase reversibles bajo carga, la influencia tanto de la anisotropía cristalina como del tamaño de grano, mecanismos dependientes del tiempo, junto con la transmisión de plasticidad y la respuesta a fatiga.

## Résumé

### Mots-clefs:

Aciers austénitiques métastables, Transformation de phase, Nano-indentation cyclique, Mécanismes de déformation plastique, Microscopie électronique en transmission (MET), Sonde ionique focalisée (FIB), Microscope ionique à balayage (SIM), Anisotropie cristalline, Taille de grain, Transfert de plasticité

Les aciers inoxydables austénitiques métastables sont le siège de différents mécanismes de déformation qui sont à l'origine des propriétés mécaniques qui distinguent ce type d'alliages. Cependant, ces dernières, dépendant de la microstructure locale, sont fortement anisotropes.

Par ailleurs, la déformation d'un échantillon massif serait différente de celle obtenue en surface. De ce fait, une étude détaillée trouve tout son intérêt. Le présent travail vise donc à identifier les principaux mécanismes de déformation et de leur évolution progressive, en se basant sur une déformation contrôlée de grains austénitiques individuels par des tests mécaniques de nanoindentation monotoniques et cycliques.

Les courbes correspondantes au chargement-déchargement révèlent des informations détaillées sur les propriétés mécaniques sous-jacentes qui pourraient être liées à une étude complète de la structure de déformation en surface et en volume par différentes techniques de caractérisation à une échelle très fine.

La déformation en fonction du temps, les phénomènes de transformation de phase réversible sous charge, l'anisotropie cristalline, l'influences de la taille des grains, la transmission de la plasticité et la tenue en fatigue ont été mis en évidence et étudiés.